Search for Non-Minimal Higgs Bosons in Z^0 Decays with the L3 Detector at LEP

Thesis-1992-Sopczak

Search for Non-Minimal Higgs Bosons in Z^0 Decays with the L3 Detector at LEP

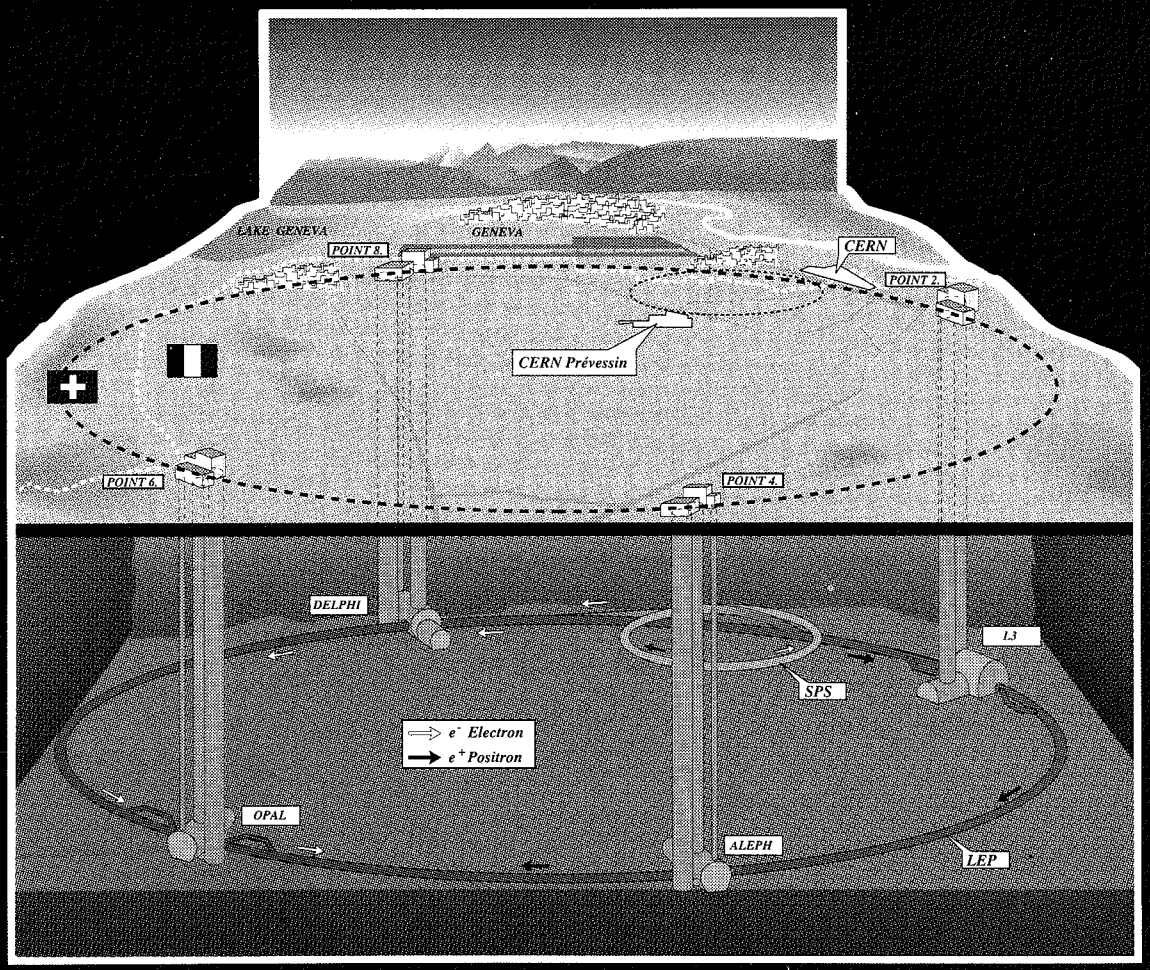

André Sopczak

CERN LIBRARIES, GENEVA

Search for Non-Minimal Higgs Bosons in Z^0 Decays with the L3 Detector at LEP

UNIVERSITY OF CALIFORNIA, SAN DIEGO

Search for Non-Minimal Higgs Bosons in Z^0 Decays with the L3 Detector at LEP

A dissertation submitted in partial satisfaction of the requirements for the degree Doctor of Philosophy in Physics

by

André Sopczak

Committee in charge:

Professor James G. Branson, Chair
Professor David B. Kaplan
Professor Hans P. Paar
Professor Linda P. Rothschild
Professor James P. Lin

October 1992

The dissertation of André Sopczak is approved, and it is acceptable in quality and form for publication on microfilm:

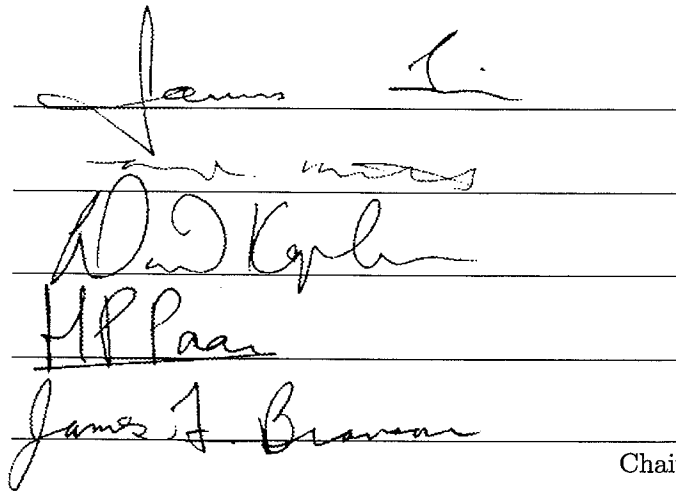

Chair

University of California, San Diego

1992

Diese Doktorarbeit ist meinen Eltern gewidmet.

Der theoretisch arbeitende Naturforscher ist nicht zu beneiden, denn die Natur, oder genauer gesagt: das Experiment, ist eine unerbittliche und wenig freundliche Richterin seiner Arbeit. Sie sagt zu einer Theorie nie *ja* sondern im günstigsten Falle *vielleicht*, in den meisten Fällen aber einfach *nein*. Stimmt ein Experiment zur Theorie, bedeutet es für letztere *vielleicht*, stimmt es nicht, so bedeutet es *nein*. Wohl jede Theorie wird einmal ihr *nein* erleben, die meisten Theorien schon bald nach ihrer Entstehung.

Albert Einstein, 11. November 1922

Table of Contents

List of Figures

List of Tables

Acknowledgments

Over the more than two years that the work described in this thesis has taken, many people have helped me. Without their support, this work would have been impossible. First, I would like to thank my collaborators from the L3 experiment and especially Prof. Samuel C.C. Ting for his impressive leadership. They provided a very stimulating and challenging environment.

I express my greatest appreciation to my thesis advisor, Prof. James G. Branson. His experience, guidance and tolerance led to fruitful results and he also made working with him very enjoyable.

I am very thankful to Prof. David Kaplan for many theoretical discussions during which he explained to me many insights of particle physics. I am indebted to Prof. Julius Kuti for sharing some of his deep understanding of this field. I would also like to thank Profs. Stefan Pokorsky and Howard Haber, and Dr. Fabio Zwirner for cheerfully answering my numerous questions on the theoretical aspects of this work.

I am grateful to Prof. Harvey Newman for his valuable instruction on Monte Carlo simulations during my first year in the L3 collaboration. I thank Martin Grünewald, Dr. Tofigh Azemoon and Dr. Torbjorn Sjöstrand for discussions and help with the many simulations.

Drs. Thomas Hebbeker, Andrey Kunin, David Stickland, Jian Qian, Robert Clare, Vincenzo Innocente and Krishna Kumar gave me much valuable advice. For assistance with figures, I acknowledge Dr. Marcel Merk, Susan Shotkin and Dr. Joachim Rose.

I enjoyed the collaboration with the Minimal Standard Model Higgs group, led by Dr. Andrey Kunin. I especially enjoyed working with Prof. Jean-Paul Martin, Dr. Patrice Lebrun, Luca Lista, Valeri Andreev, Prof. Bianca Monteleoni, Simone Paoletti, Dr. Marco Pieri, Dr. Luciano Barone and Elisabetta Gallo.

On the 1990 data analysis I gratefully acknowledge collaborating with Prof.

Panos Rasiz and Dr. Som Ganguli, and on the 1991 data analysis with Dr. Marta Felcini, Bernd Lindemann and Prof. Atul Gurtu. Their suggestions and advice greatly improved this work.

For advice and proof-reading of a large part of this thesis at an early stage, I am indebted to Dr. Irwin Sheer. For their advice on finalizing the text, I thank Profs. José Salicio, Martin Pohl, Guy Coignet, Remy van de Walle, and Drs. Mokhtar Chmeissani and Richard Mount.

I am very thankful to Dr. Jean-Jacques Blaising for teaching me about the detector run control and the complex trigger system.

I would like to acknowledge the effort of the engineers and technicians for maintaining the performance of the LEP accelerator, and Ingrid Clare and Dr. Robert Clare for running the data production.

I thank Profs. Samuel C.C. Ting and Antonio Zichichi for invitating me to the informative Erice 1992 Summer School.

For good collaboration and many discussions with Drs. Eilam Gross, Ehud Duchovni, Peter Sherwood and Jean-François Grivaz in preparation for a plenary talk on Higgs searches, I am very thankful.

Within the UCSD community, I am particularly grateful for help and assistance from Michael Hebert, Gary Greenbaum, Dirk Hartmann, Tim Mitchell, Joan Yap, Debra Bomar and Bonnie Horstmann. I thank my thesis committee Profs. David Kaplan, Hans Paar, Linda Rothschild and James Lin for taking the time to review my work.

My four years in graduate school were a great pleasure due to the support and encouragement of many friends. Thank you very much!

Finally, I would like to express gratitude to my family, especially my parents, Peter and Annette Sopczak, for their continuous support.

-André.

Vitæ

August 14, 1965	Born, Bochum, Germany
1985	Abitur, Lessing-Schule Bochum
1987	Vordiplom Physik, Ludwig-Maximilians-Universität München
1988	Collaborator in the Crystal Barrel Experiment, CERN, Geneva
1988	Vordiplom Mathmatik, Ludwig-Maximilians-Universität München
1988-1989	Teaching Assistant, Department of Physics, University of California, San Diego
1989-1992	Research Assistant, Department of Physics, University of California, San Diego Member of the L3 Collaboration, CERN, Geneva
1989	M.S. in Physics, University of California, San Diego
1992	Plenary talk given on "Higgs Searches at LEP" at the XV International Warsaw Meeting on Elementary Particle Physics, Kazimierz, Poland, May 1992
1992	Ph.D., University of California, San Diego

Publications

Publications in L3, at CERN and Conference Reports

1. A. Gurtu and A. Sopczak, L3 note #1250, September, 1992.
   Search for Z^0 Decays into Higgs Boson Pairs in Multi-Jet Channels

2. A. Sopczak, L3 note #1245, September, 1992 to be published by *World Scientific.*
   Plenary talk given on "Higgs Searches at LEP-I" at the XV International Meeting on Elementary Particle Physics, Kazimierz, Poland, 25-29 May 1992

3. A. Sopczak, L3 note #1230 and CERN preprint CERN-PPE/92-137; August 11, 1992.
   Searches for Non-Minimal Higgs Bosons in Z^0 Decays

4. M. Felcini and A. Sopczak, L3 note #1214, July, 1992.
   Search for Higgs Bosons in the $\tau\tau\tau\tau$ and $\tau\tau$bb Channels from Z^0 Decays

5. A. Sopczak *et al.*, L3 note #1213, July, 1992,
   L3 contributed paper to the XXVI International Dallas Conference on Particle Physics,
   Dallas, 6–12 August, 1992.
   Search for Non-Minimal Higgs Bosons from Z^0 Decays

6. A. Sopczak, L3 note #1169, May, 1992.
   Limits on Physics Beyond the Minimal Standard Model from LEP Line-Shape Measurements

7. A. Sopczak, L3 note #1164, December, 1990.
   Search for Z^0 Decays into Neutral and Charged Higgs Pairs

8. A. Sopczak and J. Toth, L3 computing documentation on EGSHV200, May, 1990.
   A Generator for Higgs Boson Pair-Production

9. A. Sopczak, L3 computing documentation on EGSQV200, December, 1989.
   A Generator for Supersymmetric Quarks

Publication with the L3 Experiment (370 authors)

1. O. Adriani *et al.*, Submitted to *Z. Phys. C.*
   L3 preprint 050; CERN preprint CERN-PPE/92-163; September 22, 1992.
   Searches for Non-Minimal Higgs Bosons in Z^0 Decays

2. O. Adriani *et al.*, Submitted to *Phys. Lett. B.*
L3 preprint 049; CERN preprint CERN-PPE/92-152; September 16, 1992.
High Mass Photon Pairs in $\ell^+\ell^-\gamma\gamma$ events at LEP

3. O. Adriani *et al.*, Submitted to *Phys. Lett. B.*
L3 preprint 048; CERN preprint CERN-PPE/92-140; August 21, 1992.
Searches for Non-Minimal Higgs Bosons in Z^0 Decays

4. O. Adriani *et al.*, Submitted to *Phys. Lett. B.*
L3 preprint 047; CERN preprint CERN-PPE/92-132; August 3, 1992.
A Measurement of τ Polarization in Z^0 Decays

5. O. Adriani *et al.*, Submitted to *Phys. Lett. B.*
L3 preprint 046; CERN preprint CERN-PPE/92-131; July 30, 1992.
Isolated Hard Photon Emission in Hadronic Z^0 Decays

6. O. Adriani *et al.*, Submitted to *Phys. Lett. B.*
L3 preprint 045; CERN preprint CERN-PPE/92-128; July 24, 1992.
Determination of the number of light neutrino species Decays

7. O. Adriani *et al.*, Submitted to *Phys. Lett. B.*
L3 preprint 044; CERN preprint CERN-PPE/92-121; July 20, 1992.
Measurement of the $e^+e^- \to b\bar{b}$ and $e^+e^- \to c\bar{c}$ Forward-Backward Asymmetries at the Z^0 Resonance

8. O. Adriani *et al.*, *Phys. Lett.* **B 288** (1992) 412.
L3 preprint 043; CERN preprint CERN-PPE/92-99; June 12, 1992.
Inclusive J production in Z^0 Decays

9. O. Adriani *et al.*, *Phys. Lett.* **B 288** (1992) 404.
L3 preprint 042; CERN preprint CERN-PPE/92-87; May 29, 1992.
A Test of Quantum Electrodynamics in the Reaction $e^+e^- \to \gamma\gamma(\gamma)$

10. B. Adeva *et al.*, *Phys. Lett.* **B 288** (1992) 395.
L3 preprint 041; CERN preprint CERN-PPE/92-84; May 19, 1992.
An Improved Measurement of $B^0 - \bar{B}^0$ Mixing in Z^0 Decays

11. O. Adriani *et al.*, *Phys. Lett.* **B 286** (1992) 403.
L3 preprint 040; CERN preprint CERN-PPE/92-83; May 19, 1992.
Measurement of Inclusive η Production in Hadronic Decays of the Z^0

12. O. Adriani *et al.*, *Phys. Lett.* **B 284** (1992) 471.
L3 preprint 039; CERN preprint CERN-PPE/92-58; April 15, 1992.
Determination of α_s from Hadronic Event Shapes Measured on the Z^0 Resonance

13. B. Adeva *et al.*, *Z. Phys.* **C 55** (1992) 39. L3 preprint 038; CERN preprint CERN-PPE/92-50; March 26, 1992.
Studies of Hadronic Event Structure and Comparisons with QCD Models at the Z^0 Resonance

14. B. Adeva *et al.*, *Phys. Lett.* **B 283** (1992) 454.
L3 preprint 037; CERN preprint CERN-PPE/92-40; April 2, 1992.
Search for the Neutral Higgs Boson at LEP

15. The LEP Collaborations: ALEPH, DELPHI, L3 and OPAL, *Phys. Lett.* **B 276** (1992) 247.
L3 preprint 036; CERN preprint CERN-PPE/91-232; December 20, 1991.
Electroweak Parameters of the Z^0 Resonance and the Standard Model

16. B. Adeva *et al.*, *Phys. Lett.* **B 275** (1992) 209. L3 preprint 035; November 11, 1991.
A Direct Determination of the Number of Light Neutrino Families from $e^+e^- \to \nu\bar{\nu}\gamma$ at LEP

17. B. Adeva *et al.*, *Phys. Lett.* **B 271** (1991) 453.
L3 preprint 034; August 21, 1991.
Search for Lepton Flavour Violation in Z^0 Decays

18. B. Adeva *et al.*, *Phys. Lett.* **B 271** (1991) 461.
L3 preprint 033; August 15, 1991.
Measurement of the Strong Coupling Constant α_s for Bottom Quarks at the Z^0 Resonance

19. B. Adeva *et al.*, *Phys. Lett.* **B 270** (1991) 111.
L3 preprint 032; July 3, 1991.
Measurement of the Lifetime of B-Hadrons and a Determination of $|V_{cb}|$

20. B. Adeva *et al.*, *Phys. Lett.* **B 265** (1991) 451.
L3 preprint 031; June 17, 1991.
Decay Properties of Tau Leptons Measured at the Z^0 Resonance

21. B. Adeva *et al.*, *Phys. Lett.* **B 263** (1991) 551.
L3 preprint 030; May 6, 1991.
A Test of QCD based on 3-Jet Events from Z^0 Decays

22. B. Adeva *et al.*, *Phys. Lett.* **B 262** (1991) 155.
L3 preprint 029; February 28, 1991.
Search for Narrow High-Mass Resonances in Radiative Decays of the Z^0

23. B. Adeva *et al.*, *Z. Phys.* **C 51** (1991) 179.
L3 preprint 028; February 15, 1991.
Measurement of Electroweak Parameters from Hadronic and Leptonic Decays of the Z^0

24. B. Adeva *et al.*, *Phys. Lett.* **B 261** (1991) 177.
L3 preprint 027; February 20, 1991.
Measurement of $Z^0 \to b\bar{b}$ Decays and the Semileptonic Branching Ratio $\mathrm{Br}(b \to l + X)$

25. B. Adeva *et al.*, *Phys. Lett.* **B 261** (1991) 169.
L3 preprint 026; February 6, 1991.
Search for Leptoquarks in Z^0 Decays

26. B. Adeva *et al.*, *Phys. Lett.* **B 259** (1991) 199.
L3 preprint 025; February 4, 1991.
Measurement of the Inclusive Production of Neutral Pions and Charged Particles on the Z^0 Resonance

27. B. Adeva *et al.*, *Phys. Lett.* **B 257** (1991) 450.
L3 preprint 024; December 17, 1990.
Search for the Neutral Higgs Boson with a Mass above 15 GeV

28. B. Adeva *et al.*, *Phys. Lett.* **B 257** (1991) 469.
L3 preprint 023; December 6, 1990.
Determination of α_s from Energy-Energy Correlations Measured on the Z^0 Resonance

29. Samuel C. C. Ting *et al.*, preprint SSCL-SR-1154, November 1990
Letter of Intent to the Superconducting Super Collider Laboratory by the L* Collaboration

30. B. Adeva *et al.*, *Phys. Lett.* **B 252** (1990) 713.
L3 preprint 022; November 5, 1990.
A Measurement of the $Z^0 \to b\bar{b}$ Forward-Backward Asymmetry

31. B. Adeva *et al.*, *Phys. Lett.* **B 252** (1990) 525.
L3 preprint 021; October 2, 1990.
Search for Excited Neutrinos from Z^0 Decays

32. B. Adeva *et al.*, *Phys. Lett.* **B 252** (1990) 703.
L3 preprint 020; November 2, 1990.
A Measurement of $B^0 - \bar{B}^0$ Mixing in Z^0 Decays

33. B. Adeva *et al.*, *Phys. Lett.* **B 252** (1990) 518.
L3 preprint 019; September 18, 1990.
Search for a Low Mass Neutral Higgs Boson in Z^0 Decay

34. B. Adeva *et al.*, *Phys. Lett.* **B 252** (1990) 511.
L3 preprint 018; September 14, 1990.
Search for the Charged Higgs Boson in Z^0 Decay

35. B. Adeva *et al.*, *Phys. Lett.* **B 250** (1990) 183.
L3 preprint 017; August 20, 1990.
A Determination of Electroweak Parameters from Z^0 Decays into Charged Leptons

36. B. Adeva *et al.*, *Phys. Lett.* **B 251** (1990) 321.
L3 preprint 016; August 24, 1990.
A Search for Heavy Charged and Neutral Leptons from Z^0 Decays

37. B. Adeva *et al.*, *Phys. Lett.* **B 251** (1990) 311.
L3 preprint 015; August 25, 1990.
Search for the Neutral Higgs Bosons of the Minimal Supersymmetric Standard Model from Z^0 Decays

38. B. Adeva *et al.*, *Phys. Lett.* **B 250** (1990) 205.
L3 preprint 014; August 6, 1990.
Search for Excited Taus from Z^0 Decays

39. B. Adeva *et al.*, *Phys. Lett.* **B 250** (1990) 199.
L3 preprint 013; August 3, 1990.
Test of QED in $e^+e^- \to \gamma\gamma$ at LEP

40. B. Adeva *et al.*, *Phys. Lett.* **B 248** (1990) 227.
L3 preprint 012; July 14, 1990.
A Test of QCD based on 4-Jet Events from Z^0 Decays

41. B. Adeva *et al.*, *Phys. Lett.* **B 248** (1990) 464.
L3 preprint 011; July 7, 1990.
Determination of α_s from Jet Multiplicities Measured on the Z^0 Resonance

42. B. Adeva *et al.*, *Phys. Lett.* **B 248** (1990) 203.
L3 preprint 010; June 23, 1990.
Search for Neutral Higgs Boson in Z^0 Decay

43. B. Adeva *et al.*, *Phys. Lett.* **B 249** (1990) 341.
L3 preprint 009; July 14, 1990.
A Precision Measurement of the Number of Neutrino Species

44. B. Adeva *et al.*, *Phys. Lett.* **B 247** (1990) 473.
L3 preprint 008; June 21, 1990.
A Determination of Electroweak Parameters from $Z^0 \to \mu^+\mu^-(\gamma)$

45. B. Adeva *et al.*, *Phys. Lett.* **B 247** (1990) 177.
L3 preprint 007; June 20, 1990.
Mass Limits for Excited Electrons and Muons from Z Decay

46. B. Adeva *et al.*, *Phys. Lett.* **B 241** (1990) 416.
L3 preprint 006; February 20, 1990.
Measurement of $Z^0 \to b\bar{b}$ Decay Properties

47. B. Adeva *et al.*, *Phys. Lett.* **B 238** (1990) 122.
L3 preprint 005; February 5, 1990.
A Measurement of the Z^0 Leptonic Partial Widths and the Vector and Axial Vector Coupling Constants

48. B. Adeva *et al.*, *Phys. Lett.* **B 237** (1990) 136.
L3 preprint 004; December 24, 1989.
Measurement of Z^0 Decays to Hadrons, and a Precise Determination of the Number of Neutrino Species

49. B. Adeva *et al.*, *Phys. Lett.* **B 236** (1990) 109.
L3 preprint 003; November 24, 1989.
Measurements of g_A and g_V, the Neutral Current Coupling Constants to Leptons

50. B. Adeva *et al.*, *Phys. Lett.* **B 233** (1989) 530.
L3 preprint 002; October 15, 1989.
Mass Limits for Scalar Muons, Scalar Electrons, and Winos from e^+e^- Collisions near $\sqrt{s} = 91\,\mathrm{GeV}$

51. B. Adeva *et al.*, *Phys. Lett.* **B 231** (1989) 509.
L3 preprint 001; October 11, 1989.
A Determination of the Properties of the Neutral Intermediate Vector Boson Z^0

ABSTRACT OF THE DISSERTATION

Search for Non-Minimal Higgs Bosons in Z^0 Decays with the L3 Detector at LEP

by

André Sopczak

Doctor of Philosophy in Physics

University of California, San Diego, 1992

Professor James G. Branson, Chair

A general search for neutral and charged Higgs bosons in e^+e^- collisions at the Z^0 resonance is reported. No assumption that the Higgs sector consists of one doublet as in the Minimal Standard Model (MSM) is made. In the MSM of electroweak interactions, a single Higgs doublet generates masses for the gauge bosons and for the charged fermions via spontaneous breaking of the gauge symmetry. With only one doublet, Higgs boson production and decay properties depend only on the Higgs boson mass. The LEP experiments have searched for the MSM Higgs boson and exclude it for masses less than about 60 GeV. It is quite possible that the actual scalar sector in nature has more than one doublet of Higgs bosons or has Higgs bosons in other multiplets. This is expected in many theories that go beyond the Standard Model. In Supersymmetric models, at least two Higgs doublets are predicted. A model with two Higgs doublets illustrates some processes that occur in more general models. If the Higgs sector contains more than a single doublet, rates for bremsstrahlung of the lightest Higgs boson from the Z^0 are no longer uniquely predicted and are generally lower than in the MSM. At the same time, with a richer Higgs sector, pairs of Higgs particles can be produced in Z^0 decays. Therefore, if we are to find a non-MSM Higgs boson at LEP, we must search for bremsstrahlung at lower rates than those predicted in the MSM, and for Higgs boson pair-production.

This work is based on the 1990 and 1991 L3 data sample which totals 408,000 hadronic Z^0 decays, collected at center-of-mass energies between 88.2 and 94.3 GeV. No Higgs signal inconsistent with background is observed in any of the decay channels analyzed. From the results of direct searches, model-independent limits on Higgs boson bremsstrahlung and on Higgs boson pair-production from the Z^0 are presented. The bremsstrahlung limits are interpreted in a general two-doublet model. Z^0 lineshape measurements further restrict the parameter space available in the two-doublet model. Finally, the results are interpreted in the framework of the Minimal Supersymmetric extension of the Standard Model (MSSM).

Chapter 1

The Theory

The search for Higgs particles is largely guided by theoretical predictions of signatures for Higgs decays. In this chapter, the general concept of the Higgs mechanism is outlined and the dominant Higgs production processes at LEP are reviewed.

In section 1.1, the idea of spontaneous symmetry-breaking is introduced. In section 1.2, the particle spectrum of the Standard Model of Particle Physics is reviewed. Section 1.3 summarizes the properties of the minimal Higgs sector in the framework of the Standard Model. In section 1.4, the general two-doublet Higgs model is discussed. Since an extended Higgs sector is motivated by Supersymmetry, the idea of Supersymmetry is introduced and its important implications for the Higgs phenomenology are presented in section 1.5. Higher-order corrections in the Minimal Supersymmetric extension of the Standard Model (MSSM) modify significantly the tree-level predictions. In preceding searches for Supersymmetric Higgs bosons, these corrections have not been taken completely into account. The most important implications of these new results for the Higgs search are summarized in section 1.6. Theoretical trends beyond the two-doublet model are addressed in section 1.7. In this work, all quantities are expressed in natural units: $\hbar = 1$ and $c = 1$.

1.1 Spontaneous Symmetry-Breaking

The vacuum, defined as the lowest energy state of a dynamical system, can have a complicated symmetry. The importance of understanding the vacuum structure for progress in modern physics has been pointed out [1]. Historically, the quantum theory of electromagnetism, Quantum Electrodynamics (QED), predicts a vacuum structure in which electron-positron pairs can be generated. The QED predic-

tions have been confirmed with a high level of precision. In QED, the characteristic length of the vacuum structure corresponds to an energy scale of about 1 MeV. In the theory of strong interactions, Quantum Chromodynamics (QCD), the characteristic length corresponds to the inverse of the QCD energy scale ($\Lambda \approx 150$ MeV). A very complicated QCD vacuum structure is predicted and experimental measurements are needed. In the Higgs model, the vacuum state of Higgs particles is invariant under a symmetry transformation. This symmetry has to be spontaneously broken to explain the generation of mass for all particles. It might be possible for this vacuum structure to be detected at a LEP energy scale of 100 GeV.

Spontaneous symmetry breaking can occur in a system where the Lagrangian possesses a larger symmetry than that of the ground state, i.e., the ground state changes into another ground state under a symmetry transformation that does not change the Lagrangian. Choosing a particular vacuum state spontaneously breaks the symmetry and generates particle masses.

Historically, in condensed matter physics, the importance of spontaneous symmetry breaking was realized by Nambu and Jona-Lasinio [2] in the 1960's. In the Landau-Ginzburg theory of superconductivity [3], developed earlier in the 1950's, the Meißner-Ochenfeld effect, which describes the screening of magnetic flux in a superconductor, is explained by the generation of an effective mass for photons.

The Higgs-type mechanism explains the mass generation for photons with spontaneous symmetry breaking. The Landau-Ginzburg potential is of order Φ^4: $V_{\rm LG}(\Phi) = m^2\Phi^2 + \lambda\Phi^4$, where λ is the self-coupling constant, $m^2 = a(T - T_c)$, T_c is the critical temperature and a is a positive constant. For $T > T_c$, the free energy has a minimum at the vacuum expectation $|\Phi| = 0$. If $T < T_c$, the free energy has a minimum at $|\Phi|^2 = -m^2/2\lambda > 0$. The conserved electric current, $\mathbf{j} = -\frac{i}{2}(\Phi^*\vec{\nabla}\Phi - \Phi\vec{\nabla}\Phi^*) - e|\Phi|^2\mathbf{A}$, where e is the electron charge and $\mathbf{A}$ is the photon field, corresponds to the invariance of the electromagnetic Lagrangian under a phase transformation. The second term leads to an effective photon mass, which explains why the magnetic field cannot penetrate the superconductor.

In particle physics, spontaneous symmetry breaking exists in two types of gauge theories: it can apply to a *global* or *local* gauge theory. In a global symmetry, the Goldstone theorem [4] predicts the existence of massless bosons if the Lagrangian is invariant under a larger symmetry than that possessed by the vacuum states. This idea was successfully applied in the 1960's to chiral symmetry-breaking SU(3) $\times$ SU(3) $\rightarrow$ SU(3) to explain the experimentally observed light pion spectrum [5].

Predicted consequences, like the Gell-Mann-Okubo mass relation between mesons, were in agreement with experiments and gave strong support to the idea of symmetry breaking in particle physics.

In 1964, Peter Higgs and others pointed out that the consequences of spontaneous symmetry breaking in local gauge theories are very different from those in global gauge theories [6]. Glashow, Weinberg and Salam applied Higgs' idea to the $SU(2)_L \times U(1)_Y$ gauge symmetry with left-handed doublets and right-handed singlets, establishing the basis for the present Standard Model of particle physics [7]. The renormalizability of the theory, which is necessary for sensible predictions, was proven in 1971 by 't Hooft [8]. Today, all existing experimental results are in very good agreement with the Standard Model. However, the top quark, for which indirect experimental evidence exists, and the Higgs boson, predicted by the only known mechanism to generate masses in the Standard Model, remain undiscovered.

1.2 The Standard Model of Particle Physics

This section describes the main constituents of the Standard Model of Particle Physics. All matter consists of leptons, quarks and gauge bosons. Leptons exist in three generations (families): electrons, muons and taus with their corresponding neutrinos. The six quarks are also ordered in three families with flavors: up (u) and down (d), charm (c) and strange (s), top (t) and bottom (b). Some of the basic properties of fermions are summarized in Table 1.1. The masses are given in [9] and the top mass lower limit is reported by the CDF experiment [10]. A comprehensive review of the Standard Model is given in [11].

Quarks exist in three colors. Each lepton and quark has one antiparticle with opposite charge. Thus, matter consists of 12 leptons and 36 quarks[1].

All fundamental forces (electromagnetic, weak, strong, gravitational) are transmitted by mediators. The gravitational force is many orders of magnitude weaker than the other forces, and is not included in the Standard Model. In this work, "Standard Model" includes a) the electroweak theory, which is the unification of electromagnetic (QED) and weak interactions, and b) QCD, which describes strong interactions between quarks and gluons. The mediators (gauge bosons with

[1]Normal atoms are built of up- and down-type quarks and electrons. Other fermions can be made visible in high-energy physics experiments. It is remarkable that no reason is known for the existence of the particles in the second and third family.

Generation	Flavor	El. Charge	Mass (GeV)
1	u	2/3	$0.002 - 0.008$
	d	-1/3	$0.005 - 0.015$
	e	-1	0.511×10^{-3}
	ν_e	0	0
2	c	2/3	$1.3 - 1.7$
	s	-1/3	$0.1 - 0.3$
	μ	-1	0.106
	ν_μ	0	0
3	t	2/3	> 91
	b	-1/3	$4.7 - 5.3$
	τ	-1	1.87
	ν_τ	0	0

Table 1.1: Fermion properties in the Standard Model.

spin = 1) of the three fundamental forces of the Standard Model are listed in Table 1.2.

Force	Gauge bosons	El. Charge	Mass (GeV) theory[11]	Mass (GeV) experiment[12]
electro-magnetic	γ	0	0	$\leq 1.7 \times 10^{-36}$
neutral weak	Z^0	0	91.0 ± 0.8	91.175 ± 0.021
charged weak	$W^\pm$	± 1	79.7 ± 0.9	80.35 ± 0.37
strong	g_i $(i = 1, ..., 8)$	0	0	

Table 1.2: Gauge boson properties in the Standard Model.

In the Standard Model, all fermion and boson masses are generated by a Higgs mechanism analogous to the example in condensed matter physics. Cosmological models suggest that mass generation occurred during a very early epoch of the universe, and that prior to the spontaneous breakdown of a higher symmetry, only a plasma of massless particles existed. The change of the vacuum structure to a new vacuum with a stable minimum in the Higgs potential determines the Higgs particle spectrum and their masses. The discovery of Higgs bosons, which were generated

during the transition to the massive world, would allow for conclusions about the mass generation itself and strongly support the idea of mass generation in particle physics by an experimental fact. The predicted properties of Higgs particles which could be detected with the L3 detector at LEP are discussed in the following sections.

1.3 The One-Doublet Higgs Model

The Higgs sector of the Standard Model consists of at least one complex Higgs doublet. In this section, the theoretical properties of the minimal Higgs sector are discussed, with emphasis on implications for experimental Higgs searches.

The Higgs potential has the form:

$$V(\Phi) = \mu^2 \Phi^+ \Phi + \lambda (\Phi^+ \Phi)^2, \tag{1.1}$$

where μ, λ are real constants and Φ is the complex Higgs doublet field:

$$\Phi = \begin{pmatrix} \Phi^+ \\ \Phi^0 \end{pmatrix} = \begin{pmatrix} \Phi_1 + i\Phi_2 \\ \Phi_3 + i\Phi_4 \end{pmatrix}. \tag{1.2}$$

Under the $SU(3)_C \times SU(2)_L \times U(1)_Y$ symmetry transformations, the Higgs field is a color-singlet isospin-doublet with hypercharge 1/2. The leading term in the Higgs potential has to be of order Φ^4, since odd powers of Φ would cause an unstable vacuum, i.e., the potential has no global minimum. The Φ^2 term leads to a Higgs boson mass. Terms Φ^i $(i \geq 6)$ reduce to an effective Φ^4 interaction in four-space-time dimension as shown in non-perturbative calculations [13]. The last argument is explained in a brief discussion of the implications of non-perturbative field theory for the Higgs sector (section 11).

1.3.1 Gauge Boson Masses

Without the Higgs mechanism, the Z^0 and $W^\pm$ gauge bosons of the $SU(2)_L \times U(1)_Y$ theory would be massless. In this theory, the weak interactions are short-range because they are mediated by massive bosons. This is different from the electromagnetic interactions which are long-range and mediated by massless photons.

Masses for the gauge bosons are generated explicitly through spontaneous symmetry breaking via the Higgs mechanism. The Higgs potential (eq. 1.1) for $\mu^2 < 0$ and $\lambda > 0$ has the shape of a 'Mexican hat'. The potential $V(\Phi)$ develops a minimum at finite values of $|\Phi|$:

$$|\Phi|^2 = \Phi^+ \Phi = \tfrac{1}{2}(\Phi_1^2 + \Phi_2^2 + \Phi_3^2 + \Phi_4^2) = -\frac{\mu^2}{2\lambda}. \tag{1.3}$$

This manifold of points, where $V(\Phi)$ is minimal, is invariant under $SU(2)_L$ transformations. In order to expand $\Phi(x)$ around a particular minimum, one can choose $\Phi_1 = \Phi_2 = \Phi_4 = 0$, $\Phi_3 = -\mu^2/\lambda$, thereby explicitly breaking the $SU(2)_L$ symmetry. The Higgs field $\Phi(x)$ can be expanded around that particular minimum,

$$\Phi(x) = \frac{1}{2}\begin{pmatrix} 0 \\ v + h(x) \end{pmatrix} \tag{1.4}$$

where $h(x)$ is the expanded Higgs field around the vacuum expectation value (VEV), v. The Higgs doublet has four degrees of freedom, three of which are transformed to give masses to the $W^{\pm}$ bosons and the Z^0 boson. One neutral physical Higgs field remains. The Higgs boson mass is given by:

$$m_H^2 = \frac{\partial V^2}{\partial^2 \Phi}|_{\Phi=v} = \lambda v^2/\sqrt{2}, \tag{1.5}$$

as the curvature of the physical Higgs field at the minimum of the potential. The Higgs boson mass is *not* predicted by the theory, since the Higgs self-coupling is a free parameter.

A mass term for the charged vector bosons is generated: $m_W = \frac{1}{2}vg$. The neutral physical gauge boson fields Z_μ and A_μ diagonalize the mass matrix, and their masses are:

$$m_Z = \frac{1}{2}v\sqrt{g^2 + g'^2}, \qquad m_\gamma = 0. \tag{1.6}$$

The ratio of the coupling constants for the $SU(2)_L$ and $U(1)_Y$ group defines the weak mixing angle θ_W, $\tan\theta_W \equiv g'/g$. The Higgs mechanism leads to the important mass relation:

$$m_W/m_Z = \cos\theta_W. \tag{1.7}$$

Any extension of the one-doublet Higgs scenario must keep this fundamental ratio in agreement with experimental measurements. The ρ-parameter defines the deviation from the above mass relation in terms of physical parameters:

$$\rho \equiv \frac{m_W}{m_Z \cos\ \theta_W}. \tag{1.8}$$

By definition $\rho = 1$ for the minimal Higgs model. The experimental world average

$$\rho = 0.995 \pm 0.013\ [9] \tag{1.9}$$

is in perfect agreement with the theoretical prediction in the one-doublet Higgs model. This represents a stringent constraint on extensions of the minimal Higgs models.

1.3.2 Fermion Masses

This section outlines the generation of fermion masses and their couplings to the Higgs boson in the minimal Higgs model. The Higgs field generates masses for the fermions and it can couple to the fermion fields while preserving the $SU(3)_C \times SU(2)_L \times U(1)_Y$ gauge invariance. The Lagrangian shows the interaction of the electron with the Higgs explicitly:

$$\mathcal{L}_e = -g_e[(\bar{\nu}_e e)_L \begin{pmatrix} \Phi^+ \\ \Phi^0 \end{pmatrix} e_R + \bar{e}_R(\Phi^- \bar{\Phi}^0) \begin{pmatrix} \nu_e \\ \bar{e} \end{pmatrix}_L]. \tag{1.10}$$

Analogous terms exist for the other fermions. The substitution of the Higgs field by its expansion around a particular vacuum state, v, breaks the symmetry spontaneously, and a fermion mass, m_f, is generated. One arbitrary Yukawa coupling, g_f, which is defined as the coupling constant between one boson and a fermion pair, exists for each fermion. From expansion of the Lagrangian, the relationship between Yukawa coupling and fermion mass is obtained:

$$m_f = \frac{g_f\, v}{\sqrt{2}}\,. \tag{1.11}$$

Thus, fermion masses are not predicted, although the value of the VEV, v, is known: $v = 2^{-1/4} G_F^{-1/2} = 246$ GeV. The relation of Fermi's constant, G_F, to the VEVs is based on the fact that the Fermi theory of the β-decay must be recovered in the Standard Model for low momentum transfer. Equation 1.11 has a major implication for the Higgs boson search: the Higgs boson tends to decay into the most massive kinematically accessible fermion pair.

1.3.3 One-Loop Potential

In this section, implications of one-loop radiative corrections and results of non-perturbative calculations for the Higgs boson search are summarized.

A renormalization procedure is applied in order to remove infinite terms when, in addition to the tree level, higher order loop graphs are included in the calculation. Infinities introduced by additional Feynman diagrams have different degrees of divergence. They can be absorbed by a redefinition of μ^2, λ and the Higgs field. The conventional renormalization conditions [14, page 290] are given for the renormalized Higgs boson mass, μ_R, for the renormalized coupling constant, λ_R, and for the wavefunction renormalization at a given physical energy scale, M, by:

$$\mu_R^2 \equiv -\Gamma^2(p_i = 0) = \frac{\mathrm{d}^2 V}{\mathrm{d}\Phi^2}|_{\Phi=0}, \quad \lambda_R \equiv \frac{\mathrm{d}^4 V}{\mathrm{d}\Phi^4}|_{\Phi=0}, \quad \frac{\partial \Gamma^{(2)}}{\partial p^2}|_{p^2=M^2} \equiv 1, \tag{1.12}$$

where Γ is the inverse Higgs propagator for a particle with momentum p. In the framework of the one-doublet model Higgs model, the Higgs potential acquires one-loop contributions from Higgs self-interactions (scalar), Higgs-gauge boson interactions (vector) and Higgs-fermion interactions:

$$V_{\text{eff}}(\Phi) = V_{\text{tree}} + V_{\text{radiative}}, \qquad V_{\text{radiative}} = V_{\text{scalar}} + V_{\text{vector}} + V_{\text{fermion}}. \tag{1.13}$$

The physical mass scale, M, is arbitrary: changing it redefines the renormalized Higgs boson masses and renormalized coupling constants.

Higgs Boson Mass Limits from Vacuum Stability

The relationship between the top quark and Higgs boson masses, the Coleman-Weinberg lower Higgs boson mass limit, and implications from possible phase transitions at finite temperature are described in the following sections.

Top Quark and Higgs Boson Mass Relation: The recent increase of the top mass limit, $m_{\text{top}} > 91$ GeV at 95% C.L. [10], enhances the importance of radiative corrections for V_{fermion}. This is because the fermion masses are proportional to the Yukawa coupling constants, g_{f} (eq. 1.11), and therefore, the most massive fermions contribute most to the loop diagrams. The Higgs search at LEP is kinematically restricted to $m_{\text{H}} < m_{\text{Z}}$. Thus, the main contributions to radiative corrections are due to the vector boson and fermions [14]:

$$V_{\text{radiative}}(\Phi) \simeq V_{\text{vector}} + V_{\text{fermion}} = \frac{1}{64\pi^2} B\Phi^4 \ln\frac{\Phi^4}{M^4}, \tag{1.14}$$

$$B = 1.75 \cdot 10^{-4}\left(1 - \left(\frac{m_{\text{top}}}{76.2\text{ GeV}}\right)^4\right).$$

The current experimental top mass limit requires $B \leq 0$. If B is sufficiently negative, the effective potential, V_{eff}, is unbounded and the stable minima of the 'Mexican hat' potential disappears. In this case, if the Higgs field, Φ, increases, it would gain more energy out of the vacuum to rise to even higher values. All energy of the universe could be absorbed; a clearly unacceptable scenario.

The turnover point will occur for $B + 12\lambda = 0$, for some large value of Φ. The self-coupling, λ, determines directly the Higgs boson mass, since the VEV, v, is known. Krive and Linde first realized the fermionic destabilization of the vacuum [15]. A summary of the m_{top} and m_{H} relation, when vacuum stability is required, is given in reference [14], from which Figure 1.1 is taken.

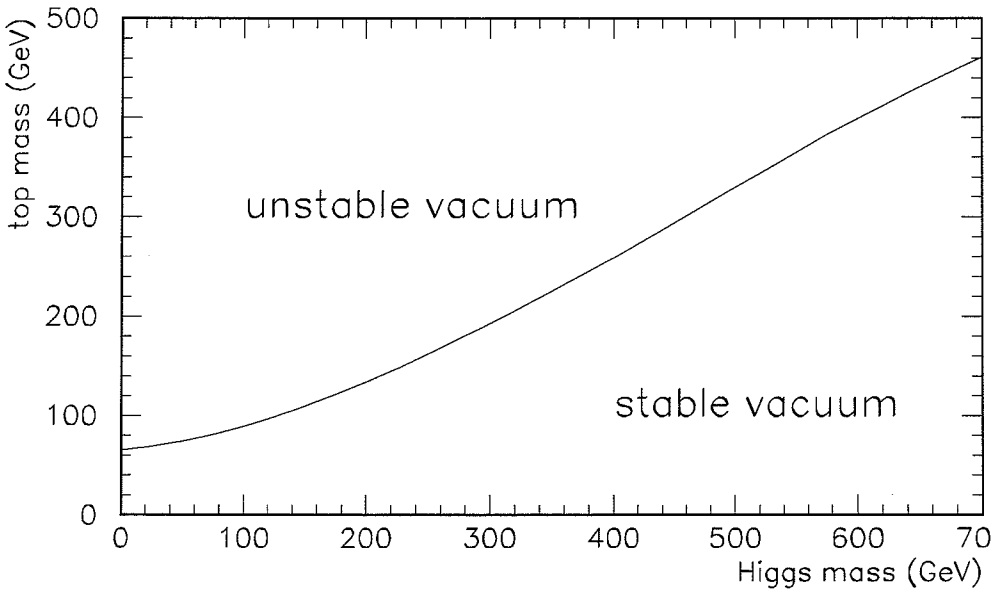

Figure 1.1: Higgs boson mass and top mass relation required for vacuum stability. The high experimental top mass limit requires a large Higgs boson mass for vacuum stability.

In the framework of the Minimal Standard Model, an important conclusion for the Higgs search at LEP can be drawn: vacuum stability requires $m_{\mathrm{H}} \geq 100$ GeV for the current top mass limit. This Higgs boson mass is too large to be produced at current LEP energies. The upcoming progress on the top search will give further information about the Higgs sector.

It must be emphasized that the conclusion drawn above is based on the assumption that perturbative one-loop calculations hold, even for $m_{\mathrm{top}} \approx 100$ GeV, corresponding to $g_{\mathrm{top}} \approx 0.6$. However, non-perturbative calculations also confirm this conclusion as outlined in section 1.3.3.

Coleman-Weinberg's Lower Limit: In 1972, S. Coleman and E. Weinberg first introduced the appealing scenario that spontaneous symmetry breaking is exclusively produced by radiative corrections [16]. By setting the Higgs tree level mass parameter μ in eq. (1.1) to zero, a lower limit on the Higgs boson mass can be obtained. As before, the Higgs self-interaction can be neglected in the effective potential. The effective one-loop potential possesses a global minimum at a non-zero Φ value. Thus,

as a result of radiative corrections, the symmetry can be spontaneously broken and masses are generated. The induced Higgs boson mass is given by:

$$m_{\mathrm{CW}} = 8Bv^2, \tag{1.15}$$

where the physical energy scale M is chosen to be at the VEV: $M = v = 246$ GeV. The lower Higgs boson mass limit is given by:

$$m_{\mathrm{H}} > m_{\mathrm{CW}}. \tag{1.16}$$

However, with the current top mass limit, m_{CW} becomes negative, and therefore, the lower Higgs boson mass limit vanishes. In more complicated Higgs models, similar expressions for the Coleman-Weinberg mass have been derived and are outlined in the discussion of the general two-doublet model in section 1.4.5.

In general, the experimentally relevant information from the one-loop effective potential is very limited. The indication that the Higgs boson mass in the Minimal Standard Model is larger than 100 GeV favors extended Higgs models as the theoretical framework for the search at the LEP energy. However, since the Coleman-Weinberg mass limit no longer exists, the low mass range for the Higgs is not theoretically disfavored. At present, none of the outlined theoretical developments satisfactorily predict the Higgs boson mass, and no promising perspectives are in sight.

Finite Temperature and Phase Transition: A new dimension can be added to the theoretical discussion via cosmological considerations described in this section. The Higgs potential has far-reaching implications in cosmology. The hope is that the interplay between particle physics and cosmology will ultimately reveal the structure of the Higgs vacuum, thus giving insight into the generation of matter at the very beginning of evolution. Experiments at large accelerators are currently able to study the physics at energies that were present during the early evolution of the universe. The understanding of the interplay between physics of the smallest and largest dimensions has improved greatly over the last years but is not conclusive. The following paragraph is therefore more speculative than factual, and the experimental usefulness is still quite limited.

In the framework of the cosmological Standard Model (Big Bang theory), energies around 100 GeV, which are investigated at LEP, correspond to the universe at an age of about 10^{-10} s.

By drawing the analogy with the Meißner-Ochsenfeld effect, Kirzhits and Linde [17] considered the possibility that at the high temperatures present in the early stages of the universe, symmetries were restored which are spontaneously broken today. Consequently, during the evolution of the universe, there was a phase transition.

In finite-temperature calculations, new terms are added to the Higgs potential as for the one-loop corrections. These field theoretical calculations at finite temperatures can be done in a similar way to calculations on the lattice, since the Green functions obey periodic boundary conditions in both cases. The additional terms have the form of the free energy of an ideal massive Fermi and Bose gas, summed over all contributing fermions and bosons. The predictions of the modified potential cannot solve the main question of whether the required phase transition can reveal the Higgs sector and the Higgs boson mass. The underlying reason is cosmological in nature. In the case of a first-order phase transition at temperature $T \approx m_Z$, energy is released and a perturbation, a so-called bubble, is introduced in the homogeneous space. These bubbles would contribute to cluster and galaxy formation, having observable effects. Unfortunately, the initially created bubbles are so small that the inhomogeneities are washed out in the further development of the universe due to the high temperatures present in that epoch. In our present understanding, the information about the origin of Higgs bosons is lost [18]. Conclusive information about the Higgs bosons will not be discovered until more aspects of the interplay of cosmology and particle physics are known.

Triviality Upper Higgs Boson Mass Bound

This section outlines a very general theoretical upper limit on the Minimal Standard Model Higgs boson mass. Non-perturbative calculations in field theory, which address the significance of the Higgs potential in a very general context, are not only an intellectual challenge, but they also give a stringent upper limit on the Higgs boson mass. In the following section, first the one-loop approximation, then the non-perturbative triviality Higgs boson mass limit in the one-doublet model are discussed. This summary is mainly based on references in [19]. Recently, upper limits on the Higgs boson masses in multi-doublet models have been made, derived from triviality arguments (section 1.4.5).

The upper Higgs boson mass limit is due to the renormalization behavior of the Higgs self-interaction coupling constant and its proportionality to the Higgs

boson mass. The renormalization group equations (RGE) require that the Higgs self-coupling goes to its critical value zero as the energy cut-off, Λ (defined as the energy scale up to which the theory is valid), increases. Thus, by removing the cut-off, the Higgs fields becomes non-interacting — trivial. Consequently, the Higgs boson mass goes to zero as the cut-off increases and vice versa. The energy scale where cut-off energy and Higgs boson mass are equal defines the upper Higgs boson mass limit.

One-loop analysis: The RGE govern the scale dependence of the Higgs self-coupling: $\mathrm{d}\lambda/\mathrm{d}t = \beta(t)$, where $t \equiv \ln M$ at the energy scale M. The β-function is given in the first-order loop calculation by:

$$\beta(t) = \frac{6}{\pi^2}\lambda^2(t). \tag{1.17}$$

By focusing on large Higgs boson masses with a strong self-coupling, the contributions from gauge bosons and fermions to one-loop calculations can be neglected[2].

The RGE relate the coupling constant $\lambda(M)$ to $\lambda(\Lambda)$:

$$\frac{1}{\lambda(M)} = \frac{1}{\lambda(\Lambda)} + \frac{6}{\pi^2}\ln\frac{\Lambda}{M}. \tag{1.18}$$

By removing the cut-off ($\Lambda/M \to \infty$), the one-loop calculation results in the triviality of the theory ($\lambda \to 0$). For a fixed finite cut-off, the largest value $\lambda(M)$ for a given M is obtained in the limit of infinite bare coupling ($\lambda(\Lambda) \to \infty$):

$$\lambda(M) \leq \frac{\pi^2}{6\ln\Lambda/M} \quad \Longrightarrow \quad m_{\mathrm{H}}^2 \leq \frac{8v^2\pi^2}{6\ln\Lambda/M}. \tag{1.19}$$

The physical mass scale of the Standard Model is of order $M = m_{\mathrm{W}}$. The choice of $\Lambda/m_{\mathrm{W}} = 10$, which contributes only logarithmically, leads to a Higgs boson mass limit: $m_{\mathrm{H}} \leq 600$ GeV.

Non-perturbative triviality bound: The justification of the one-loop Higgs boson mass upper limit is given by Monte Carlo lattice calculations. As for the one-loop calculation, the gauge couplings and the Yukawa coupling are switched off. The Monte Carlo study supports the existence of a trivial Gaussian fixed point at $\lambda_R = 0$. Simulations show that for different values of the bare coupling λ, the renormalized coupling goes to zero as the bare mass m goes to its critical value $m_c(\lambda)$. The simulated flow of λ_R can be fitted by:

$$\lambda_R = const \cdot \ln(\mid \tau \mid)^{-\eta}, \qquad \tau = 1 - m^2/m_c^2(\lambda), \tag{1.20}$$

[2]Complementary assumptions were made in the discussion on page 8.

where the logarithmic dependence is due to the RGE with the marginal critical exponent ($\eta = 1$) at the trivial Gaussian fixed point of the Φ^4 potential. The computer simulation leads to a triviality upper mass bound, which confirms the perturbative conclusion. On the lattice, the dimensionless Higgs correlation length $\xi = 1/am_{\mathrm{H}}$, where $a = \pi/\Lambda$ is the lattice spacing, relates the Higgs boson mass to the cut-off:

$$\frac{\Lambda}{m_{\mathrm{H}}} = \pi\xi. \tag{1.21}$$

On approaching the critical line (infinite correlation length), which separates the area of broken and unbroken symmetry, the existence of the trivial Gaussian fixed point implies that $\lambda_R \to 0$ for any fixed bare λ, manifesting that after renormalization, the macroscopic physics is independent of the chosen microscopic configuration. This is the underlying idea of universality in the renormalization theory.

The critical area is defined by having small cut-off artifacts. The boundary of the critical area near the critical line is determined by Monte Carlo simulations. The result is a relative small value, $\xi_{min} = 2$, on the boundary. The corresponding upper Higgs boson mass limit is determined to be: $m_{\mathrm{H}} \leq 2.6v = 640$ GeV.

In conclusion, one can speculate that the impressive agreement between the one-loop calculation and the lattice simulation extends to the other results drawn from the perturbative calculation. The uniqueness of the Φ^4 potential lies in the logarithmic evolution of the renormalized coupling. In perturbation theory, this corresponds to a renormalizable theory. The ultimate success of lattice calculations would be to find a non-trivial fixed point which predicts the Higgs boson mass.

1.3.4 Implications for the Higgs Boson Search at LEP

This section summarizes Higgs production and decay at LEP, as predicted in the Minimal Standard Model. Based on these predictions, the combined negative search results of the four LEP experiments excludes the Higgs in the mass range:

$$0 \leq m_{\mathrm{H}} \leq 59 \text{ GeV [20]}. \tag{1.22}$$

In the Higgs bremsstrahlung process (Bjorken process [21]) the Z^0 decays into a Higgs and an off-mass-shell Z^0: $\mathrm{e^+e^-} \to \mathrm{Z}^0 \to \mathrm{H}^0\mathrm{Z}^{0*}$, shown in Figure 1.2. The differential rate for this process, normalized to the $\mathrm{Z}^0 \to \mathrm{f\bar{f}}$ decay rate, is given at

the tree level as a function of the Higgs boson mass by [22]:

$$\frac{1}{\Gamma(Z^0 \to \mu^+\mu^-)}\frac{d\Gamma(Z^0 \to H^0 f\bar{f})}{dx} = \frac{\alpha}{4\pi \sin^2\theta_W \cos^2\theta_W} \times \frac{(1 - x + x^2/12 + 2r^2/3)(x^2 - 4r^2)^{1/2}}{(x - r^2)^2 + (\Gamma_Z/m_Z)^2}, \quad (1.23)$$

where α is the fine structure constant, θ_W is the Weinberg angle, $x = 2E_H/m_Z$ where E_H is the energy of the Higgs and $r = m_H/m_Z$. The total production rate is obtained by integration over the kinematic range: $2r \leq x \leq 1 + r^2$.

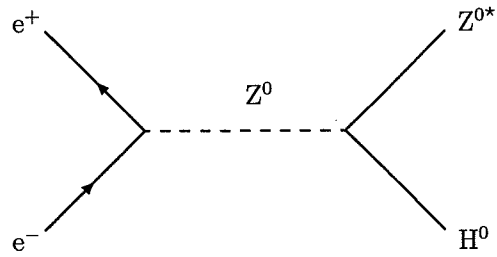

Figure 1.2: Diagram of Higgs bremsstrahlung production.

In Figure 1.3, the number of expected Higgs events, normalized to 400,000 hadronic Z^0 decays, is shown for a) the neutrino channel where Z^{0*} decays into neutrino pairs, and b) the muon channel where Z^{0*} decays into a muon pair. Radiative corrections have been taken into account by the Improved Born Approximation [23, page 39] and by top triangle graph contributions [24].

Higgs production in association with $Z^{0*} \to q\bar{q}$ is the dominant channel. However, this production mode is irrelevant for increasing the sensitivity of minimal Higgs searches since a low rate is expected in the high-mass range and the signal is very similar to background from hadronic Z^0 decays. The experimental search strategy in the charged lepton channels and the neutrino channel is outlined in chapter 4. Figure 1.4 presents the possible Higgs decays rates in a Higgs boson mass range between 10 MeV and 100 GeV. For the experimental analysis, a high and a low Higgs boson mass range can be distinguished.

a) High-Mass Higgs Range: In the high-mass Higgs range ($m_H > 15$ GeV) the dominant Higgs decay is $H^0 \to b\bar{b}$.

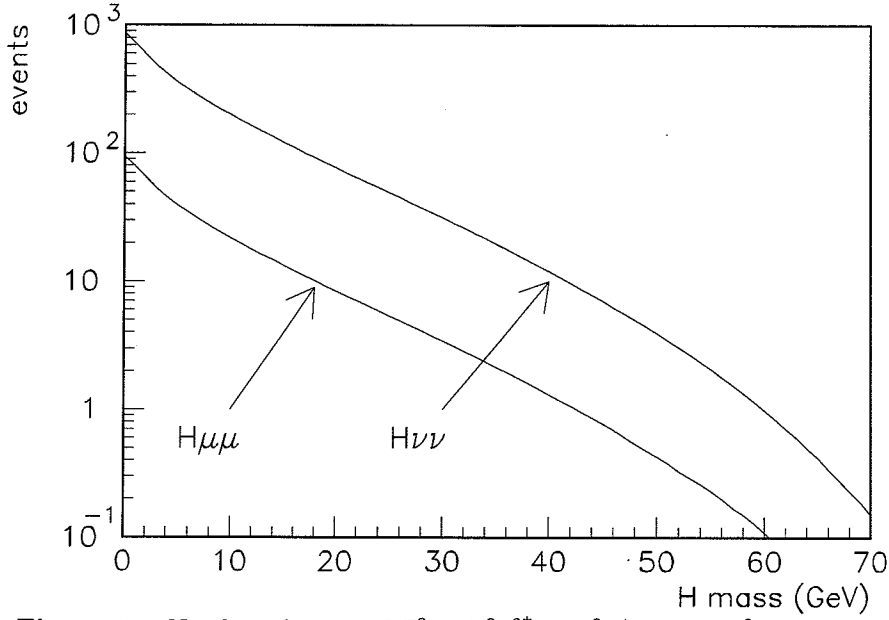

Figure 1.3: Number of expected $Z^0 \rightarrow H^0 Z^{0*} \rightarrow H^0 \mu^+ \mu^-$ and $H^0 \nu\bar{\nu}$ events per 400,000 hadronic Z^0 decays in the Minimal Standard Model.

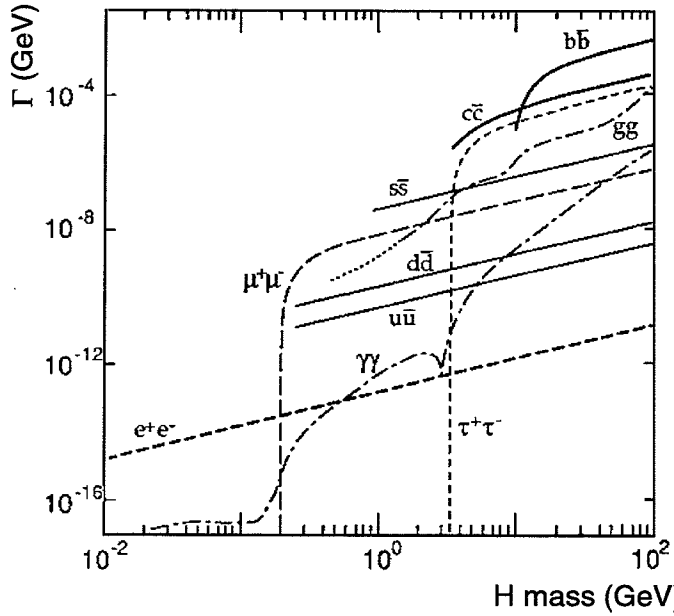

Figure 1.4: Higgs boson branching ratios in the Minimal Standard Model. For large Higgs boson masses, the decay into $b\bar{b}$ quarks is dominant, while for smaller masses, the Higgs is expected to decay into various quark and lepton pairs.

b) Low-Mass Higgs Range: In the low-mass Higgs range ($m_H < 15$ GeV) the Higgs can decay into many different quark and lepton channels, if the decay is kinematically allowed. An uncertainty on the Higgs decay branching ratios is due to the uncertainty on the bare quark masses, which determine the coupling for the quarks to the Higgs. In Figure 1.4 the following bare quark masses are taken: $m_u = 5$ MeV, $m_d = 10$ MeV, $m_s = 150$ MeV, $m_c = 1.5$ GeV, $m_b = 5$ GeV. However, the experimental thresholds for Higgs decay into quark pairs are determined by the mass of the corresponding meson pair. The lightest possible Higgs decay into quarks is $h^0 \rightarrow \pi\pi$ for $m_H > 270$ MeV. In the range between 2 m_π and 2 GeV, the gluon pair-production via a triangle loop-diagram involving all fermions can be the dominant channel as pointed out in [25]. In this region non-perturbative fragmentation effects are important and the expected branching ratio into muons, pions and kaons is uncertain. QCD corrections [26, page 65] decrease the partial width into quarks, thus enhancing the $\tau^+\tau^-$ branching ratio.

In order to search for Higgs signatures in models beyond the Minimal Standard Model, all decay channels which have at least about 1% branching fraction in the Minimal Standard Model are investigated separately. This model-independent search for Higgs bremsstrahlung is summarized in chapter 4.

Figure 1.5 gives a schematic overview of the expected Higgs signatures for different Higgs boson masses in channels which are relevant for the experimental search. The following signatures are shown:

a) Mass range $m_h \gg 10$ GeV, electron and muon channel.

b) Mass range $m_h \gg 10$ GeV, tau channel.

c) Mass range $m_h \gg 10$ GeV, neutrino channel.

d) Mass range $m_h \approx 10$ GeV, electron and muon channel.

e) Mass range $m_h \approx 10$ GeV, neutrino channel.

f) Mass range $m_h \leq 2m_\tau$, electron and muon channel.

g) Mass range $m_h \leq 2m_\mu$, electron and muon channel.

h) Mass range $m_h \ll 2m_\mu$, electron and muon channel.

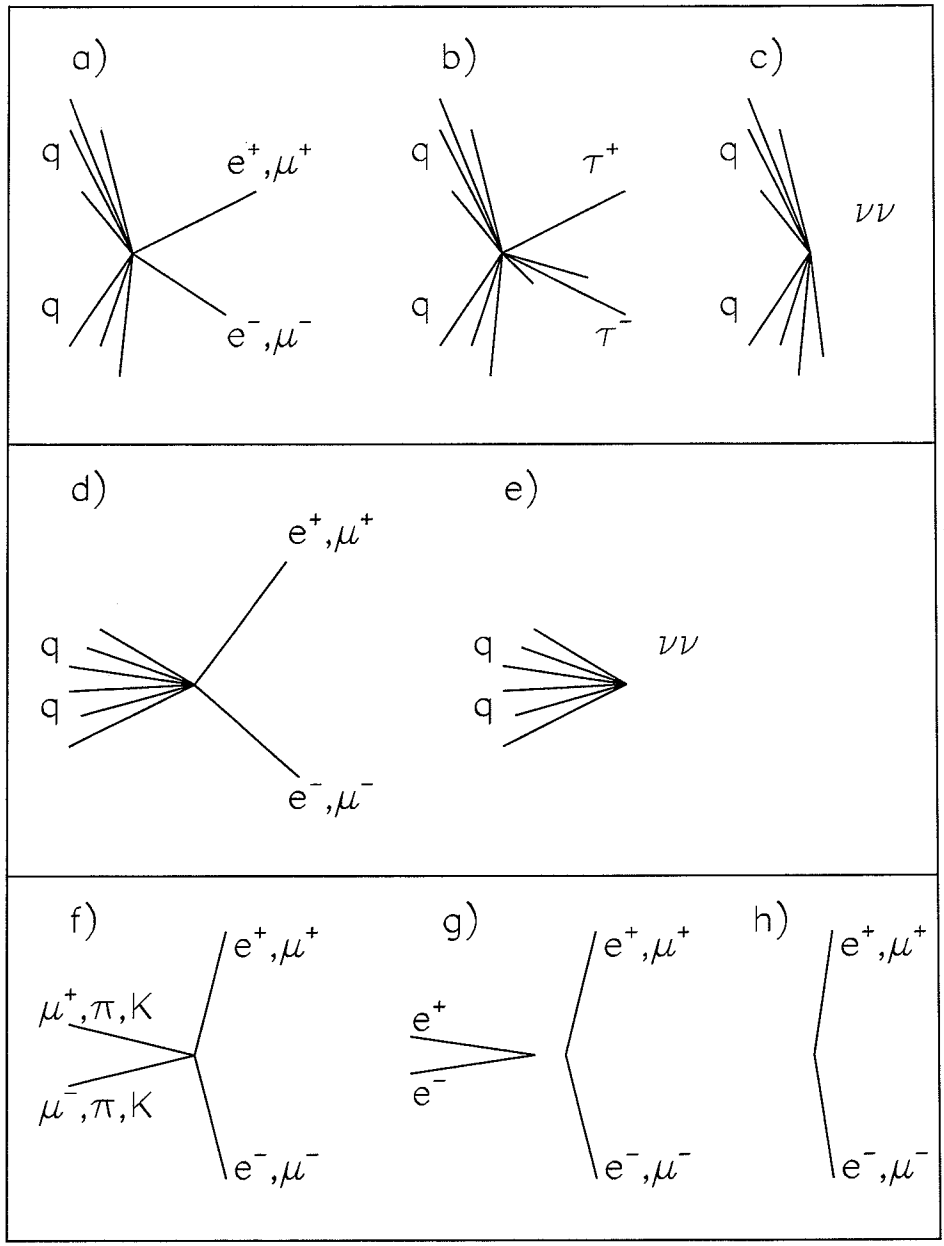

Figure 1.5: Schematic view of bremsstrahlung-produced Higgs signatures in the mass ranges $m_h \gg 10$ GeV (a-c), $m_h \approx 10$ GeV (d-e), $m_h \leq 2m_\tau$ (f-g) and $m_h \ll 2m_\mu$ (h).

1.4 The Two-Doublet Higgs Model

To date, no experiment has found evidence which favors the one-doublet Higgs sector of the Standard Model over more complicated structures. The simplest extensions, beyond the minimal one-doublet version, are models with two doublets. Among these, of particular interest (see section 1.5), are Supersymmetric extensions of the Standard Model. The two-doublet Higgs models imply the existence of a larger number of Higgs particles, with additional possibilities for a discovery.

Two-doublet models also include the one-doublet Higgs signatures with a reduced production rate. Consequently, Higgs signatures predicted in the one-doublet model, which are already experimentally excluded for a certain Higgs boson mass, can still be found when the experiment is sensitive to a lower Higgs production rate. Such a discovery would give strong support to the two-doublet Higgs theory. This section outlines the implications of the two-doublet Higgs model for an experimental search.

1.4.1 General Constraints

Extensions of the Minimal Standard Model Higgs sector must satisfy three general constraints, arising from a) the ρ-parameter measurement, b) absence of flavor-changing neutral currents, and c) unitarity requirement.

a) ρ-parameter: An extension of the minimal Higgs sector must not spoil the successful predictions of the Standard Model, among these are the correct prediction of the Z^0 and $W^{\pm}$ mass relation. A general Higgs scenario with an arbitrary number of singlets and doublets is compatible with $\rho = 1$ (eq. 1.8). Higgs representations beyond two doublets, where ρ is given as a function of the total $SU(2)_L$ isospin, T, the $U(1)_Y$ hypercharge, Y, and the VEV, $v_{(T,Y)}$, of each multiplet, require complicated parameter arrangements to match the measured ρ value. The largest contribution to the error on ρ (eq 1.9) is due to the uncertainty of the $W^{\pm}$ mass (Table 1.2). The increase of the LEP energy above the WW production threshold in a few years will reduce the error on m_W and therefore the error on ρ. Also, the CDF and D0 experiments [27] will reduce the error on m_W. A precise determination of ρ is very important, since any deviation from $\rho = 1$ requires 'New Physics' beyond the Minimal Standard Model. Unless a deviation from $\rho = 1$ is found, Higgs models consisting of only singlets and doublets are favored.

b) Flavor-Changing Neutral Currents: The absence of flavor-changing neutral currents (FCNC) [28] strongly constrains extensions of the Minimal Standard Model. In the Minimal Standard Model, FCNC are forbidden at the tree-level. In a more general Higgs model, this is no longer the case. In order to avoid unacceptable FCNC, one of the two following requirements must be satisfied: the Higgs boson masses are of order 1 TeV which will suppress FCNC, or all fermions of a given electric charge must couple to the same Higgs doublet. In the latter case, a theorem by Glashow and Weinberg [29] assures that FCNC, mediated by gauge bosons, are absent. This possibility is favored over an unnaturally high Higgs boson mass.

Glashow's and Weinberg's theorem does not determine the fermion couplings uniquely. In a general two-doublet model, there are two possible scenarios for the couplings of the Higgs bosons to fermions:

1) One doublet couples to up-type fermions and the other doublet couples to down-type fermions. This structure is required in the Minimal Supersymmetric extension of the Standard Model.

2) One doublet couples to up-type and down-type fermions, while the other doublet does not couple to fermions at all.

c) Unitarity: An extended Higgs model has to fulfill the unitarity bound, which prevents scattering amplitudes from growing without bounds as a function of energy. This is achieved by a renormalizable gauge theory with a non-trivial cancellation among Feynman diagrams that involve Higgs fields.

In the Minimal Standard Model, the unitarity requirement yields the tree level relation $g_{HZZ} = g\, m_Z$, where g is the gauge coupling and g_{HZZ} the coupling between the Minimal Standard Model Higgs and a Z^0 pair. In a more elaborate Higgs sector, the unitarity problems are cured by a combination of Feynman diagrams involving additional Higgs fields. Thus, unitarity relates the Minimal Standard Model Higgs couplings to the Higgs couplings of an extended Higgs sector.

A Higgs sector consisting of doublets and singlets H_i, which couple to the Z^0 with the coupling g_{H_iZZ} and to fermions with a coupling g_{H_iff}, must obey the following sum rules:

$$\sum_i (g_{H_iZZ})^2 = (g_{HZZ})^2, \qquad \sum_i (g_{H_iZZ})(g_{H_iff}) = (g_{HZZ})(g_{Hff}), \tag{1.24}$$

where g_{HZZ} and g_{Hff} are the corresponding couplings in the Minimal Standard Model. An obvious consequence of these sum rules is that the production rate of a Higgs

particle in an extended Higgs sector must always be smaller than or equal to the production rate of the Higgs boson in the Minimal Standard Model[3].

In summary, within the above three constraints, the Higgs sector of the Standard Model may have a variety of structures that are consistent with the observed experimental data. The simplest extension of the minimal Higgs model is the two-doublet model. In this extension, the absence of FCNC and $\rho = 1$ are guaranteed without unnaturally fine-tuning any parameter. The couplings between Higgs bosons and gauge bosons as well as between Higgs bosons and fermions are smaller than those in the Minimal Standard Model.

1.4.2 Higgs Boson Mass Spectrum

The Higgs spectrum in the two-doublet model is richer than that of the Minimal Standard Model. Two complex doublets of Higgs fields, $(1,2)_{1/2}$, have eight degrees of freedom:

$$\Phi_1 = \begin{pmatrix} \Phi_1^+ \\ \Phi_1^0 \end{pmatrix}, \qquad \Phi_2 = \begin{pmatrix} \Phi_2^+ \\ \Phi_2^0 \end{pmatrix}. \tag{1.25}$$

The most general gauge invariant Higgs potential must respect the discrete symmetry $\Phi_1 \leftrightarrow -\Phi_1$ in order to avoid FCNC. It has the form:

$$\begin{aligned} V(\Phi_1,\Phi_2) \;=\; & \lambda_1(\Phi_1^\dagger\Phi_1 - v_1^2)^2 + \lambda_2(\Phi_2^\dagger\Phi_2 - v_2^2)^2 \\ & +\lambda_3[(\Phi_1^\dagger\Phi_1 - v_1^2)(\Phi_2^\dagger\Phi_2 - v_2^2)]^2 \\ & +\lambda_4[(\Phi_1^\dagger\Phi_1)(\Phi_2^\dagger\Phi_2) - (\Phi_1^\dagger\Phi_2)(\Phi_2^\dagger\Phi_1)] \\ & +\lambda_5[\mathrm{Re}\ (\Phi_1^\dagger\Phi_2) - v_1 v_2 \cos\ \xi]^2 \\ & +\lambda_6[\mathrm{Im}\ (\Phi_1^\dagger\Phi_2) - v_1 v_2 \sin\ \xi]^2. \end{aligned} \tag{1.26}$$

The VEV

$$v_1 = <\Phi_1> = \begin{pmatrix} 0 \\ v_1 \end{pmatrix} \text{ and } v_2 = <\Phi_2> = \begin{pmatrix} 0 \\ v_2 e^{i\xi} \end{pmatrix} \tag{1.27}$$

minimize the potential for arbitrary positive parameters λ_i $(i = 1,\ldots,6)$ and arbitrary phase ξ. This potential with spontaneously broken symmetry is analogous to the Minimal Standard Model potential (eq. 1.1).

For $\sin\xi \neq 0$, the CP symmetry of the Lagrangian is broken due to the phase ξ. This leads to large CP violation, in contradiction to measurements, thus, ξ is

[3]The effect of radiative corrections on the sum rules has not been theoretically worked out yet, but is expected to be large [30].

set to zero. (In the Minimal Standard Model, CP violation can be incorporated by introducing a CP violating phase in the CKM matrix.)

The Higgs spectrum is obtained by expanding the Higgs fields around their minima. Three Goldstone bosons are identified by their derivative couplings to the gauge fields. Performing the expansion of the gauge invariant terms in the Lagrangian $\mathcal{L} = |D_\mu \Phi_1|^2 + |D_\mu \Phi_2|^2 + \ldots$ with the covariant derivative $D_\mu = (\partial_\mu - \frac{i}{2} g \tau \cdot \mathbf{W}_\mu - \frac{i}{2} g' \tau X_\mu)$, the gauge boson masses and an orthogonal basis of the neutral gauge boson mass eigenstates are obtained. The resulting gauge boson masses are given by:

$$m_{\mathrm{Z}} = (v_1^2 + v_2^2) \frac{g^2}{2 \cos \theta_W}, \qquad m_\gamma = 0, \qquad m_{\mathrm{W}} = (v_1^2 + v_2^2) \frac{g^2}{2}. \tag{1.28}$$

Thus, the quadratically summed VEV must be equal to the VEV of the Minimal Standard Model. The ratio of the VEV defines a key parameter:

$$\tan \beta \equiv v_2 / v_1. \tag{1.29}$$

The mass eigenstates of the neutral Higgs bosons are derived from their mass mixing matrix:

$$M = \begin{pmatrix} 4v_1^2(\lambda_1 + \lambda_3) + v_2^2 \lambda_5 & 4(\lambda_3 + \lambda_5) v_1 v_2 \\ 4(\lambda_3 + \lambda_5) v_1 v_2 & 4v_2^2(\lambda_2 + \lambda_3) + v_1^2 \lambda_5. \end{pmatrix} \tag{1.30}$$

Diagonalization introduces a second key parameter:

$$\alpha: \quad \text{neutral mixing angle.} \tag{1.31}$$

Physical Higgs boson masses for 2 charged Higgs bosons, $\mathrm{H}^\pm$, and 3 neutral Higgs bosons, h^0, H^0, A^0, are obtained:

$$\begin{aligned} m_{\mathrm{H}^\pm} &= \lambda_4 (v_1^2 + v_2^2), \qquad m_{\mathrm{A}} = \lambda_6 (v_1^2 + v_2^2), \\ m^2_{\mathrm{H,h}} &= \tfrac{1}{2} [M_{11} + M_{22} \pm \sqrt{(M_{11} - M_{22})^2 + 4 M_{12}^2}]. \end{aligned} \tag{1.32}$$

The convention $m_{\mathrm{H}} > m_{\mathrm{h}}$ is adopted.

Thus, the mass spectrum, which is derived from the gauge invariant CP-conserving Higgs potential with spontaneously broken symmetry, consists of five physical Higgs bosons. Eight initial degrees of freedom (six from the λ-parameters and two from the VEV) can be expressed as four Higgs boson mass parameters $m_{\mathrm{H}^\pm}$, m_{A}, m_{H}, m_{h} and $\tan \beta$, while the remaining three degrees of freedom are absorbed giving masses to the gauge bosons.

Charge conjugation, C, parity, P, and total angular momentum, J, quantum numbers of the Higgs bosons allow one to identify the possible Higgs production

mechanisms at the Z^0 resonance[4]. The J^{CP} quantum numbers are 1^{--} (1^{++}) for the photon, 1^{--} (1^{++}) for the Z^0, and 1^- (1^+) for the $W^\pm$. These must be conserved during the Higgs production process.

Applying the parity and charge conjugation operators to the Higgs fields, the following quantum numbers are assigned:

$$J^{CP}(A) = 0^{+-}, \quad J^{CP}(H) = 0^{++}, \quad J^{CP}(h) = 0^{++}, \quad J^{P}(H^\pm) = 0^+. \tag{1.33}$$

The A^0 Higgs boson is CP-odd; it is referred to as 'pseudoscalar' although it transforms as a scalar.

In summary, the Higgs spectrum of the two-doublet model consists of:

- one neutral pseudoscalar, A^0,
- two neutral scalars, H^0 and h^0, and
- two charged scalars, $H^\pm$.

The CP-odd nature of the A^0 boson forbids its bremsstrahlung emission off the Z^0 or the $W^\pm$. Furthermore, the interactions $Z^0 \to h^0h^0$ and $Z^0 \to A^0A^0$ are forbidden by Bose statistics (the Z wave function is antisymmetric, while Bose statistics requires a symmetric wave function for the AA state). The only remaining interactions for the Higgs production, near the Z^0 resonance, are:

a) the Bjorken process: $Z^0 \to Z^{0*}h^0$ or $Z^0 \to Z^{0*}H^0$,

b) neutral pair production: $Z^0 \to h^0A^0$ or $Z^0 \to H^0A^0$, and

c) charged pair production: $Z^0 \to H^+H^-$.

Corresponding Feynman diagrams are shown in Figure 1.6.

It is important to point out that the Higgs bremsstrahlung coupling g_{hZZ} and neutral Higgs pair production coupling g_{ZhA} are complementary functions of the mixing angle α and $\tan\beta$:

$$g_{hZZ} \propto \sin(\beta - \alpha), \qquad g_{ZhA} \propto \cos(\beta - \alpha). \tag{1.34}$$

[4]For charged particles only the parity quantum number is defined.

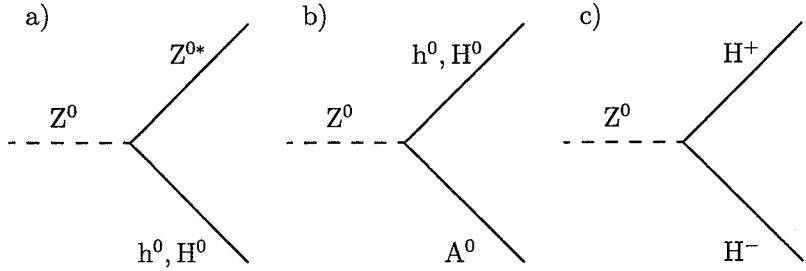

Figure 1.6: Diagrams of Higgs production processes in the two-doublet Higgs model by a) Higgs bremsstrahlung, b) neutral Higgs pair-production, and c) charged Higgs pair-production.

1.4.3 Neutral Higgs Bosons

The production width for the h^0 of the two-doublet model and the H^0_{SM} boson of the Minimal Standard Model, are related by:

$$\sin^2(\beta-\alpha) = \frac{\Gamma(Z^0 \to h^0 Z^{0*})}{\Gamma(Z^0 \to H^0_{SM} Z^{0*})}. \tag{1.35}$$

The Z^0 partial width in Higgs pairs is proportional to $\cos^2(\beta-\alpha)$:

$$\Gamma(Z^0 \to h^0 A^0) = \Gamma(Z^0 \to \nu\bar{\nu})\frac{1}{2}\lambda^{3/2}\left(\frac{m_h^2}{m_Z^2}, \frac{m_A^2}{m_Z^2}\right) \times \cos^2(\beta-\alpha), \tag{1.36}$$

where $\lambda(a,b) = (1-a-b)^2 - 4ab$.

Two experimentally relevant conclusions can be drawn:

- First, it follows that the same Higgs production and decay process for a certain mass that has been excluded in the Minimal Standard Model can still have escaped detection. A discovery of Higgs bosons with low production rate and with the kinematics of the Bjorken process would strongly suggest that a non-minimal Higgs structure is realized in nature.

- Second, in the two-doublet model, the Higgs production via the Bjorken process and the neutral Higgs pair production are complementary. However, the Higgs bremsstrahlung production and neutral Higgs pair-production are not explicitly predicted, since α and $\tan\beta$ are unknown parameters of the theory.

The Yukawa interaction determines the Higgs decay branching ratios into fermion pairs. This also depends on α and $\tan\beta$. The Higgs coupling has the

general form of:

$$g_{\Phi ff} = const \cdot m_f \cdot f(\alpha, \tan\beta), \tag{1.37}$$

where $\Phi = h^0, H^0, A^0$ and $f(\alpha, \tan\beta)$ depends on which of the two possible Higgs couplings to the fermions is chosen (see section 1.4.1). Table 1.3 summarizes the dependence of the function f on α and $\tan\beta$ for the case when up-type quarks and leptons couple to Higgs doublet Φ_1 and down-type quarks couple to Higgs doublet Φ_2. The factors are identical for the second and third family. The ratios described by f satisfy the second unitarity sum rule eq. (1.24) for all α and $\tan\beta$.

Decay	$h^0 \to e^+e^-$	$\to u\bar{u}$	$\to d\bar{d}$	$A^0 \to e^+e^-$	$\to u\bar{u}$	$\to d\bar{d}$
$f(\alpha, \tan\beta) =$	$\frac{\sin\alpha}{\cos\beta}$	$\frac{\cos\alpha}{\sin\beta}$	$\frac{\sin\alpha}{\cos\beta}$	$\tan\beta$	$\cot\beta$	$\tan\beta$

Table 1.3: Higgs-fermion coupling in the two-doublet Higgs model for the case when one doublet couples to up-type fermions and the other couples to down-type fermions. This structure is required in the Minimal Supersymmetric extension of the Standard Model.

The Yukawa interaction of the Higgs with the fermions implies that the Higgs bosons decay into the heaviest kinematically accessible fermion pair. This general feature guides the search for the neutral Higgs bosons. In a two-doublet model, many Higgs decay channels are possible for a given Higgs boson mass due to the two arbitrary parameters α and $\tan\beta$. Independently of the choice of α and $\tan\beta$, the following general features are found (if the decays are kinematically allowed):

- Higgs bosons decays into $\tau^+\tau^-$ pairs are dominant over decays into e^+e^- or $\mu^+\mu^-$,
- decay rates into c-quarks are larger than decay rate into u-quarks (where the t-quark is kinematically not accessible), and
- decays into b-quarks are the leading down-type decay modes.

The ratio of Higgs decays into leptons and hadrons depends on α and $\tan\beta$, since only the charged leptons couple to the Higgs. It is important to note that due to the trigonometric functions, the Higgs branching ratio into a $\tau^+\tau^-$ or $b\bar{b}$ pair can vanish simultaneously. In this case, the $c\bar{c}$ branching fraction dominates.

In Supersymmetric models, α and $\tan\beta$ are related to the Higgs boson masses. The Higgs branching fractions are uniquely determined at the tree level

in the framework of the Minimal Supersymmetric extension of the Standard Model for a given Higgs boson mass pair, as discussed in section 1.5. The measurement of leptonic and hadronic Higgs decay ratios, after a possible discovery of the two-doublet Higgs bosons, would support or exclude Supersymmetric models.

1.4.4 Charged Higgs Bosons

The existence of charged Higgs bosons would add new phenomena to the Minimal Standard Model. This section summarizes the predictions on charged Higgs production and decay in the mass range which had not been excluded before LEP began operation of 20 GeV [31] and the present kinematic production limit of 45 GeV. Also, prospective constraints on the charged Higgs sector from $B^0 - \overline{B}^0$ meson mixing measurements are outlined.

The partial width of the Z^0 decay into a charged Higgs pair at the tree-level approximation depends only on the mass of the charged Higgs [23]:

$$\Gamma(Z^0 \to H^+H^-) = \frac{G_F m_Z^3}{6\sqrt{2}\pi}(\tfrac{1}{2} - \sin^2\theta_W)^2\beta_{H^\pm}^3, \;\; \beta_{H^\pm} = \sqrt{1 - \frac{4m_{H^\pm}^2}{m_Z^2}}. \qquad (1.38)$$

The number of expected charged Higgs events per 400,000 collected hadronic Z^0 boson decays is shown in Figure 1.7. More than 2500 charged Higgs events are expected for a Higgs boson mass of about 20 GeV and about 100 events are expected at 40 GeV.

The following decay channels may be open:

$$H^+ \longrightarrow \nu e^+, \; \nu\mu^+, \; \nu\tau^+; \; u\bar{d}, \; c\bar{d}, \; t\bar{d}, \; u\bar{s}, \; c\bar{s}, \; t\bar{s}, \; u\bar{b}, \; c\bar{b}, \; t\bar{b}. \qquad (1.39)$$

The decay channels involving the top quark will be ignored in this work, since the top mass is higher than the available LEP energy. Thus, the Higgs decays into the three heaviest quark pairs, $H^\pm \to u\bar{b}, \; c\bar{s}, \; c\bar{b}$ are the dominant hadronic decay channels. Furthermore, the $\nu\tau^+$ channel is dominant over other leptonic channels. Taking the experimental and theoretical knowledge of the Cabbibo-Kobayaschi-Maskawa (CKM) matrix elements into account [32], Higgs decays are constrained further. The CKM-matrix has the form:

$$V_{ij} = \begin{pmatrix} V_{ud} & V_{us} & V_{ub} \\ V_{cd} & V_{cs} & V_{cb} \\ V_{td} & V_{ts} & V_{tb}. \end{pmatrix} \qquad (1.40)$$

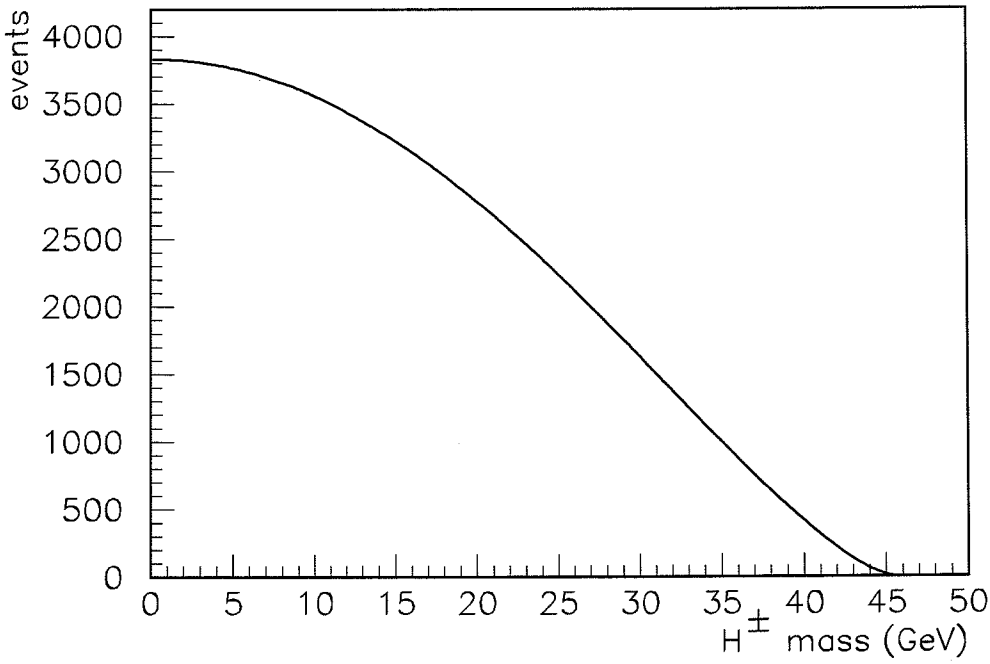

Figure 1.7: Number of expected $Z^0 \to H^+H^-$ events per 400,000 hadronic Z^0 decays in the general two-doublet model.

The charged Higgs decay coupling to the quark pair ij is proportional to the factor V_{ij}. The diagonal elements of the matrix V_{ij} are of order 1 while the off-diagonal elements are largely suppressed. Therefore, $H^+ \to c\bar{s}$ is the dominant hadronic decay channel. In summary, the most important decay channels are: $H^+ \to \nu\tau^+$ and $H^+ \to c\bar{s}$. The relative rates of the resulting final states can be parametrized in terms of the leptonic branching ratio $R_l \equiv \mathrm{BR}(H^+ \to \tau^+\nu)$. The relative decay fractions are given by:

$$\begin{aligned} \Gamma(Z^0 \to H^+H^- \to cs\tau\nu) &\propto 2R_l(1-R_l) \\ \Gamma(Z^0 \to H^+H^- \to c\bar{s}cs) &\propto (1-R_l)(1-R_l) \\ \Gamma(Z^0 \to H^+H^- \to \tau^+\nu\tau^-\bar{\nu}) &\propto R_l^2. \end{aligned} \tag{1.41}$$

In addition to direct searches, measurements of the $B^0 - \overline{B}^0$ mixing can give important information about the charged Higgs sector of the two-doublet model. At LEP and other accelerators, $B^0 - \overline{B}^0$ mixing measurements have recently been

improved. A detailed description of the L3 mixing measurements is given in reference [33]. The contribution of the charged Higgs to B^0 meson mixing is illustrated in Figure 1.8. The virtual top quark is dominant in the fermionic part of the loop.

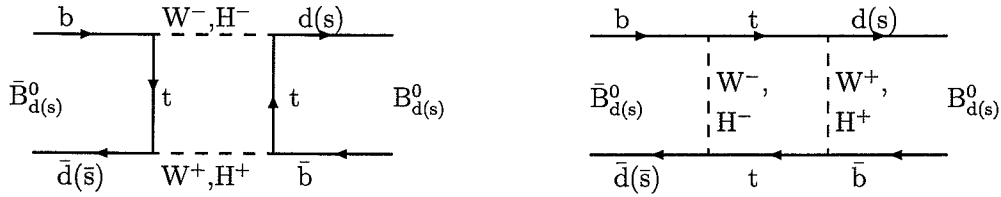

Figure 1.8: Diagrams of charged Higgs contributions to $B^0_{d(s)} - \overline{B}^0_{d(s)}$ mixing. In the Minimal Standard Model, mixing results only via $W^{\pm}$ exchange. In the two-doublet model, one or two charged Higgs bosons can be exchanged in addition to the $W^{\pm}$ bosons, thus, the expected mixing is larger.

In the Standard Model with two Higgs doublets, the parameters m_H, $\tan\beta$, and m_t are related to the measurable mixing parameter:

$$r_{d(s)} \equiv \frac{P(B^0_{d(s)} \to \overline{B}^0_{d(s)})}{P(B^0_{d(s)} \to B^0_{d(s)})}, \tag{1.42}$$

where P is the probability for each process. This relation, evaluated in reference [34], is independent of the choice of two possible Higgs-fermion couplings scenarios (page 19).

Although the possible mechanism of the mixing due to the charged Higgs bosons is well understood, at the moment, experimental data is not conclusive and no relevant constraints on the charged Higgs sector can be obtained. To date the mixing has been measured to be [35]:

$$r_d = 0.20 \pm 0.03, \qquad r_s = 1.13 \pm 0.45. \tag{1.43}$$

A value $r = 1$ corresponds to maximal mixing. Owing to the large errors, no conclusion on the existence of charged Higgs boson can be drawn.

In the future, higher statistics will improve the mixing measurements. Conclusive experimental information on the charged Higgs sector from $B^0 - \overline{B}^0$ mixing measurement also requires the discovery of the top quark, since the mass and the CKM matrix elements of the top quark are crucial parameters for the theoretical prediction of the mixing. If charged Higgs bosons are required to explain $B^0 - \overline{B}^0$ mixing, then their mass can also be estimated in meson mixing experiments.

1.4.5 One-Loop Potential

Much progress has been made in theoretical investigations of the effects of radiative corrections in the framework of the two-doublet model. Four main aspects already discussed in section 1.3.3 for the Minimal Standard Model (vacuum stability, Coleman-Weinberg limit, phase transitions at finite temperature and the triviality Higgs boson mass bound) are briefly outlined for the two-doublet model in the next paragraphs.

Top Quark and Higgs Boson Mass Relation: The existence of a second Higgs doublet destabilizes the vacuum further in the presence of a heavy top quark. For a given top mass ($m_t \propto g_t v_2$), the Higgs-fermion coupling, g_t, has to be larger in the two-doublet model than in the minimal Higgs model, since the VEV, v_1, and v_2, of the doublets are smaller, while the quadratic sum of the VEV is identical in both models eq. (1.28). A study [36] of the vacuum destabilization based on one-loop calculations shows that in the top quark and Higgs boson mass parameter space, a region similar to that in the one-doublet case is excluded by vacuum instability. However, no experimentally relevant conclusions for the two-doublet Higgs search can be drawn.

Coleman-Weinberg lower limit: The lower Higgs boson mass limit in the Coleman-Weinberg case, where the tree-level Higgs boson mass is set to zero, can be obtained in complete analogy to the one-doublet Higgs model. In the two-doublet model, the B factor of eq. 1.14 includes the contributions of all five Higgs bosons. The new bosonic contribution increases the Coleman-Weinberg mass m_{CW}. It can become positive while m_t is large. In the neutral Higgs sector of the one-doublet model, relation 1.16 is replaced by [14]:

$$m_H^2 \cos^2(\alpha - \beta) + m_h \sin^2(\alpha - \beta) > m_{CW}^2. \tag{1.44}$$

This relation becomes relevant as a consistency check if Higgs bosons with different masses have been found.

Finite temperature and phase transition: The possibility of a phase transition in the framework of the two-doublet model at the electroweak energy scale ($\approx$ 100 GeV) has been investigated [37] . An upper Higgs boson mass limit can be obtained, based on the idea that the matter-antimatter asymmetry, which is present in

the universe, is generated at the electroweak phase transition. The recently experimentally determined lower Higgs boson mass limit excludes, in the one-doublet Higgs model, this cosmological theory by several GeV [38]. In the two-doublet model, the upper Higgs boson mass limit vanishes when heavy Higgs bosons are also present. Therefore, the above cosmology argument favors a Higgs scenario beyond the Minimal Standard Model.

Triviality Upper Higgs Boson Mass Bound: An upper Higgs boson mass bound on the doublet version of the Standard Model has recently been presented [39]. Encouraged by the fact that in the one-doublet case the one-loop calculation and the correct lattice calculation give a very similar upper Higgs boson mass limit, the one-loop investigation is pursued in the two-doublet case. The upper Higgs boson mass limit increases to 1 TeV in the two-doublet model for most choices of α and $\tan\beta$.

In summary, one-loop radiative correction calculations for the two-doublet model do not yet lead to conclusive predictions for experimental Higgs search.

1.4.6 Implications for the Higgs Boson Search at LEP

A summary of the theoretical implications for the Higgs search at LEP in the framework of the general two-doublet Higgs model is in order. Extensions of the Standard Model Higgs sector must be consistent with two important experimental results on neutral currents: first, the ρ parameter is very nearly equal to one; and second, there are stringent limits on flavor-changing neutral currents. Models that contain only Higgs doublets automatically satisfy the first constraint, and can satisfy the second without unnatural fine-tuning of parameters. A model with two Higgs doublets illustrates new phenomena of more general models:

- The rate of Higgs bremsstrahlung is suppressed compared to the Minimal Standard Model prediction by a factor of $\sin^2(\beta-\alpha)$, where α and β are free parameters of the two-doublet model. If kinematically allowed, the process $h^0 \to A^0A^0$ may dominate h^0 decays, giving rise to more complex final states. In section 4, searches for Higgs bremsstrahlung from the Z^0 in the high mass range around 50 GeV are summarized. An update of searches for Higgs bremsstrahlung for Higgs boson masses less than 30 GeV is reported. From negative results, a limit on $\sin^2(\beta-\alpha)$ can be obtained.

- Independent, limits on $\cos^2(\beta-\alpha)$ can be obtained from constraints on non-standard contributions to the Z^0 width and from direct searches for $h^0 \rightarrow A^0A^0$ signatures from singly-produced Higgs. This analysis is reported in section 7. The limits on $\sin^2(\beta-\alpha)$ and $\cos^2(\beta-\alpha)$ can be combined to exclude a region in the (m_h,m_A)plane. A mass pair (m_h,m_A) will be excluded if the corresponding upper limit on $\sin^2(\beta-\alpha)$ from the bremsstrahlung process is lower than the lower limit coming from the pair-production process.

- The neutral pair-production mechanism leads to multi-jet and/or multi-lepton final states, such as

$$\begin{aligned} &Z^0 \rightarrow h^0A^0 \rightarrow b\bar{b}b\bar{b}, \quad \tau^+\tau^-b\bar{b}, \quad \tau^+\tau^-\tau^+\tau^-, \\ &Z^0 \rightarrow h^0A^0 \rightarrow A^0A^0A^0 \rightarrow b\bar{b}b\bar{b}b\bar{b}. \end{aligned} \tag{1.45}$$

  Although Higgs bosons tend to decay into the most massive kinematically accessible fermion pair, no unique prediction of the branching ratios can be made due to the unknown values of the parameters α and $\tan\beta$. Therefore, negative search results for each channel are given as limits on the production branching ratio:

$$\Gamma(Z^0 \rightarrow h^0A^0)BR(h^0A^0 \rightarrow X)/\Gamma(Z^0 \rightarrow q\bar{q}), \tag{1.46}$$

  as a function of the (m_h,m_A) masses, where X stands for the visible final states as defined in processes (1.45). The searches for these signatures are reported in chapter 5 and 6.

- In the charged Higgs sector of the two-doublet model, the predicted production rate depends only on the charged Higgs boson mass. The decays of the pair-produced charged Higgs can be constrained to three dominant channels and the relative branching fractions are parametrized by one parameter. The searches for the signatures of the charged Higgs bosons in the three dominant processes

$$Z^0 \rightarrow H^+H^- \rightarrow \quad c\bar{s}\bar{c}s, \quad \tau\nu cs, \quad \tau^+\nu\tau^-\nu \tag{1.47}$$

  are reported in chapters 6.1 to 6.3. Negative results can be reported in each channel as limits on the charged Higgs boson mass and the leptonic Higgs decay branching ratio.

The $B^0 - \overline{B}^0$ meson mixing measurements could be very important for the discovery of charged Higgs bosons. However, the errors on mixing measurements and theoretical uncertainties are still large, and the predictions for the mixing can only be conclusive after the discovery of the top quark.

1.5 The Supersymmetric Model

Supersymmetry models [40] have gained much attention over the last ten years. They are promising extensions of the Standard Model due to some very attractive theoretical features. First, their theoretical motivations are outlined. Subsequently, the experimental status of Supersymmetric models is summarized. The two-doublet Higgs model, described in the previous sections, is the underlying Higgs structure of the MSSM. In the MSSM, important mass relations are obtained. The implications at the tree-level for the Higgs phenomenology at LEP are summarized. Recent theoretical studies reveal that radiative corrections to the MSSM change its predictions for the neutral Higgs sector dramatically (section 1.6).

1.5.1 Motivation of Supersymmetry

Supersymmetry is mostly motivated by its attractive solution to the gauge hierarchy problem of the Minimal Standard Model. Parameters in the Higgs sector of the Minimal Standard Model have to be fine-tuned when loop corrections to the Higgs boson mass are taken into account. Otherwise, the Higgs boson mass could not be in agreement with the upper mass bound of 640 GeV (section 1.3.3). The fine tuning is a major theoretical flaw of the Minimal Standard Model Higgs sector. The Standard Model becomes an unnatural theory in the sense of 't Hooft's definition of *natural* [41]:

> "At any energy scale μ, a physical parameter or set of physical parameters $\alpha_i(\mu)$ is allowed to be very small only if the replacement $\alpha_i(\mu) = 0$ would increase the symmetry of the system."

Supersymmetry is exactly this larger symmetry and the Minimal Standard Model becomes an effective low-energy theory. The Standard Model is recovered in the limit when Supersymmetry particles decouple (their masses are set to infinity). Many other examples of an effective theory exist where the deeper underlying structure escaped detection for a long time. For example, in the Newtonian theory of mechanics

for small velocities and Special Relativity, or the Euclidian nature of space for small distances and the curvature of space in General Relativity.

In the Minimal Standard Model, radiative corrections to the Higgs boson mass, m_{H}, depend on the cut-off scale, Λ, and are of the form $m_{\mathrm{H}}^2 = m_0^2 + cg^2\Lambda^2$, where m_0 is the bare Higgs boson mass, g is the Higgs coupling constant and c is a constant of order one [14]. An analogous cut-off dependence has been known for a long time, the corrections to the fermion masses diverge proportional to $\ln(\Lambda/m_{\mathrm{f}})$. The significant difference is that the divergence is logarithmic and not quadratic as in the Higgs case. Even when the QED cut-off is at the Planck scale ($\approx 10^{19}$ GeV), the corrections are still of the order of the physical fermion masses. Assuming the Standard Model describes the physics up to the unification energy scale of the electromagnetic, weak and strong force ($\approx 10^{15}$ GeV), and taking the upper Higgs boson mass limit into account, a fine-tuning of the bare mass to at least one part in 10^{24} is required [42].

The most promising approach towards solving this problem is Supersymmetry. In Supersymmetry, each fermion has a bosonic partner. For each particle which contributes in a Feynman loop diagram, there exists a second loop. The fermion loops contribute with a factor of (-1) compared to the bosonic graphs, thus, all loop graphs cancel for exact Supersymmetry. In exact Supersymmetry, the masses of the Supersymmetric partners are equal to the masses of the Standard Model particles. Consequently, the cancellation is to all orders of perturbation theory (renormalization theorem).

Evidently, Supersymmetry can not be an exact symmetry, since many experiments have shown that the Supersymmetric partners must have a much larger mass than their counterparts. The mass differences between the Standard Model and Supersymmetric particles cannot be larger than the cut-off scale, $\Lambda^2 \approx |m_{\mathrm{SM}}^2 - m_{\mathrm{SUSY}}^2|$. The fine-tuning problem appears when Λ is of the order of the electroweak scale (100 GeV). Masses of the Supersymmetric particles are expected to be at this energy scale, explaining the intense search at LEP for these particles.

Since Supersymmetry is not exact, Supersymmetric models improve the renormalization behavior but do not cancel all loop diagrams completely. Therefore, radiative corrections in the MSSM have to be considered. They have strong impact on the Higgs sector, as outlined in section 1.6.

Another important theoretical argument for considering Supersymmetry as an extension of the Standard Model is based on the Supersymmetric group algebra.

In Supersymmetric models, an operator, Q, exists which transforms a bosonic field into a fermionic field, $QB = F$. Let P_μ be a 4-momentum, then Supersymmetry can be defined by the algebra:

$$\{Q^i_\alpha, \bar{Q}^j_\beta\} = 2(\gamma^\mu)_{\alpha\beta} P_\mu \delta_{ij}, \qquad [Q^i_\alpha, P_\mu] = 0, \qquad [P_\alpha, P_\beta] = 0, \tag{1.48}$$

where latin indices label the different generators and greek subscripts are Dirac indices. Unlike the Standard Model algebra, the Supersymmetry algebra is related to space-time translations. This feature has far-reaching consequences, since General Relativity also arises from local space-time translations. Thus, Supersymmetric models can be the framework for the unification of electromagnetic, weak and strong forces of the Standard Model with the gravitational force. Owing to the renormalization theorem, theories based on Supersymmetry promise a better renormalization behavior than quantum gravity models.

In regard to the two-doublet Higgs model, Supersymmetry constrains the Higgs sector, which results in precise experimental predictions as outlined in section 1.5.3. The Supersymmetric Higgs sector is important for the verification or exclusion of the MSSM. In the future, when higher energies at LEP are available, either the lightest MSSM Higgs boson will be found, or the MSSM will be excluded as discussed in section 1.6.

1.5.2 Experimental Status of Supersymmetry

No direct experimental evidence for Supersymmetry has been found. Many searches for Supersymmetric particles have recently been performed by the LEP experiments, resulting in improvements on existing lower mass limits. The negative results of the L3 searches for Supersymmetric particles are summarized in Table 1.4 [43]. All mass limits are close to the kinematic limit for pair-produced particles of 45 GeV, set by the present center-of-mass energy of the LEP accelerator.

Experimental indications that Supersymmetry may be the correct extension of the Standard Model are obtained in the framework of Grand Unification Theories [44]. These theories predict the unification of electromagnetic, weak, and strong coupling constants at an energy scale of about 10^{15} eV. The LEP experiments have contributed to measuring the slope of the three running coupling constants, leading to the conclusion that the unification of the forces is not possible in the Standard Model, while it is possible in Supersymmetry models.

Particle	Mass Limit (GeV)
$\tilde{e}$	41
$\tilde{\mu}$	41
$\tilde{u}$	45.5
$\tilde{d}$	45.5
$\chi^{\pm}$	44

Table 1.4: Lower mass limits on selectron, smuon, sup-and sdown-quarks and charginos from the L3 experiment.

1.5.3 Higgs Boson Mass Relations in the Minimal Supersymmetric Standard Model

As in the Minimal Standard Model, the fermions obtain masses via a Yukawa coupling to the Higgs bosons. Supersymmetry not only constrains the two-doublet model, but also requires the existence of a second Higgs doublet[5] because of the following two arguments.

First, the most general $SU(2)_L \times U(1)_Y$ invariant superpotential, which consists of two Higgs superfields $\hat{H}_1 = (H_1, \tilde{H}_1)$ and $\hat{H}_2 = (H_2, \tilde{H}_2)$, where $\tilde{H}_{1,2}$ are the fermionic superpartners (Higgsinos) of the Higgs boson fields, has the form:

$$W_F = \epsilon_{ij}[g_l \hat{H}_1^i \hat{\bar{L}}^j \hat{R} + g_d \hat{H}_1^i \hat{\bar{Q}}^j \hat{D} + g_u \hat{H}_2^i \hat{\bar{Q}}^j \hat{U}]. \tag{1.49}$$

Here $\hat{Q}$, $\hat{L}$ are $SU(2)_L$ quark and lepton superfields, $\hat{U}$, $\hat{D}$ are the $SU(2)_L$ singlets quark superfields, $\hat{R}$ is the $SU(2)_L$ charged lepton singlet superfield, i, j are the $SU(2)_L$ indices, and $g_{l,d,u}$ are the Yukawa coupling constants for leptons, down and up-type quarks, respectively. The second Higgs doublet with opposite hypercharge is needed in order to give masses to down quarks while conserving the $SU(2)_L \times U(1)_Y$ invariance. This is the Supersymmetric analog of eq. (1.10). The $SU(2)_L$ and $U(1)_Y$ quantum numbers of the superfields are summarized in Table 1.5. In the Supersymmetry Model, it is not possible to generate a second Higgs doublet from the first doublet with opposite hypercharge, as in the Minimal Standard Model case, since Supersymmetry would be explicitly broken.

The second argument, why two Higgs doublets are needed, arises because the sum of triangle graphs involving fermions must vanish to ensure the absence of

[5]Any even number of Higgs doublets is supported by Supersymmetry. In this work, only the simplest version with two Higgs doublets is considered.

$\hat{H}_1$	$\hat{H}_2$	$\hat{Q}$	$\hat{L}$	$\hat{U}$	$\hat{D}$	$\hat{R}$
$\mathbf{2}_{1/2}$	$\mathbf{2}_{-1/2}$	$\mathbf{2}_{1/6}$	$\mathbf{2}_{-1/2}$	$\mathbf{1}_{1/3}$	$\mathbf{1}_{-1/3}$	$\mathbf{1}_{-1}$

Table 1.5: $SU(2)_L \times U(1)_Y$ superfield quantum numbers. Under $SU(3)_C$ transformations, all fields are singlets. Mass terms for charged leptons and up- and down-type quarks can be constructed while the gauge symmetry is preserved.

anomalies which destroy the renormalizability of the theory. An analogous argument in the Standard Model exists: fermionic contributions to triangle graphs require the existence of the top quark to cancel the anomalies. Anomalies in the Higgs sector of the Standard Model do not appear, since only a bosonic Higgs exists.

In the following study, only the bosonic part of the Higgs sector in the Supersymmetry model will be of interest. These Higgs fields are analogous to the two-doublet Higgs fields of section 1.4, and have the form:

$$H_1 = \begin{pmatrix} \Phi_1^0 \\ \Phi_1^- \end{pmatrix}, \quad H_2 = \begin{pmatrix} \Phi_2^+ \\ \Phi_2^0 \end{pmatrix}, \tag{1.50}$$

with hypercharge $-\frac{1}{2}$ and $+\frac{1}{2}$, respectively.

The Supersymmetry breaking terms in the Lagrangian are constrained in order not to destroy the main motivation for Supersymmetry, the cancellation of the quadratic cut-off contributions to the Higgs boson mass. Soft Supersymmetry breaking terms, defined as being associated with a dimensionful parameter and spontaneous Supersymmetry breaking terms, both of dimension four, must respect Supersymmetry in order not to regenerate quadratic divergencies. The required cancellation relates the gauge boson couplings to the Higgs couplings and results in the experimentally relevant masses relations between the five physical Higgs bosons [45].

The introduction of complex $SU(2)_L \times U(1)_Y$ singlet fields, N, in addition to the two Higgs doublets is consistent with the Supersymmetry requirement. Although these singlets arise in superstring theories naturally, they could cause problems with the naturalness motivation of Supersymmetry. The introduction of singlet fields goes beyond the MSSM and decreases the predictive power of the theory.

In the absence of singlet fields, the most general superpotential that respects the global symmetry of baryon and lepton conservation has the form:

$$W = \mu \epsilon_{ij} H_1^i H_2^j + W_F, \tag{1.51}$$

where μ has the dimension of mass and W_F is given by equation 1.49.

The scalar field potential, V, which describes the bosonic Higgs sector is derived from the superpotential, W. After adding soft Supersymmetry breaking mass terms and rearranging the terms to recover the form of the potential of the general two-doublet model eq. (1.26), the bosonic Higgs potential is given by:

$$\begin{aligned} V &= (m_1^2 + |\mu|^2) H_1^{i*} H_1^i + (m_2^2 + |\mu|^2) H_2^{i*} H_2^i \\ &\quad - m_{12}^2 (\epsilon_{ij} H_1^i H_2^j + h.c.) \\ &\quad + \tfrac{1}{8}(g^2 + g'^2)[H_1^{i*} H_1^i + H_2^{i*} H_2^i] + \tfrac{1}{2} g^2 |H_1^{i*} H_2^i|^2 . \end{aligned} \tag{1.52}$$

Hence, the same five physical Higgs fields, which are identified in the general two-doublet model (section 1.4), are expanded around their VEV. The comparison of the above Supersymmetric Higgs potential with the potential of the general two-doublet model eq. (1.26) leads to constraints on the six degrees of freedom of the general two-doublet model:

$$\lambda_1 = \lambda_2, \tag{1.53}$$

$$\lambda_3 = \frac{1}{8}(g^2 + g'^2) - \lambda_1, \tag{1.54}$$

$$\lambda_4 = 2\lambda_1 - \tfrac{1}{2} g'^2, \tag{1.55}$$

$$\lambda_5 = \lambda_6 = 2\lambda_1 - \tfrac{1}{2}(g^2 + g'^2). \tag{1.56}$$

The last relation assures CP conservation, since the complex phase ξ of the general two-doublet model can be absorbed by a field redefinition.

Relations for the m_i parameters are also found by comparison with the two-doublet potential:

$$m_1^2 = |\mu|^2 + 2\lambda_1 v_2^2 - \tfrac{1}{2} m_Z^2, \tag{1.57}$$

$$m_2^2 = |\mu|^2 + 2\lambda_1 v_1^2 - \tfrac{1}{2} m_Z^2, \tag{1.58}$$

$$m_{12}^2 = -\tfrac{1}{2} v_1 v_2 (g^2 + g'^2 - 4\lambda_1). \tag{1.59}$$

In the general two-doublet model, the Higgs boson masses are expressed in terms of the VEV v_1, v_2 and the parameters λ_i, $i = 1, \ldots, 6$ (1.30), (1.32). From (1.55) and (1.56), the mass of the neutral pseudoscalar, m_{A}, and the mass of the charged Higgs, $m_{\mathrm{H}^\pm}$, are related to the charged gauge boson mass m_{W}:

$$m_{\mathrm{A}}^2 = m_{\mathrm{H}^\pm}^2 - m_{\mathrm{W}}^2. \tag{1.60}$$

The neutral scalar masses are related to the neutral gauge boson mass (m_Z), m_A, and $\tan\beta$ by:

$$m^2_{H,h} = \tfrac{1}{2}[m^2_A + m^2_Z \pm \sqrt{(m^2_A + m^2_Z)^2 - 4m^2_Z m^2_A \cos^2\beta}]. \tag{1.61}$$

These relations have crucial implications for the Higgs search at LEP:

$$\begin{gathered} m_{H^\pm} \geq m_W, \qquad m_H \geq m_Z, \qquad m_A \geq m_h, \\ m_h \leq m_Z |\cos 2\beta| \leq m_Z. \end{gathered} \tag{1.62}$$

The last relation is very important, one neutral Higgs boson must have a mass less than m_Z. This exciting prediction gives a much higher probability for discoveries of the neutral Higgs arising in the MSSM than that of the Higgs boson in the Minimal Standard Model. As shown in section 1.3.3, the theoretical upper mass bound for the Minimal Standard Model Higgs is much higher than m_Z. The first and second mass in eq. (1.62) implies that the search for the charged and the second neutral Higgs bosons at current LEP energies is not fruitful in the framework of the MSSM.

In addition, Supersymmetry is a promising framework for the Higgs search at LEP since the mixing angle α and $\tan\beta$ are functions of the Higgs boson masses, based on the relations (1.53) to (1.56):

$$\sin 2\alpha = -\sin 2\beta \left(\frac{m^2_H + m^2_h}{m_H - m^2_h}\right), \qquad \cos 2\alpha = -\cos 2\beta \left(\frac{m^2_A - m^2_Z}{m_H - m^2_h}\right). \tag{1.63}$$

Therefore, the expected production cross-section, which is dependent on two arbitrary parameters in the general two-doublet model, can be expressed as a function of the two neutral Higgs boson masses. For the experimental search, it is convenient to chose (m_h,m_A) as free parameters.

If Supersymmetry is the deeper underlying structure of the Standard Model, then, at the limit where Supersymmetry effects decouple, the Higgs structure of the Minimal Standard Model has to be recovered. By removing the pseudoscalar Higgs ($m_A \to \infty$ for arbitrary fixed $\tan\beta$) eq. (1.60) requires $m_H \to \infty$, then eq. (1.63) implies $\sin 2\alpha = -\sin 2\beta$ and $\cos 2\alpha = -\cos 2\beta$. Consequently, the hZZ coupling suppression factor $\sin(\beta - \alpha) \to 1$ and the h^0 production in the Supersymmetric model becomes indistinguishable from the production in the Minimal Standard Model Higgs. The $H^\pm$, H^0 and A^0 bosons are removed simultaneously, and the Standard Model scenario is recovered.

1.5.4 Implications for the Higgs Boson Search at LEP

This section outlines the implication of these theoretical considerations for the searches for Higgs bosons at LEP in the framework of the MSSM *at the tree-level.* The MSSM is a special case of the general two-doublet model discussed before. Owing to the mass relations in (1.62), only the search for the neutral scalar h^0 and the neutral pseudoscalar A^0 at the present LEP energy is possible. The lightest neutral scalar h^0 can be produced via the Bjorken process:

$$Z^0 \rightarrow h^0 Z^{0*}, \tag{1.64}$$

or via the Higgs pair-production process:

$$Z^0 \rightarrow h^0 A^0. \tag{1.65}$$

The production rate of these processes are complementary and only a function of the neutral Higgs boson masses (m_h,m_A). The partial width of the Z^0 decay via process (1.64) is proportional to $\sin^2(\beta - \alpha)$ and in process (1.65) proportional to $\cos^2(\beta - \alpha)$, given by:

$$\cos^2(\beta - \alpha) = \frac{m_h^2(m_Z^2 - m_h^2)}{m_A^2(m_Z^2 + m_A^2 - 2m_h^2)}. \tag{1.66}$$

The pair-production is dominant when $m_h \approx m_A$, i. e. $\tan\beta \gg 1$. Several thousand pair-produced Higgs bosons are expected per 400,000 collected hadronic Z^0 events within the kinematically accessible parameter space (m_h,m_A), where $m_h + m_A < m_Z$. Figure 1.9 shows the regions of the (m_h,m_A) plane where the number of pair produced neutral Higgs events is larger than 100, 500 and 5000, respectively.

The MSSM also predicts the branching ratios of the various allowed Higgs decay channels as a function of (m_h,m_A). Owing to the structure of the Higgs-fermion couplings, Higgs decays into up-type fermions (up-type quarks and charged leptons) are suppressed in the region of dominant Higgs pair production, where $\tan\beta \gg 1$, as seen from Table 1.3. Quantitatively, an example of the relative Higgs decay branching ratios in given in Table 1.6.

The effects of possible Higgs decays into Supersymmetric counterparts of Standard Model particles is expected to be small, since low-mass Supersymmetric particles are excluded (Table 1.4).

Previous negative searches for the three dominant final states

$$Z^0 \rightarrow h^0 A^0 \rightarrow b\bar{b}b\bar{b}, \quad \tau^+\tau^- b\bar{b}, \quad \tau^+\tau^-\tau^+\tau^- \tag{1.67}$$

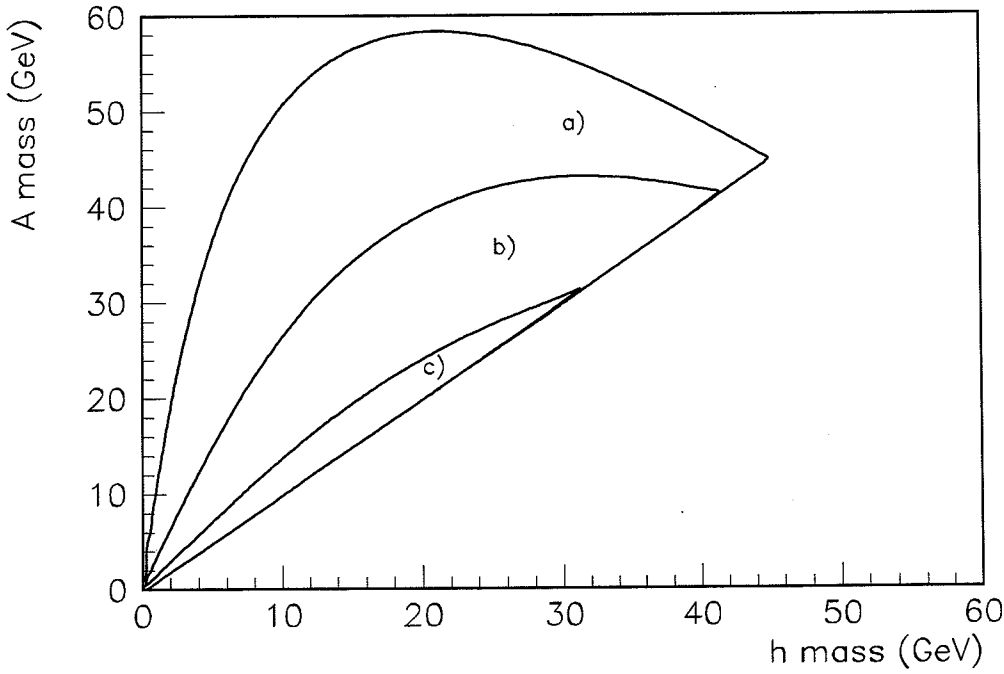

Figure 1.9: Number of expected $Z^0 \rightarrow h^0A^0$ events in the Minimal Supersymmetric Standard Model in tree level calculation per 400,000 hadronic Z^0 decays in the (m_h,m_A) parameter space. In region a) more than 100, in region b) more than 500, and in region c) more than 5000 Higgs events are expected.

and the resulting excluded (m_h,m_A) mass regions were reported in our publication [46]. The implication of recent studies on radiative corrections in the MSSM alters the excluded mass regions which were derived from tree-level calculations. In order to interpret the experimental results of this work, reported in sections 5.1 to 6.3, in the framework of the MSSM as an exclusion of a (m_h,m_A) domain, a detailed study of effects of radiative corrections is crucial.

$h^0 \backslash A^0$	$\tau^+\tau^-$	$s\bar{s}$	$b\bar{b}$
$\tau^+\tau^-$	0	0	4
$s\bar{s}$	0	0	1
$b\bar{b}$	4	1	89

Table 1.6: Branching fractions into fermions (in %) of the neutral Higgs bosons h^0 and A^0 in the Minimal Supersymmetric Standard Model for $m_h = m_A = 42$ GeV at tree level calculation. On the horizontal the h^0 decay products and on the vertical the A^0 decay products are listed. All other modes have negligible branching fractions.

1.6 Radiative Corrections in the Minimal Supersymmetric Standard Model

The importance of radiative corrections for the Higgs boson mass spectrum in the MSSM was recently pointed out by several authors [47]. Owing to these corrections, the neutral Higgs boson masses can increase by several tens of GeV and the Higgs couplings can change substantially. In particular, the mass relations in (1.62) are no longer valid. Previous studies of radiative corrections in the MSSM did not take into account the possibility that the top-quark mass and its supersymmetric partner, the stop-quark, could be very massive [48]. Much theoretical progress has been made [49], and the consequences for the experimental Higgs search have been worked out [50]. Theoretical research is in progress which will improve the precision of the predictions by including the contribution of additional particles to the one-loop graphs [30]. This section outlines the implications for the Higgs search within the framework of the MSSM.

1.6.1 Primary Assumptions

The main implications of the MSSM for the Higgs search can be extracted by making the following assumptions [51].

When top and stop quarks have large masses, they contribute most to the corrections of the tree-level calculations. The radiative corrections to the Higgs potential include m_{top} independent terms, and terms proportional to m_t^2 and m_{top}^4, only one term depends on m_{top}^4. Owing to the large top mass, only this term is considered to give the leading effect. Since only the m_t^4 term concerns the neutral

Higgs sector, the effects of radiative corrections to the charged Higgs sector are small in this approximation. It is further assumed that the value of $\tan\beta$ is not too large ($\tan\beta \leq m_{\rm top}/m_{\rm b} \approx 30$), otherwise, bottom and sbottom couplings to the Higgs are large and the bottom-sbottom loops can no longer be neglected. In addition, it is assumed that all Supersymmetric partners are degenerate in mass and do not mix.

Their common mass, $m_{\tilde{\rm q}}$, is related to the Supersymmetry breaking mass scale, m, by $m_{\tilde{\rm q}}^2 = m_{\rm top}^2 + m^2$. These assumptions are discussed in reference [52].

1.6.2 Higgs Production and Decays

Under the above assumptions, the effects of radiative corrections to tree-level calculations can be summarized with a single parameter for a given $m_{\rm top}$ and $m_{\rm stop}$:

$$\epsilon \equiv \frac{3\alpha_W}{2\pi}\frac{m_{\rm top}^4}{m_{\rm W}^2 m_{\rm Z}^2}\ln(\frac{m_{\rm stop}^2}{m_{\rm top}^2}), \tag{1.68}$$

where $\alpha_W = \alpha_{EM}/\sin^2\theta_W$. Radiative corrections alter the mass relations and the mass mixing angle. The correction $\epsilon/\sin\beta$ is added to the squared mass mixing matrix for the neutral scalars. The diagonalization of the radiative corrected mass matrix gives the physical Higgs boson masses:

$$m_{\rm H,h}^2 = \tfrac{1}{2}[m_{\rm A}^2 + m_{\rm Z}^2(1+\frac{\epsilon}{\sin\beta}) \pm \Delta], \tag{1.69}$$

where

$$\Delta = [(m_{\rm A}^2 + m_{\rm Z}^2(1+\frac{\epsilon}{\sin\beta})^2)^2 - 4m_{\rm A}^2 m_{\rm Z}^2\cos^2 2\beta \tag{1.70}$$
$$-4\frac{\epsilon}{\sin\beta}m_{\rm A}^2 m_{\rm Z}^2 \sin\beta - 4\frac{\epsilon}{\sin\beta}m_{\rm Z}^4\cos^2\beta]^{1/2}.$$

Equation (1.32) is recovered when the radiative corrections are set to zero ($\epsilon = 0$). The weak mixing angle α and $\tan\beta$ are related by:

$$\sin 2\alpha = \frac{-(m_{\rm A}^2 + m_{\rm Z}^2)\sin 2\beta}{\Delta}. \tag{1.71}$$

This relation is analogous to the tree-level relation (1.63) where ($m_{\rm h}$,$m_{\rm A}$) are chosen as free parameters. The ($\beta-\alpha$) value has changed after radiative corrections, and so does the expected number of pair-produced Higgs events compared to the tree-level prediction.

1.6.3 Top and Stop Quark Mass Range

The mass of the top quark and its supersymmetric partner, the stop boson, determines the size of the radiative corrections. The stop mass is unknown, only an experimentally lower mass limit of 106 GeV exists [53]. The natural upper mass limit is the upper energy scale of low-energy Supersymmetry which is around 1 TeV.

Limits on the top mass are tighter. The existence of the top is required by the Standard Model. A lower limit on the top mass of 91 GeV exists [10], and progress has been made in constraining the top mass at LEP. The LEP precision measurements of the line-shape, the $b\bar{b}$, e^+e^-, $\mu^+\mu^-$and $\tau^+\tau^-$ forward-backward asymmetry and the tau polarization asymmetry constrain the top-quark mass significantly due to its contributions to radiative corrections in the measured parameters. The combination of the top-mass measurements of all four LEP experiments and neutrino-scattering experiments results in a top-mass value [54] of:

$$m_{\mathrm{top}} = 141^{+17+17}_{-19-18}\ \mathrm{GeV}, \tag{1.72}$$

where the first error is experimental and the second error corresponds to the uncertainty in m_{H}. Here, m_{H} has been varied in the range $50 - 1000$ GeV, where H is the Higgs boson in the one-doublet Higgs model.

In order to evaluate the effects of radiative corrections on the expected Higgs signal, a conservative mass range of the top and stop masses is chosen:

$$90 < m_{\mathrm{top}} < 250\ \mathrm{GeV}, \quad m_{\mathrm{top}} < m_{\mathrm{stop}} < 1000\ \mathrm{GeV}. \tag{1.73}$$

This mass range corresponds to an ϵ range of $0 < \epsilon < 1.45$.

1.6.4 Implications for the Higgs Boson Search at LEP

Limits obtained in the general two-doublet model can be reinterpreted in the MSSM as excluded regions in the mass parameter space. The theoretically preferred parametrization (m_A,$\tan\beta$) of the available phase space is transformed into the experimental relevant (m_h,m_A) plane. Without radiative corrections, there is a one-to-one correspondence. However, with radiative corrections, one or two (m_h,m_A) pairs can correspond to one given (m_A,$\tan\beta$) pair, while $\tan\beta$ is constrained to the range: $1.0 < \tan\beta \leq 50$. This ambiguity exists only in a small (m_h,m_A) region. Conservatively, for the prediction of the number of expected events, the $\tan\beta$ value which corresponds to the smaller Higgs production cross-section is chosen.

The effect of radiative corrections in the (m_h,m_A) plane is shown in Figure 1.10. The case $\epsilon = 0$ corresponds to the tree-level (Figure 1.9). The region where more than 100 $Z^0 \rightarrow h^0A^0$ events per 400,000 hadronic Z^0 decays are expected shifts to the region below the diagonal for large values of m_{top} or m_{stop} when radiative corrections become large. In this case, the situation is analogous to the tree level prediction with m_h and m_A exchanged. Thus, all the parameter space is relevant for the experimental search in the MSSM.

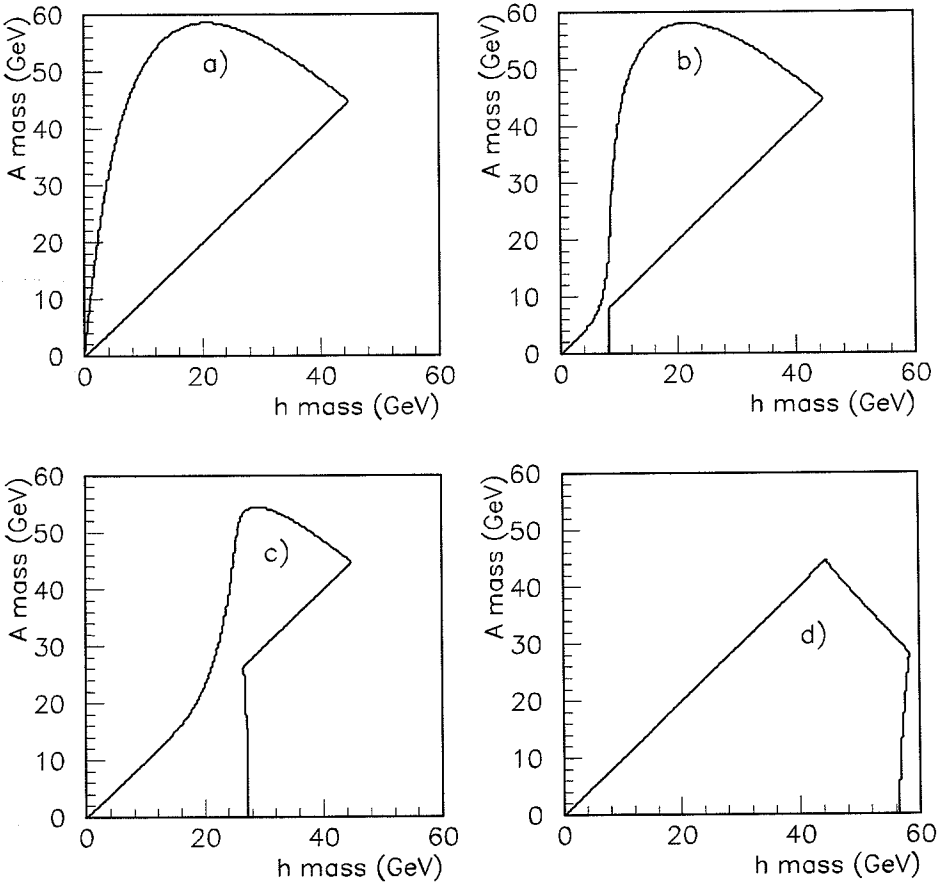

Figure 1.10: Number of expected $Z^0 \rightarrow h^0A^0$ events per 400,000 hadronic Z^0 decays in the (m_h,m_A) parameter space of the Minimal Supersymmetric Standard Model including radiative corrections. The regions, where more than 100 events are expected, are shown with radiative corrections parameterized by ϵ for a) $\epsilon = 0.00$, b) $\epsilon = 0.01$, c) $\epsilon = 0.10$ and d) $\epsilon = 1.00$.

The Higgs decay $h^0 \rightarrow A^0A^0$, which is forbidden at the tree-level, becomes possible after radiative corrections, and can even dominate, if kinematically allowed. The search for the altered signatures (decay products of the h^0 boson are doubled compared with the Minimal Standard Model), produced by the Bjorken process, is described in chapter 4. The search for neutral pair-produced Higgs, including the new Higgs decay channel, is described in chapter 9.

The general unitarity constraint (1.24), requires that Bjorken Higgs production and Higgs pair-production be complementary. Consequently, even in the most involved radiative correction scenario, the Higgs cannot escape detection if it is kinematically accessible and all (m_h,m_A) mass combinations are included in the search for Higgs signatures.

Radiative corrections also have important implications for the Higgs search at LEP200. In 1994 or 1995, the center-of-mass energy of LEP will be increased to about 190 GeV. Most of the allowed mass range for the lightest Higgs in the MSSM can be investigated with this upgrade of the LEP accelerator. However, because of the possibly large effects of radiative corrections to the allowed range of the lightest Higgs boson mass, an additional increase up to $\sqrt{s} = 240$ GeV would be auspicious. This would allow a definitive search for the Higgs bosons in the MSSM.

1.7 Beyond the Two-Doublet Higgs Model

Additional Higgs singlets can mix with the two Higgs doublets. Extensions of the MSSM result in non-minimal Supersymmetric models [55] (NMSSM). In these models, the mass relations between the Higgs bosons of the MSSM vanish. The particle spectrum is enlarged while cross-sections for individual processes are reduced, due to a generalized sum rule. The signatures are more complex but have many similarities with the MSSM scenario.

A larger, even number of doublets in the Supersymmetric extension of the Standard Model results in a wider particle spectrum, less predictive power and similar general features. Therefore, the simple MSSM with only two Higgs doublets, is preferred as an extension of the Standard Model.

Models with Higgs triplets, which respect the $\rho = 1$ constraint, have gained much attention in cosmology. An experimental search for signals of Higgs triplets is difficult because of the large number of free parameters involved in the prediction of production and decay rates.

Theoretical investigations to explain a large top mass have led to speculations that a $t\bar{t}$ condensate can substitute the Higgs boson [56]. At present, the expected signatures of the $t\bar{t}$ condensate are experimentally indistinguishable from the Standard Model Higgs signatures. In composite models, excited leptons and quarks are expected. The search by the four LEP experiments [57] has excluded the existence of these excited states up to the kinematically accessible threshold of about 45 GeV. In addition, the precision measurements of the Z^0 parameters disfavor composite models [58].

Chapter 2

LEP and the L3 Detector

The L3 detector at LEP is an ideal tool to search for new physics. Compared to a hadron machine, e^+e^- collisions offer a much clearer environment to search for signals of new particles. Details which are necessary for the Higgs identification can be reconstructed. This is especially important in the identification of events compatible with Higgs particle decays. In conjunction with the accurate particle identification at L3, the LEP accelerator offers a sufficient luminosity to search for Higgs events with low production rates.

2.1 The LEP Accelerator

The first interactions in the Large Electron Positron (LEP) collider at the Centre Européenne pour la Recherche Nucléaire (CERN) on August 13, 1989 set a milestone in the history of experimental particle physics. After seven years of construction, the first high luminosity e^+e^- collider running at center-of-mass energies in the range between 87 and 95 GeV began operating.

The goal of particle physics, to gain a deeper understanding of the fundamental constituents and interactions, is closely related to the available accelerator energy. Higher energies allow one to study smaller distances and the production of more massive elementary particles.

LEP is currently the largest e^+e^- storage ring in the world and, perhaps, the most promising for a major discovery in particle physics. In the LEP storage ring, counter-rotating beams of electrons and positrons are accelerated to an energy of about 46 GeV. A head-on e^+e^- collision will have a center-of-mass energy which is approximately equal to the Z^0 gauge boson mass. The e^+e^- bunches are brought into collision at four interaction points, in the center of each LEP detector. In the

annihilation of an e^+e^- pair, a Z^0 or a photon is produced. The Z^0 bosons decay with a lifetime of $(2.65 \pm 0.01) \times 10^{-25}$ s, and the outwardly moving decay products are studied.

The location of the LEP tunnel at CERN, on the border of France and Switzerland, near Geneva, is shown in Figure 2.1.

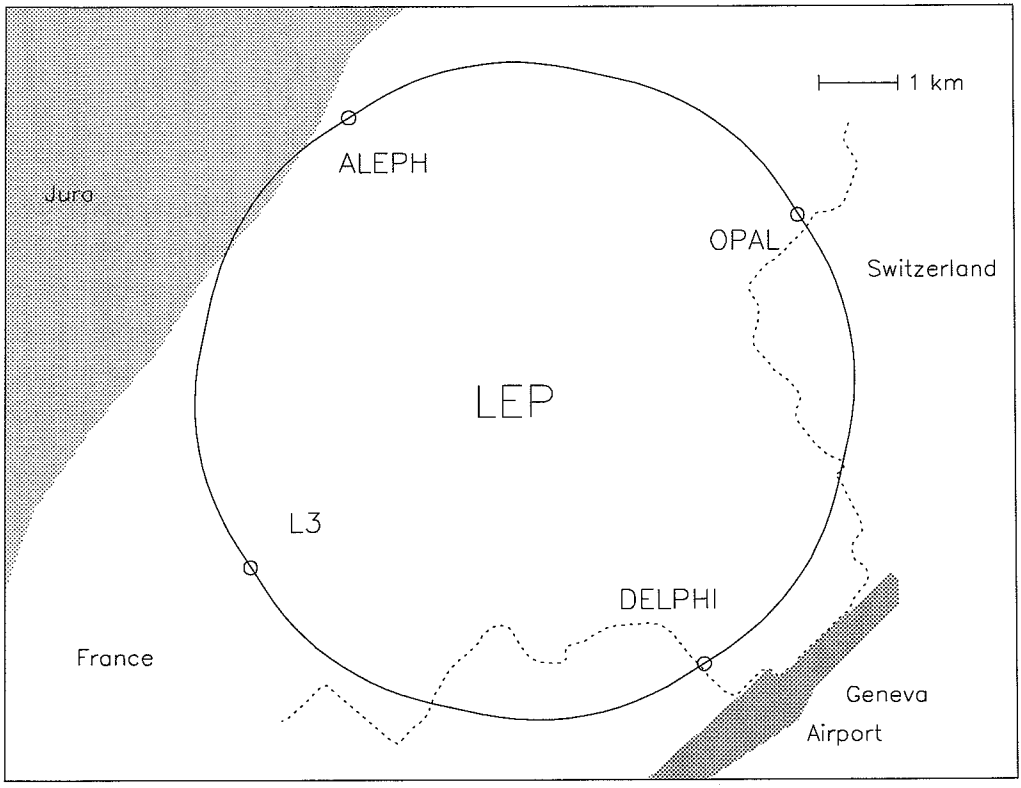

Figure 2.1: Location of the LEP accelerator between Geneva's airport and the French Jura mountain range.

The LEP tunnel lies 50 to 100 m below the surface with a circumference of 26.7 km. The storage ring consists of 8 circular segments of 2840 m and 8 straight segments of 490 m. Four of the straight segments house the detectors: ALEPH, DELPHI, L3 and OPAL [59]. Two straight segments are occupied by radio-frequency (RF) cavities, which accelerate 4 bunches of electrons and 4 bunches of positrons simultaneously from 20 GeV to the nominal beam energy. They also compensate the synchrotron radiation energy loss which averages 117 MeV per electron (positron) per turn. A schematic overview of the injection system, residing on the CERN site,

is given in Figure 2.2. The injection system [60] for introduction of e^+e^- bunches into the LEP ring at the beginning of each fill consists of four facilities:

- Two LEP Injection Linacs (LIL): The first linac accelerates electrons, which are produced by an electron gun, to 200 MeV and shoots them at a tungsten target (converter) to create hard gammas which convert into e^+e^- pairs. The second linac accelerates the resulting electrons and positrons to 600 MeV.

- Electron Positron Accumulator ring (EPA): The EPA collects e^+e^- into bunches and serves as a buffer for the slow-cycling synchrotron accelerators.

- Proton Synchrotron (PS): After the injection from the EPA, the PS accelerates the e^+e^- bunches to 3.5 GeV.

- Super Proton Synchrotron (SPS): In the SPS ring, the e^+e^- bunches are accelerated from 3.5 to 20 GeV and injected into the LEP ring.

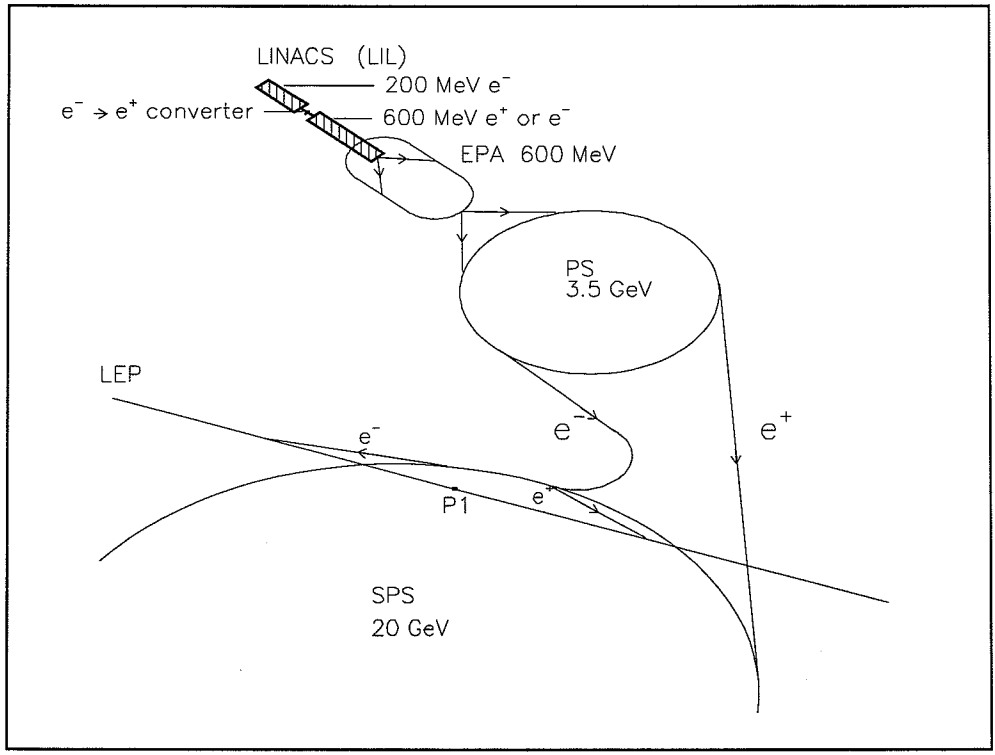

Figure 2.2: Overview of the LEP injection system.

The beam energy is obtained by measuring the magnetic field which keeps the electrons and positrons on their trajectory in the LEP ring. Protons of 20 GeV, which are non-ultrarelativistic, are used for the calibration of the magnetic field. The main error is due to the uncertainty of the contribution of a few micrometer layer of nickel inside the beampipe. The absolute error on the beam energy is 20 MeV at 45 GeV. An improvement of the beam energy measurement is in progress, based on the study of transversal beam polarization and depolarization. The error on the beam energy is expected to be reduced to between 5 and 10 MeV [61].

The main LEP parameters are summarized in Table 2.1.

Maximum beam energy	$\approx$ 60 GeV
Nominal beam energy	$\approx$ 45.6 GeV
Circumference	26658.883 m
Number of interaction points	4
RF frequency	352.20904 MHz
Total RF power	16 MW
Revolution time	88.92446 μs
Number of bunches per beam	4
Injection energy	20 GeV
Design luminosity	2×10^{31} cm^{-2}s^{-1}
Luminosity[1]	0.7×10^{31} cm^{-2}s^{-1}
Beam current[1]	2 mA
Integrated luminosity per fill[1]	150 nb
Beam lifetime[1]	10 h
[1](typical values for the 1991 running period)	

Table 2.1: Parameters of the LEP accelerator. General features and machine parameters from the 1991 data-taking period are summarized.

2.2 The L3 Detector

The history of particle physics shows that major discoveries were made in accelerator machines with detectors designed for very precise gamma, electron and muon momentum measurements. The discoveries of the J/Ψ at BNL and SLAC [62], and the discovery of the Z^0 at the UA1 experiment [63] are outstanding examples. The L3 detector was designed in this tradition. Out of the four experiments at LEP, L3 concentrates on very high resolution for gammas, electrons and muons. The characterizing features of the L3 detector are:

- Energy resolution $\delta E/E \approx 1\%$ for 45 GeV photons,
- Energy resolution $\delta E/E \approx 1\%$ for 45 GeV electrons,
- Momentum resolution $\delta p/p \approx 2.4\%$ for 45 GeV muons,
- Hadronic energy resolution $\delta E/E \approx 10\%$ for 45 GeV jets,
- Precise vertex reconstruction, charge identification and track separation.

The L3 detector is illustrated in Figures 2.3 and 2.4 and described in detail in reference [64]. The subdetectors reside inside a magnetic coil of 12 m inner diameter and 12 m inner length which provides a homogeneous magnetic field of 0.5 T along the beam direction.

For the Higgs search, all subdetectors are relevant. In the description which follows, the L3 subdetectors are presented in order of their location relative to the interaction points from the inner region outward:

- the Central Tracking Detector,
- the Electromagnetic Calorimeter,
- the Scintillation Counters,
- the Hadron Calorimeter, and
- the Muon Chambers.

The descriptions of the luminosity monitor, trigger and data acquisition system complete the chapter.

2.2.1 Central Tracking Detector

The central tracking detector [65] is the subdetector closest to the interaction point. It is used to reconstruct charged tracks in the bending plane (r,ϕ) of the magnetic field and along the beam axis (z-direction). By doing so, it serves multiple purposes:

- reconstruction of the primary interaction vertex and secondary vertices, for short-lived particles;
- determination of the track multiplicity for event type recognition;

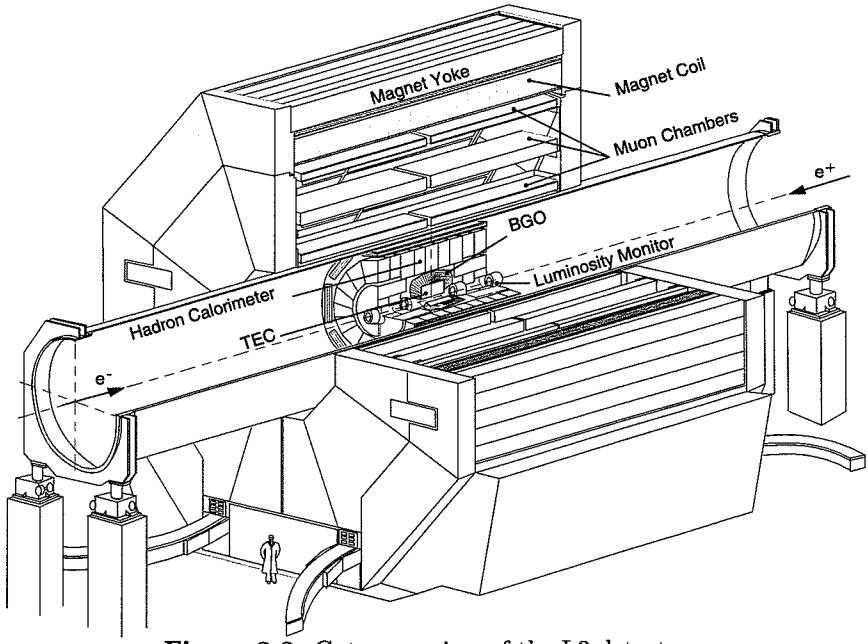

Figure 2.3: Cut-away view of the L3 detector.

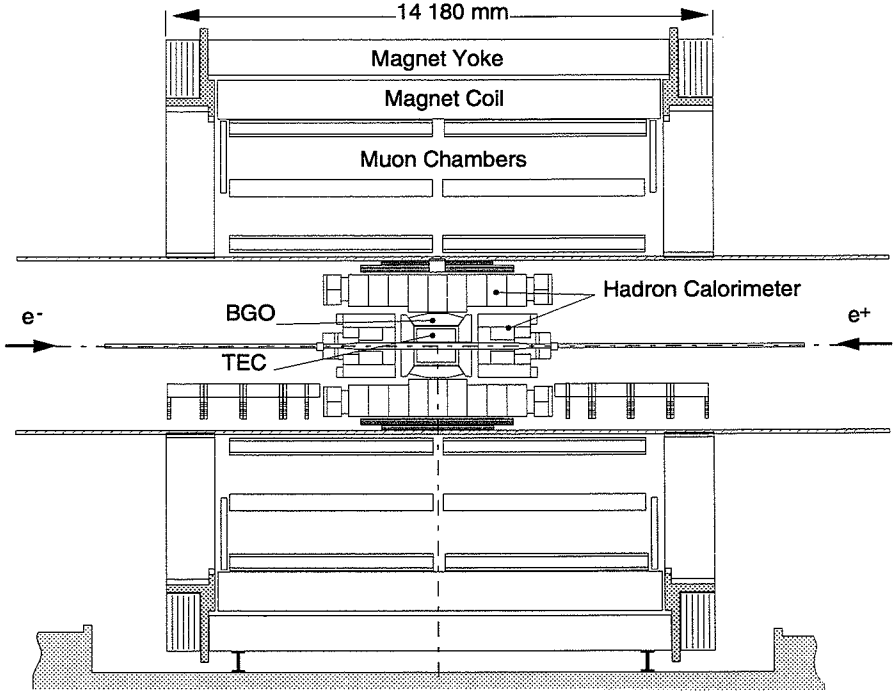

Figure 2.4: Side view of the L3 detector.

- photon and electron discrimination in the electromagnetic calorimeter by determining the precise location of the penetration point for charged particles.

The detector consists of a cylindrical Time Expansion Chamber (TEC) surrounded by two layers of drift chambers to measure the z-coordinate. A layer of plastic scintillator fibers is located around the TEC to be used as a calibration system. The central detector has a length of about 1 m and extends from 11 cm (beam pipe radius) to 47 cm (inner electromagnetic calorimeter radius). Charged particles are measured within a polar angle of $45° \leq \theta \leq 145°$.

The TEC is a new type of drift chamber based on the separation of a low-field drift region from the high-field amplification region. The drift region has a low — time expanded — drift velocity (5 μm/ns) which is achieved by using a low-diffusion gas mixture (80% CO_2, 20%C_4H_{10}). The high electric field region near the anode (detection gap) ensures a good signal amplification.

The TEC chamber consists of two concentric cylinders. The inner one is divided, in the plane transverse to the beam axis, into 12 sectors and the outer one into 24 sectors. The single hit resolution is 60 μm for the inner sectors, and 50 μm for the outer sectors. The double track resolution is about 640 μm. Each sector consists of:

1) High-precision anodes (8 per inner sector and 54 per outer sector) for the determination of the (r,ϕ) coordinates.

2) Charge division anodes which are identical with the previous ones, except that they are read out on both ends in order to provide a z-coordinate measurement through charge division.

3) Grid wires that separate the drift region from the amplification region.

4) Groups of 5 grid wires on either side of the amplification region that are read out. Their differential signal helps to resolve the left-right ambiguity.

5) Cathode wires which shape the electric field.

6) Focus cathode wires which alternate with anode wires in order to increase the homogeneity of the electric field.

The wiring in one sector of the TEC is shown in Figures 2.5 and the electric field lines in a TEC cell are illustrated in Figure 2.6.

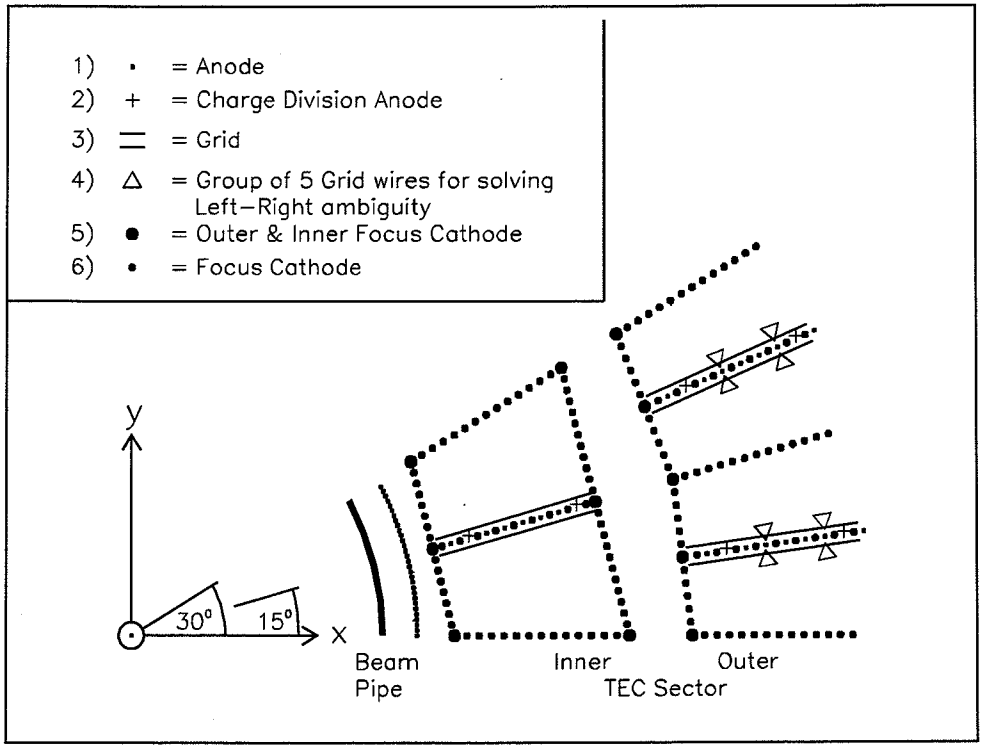

Figure 2.5: Wiring in one sector of the TEC. One inner and two outer sectors cover a 30° arc.

A 100 MHz Flash Analog to Digital Converter (FADC) determines the drift time by the center-of-gravity method.

The z-chamber is located on the outer shell of the TEC and enhances the z-coordinate measurement. The z-chamber consists of two layers of proportional chambers with cathode readout and a gas mixture of 80% argon and 20% CO_2. The single wire resolution is 400 μm.

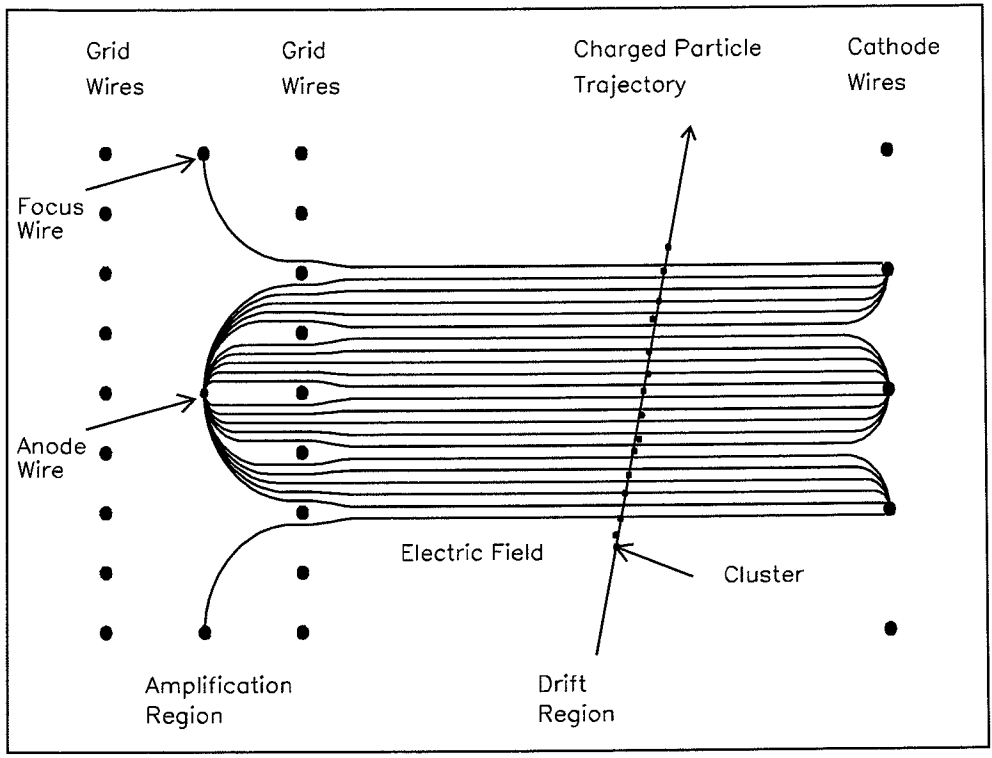

Figure 2.6: Electric field lines in a TEC cell.

2.2.2 Electromagnetic Calorimeter

The electromagnetic calorimeter (ECAL) [66] surrounds the central vertex chamber and has the following features:

- precise measurement of photon and electron energy,
- good spatial resolution, and
- strong rejection of hadronic showers.

The electromagnetic calorimeter consists of a cylindrical barrel of 7700 bismuth germanium oxide (BGO) crystals, two endcaps with 1500 crystals each, and two forward tracking chambers.

The energy of photons, electrons or positrons is measured by their total absorption in the BGO crystals. A particle which undergoes electromagnetic inter-

action in the BGO material produces an intense electromagnetic shower. Figure 2.7 shows a typical shower in the calorimeter for a 45 GeV electron, simulated with the L3 version of the GEANT program [67].

The electromagnetic energy is converted into scintillation light which in turn is read out by photodiodes. The collected amount of light is used to determine the energy of the incident particles.

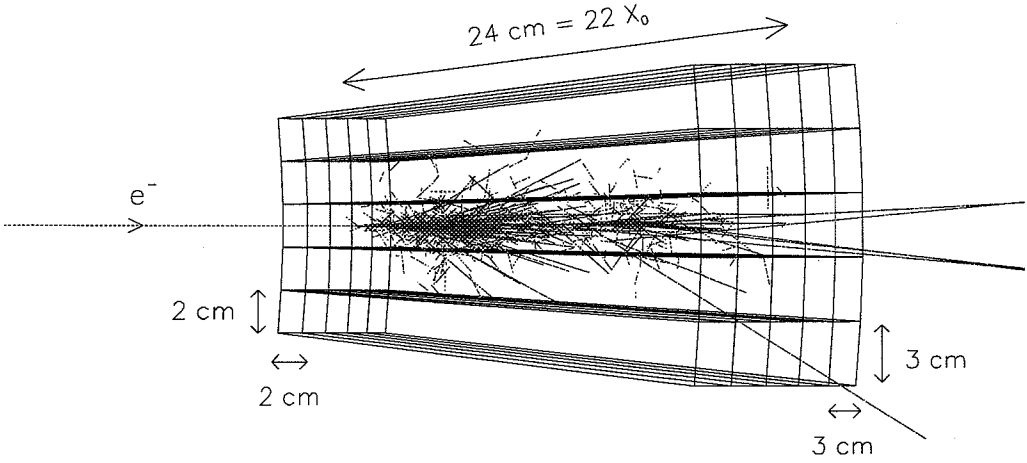

Figure 2.7: BGO crystal shower shape for a 45 GeV electron simulated with the L3 version of the GEANT program package.

A BGO crystal is an ideal medium for an electromagnetic calorimeter since it has a short electromagnetic radiation length, and a large nuclear interaction length allows a compact construction with a good separation of electromagnetic and hadronic particles. The crystals have a length of 24 cm corresponding to 22 radiation and 1.1 nuclear interaction lengths. BGO is non-hygroscopic; it can resist high doses of radiation, the light output is very linear with respect to the energy deposited and it has a high intrinsic resolution of $0.5/\sqrt{E}$.

The crystals are cut in the shape of a truncated pyramid with 2×2 cm^2 cross-section at the inner end and 2.9×2.9 cm^2 cross-section at the outer end. They are mounted in a carbon fiber support structure which minimizes the dead space. The crystals are positioned so that they point towards the interaction point. A cross-sectional view of the calorimeters and the forward tracking chambers is shown in Figure 2.8. In spring 1991, during shutdown of the LEP accelerator, the BGO endcaps were installed, extending the polar angle range from $42° < \theta < 138°$ to

$10° < \theta < 170°$.

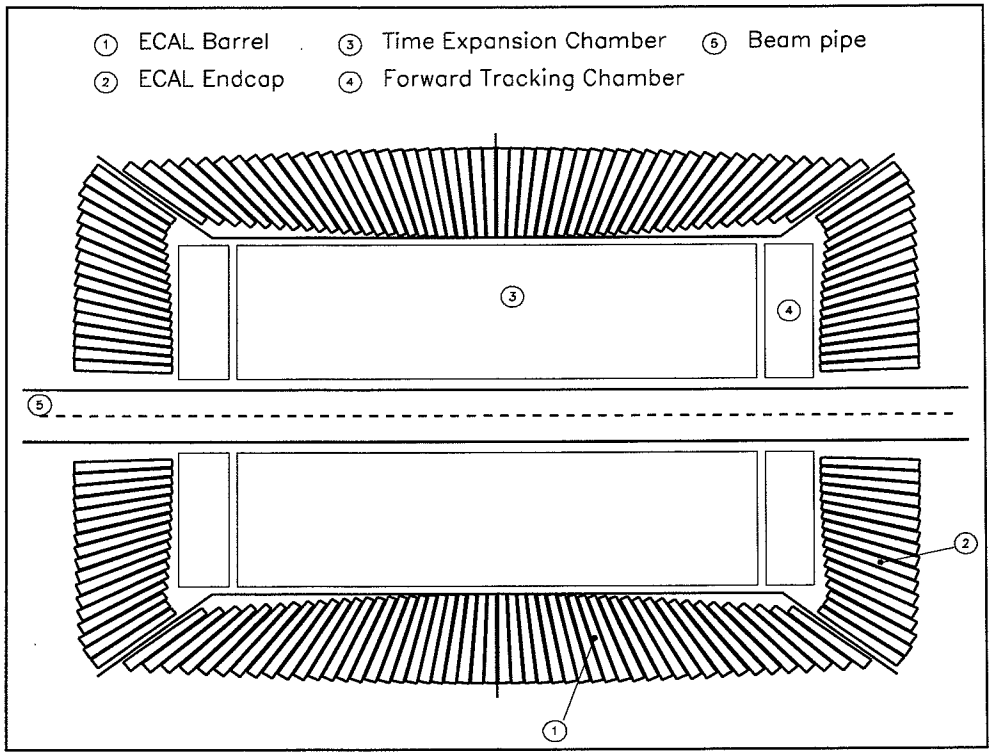

Figure 2.8: BGO crystal positions in the Electromagnetic Calorimeter.

Readout of the scintillation light is performed with two silicon photodiodes and an amplification unit mounted on the outer end of each crystal.

In a test beam, each crystal of the barrel and endcaps has been calibrated. The dependence of the calibration constants on temperature and impact point has been determined. An energy resolution of 4% at 180 MeV, 1.5% at 2 GeV and 0.6% at 50 GeV has been measured.

The temperature in the detector is monitored with 640 temperature sensors and is held constant within a few tenths of a degree because the light produced in the crystals depends strongly on temperature ($-1.55\%/°C$). Xenon light pulses corresponding to energy deposits of 1.5 GeV and 35 GeV are continually sent into the BGO crystals to calibrate the light-collection efficiency, gain for each crystal, and to monitor the aging of the crystals.

The two forward tracking chambers consist of four drift chambers mounted in front of the BGO endcaps. They measure the entrance point of tracks from charged particles into the BGO endcaps. An angular resolution of better than 1 mrad and a spatial resolution better than 200 μm have been achieved.

2.2.3 Scintillation Counters

The scintillation counters [68] consist of a ring of 30 plastic scintillator counters installed between the electromagnetic and the hadronic calorimeters. Their purpose is two-fold: first, they measure the time-of-flight of particles in order to reject cosmic muons and, second, they serve as a fast trigger signal for hadronic events.

In the barrel region, 93% of the full 2π range of the azimuthal angle, ϕ, is covered by the scintillator counters which are contoured to fit the shape of the hadron calorimeter. The scintillation light from the 2 m long and 1 cm thick plastic scintillator counters is read out by phototubes on each end. The signal from the phototubes is processed by high-precision Time to Digital Converters (TDC).

The time resolution measured with $Z^0 \rightarrow \mu^+\mu^-$ events is 0.48 ns. This resolution allows a good separation of Z^0 and cosmic muon events. In Z^0 events, the decay products reach simultaneously opposite scintillator segments, while cosmic muons travel the distance between opposite counter segments in more than 5.8 ns.

2.2.4 Hadron Calorimeter

The hadron calorimeter (HCAL) [69] is located between the ECAL and the support tube, at a radial distance from 1.0 m to 1.8 m. It consists of three parts: barrel, endcaps and muon filter. The hadron calorimeter, together with the ECAL, measures the energy and direction of hadronic jets. Along with the support tube, it shields the muon chambers in order to reduce contamination from particles other than muons (punch through).

The barrel and endcaps consist of layers of depleted uranium absorber plates, interleaved with proportional wire chambers. In the uranium plates, hadrons undergo nuclear interactions, producing hadronic showers. The direction and energy of the incident hadron is determined by measuring the direction and energy of the hadronic shower.

An advantage of uranium as an absorbing material is its short nuclear in-

teraction length. A particle originating from the interaction point will traverse a total of 5 to 6 nuclear interaction lengths in the ECAL and HCAL. The natural radioactivity of uranium is used to calibrate the wire chambers. On the inner side of the hadron calorimeter, the ECAL barrel is shielded from the uranium radioactivity by layers of stainless steel. The gas (80% Ar, 20% CO_2) wire chambers are made of brass tubes with 0.3 mm thick walls and 5×10 mm^2 inner cross-section. Their lengths vary with module size.

Owing to their low production cost, the wire chamber tubes are well suited for large-scale detectors. These reliable wire chambers can operate in the magnetic field and are very uniform, which is important for good energy resolution. The wire chambers are read out with preamplifiers and fastbus Analog to Digital Converters (ADC).

The barrel consists of 9 rings, each of which contains 16 modules. Both endcaps have one outer and two inner rings with 12 modules. The HCAL barrel extends over a polar angle of $35° < \theta < 145°$, while the endcaps cover polar angles of $5.5° < \theta < 35°$ and $145° < \theta < 174.5°$. Both parts cover the full azimuthal range; thus, the geometrical acceptance is 99.5% of the 4π solid angle. A quadrant of the hadron calorimeter is shown in Figure 2.9.

The wires in the barrel modules are arranged parallel and perpendicular to the beam axis with alternating layers of wire chambers to allow position measurement. In the HCAL barrel, an angular resolution of $\Delta\theta = 2.2°$ and $\Delta\phi = 2.2°$ is obtained. The L3 hadron calorimeter was calibrated at the CERN SPS test beam with pions and muons and the calibration is updated with Z^0 events at LEP. The measured energy resolution for the hadron calorimeter is given by:

$$\frac{\Delta E}{E} = (\frac{55}{\sqrt{E}} + 5)\%, \tag{2.1}$$

where E is the total energy deposited in GeV.

The muon filter is mounted on the inner side of the support tube. Its thickness is 1.1 nuclear absorption lengths. It increases the energy absorption, the rejection of punch-through and the shielding from the uranium radioactivity.

The muon filter consists of 8 octants corresponding to the octants of the muon chambers. Each sector consists of 6 brass absorber plates of 1 cm thickness and a length of 4 m interleaved with 5 proportional chambers, with wires running parallel to the beam direction. Unlike the HCAL, the wires are readout individually to improve pattern recognition for muons.

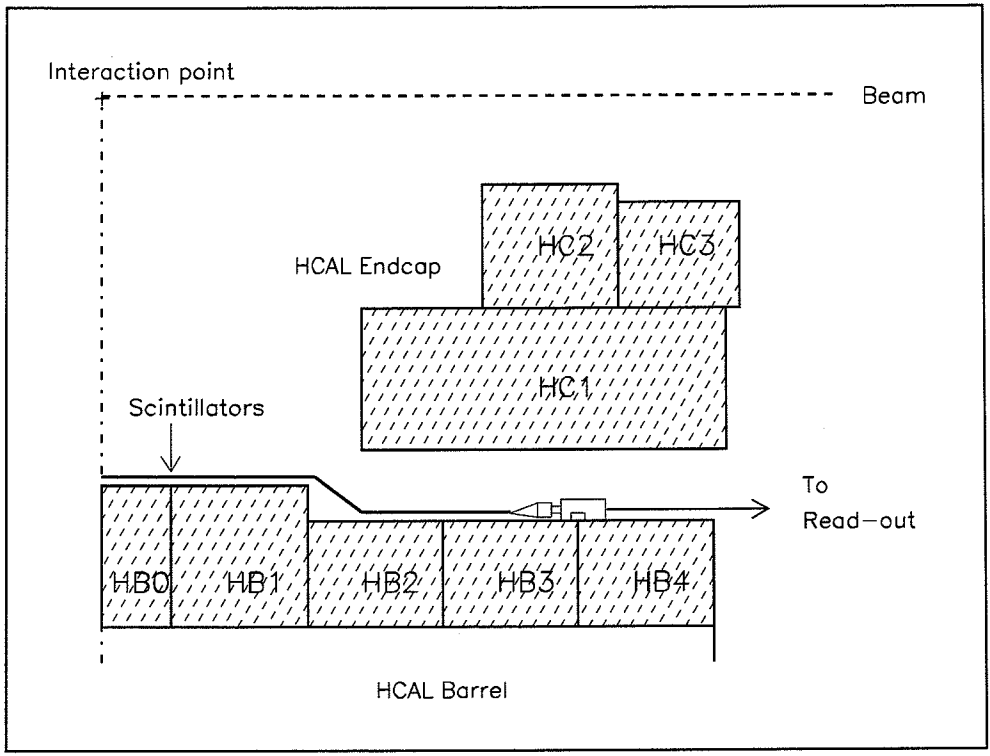

Figure 2.9: Quadrant of the hadron calorimeter. The position of the HCAL modules and the location of the scintillator counters in front of the barrel HCAL modules is shown.

2.2.5 Muon Chambers

The muon chambers (MUCH) [70] cover the outer surface of the support tube (radius 2.2 m) and the inner side of the magnetic coil (radius 5.9 m). They measure the muon momentum with very high accuracy.

The muon spectrometer consists of two ferris wheels with eight independent octants. Each octant supports five high-precision drift chambers arranged in three layers, one inner chamber (MI), two middle chambers (MM) and two outer chambers (MO). Figure 2.10 illustrates this construction. These chambers are called p-chambers because they measure the muon transverse momentum by determining the curvature of the muon track in the magnetic field. The top and bottom covers of the MI and MO chambers consist of four z-chambers with sense wires stretched

perpendicular to the beam direction to measure the z-coordinate of the muon track.

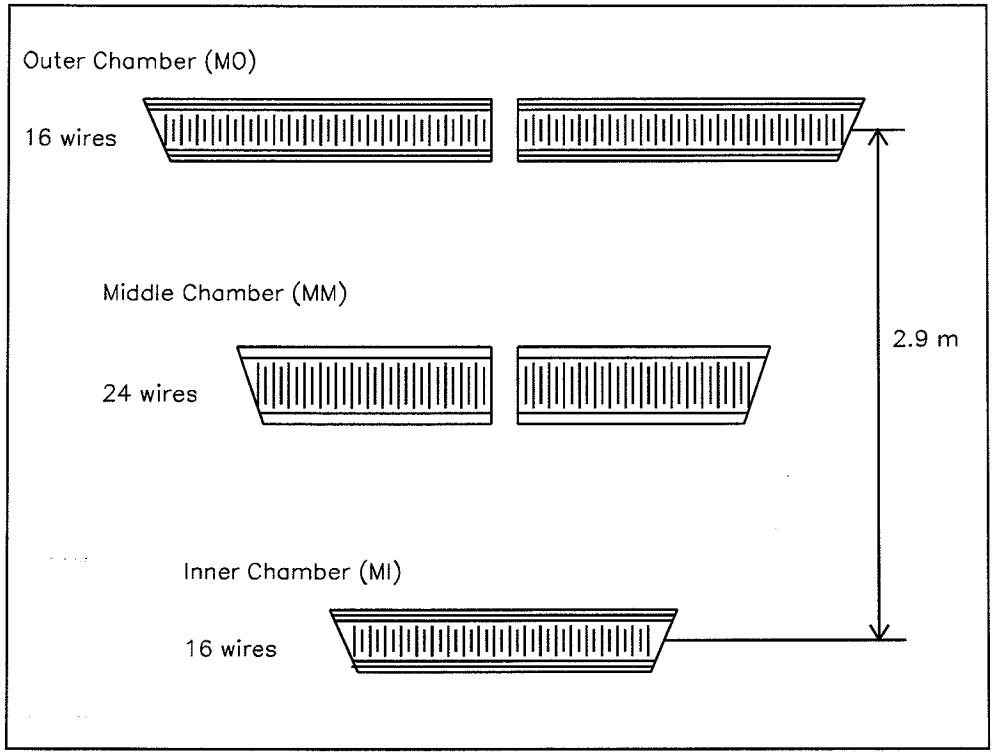

Figure 2.10: Octant of the muon chambers. One inner, two middle and two outer chambers with 16, 24, 16 radial wires, respectively. The z-chambers in the inner and outer muon chambers are indicated.

The large dimensions of the muon detector are dictated by the required high-precision measurement of the muon momentum. The sagitta, s, of the muon trajectory is defined as the distance between the track position in MM and the line connecting the track positions in MI and MO as shown in Figure 2.11. Assuming a homogeneous magnetic field and no multiple scattering, the transverse muon momentum, p_T (in GeV), is approximately given by:

$$p_T = \frac{0.30BL^2}{8s}, \tag{2.2}$$

where B (in Tesla) is the magnetic field, L (in meters) is the distance between track positions in MI and MO and s (in meters) is the sagitta. The resolution improves

with B and L^2. For L3, $B = 0.51$ T and $L = 2.9$ m. The error contribution of the total momentum, $p = p_T/\sin\theta$, from the uncertainty in the polar angle θ as measured by the z-chamber is negligible. The muon energy loss is of about 2 GeV in the inner calorimeters.

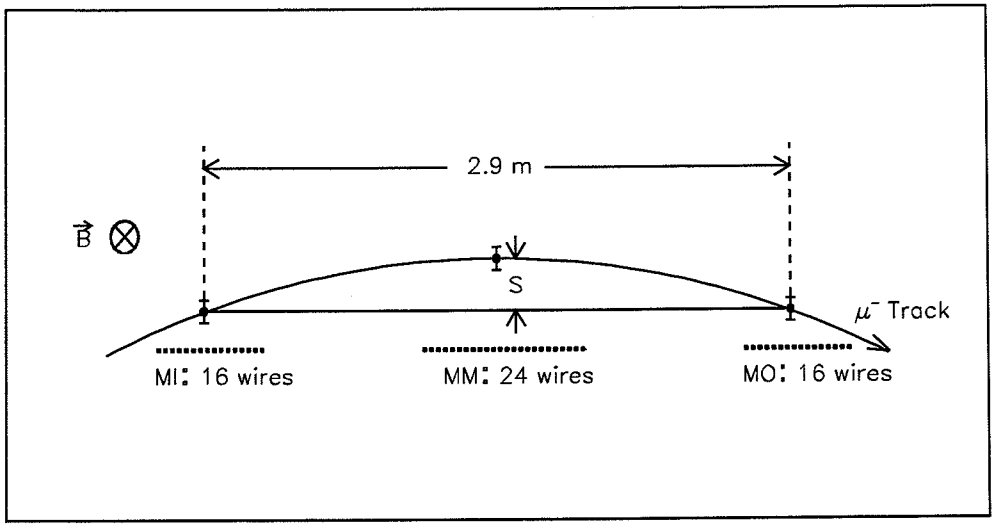

Figure 2.11: Sagitta measurement in the muon detector.

The L3 muon spectrometer is designed to minimize the error of the sagitta measurement. The sagitta for a 45 GeV muon is 3.7 mm. In order to achieve a momentum resolution $\Delta p/p = \Delta s/s \approx 2\%$, the sagitta, s, must be measured to better than 75 μm. The main contributions to the sagitta error are:

a) the intrinsic drift chamber resolution (including electronics),

b) multiple scattering, and

c) the uncertainty in the relative alignment of the different chamber layers.

The p-chambers contain alternating planes of signal wires and cathode wires, located 50.75 mm apart. The division of the chamber into cells of 101.5 mm, with cathode planes on both sides, ensures a very uniform electric field. Each chamber contains about 20 cells. In MM, a signal wire plane consists of 28 signal wires spaced 9 mm apart and interspersed with field shaping wires. The wires in the cathode plane

are 2.25 mm apart. Each wire is supported by a precision pyrex glass and carbon fiber construction and aligned with an optical alignment system that has a tolerance of less then 10 μm. The gas mixture in the chamber consists of 61.5% argon and 38.5% ethane with an electric field of 1140 V/cm in the drift region. This results in an average drift velocity of 50 μm/ns. Signal wire pulses are preamplified and read out with a TDC which has a time resolution of 2.4 ns. A single wire resolution of better than 250 μm has been obtained. The large number of signal wires improves the intrinsic chamber resolution and results in a error contribution to the sagitta measurement of 43 μm.

The z-chamber consists of two layers of drift cells with a gas mixture of 91.5% argon and 8.5% methane with an average drift velocity of 30 μm. The single wire resolution is 500 μm. No z-chambers are installed on the bottom and top of the middle layer of the p-chamber to avoid an increase of multiple scattering. The middle p-chamber is closed by thin aluminum honeycomb panels of only 0.45% radiation lengths each. The total sagitta error due to multiple scattering was determined to be about 30 μm at 45 GeV.

A built-in optical alignment system is used to precisely determine the position of the drift chambers. Only the relative alignment of the chambers within each octant is important, since high energy muons are confined within one octant. An additional pulsed UV laser system, which simulates an infinite momentum muon coming from the vertex, monitors the chamber alignment and drift velocity. Independently, cosmic muons in the absence of the magnetic field are used for checking the alignment. The error on the sagitta resulting from the alignment uncertainty is less than 30 μm for all octants.

The combined sagitta error is less than 70 μm, corresponding to $\Delta p/p = 1.8\%$. Accounting for the limited time resolution of the readout electronics, the measured muon momentum resolution is

$$\Delta p/p = 2.4\% \tag{2.3}$$

for 45 GeV muons which penetrate all three drift chamber layers. This corresponds to a polar angle range $44 \leq \theta \leq 136$. In the region $35 \leq \theta \leq 44$ and $136 \leq \theta \leq 145$ the curvature of muon is measured with only two drift chamber layers to determine the muon momentum with a resolution of about 15%.

2.2.6 Luminosity Monitor

The luminosity monitor [71] is located around the beam pipe at $z = \pm 2.8$ m. It measures the rate of small-angle Bhabha events, $e^+e^- \rightarrow e^+e^-$, in polar angle range 31 mrad $\leq \theta \leq$ 64 mrad. The luminosity monitor system consists of two identical calorimeters composed of BGO crystals. Finely segmented arrays of BGO crystals cover the full azimuthal region. This detector has an energy resolution of about 2% and a spatial resolution of 0.5° for 45 GeV electrons. Bhabha events are produced via s-channel and t-channel diagrams, as shown in Figure 2.12. A reconstructed Bhabha event in the luminosity monitor is shown in Figure 2.13.

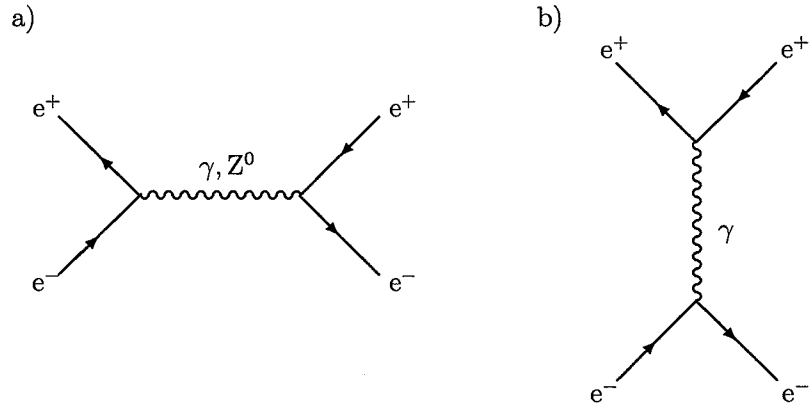

Figure 2.12: Diagrams of Bhabha scattering in the a) s-channel and b) t-channel.

For small-angle scattering, the t-channel dominates. This process is largely independent of Z^0 parameters and theoretically well understood in QED. Therefore, small-angle Bhabha scattering serves as normalization for the number of produced Z^0 events. The integrated total luminosity, L_{tot}, is determined from the Bhabha cross-section, the measured acceptance of the luminosity monitor and the measured Bhabha rate. The number of corresponding hadronic Z^0 decays, $N_{had} = L_{tot}\sigma_{had}$, is used throughout this work as normalization for the rate of expected Higgs and background events. Monte Carlo simulations based on the BABAMC program [72] are used to determine the visible cross-section. The visible cross-section for Bhabha events at $\sqrt{s} \approx 91$ GeV is 88.5 nb with a theoretical uncertainty of 0.5%. Sources of the experimental systematic uncertainties are mainly due to the geometry of the calorimeter and Bhabha event selection criteria. The total experimental error is

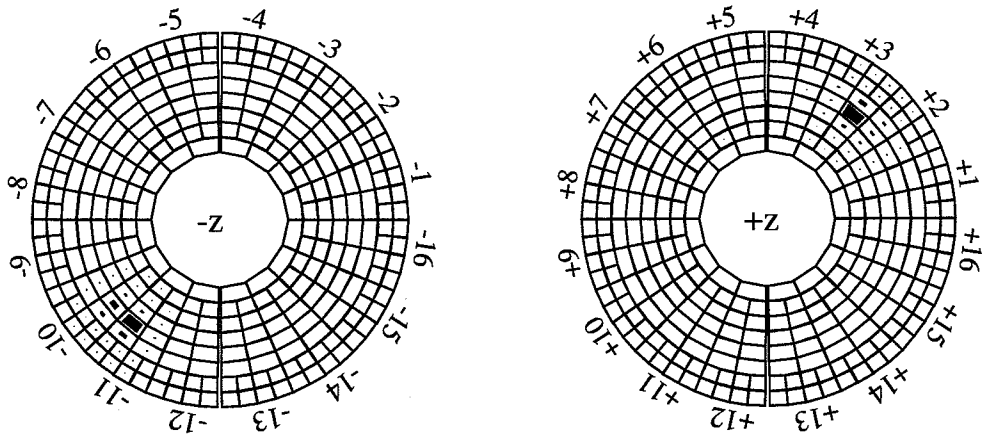

Figure 2.13: Bhabha event as seen in the luminosity monitor. The size of each dark box is proportional to the energy deposit in the corresponding crystal. Only energy deposits exceeding 250 MeV are shown.

0.7%; adding in the 0.5% theoretical error gives an overall systematic error of 0.9% in the lumi measurement, corresponding to the same relative error on the hadronic cross-section.

2.2.7 Trigger and Data Acquisition

The L3 trigger and data acquisition system [73] performs the following major tasks:

- selection of interesting physics events,
- recording of data on magnetic tape for later off-line analysis,
- control of subdetectors and data flow, and
- on-line monitoring of data quality.

A trigger system is required since electron and positron bunches cross with a frequency of 45 kHz (each 22 μs), whereas, the rate of interesting physics events is less than 1 Hz. The fast rejection of unwanted events, such as beam gas interactions or cosmic ray muons, is achieved with a trigger system consisting of three levels. A fast decision is essential to minimize detector dead time. A trigger decision is based on a logical OR of the muon trigger, energy trigger, TEC charged track trigger,

scintillator trigger and luminosity trigger. The large redundancy of positive trigger decisions makes it possible to determine the trigger acceptance for specific event types.

The level-1 trigger receives digitized compressed data from all subdetectors after each bunch crossing. It decides before the next bunch crossing if the event should be processed or rejected. If the level-1 trigger decision is positive, the complete data of all subdetectors are digitized and stored in memory. Next, the event is built while the level-2 trigger analyzes the data by searching for energy deposits in the calorimeters and tracks in the tracking chambers. For a positive level-2 trigger decision, the main and trigger data are assembled, and the combined event data are formatted for storage on tape. The decision of the level-3 trigger is based on the complete event information. The average rate of accepted events written on tape was 2.5 Hz for the 1991 running period. Further rejection of background and event selection is done off-line with selection criteria based on defined event signatures. Event selections for the non-minimal Higgs events are described in detail in sections 5.1 to 6.3.

The expected Higgs bosons are recorded in the L3 detector if at least one of the following trigger requirements is fulfilled:

- Energy trigger: At least 10 GeV is registered in the BGO calorimeter, or 15 GeV in the BGO and barrel hadron calorimeter, or 20 GeV in all calorimeters (including the end-cap calorimeters).

- Dimuon trigger: At least two tracks are detected in the muon chambers in non-adjacent octants and at least one scintillation counter has fired.

- Single muon trigger: At least one track with a transverse momentum greater than 1.5 GeV is detected in the muon chambers and at least one scintillation counter has fired.

- Charged-track trigger: At least two tracks with a transverse momentum greater than 0.15 GeV and with an angular separation greater than 120° in the transverse plane are observed in the TEC.

- Scintillation counter trigger: At least 5 out of the 30 barrel scintillation counters fire within 13 ns of the beam gate and at least one pair of the counters hit is separated by more than 45° in azimuth.

- Cluster trigger: At least 6 GeV of energy is deposited in a solid angle subtended by one hadron calorimeter module.

These trigger requirements have a large redundancy. Typically, at least two trigger requirements are fulfilled. This allows a check on the trigger efficiency of the individual triggers. The combined trigger efficiency for all of the investigated reactions is larger than 99%.

The data acquisition (DAQ) system also controls the calibration of all subdetectors before each data-taking and controls the data flow. Under running conditions, the general DAQ system controls all subdetector DAQ systems (TECH, ECAL, HCAL, MUCH) and the trigger system. The complete DAQ system is synchronized by a 'trigger box'. The trigger box also continuously monitors the level-1 trigger rates of each subdetector, therefore, problems during data-taking due to software or hardware failures can be identified immediately. Important for the off-line data analysis is the recording of all detector parameters in the L3 data base [74].

Chapter 3

Simulation and Reconstruction

Monte Carlo simulations play an important role in any new particle search. These simulations allow one to convert theoretical predictions for signals and backgrounds into expected signatures in the detector. In order to detect a small Higgs signal buried in a large background of known physics processes, the Monte Carlo simulation must precisely describe all known leptonic and hadronic reactions. The process of Monte Carlo simulation consists of event generation, for both signal and background, and of detector simulation. An overview of the analysis chain is given in Figure 3.1.

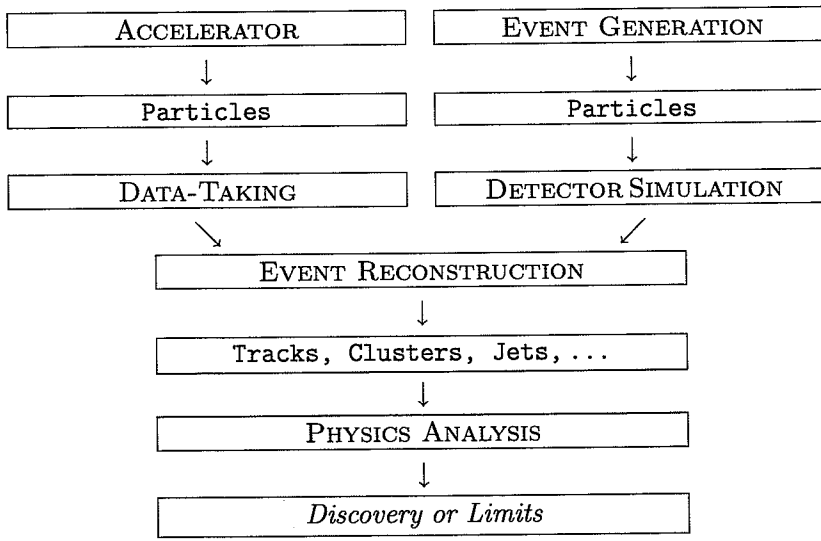

Figure 3.1: Overview of the analysis chain.

The first section of this chapter describes the hadronic event generation with JETSET, which is the most important part of the signal and background simula-

tion. The primary generation steps of the $Z^0 \rightarrow \tau^+\tau^-$ background and Higgs signal are based on KORALZ and PYTHIA as described in subsequent sections. The L3 detector simulation is based on GEANT as outlined in section 3.4. The reconstruction of hadronic clusters and jets are described in section 3.6. Finally, a comparison between data and simulations in reconstructing mass resolutions is presented.

A detailed comparison between data, background and signal simulation is presented in sections 5.1 to 6.3, and in the corresponding appendices A to G.

3.1 Hadronic Event Generation with JETSET

The most complex part of the signal and background simulation is the hadronic event generation. Events from the reactions $Z^0 \rightarrow$ hadrons and $Z^0 \rightarrow \tau^+\tau^-$ are the main background to Higgs signatures. In the decay channels under investigation, the Higgs bosons decay preferentially into b quarks and taus, which also predominantly decay hadronically. Hadronic events are simulated with JETSET 7.3 [75].

In the Standard Model, Quantum Chromodynamics (QCD) is the underlying theory of hadronic interaction. Because of the large coupling constant, α_s, of the strong interaction, perturbative calculations cannot describe the transformation of the primary quarks (which are initially produced in the Z^0 decay) into observable hadrons. In JETSET, a QCD-inspired model has been incorporated to perform the hadronization of the primary quarks.

The evolution of the primary quarks into hadronic final states dependents only weakly on the center-of-mass energy, thus the results obtained from earlier accelerators like PETRA, PEP or TRISTAN are important for tuning the parameters of the model. The steps in the generation of a hadronic JETSET event are:

- initial photon radiation,
- e^+e^- pair annihilation into a virtual γ or Z^0,
- decay of the gauge boson into a $q\bar{q}$ pair,
- gluon radiation based on the parton shower model,
- hadronization based on the Lund model of string fragmentation, and
- decay of short-lived particles into observable final states.

Figure 3.2 gives a schematic description of a hadronic event as performed by JETSET. In the next sections, the steps in event generation are described in detail.

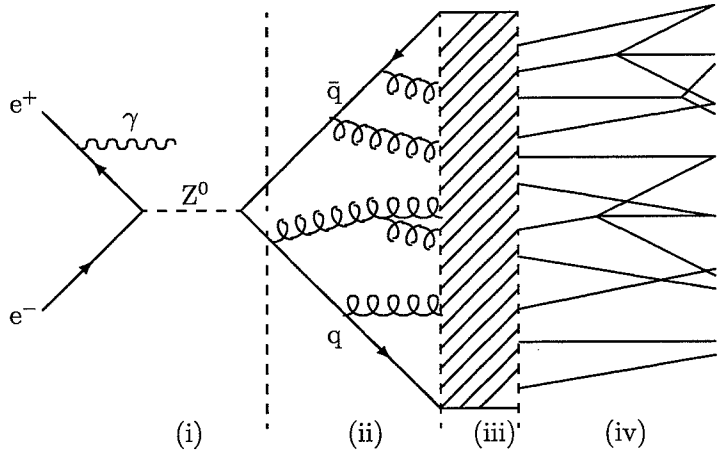

Figure 3.2: Schematic illustration of hadronic event generation: (i) initial photon radiation, Z^0 production and decay, (ii) quark and gluon emission, (iii) hadronization, and (iv) decay of unstable particles.

3.1.1 Z^0 Production and Initial Photon Radiation

The e^+e^- annihilation and the Z^0 decay into quarks or leptons is well understood in the Standard Model. Precise predictions are obtained with perturbative calculations.

Initial state radiation, which is described by QED, changes the expected hadronic peak cross-section by about 30%. This is because initially emitted photons reduce the available center-of-mass energy to below the peak of the Z^0 resonance. Initial photon emission is implemented in JETSET to account for this effect. The reduction of the cross-section, due to initial photon radiation, is independent of the final states to a precision of better than 1% as determined by comparison of Higgs and $Z^0 \rightarrow q\bar{q}$ simulations. This small value allows the usage of the number of hadonic Z^0 decays for normalization of expected Higgs event in the detector.

3.1.2 The Parton Shower Model

In JETSET, the parton shower model has been used in order to generate quark and gluon emission. In the parton shower model, an arbitrary number of branchings of one parton into several partons is combined to describe the origin of multi-jet events. Kinematics, interferences and helicities are approximately described.

An alternative to the parton shower model is the matrix element model which was developed in order to describe the parton shower evolution from the quarks within the framework of perturbative QCD. The matrix element method is based on an 'order-by-order' calculation of Feynman graphs. Complete calculations are only available to order ${\alpha_s}^2$ of the strong coupling constant.

QCD studies at LEP have shown that the observed event shapes are better described by the parton shower model [76]. Thus, this model has been used in the simulation.

The emission of quarks and gluons determines the signatures of the $Z^0 \rightarrow h^0A^0 \rightarrow b\bar{b}b\bar{b}$ Higgs signal and the 4-jet hadronic background. The primary source of 4-jet events in the Standard Model, as part of the background simulation, is shown in Figure 3.3. The parton shower model describes well the substructure of jets and therefore the event shape, but the model tends to predict the 4-jet rate only approximately [77, page 151]. Thus, in the quantitative analysis, the generated 4-jet analysis has to be normalized with regard to the observed 4-jet rate.

3.1.3 String Fragmentation (Lund Model)

Fragmentation models must incorporate the basic idea of quark confinement in QCD. In JETSET, the concept of string fragmentation (Lund model) has been used. When two colored quarks move apart, a color flux tube develops and is stretched between the $q\bar{q}$ pair. Lorentz invariance and a causal description of the energy flow is mathematically realized by a relativistic string with no transverse degrees of freedom. The energy density of the string is taken to be 1 GeV/fm [77, page 167]. As the quarks move apart, the string energy increases until it breaks. String fragments form new pairs of hadrons. This process continues until the invariant mass of all quark pairs is small and only on-mass-shell mesons and baryons remain.

A string tube can only develop between causally connected partons. This leads to a difference in the fragmentation of a Higgs event with four initial partons and a hadronic background event. The simulation of $Z^0 \rightarrow h^0A^0 \rightarrow b\bar{b}b\bar{b}$ events must take into account that strings can only develop between $b\bar{b}$ pairs coming from the decay of a Higgs particle, while strings can develop between all four quarks in the process $Z^0 \rightarrow q\bar{q}q\bar{q}$ (shown in Figure 3.3). In the latter case, all four b-quarks could be causally connected and a larger number of strings may develop.

The Lund string fragmentation function [78] describes the fragmentation en-

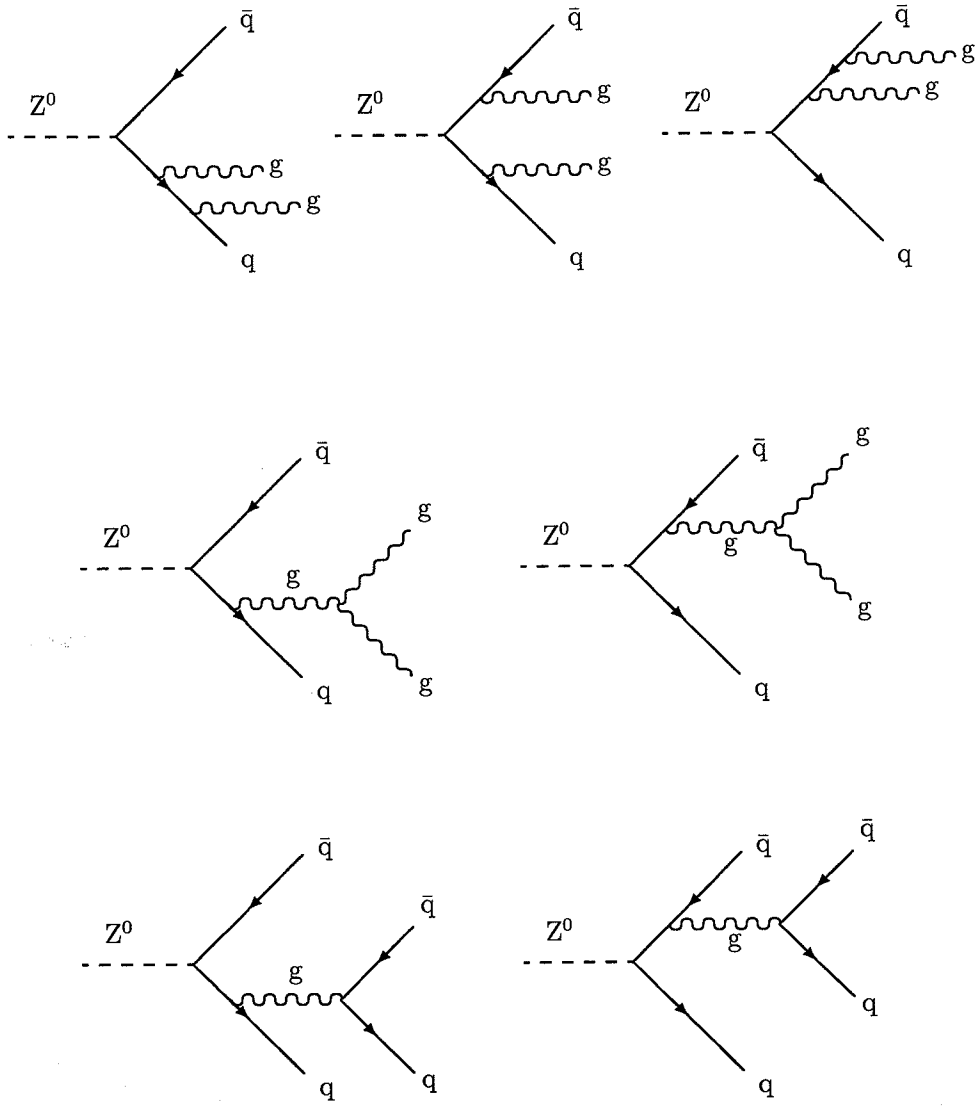

Figure 3.3: Diagrams for 4-jet production processes in the Standard Model as the main background for the $Z^0 \rightarrow h^0A^0 \rightarrow b\bar{b}b\bar{b}$ Higgs signature. The first five diagrams show the reaction $Z^0 \rightarrow q\bar{q}gg$ and the last two diagrams show the reaction $Z^0 \rightarrow q\bar{q}q\bar{q}$.

ergy spectrum of the light quarks (u,d,s) well [79]:

$$f(z) \propto \frac{1}{z}(1-z)^a \exp(\frac{-bm_T^2}{z}), \tag{3.1}$$

where z is the fraction of energy taken away by the hadron, m_T is the transverse mass of the system, a and b are fragmentation parameters. A harder fragmentation energy spectrum for c-quarks and for b-quarks has been observed.

The measured fragmentation energy spectrum can be described by the Peterson fragmentation function [80]:

$$f(z) \propto [z(1-\frac{1}{z}-\frac{\epsilon_q}{1-z})^2]^{-1}. \tag{3.2}$$

The fragmentation parameters, ϵ_q (where q stands for c and b quarks), of the hard heavy quark spectrum, were measured to be $\epsilon_c = 0.49$ and $\epsilon_b = 0.71$ [81].

Details of the fragmentation energy spectrum have little influence on the event shape, since most of the event topology is determined by the quark and gluon emission.

3.1.4 Unstable Particle Decay

The final step in event generation is the decay of short-lived particles ($\tau c <$ 1 cm). A decay table based on [9] is used by the Monte Carlo simulation. Experimental data concerning the lifetime of the majority of unstable particles, their masses and decay branching ratios are well known. In the analysis of multi-jet channels (sections 5.1 and 5.2), a semileptonic b-quark decay selection is applied. The semileptonic b-quark decay rate is 0.110 ± 0.006 for electrons and muons (combined LEP results) [82]. This value is used in the simulation. About 444,000 and 165,000 $Z^0 \rightarrow q\bar{q}$ events have been simulated for the 1991 and 1990 detector configuration, respectively.

3.2 Tau Event Generation with KORALZ

As an additional background to the Higgs signal, the process $Z^0 \rightarrow \tau^+\tau^-$ has been generated with the KORALZ [83] program. The KORALZ program simulates the production of tau pairs and their subsequent decay into electrons, muons and hadrons. Hadronic tau decay products, mainly ρ, K and π, are decayed in the detector simulation. A total of about 20,000 $\tau^+\tau^-$ events have been simulated, corresponding to about 410,000 hadronic Z^0 decays.

3.3 Higgs Event Generation with PYTHIA

The PYTHIA 5.6 [84] Monte Carlo program has been used for the generation of different Higgs signatures. PYTHIA generates the initial partons and initial photon emission. JETSET is then used to simulate further particle evolution.

The consistent simulation of the parton shower, hadronization and particle decay with one program package, namely JETSET, ensures a high consistency in the simulation of Higgs and background events.

The Monte Carlo Higgs signal events, summarized in Table 3.1, were generated according to the theoretical considerations presented in Chapter 1.

In the Bjorken process for $m_{\mathrm{H}} < 2m_{\mu}$, the Higgs decay length is non-negligible. Figure 3.4 shows the distance of the Higgs decay vertex from the interaction point for $m_{\mathrm{H}} = 100$ MeV, where the calculation is based on [85]. The light Higgs is strongly boosted and would often decay outside the beampipe in the central tracking detector. Such a low-mass Higgs can have a signature completely different from that of a Higgs with the same mass which decays at the interaction point because it interacts less with the detector. For smaller masses, the Higgs bosons can even decay predominantly outside the detector.

3.4 Detector Simulation with GEANT

After the simulation of the signal and background events, the response of the L3 detector has been simulated. The detector simulation program is based on GEANT [67]. The decays of the following particles (and their antiparticles): $\mathrm{K}^0_{\mathrm{L}}$, $\mathrm{K}^0_{\mathrm{S}}$, Λ, Σ^+, Σ^-, Ξ_0, Ξ^- and Ω , which have a decay length $\tau c > 1$ cm and can decay outside the beampipe is simulated in GEANT.

Energy loss, multiple scattering and showering in the detector material and beampipe are simulated for the geometry of the L3 detector. The energy resolutions in the different subdetectors, as described in section 2.2, are predicted in the simulation. If the simulation disagrees with the measurements obtained when higher precision in the measurements is reached, further details of the detector configuration are incorporated in the simulation.

Simulated events are reconstructed by the same program used to reconstruct data events in order to minimize uncertainties in the data processing. Important elements of event reconstruction, clusters, jets and tracks, are defined below.

	Z^0 Decay	Higgs Decay	Mass Range (GeV)
Bjorken Process			
$e^+e^- \to Z^0 \to h^0Z^{0\star}$	e^+e^-, $\mu^+\mu^-$, $\nu\bar{\nu}$	$l\bar{l}$, $q\bar{q}$	$2 < m_h < 70$
$e^+e^- \to Z^0 \to h^0Z^{0\star}$	e^+e^-, $\mu^+\mu^-$,	e^+e^-, $\mu^+\mu^-$, $\pi^+\pi^-$, $\pi^0\pi^0$, K^+K^-, K^0K^0, $\rho^+\rho^-$, $\rho^0\rho^0$, $\eta\eta$, $\omega\omega$	$m_h < 2$
$e^+e^- \to Z^0 \to h^0Z^{0\star}$ $(h^0 \to A^0A^0)$	e^+e^-, $\mu^+\mu^-$, $\nu\bar{\nu}$	$b\bar{b}b\bar{b}$, $s\bar{s}s\bar{s}$, $d\bar{d}d\bar{d}$, $\tau^+\tau^-\tau^+\tau^-$	$3 < m_h < 48$ $1 < m_A < 22$
Charged Higgs Pair Production			
$e^+e^- \to Z^0 \to H^+H^-$		$c\bar{s}c\bar{s}$, $cs\tau\nu$, $\tau^+\nu\tau^-\bar{\nu}$	$20 < m_{H^\pm} < 40$
Neutral Higgs Pair Production			
$e^+e^- \to Z^0 \to h^0A^0$		$b\bar{b}b\bar{b}$, $\tau^+\tau^-b\bar{b}$, $\tau^+\tau^-\tau^+\tau^-$	$12 < m_{h,A} < 62$ $4 < m_{h,A} < 62$ $4 < m_{h,A} < 12$
$e^+e^- \to Z^0 \to h^0A^0$ $(h^0 \to A^0A^0)$		$b\bar{b}b\bar{b}$	$50 < m_h < 60$ $22 < m_A < 27$

Table 3.1: Overview of generated processes for non-minimal Higgs searches. For all generated events, the L3 detector response has been simulated with the L3 version of the GEANT program.

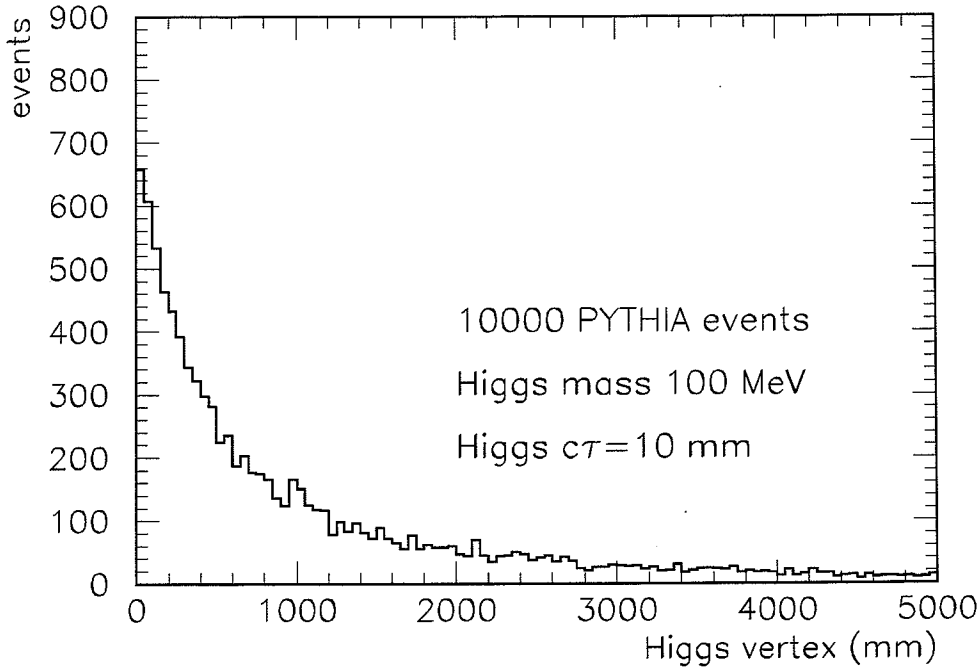

Figure 3.4: Distribution of simulated Higgs vertex distances from the interaction point for a 100 MeV Higgs boson.

3.5 Calorimetric Clusters

Throughout all searches, the number of calorimetric clusters is an important variable. These clusters are constructed by grouping together neighboring calorimeter hits which are likely to be produced by the same particle. Only clusters with a total energy above 100 MeV are used. The algorithm normally reconstructs one cluster for each particle produced near the interaction point. For a cluster energy of 2 GeV, the angular resolution is approximately 0.4° for isolated electrons and photons, and better than 3° for hadrons.

The energy of each cluster is calibrated depending on its position in the detector. This energy calibration is based on a subdivision of the detector in 12 regions. The calibration factors in these regions are determined by a maximal likelyhood fit which minimizes the energy resolution for well-identified hadronic Z^0 decays.

3.6 Hadronic Jets

In all search channels for pair-produced Higgs bosons, hadronic jets are reconstructed from clusters in the calorimeters by using an invariant-mass jet algorithm [86]. For each pair of clusters, i and j, the invariant mass squared

$$y_{ij} = (p_i + p_j)^2/s \tag{3.3}$$

is then evaluated, where p_i and p_j are the four momenta of the clusters. The cluster pair for which y_{ij} is smallest is replaced by a pseudocluster, k. This procedure is repeated until all scaled invariant masses squared, y_{ij}, exceed the jet resolution parameter $y_{\rm cut}$. Two types of jets are defined, wide jets with a minimum invariant mass of resolution of 13 GeV ($y_{\rm cut} = 0.02$), and narrow jets with a minimum mass resolution of 2.9 GeV ($y_{\rm cut} = 0.001$).

3.7 Charged Tracks

Charged tracks are reconstructed from hits in the TEC. A good charged track must have: $N_{span} \geq 40$, where N_{span} is the number of wires along the track in the transverse plane; $N_{hits} \geq 0.75 \times N_{span}$, where N_{hits} is the number of hits along the track; $d_{ca} \leq$10 mm, where d_{ca} is the distance of closest approach of the track to the primary vertex in the transverse plane; and $p_{tr}^T \geq 100$ MeV, where p_{tr}^T is the momentum of the track in the transverse plane.

3.8 Higgs Mass Resolutions

The precision of the Monte Carlo simulations in reconstructing mass resolutions was studied with $q\bar{q}\gamma$ events [87]. In order to compare the predicted mass resolution of hadronically decaying Higgs bosons with data events, a sample of $q\bar{q}\gamma$ events with a hard photon is selected. After removing the photon from the reconstruction, their topology is similar to $Z^0 \rightarrow h^0\nu\bar{\nu}$ events. For data, the quantity $\Delta m_{q\bar{q}}$ is defined as the difference between the invariant mass of the hadronic system and the mass of the hadronic system computed only from the photon energy. For the simulated Higgs signal, $\Delta m_{q\bar{q}}$ is the reconstructed Higgs mass. Figure 3.5 shows the result of the comparison. The mass resolution of the hadronic system is 15%. The energies of the hard photon in the $q\bar{q}\gamma$ data sample allow for investigation of

a hadronic invariant mass range of about 25 to 65 GeV. Data and Monte Carlo simulations agree very well within the statistical errors.

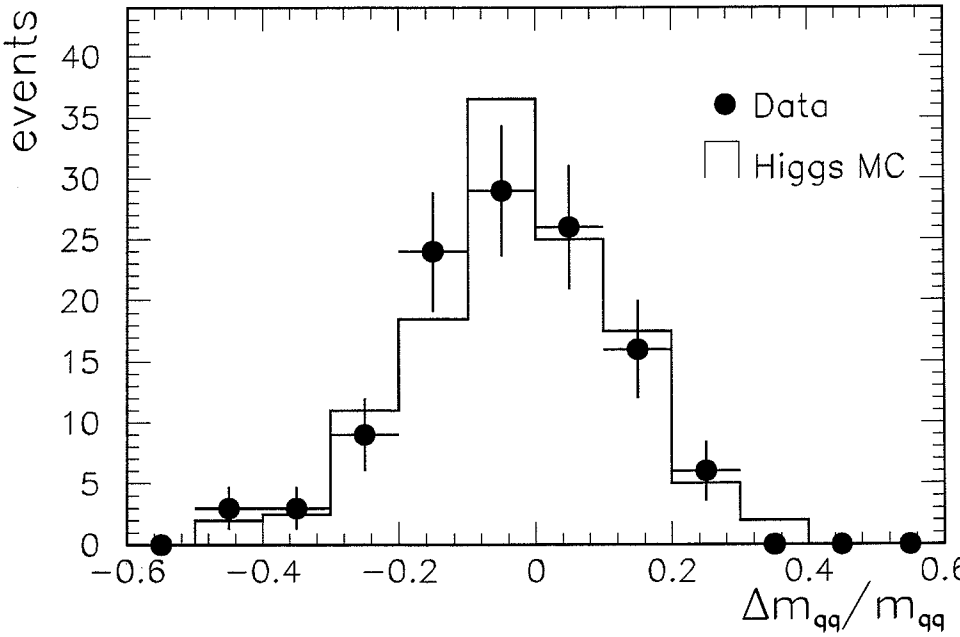

Figure 3.5: Comparison of data and simulated Higgs mass resolution. For details see text.

Chapter 4

Searches for Higgs Boson Bremsstrahlung

This chapter summarizes searches for Higgs boson bremsstrahlung from the Z^0. Details of the searches in the Higgs boson mass range lower than 30 GeV and searches with non-standard Higgs boson decays are reported in an L3 publication [88], and searches by L3 for the Higgs boson of the Minimal Standard Model with mass larger than 30 GeV are reported in [89]. The Higgs boson is searched for in the following channels:

$$\begin{aligned} &Z^0 \to h^0 Z^{0\star} \to h^0 \ell\ell, \qquad \ell\ell = \nu\bar{\nu}, e^+e^-, \mu^+\mu^-, \tau^+\tau^- \\ &Z^0 \to h^0 Z^{0\star} \to A^0 A^0 \ell\ell, \end{aligned} \tag{4.1}$$

where h^0 is a CP-even Higgs boson and A^0 is a CP-odd Higgs boson of some general model with decay properties similar to those of the Higgs boson of the Minimal Standard Model described in section 1.3. The bremsstrahlung Higgs search concentrates mainly on signatures with electrons and muons as the decay products of the Z^0, due to high selection efficiency for these leptons. If, in a Higgs boson mass range, different Higgs boson decay modes are possible, like $h^0 \to c\bar{c}$ or $h^0 \to \tau^+\tau^-$ below the $b\bar{b}$ threshold, the lower selection efficiency is used to set a limit. For Higgs boson masses larger than 2 GeV, the expected standard-Higgs boson decay rates into fermions are well known, however, in the mass range below 2 GeV the decay rates into hadrons are less certain (see section 1.3). Searches for Higgs bosons are optimized for each of the mass ranges: a) larger than 30 GeV, b) between 2 GeV and 30 GeV, c) between $2m_\mu$ and 2 GeV, and d) below $2m_\mu$.

4.1 The Search in the $Z^0 \to h^0 Z^{0\star} \to h^0 \nu\bar{\nu}$ Channel

A Higgs boson with mass between 2 GeV $< m_h <$ 60 GeV is investigated. Below about 2 GeV, Higgs events are not triggered due to their small energy deposit in the detector. The selection has been optimized for the following two mass regions:

- 30 GeV $< m_h <$ 60 GeV: In this mass range, the Higgs boson is expected to decay predominantly into heavy quarks, while the Z^0 decay gives invisible final states. Thus, the selection is based on the identification of isolated hadronic jets in events with large energy imbalance. No candidate is found.

- 2 GeV $> m_h >$ 30 GeV: If the Higgs boson mass is much smaller than the Z^0 mass, it has a large Lorentz boost. Such events are characterized by one or two jets, large missing energy and large energy imbalance. No event passes the selection.

4.2 The Search in the $Z^0 \to h^0 Z^{0\star} \to \tau^+\tau^- q\bar{q}$ Channel

The search for the Higgs boson signal with τ leptons in the final state was performed using two channels: $(h^0 \to \tau^+\tau^-)(Z^{0\star} \to q\bar{q})$ and $(h^0 \to q\bar{q})(Z^{0\star} \to \tau^+\tau^-)$, and in the mass range 30 GeV $< m_h <$ 60 GeV. In both channels, mostly four-jet events are expected with at least two tau jets. Low visible energy and some energy imbalance is required. No event survives the selection.

4.3 The Search in the $Z^0 \to h^0 Z^{0\star} \to h^0 \mu^+\mu^-$ Channel

The search in this channel covers the mass range between $0 < m_h <$ 60 GeV:

- 30 GeV $< m_h <$ 60 GeV: The event selection is based on the identification of a pair of muons from the virtual Z^0 decay, while hadronic activity is expected from the Higgs boson decay. One event with a well-isolated muon pair and a recoiling mass of 70.4 ± 0.7 GeV survives the selection. A study of four-fermion background ($e^+e^- \to \mu^+\mu^- f\bar{f}$) [90] shows that this event is consistent with the background expectation of 1.7 ± 0.2 events.

- 2 GeV $< m_h <$ 30 GeV: In this mass range, Higgs boson events contain a high-momentum muon pair and charged tracks produced by the decay of Higgs bosons. No event survives the selection.

- $2m_\mu < m_h <$ 2 GeV: The selection in this mass range requires two muons and two additional charged tracks. In order to calculate the Higgs boson detection efficiency, Higgs boson decays into pairs of μ, π, K at different masses are simulated. Six data events are selected. The expected background from four-fermion processes is 7.7 ± 1.2 events.

- $0 < m_h < 2m_\mu$: Below the $\mu^+\mu^-$ threshold the Higgs boson decays predominantly into an e^+e^- or $\gamma\gamma$ pair. A very low mass Higgs has a long lifetime and often decays far from the interaction region. The typical signature is a pair of acolinear muons together with a small energy deposit (or even no energy) outside the inner region of the detector. For Higgs boson masses of about 100 MeV, the Higgs boson can also decay inside the TEC chamber. The expected decay length distribution is shown in Figure 3.4. In this case, the same selection procedure used in the range 2 $m_\mu < m_h <$ 2 GeV is applied. No candidate is found.

4.4 The Search in the $Z^0 \to h^0 Z^{0\star} \to h^0 e^+ e^-$ Channel

The search in this channel covers the mass range between $0 < m_h <$ 60 GeV:

- 30 GeV $< m_h <$ 60 GeV: Higgs boson events in this mass range contain a pair of electrons from the virtual Z^0 decay with large hadronic activity from the Higgs boson decay. One event passes the selection. The missing mass recoiling against the electron pair is 31.4 ± 1.5 GeV. This event is consistent with a four-fermion background where 1.6 ± 0.3 events are expected.

- 2 GeV $< m_h <$ 30 GeV: The distinctive signature in this mass range is two high-energy, well-separated electrons recoiling against one or two hadronic jets coming from the Higgs boson decay. The event described earlier in this mass range passes the event selection.

- $2m_\mu < m_h <$ 2 GeV: In this mass region, the Higgs boson decays into muons or light hadrons. Simulated Higgs boson decays into pairs of μ, π, K at various

masses have been investigated. Two events pass the selection, consistent with the 2.8 ± 0.2 expected background events from four-fermion processes.

- $0 < m_{\mathrm{h}} < 2m_{\mu}$: A search for Higgs bosons with masses below the $\mu^+\mu^-$ threshold, where the Higgs boson can only decay into an $\mathrm{e^+e^-}$ or $\gamma\gamma$ pair, is performed. For Higgs boson masses below 100 MeV, the Higgs boson event would contain only two acolinear electrons. Three candidate events are found, while 4.2 ± 0.2 background events are expected. The background events come from four-fermion events and Bhabha events with a radiative photon converting in the beampipe or in the material of the TEC.

4.5 The Search in the $\mathrm{Z^0 \longrightarrow h^0 Z^{0\star} \longrightarrow A^0 A^0 \ell\ell}$ Channel

Possible decays of a bremsstrahlung-produced Higgs boson into a pair of CP-odd Higgs bosons lead to new signatures in Higgs boson decays, as pointed out in section 1.4. Searches for Higgs boson bremsstrahlung involving $\mathrm{h^0 \longrightarrow A^0 A^0}$ are summarized. The leptonic channels $\ell\ell = \nu\bar{\nu}$, $\mu^+\mu^-$, and $\mathrm{e^+e^-}$ have been investigated. Based on the event selection for the high-mass Minimal Standard Model Higgs boson [89], the change in detection efficiencies for a possible $\mathrm{h^0 \longrightarrow A^0 A^0}$ decay has been studied. The selection has been optimized in four m_{A} mass regions:

- $2m_{\mathrm{b}} < m_{\mathrm{A}} < 30$ GeV: Above the $\mathrm{b\bar{b}}$ threshold, the search technique, that was developed for the high mass Higgs boson range, can be applied. In the $\mathrm{h^0}\nu\bar{\nu}$ channel, the hadronic cluster multiplicity is expected to be larger due to four-quark final states. In the $\mathrm{h^0}\mu^+\mu^-$ and $\mathrm{h^0 e^+ e^-}$ channels, the selection relies on the identification of the lepton pair. Only minor modifications on the selection are made as compared to the searches for the Standard Model Higgs boson.

- $2m_{\tau} < m_{\mathrm{A}} < 2m_{\mathrm{b}}$: In this mass region, the relative ratio of $\mathrm{c\bar{c}}$ and $\tau^+\tau^-$ in $\mathrm{A^0}$ decays is unknown. In order to stay model-independent, the four-τ final states with lower selection efficiency are assumed to be dominant. Two tau pairs lead to larger missing energy and smaller cluster multiplicity in the $\mathrm{h^0}\nu\bar{\nu}$ channel compared with signatures from $\mathrm{h^0 \longrightarrow q\bar{q}}$ decays.

- $2m_{\mu} < m_{\mathrm{A}} < 2m_{\tau}$: The decay modes of $\mathrm{A^0}$ in this mass range are unknown and low-mass quark final states at various masses have been investigated similar to

those from direct h^0 decays. Both A^0 bosons can decay into these particles. Therefore, typically four charged tracks are expected in addition to a lepton pair.

- $0 < m_A < 2m_\mu$: Like the h^0, a very light A^0 can either decay outside the detector or it can decay into electromagnetic final states. The event characteristic in the first case is identical to signature expected without $h^0 \to A^0A^0$ decays. In the latter case, the same search technique is applied as in the very low mass range described before.

4.6 Results of Higgs Bremsstrahlung Searches

No indication of a Higgs boson signal has been observed. The number of events which pass the selection are found to be consistent with the expected background. The selection efficiencies given in Table 4.1 are for the high Higgs boson mass range, while those in Table 4.2 are for the intermediate mass range, and thoses in Tables 4.3 and 4.4 for the low mass range.

Systematic errors of about 5% due to uncertainties in the Monte Carlo simulation, and statistical errors due to Monte Carlo statistics between 5–9% depending on the Higgs boson mass and the investigated channel are used to reduce the selection efficiency. The results of the searches are presented as a 95% CL limit on the branching ratio for Higgs boson bremsstrahlung from the Z^0:

$$\Gamma(Z^0 \to h^0 Z^{0\star})/\Gamma(Z^0 \to q\bar{q}) < \frac{N^l}{N^{had} \times \epsilon} \tag{4.2}$$

where $N^l = 3.0$ if there is no candidate event. Candidate events are accounted for by using Poisson statistics to increase N^l, $N^{had} = 408,000$ is the total number of collected hadronic Z^0 decays and $\epsilon = \sum_f \mathrm{BR}(h^0 \to f\bar{f}) \times \epsilon_f$ is the selection efficiency weighted with the braching ratios of the investigated Higgs boson decay modes. Figure 4.1 shows the limit as a function of the Higgs boson mass.

The searches involving $h^0 \to A^0A^0$ decays achieve similar efficiencies to those in the Minimal Standard Model Higgs boson search. In the mass range $m_A > 2m_b$, typically the selection efficiency is increased by 5%, while in the range $2m_\tau < m_A < 2m_b$ the efficiency is reduced by 10%. For $m_A < 2m_\tau$, the selection efficiency is increased by about 15% in the $h^0\nu\bar{\nu}$ channel and is reduced by about 5% in both leptonic channels. Interpretations are given as effects on excluded mass regions in the framework of the two-doublet Higgs model in chapter 8.

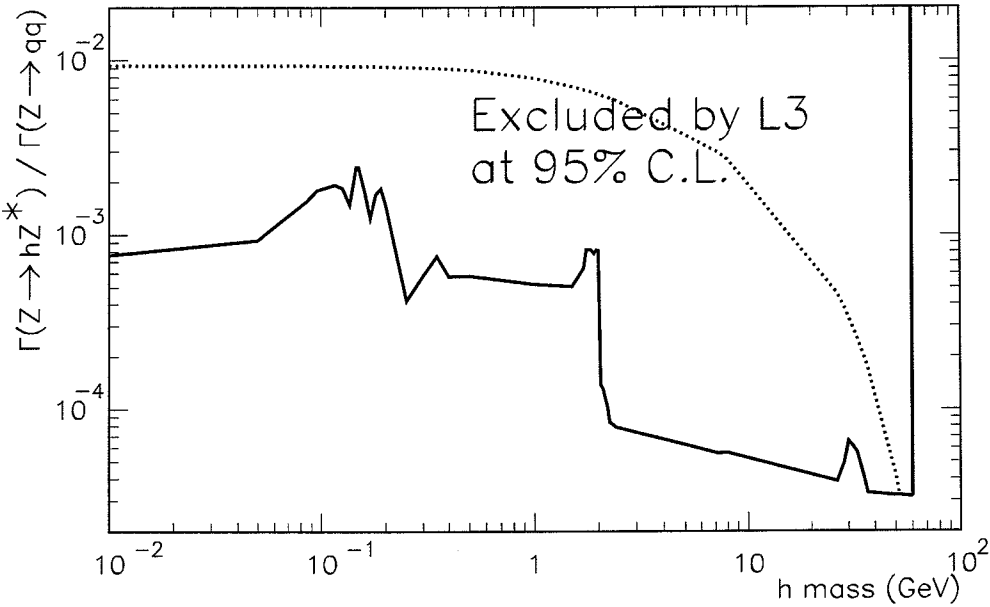

Figure 4.1: Limits on Higgs boson bremsstrahlung branching ratios, $\Gamma(Z^0 \to h^0 Z^{0*})/\Gamma(Z^0 \to q\bar{q})$. The dotted line shows the expected branching ratio in the Minimal Standard Model.

Higgs Mass (GeV)	30	40	50	55	60
$h^0\nu\bar{\nu}$ channel	36.4	60.6	59.0	50.3	37.4
$h^0e^+e^-$ channel (1991)	58.2	55.2	52.2	50.5	49.4
$h^0e^+e^-$ channel (1990)	45.5	38.0	35.0	32.0	29.0
$h^0\mu^+\mu^-$ channel	62.6	61.2	61.6	60.6	55.4
$(h^0 \to \tau^+\tau^-)(Z^0 \to q\bar{q})$ (1991)	3.8	10.2	15.6	17.8	14.8
$(h^0 \to q\bar{q})(Z^0 \to \tau^+\tau^-)$ (1991)	14.6	8.6	4.0	2.2	1.4
$(h^0 \to \tau^+\tau^-)(Z^0 \to q\bar{q})$ (1990)	2.4	5.4	9.4	12.4	8.8
$(h^0 \to q\bar{q})(Z^0 \to \tau^+\tau^-)$ (1990)	8.0	4.2	2.2	1.4	1.2

Table 4.1: Selection efficiencies (in %) for Higgs boson bremsstrahlung searches Standard Model Higgs boson search in the mass range 30 to 60 GeV.

Higgs Mass (GeV)	2	5	9	15	20
$h^0\nu\bar{\nu}$ channel	24	37	35	44	48
$h^0e^+e^-$ channel	22	40	51	57	62
$h^0\mu^+\mu^-$ channel	24	27	31	46	54

Table 4.2: Selection efficiencies (in %) for Higgs boson bremsstrahlung searches in the mass range 2 to 20 GeV.

Higgs Mass (GeV)	0.01	0.1	0.22	0.3	1.0	3.6
$h^0 \rightarrow e^+e^-$	14	7	-	-	40	-
$h^0 \rightarrow \mu^+\mu^-$	-	-	36	-	42	44
$h^0 \rightarrow \pi^+\pi^-$	-	-	-	34	35	38
$h^0 \rightarrow K^+K^-$	-	-	-	-	31	35

Table 4.3: Selection efficiencies (in %) for Higgs boson bremsstrahlung searches in the $h^0\mu^+\mu^-$ channel in the mass range 0 to 3.6 GeV.

Higgs Mass (GeV)	0.01	0.1	0.22	0.3	1.0	3.6
$h^0 \rightarrow e^+e^-$	14	14	-	-	25	-
$h^0 \rightarrow \mu^+\mu^-$	-	-	26	-	30	33
$h^0 \rightarrow \pi^+\pi^-$	-	-	-	20	26	28
$h^0 \rightarrow K^+K^-$	-	-	-	-	28	28

Table 4.4: Selection efficiencies (in %) for Higgs boson bremsstrahlung searches in the $h^0e^+e^-$ channel in the mass range 0 to 3.6 GeV.

Chapter 5

Searches for Neutral Higgs Boson Pair-Production

Searches for pair-produced Higgs bosons are presented in the channels $b\bar{b}b\bar{b}$, $b\bar{b}b\bar{b}b\bar{b}$, $\tau^+\tau^-b\bar{b}$ and $\tau^+\tau^-\tau^+\tau^-$. No assumption on the cross-section is made and results are shown as limits on individual branching ratios for the Higgs boson production and Z^0 decays.

5.1 The Search in the $Z^0 \rightarrow h^0A^0 \rightarrow b\bar{b}b\bar{b}$ Channel

A simulated Higgs boson event in this channel is shown in Figure 5.1. The search for $Z^0 \rightarrow h^0A^0 \rightarrow b\bar{b}b\bar{b}$ is made in the hadronic event sample using the following cuts:

$$E_{\parallel}/E_v < 0.60, \quad E_{\perp}/E_v < 0.60, \quad 0.4 < E_v/\sqrt{s} < 1.4, \quad N_{\rm cl} \geq 7, \tag{5.1}$$

where $E_{\parallel}$ is the energy imbalance along the beam direction, $E_{\perp}$ the transverse energy imbalance, E_v the total measured calorimetric energy and $N_{\rm cl}$ the number of calorimetric clusters. In order to distinguish the signal from the main background due to $Z^0 \rightarrow q\bar{q}$ decays, use is made of both the different topological properties of the events and of the higher inclusive semileptonic branching ratio of the b quarks compared to lighter quarks in Z^0 decays. The mass region from 18 GeV up to the $m_Z = m_h + m_A$ kinematical limit is investigated. The 18 GeV limit results from the limit set by the cluster algorithms ($y_{\rm cut}$= 0.02, see section 3.6); it exceeds this limit by two standard deviations of the mass resolution.

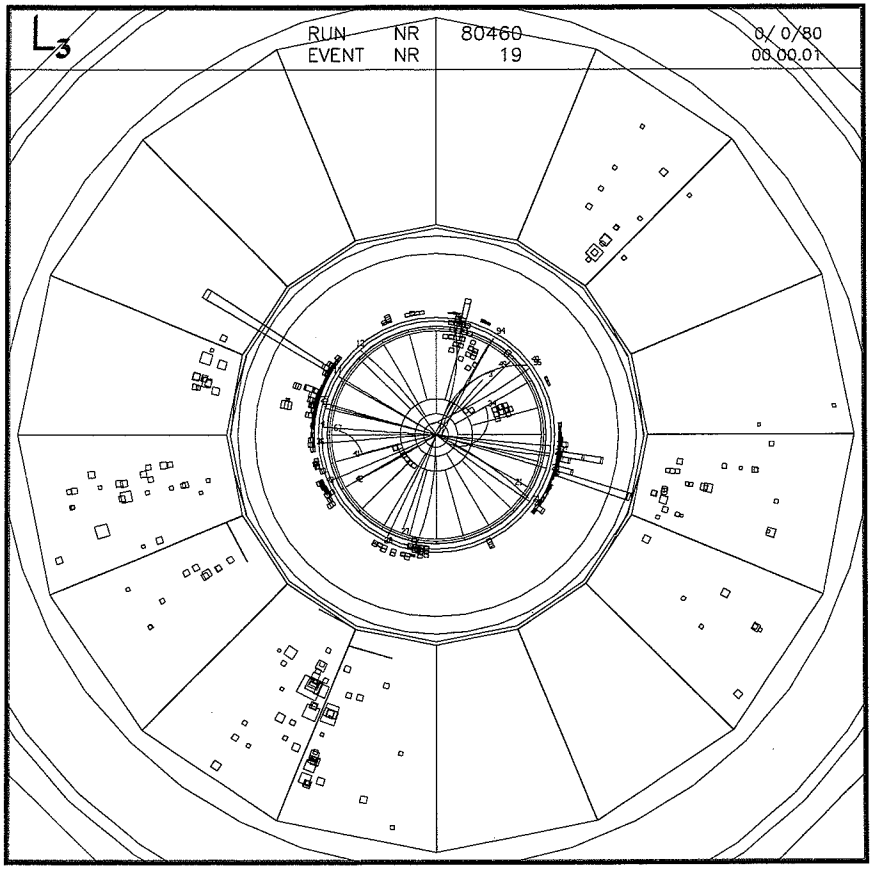

Figure 5.1: Simulated $Z^0 \rightarrow h^0A^0 \rightarrow b\bar{b}b\bar{b}$ event after full detector simulation and reconstruction, shown in the plane perpendicular to the beam axis. An electron with large transverse momentum with respect to the nearest jet can be seen in the first quadrant.

5.1.1 Selection Details

Events with either 4 or 5 jets are selected. The $Z^0 \rightarrow q\bar{q}$ background contribution is normalized to the data. More than 85% of the signal events in the (m_h,m_A) mass range of interest and about 8% of the background events from $Z^0 \rightarrow q\bar{q}$ survive the cut on the number of jets. The 5-jet events are transformed into 4-jet events by combining the two jets with the smallest invariant mass. The next step is to identify the two jets potentially coming from the $h^0 \rightarrow b\bar{b}$ decay and those coming from the $A^0 \rightarrow b\bar{b}$ decay and to select events corresponding to a given (m_h,m_A) mass combination. For this purpose, a mass-χ^2 is calculated for each $h^0 \rightarrow$ jet jet

and $A^0 \rightarrow$ jet jet combination:

$$\chi_i^2 = \frac{(m_{h_i}^{rec} - m_h)^2}{\sigma_{h_i}^2} + \frac{(m_{A_i^{rec}} - m_A)^2}{\sigma_{A_i}^2} \tag{5.2}$$

where i runs over the three possible jet-jet combinations, $m_{h_i}^{rec}, m_{A_i}^{rec}$ are the reconstructed masses, (m_h,m_A) the mass point under investigation and $\sigma_{h_i}, \sigma_{A_i}$ the mass resolutions at (m_h,m_A). The mass resolutions are determined from the simulated signal events by taking the reconstructed mass distribution with the minimum χ^2. An example of such a distribution for $m_h = 22$ GeV and $m_A = 52$ GeV is shown in Figure 5.2. The two mass peaks are clearly separated with mass resolutions of 3.7 GeV and 7.7 GeV, respectively. These resolutions agree with the 15% mass resolution obtained by the study of $q\bar{q}\gamma$ data events described in section 3.8. The procedure is repeated for each of the nine (m_h,m_A) points for which signal events were simulated. The resolutions σ_h and σ_A are then parameterized as a function of (m_h,m_A).

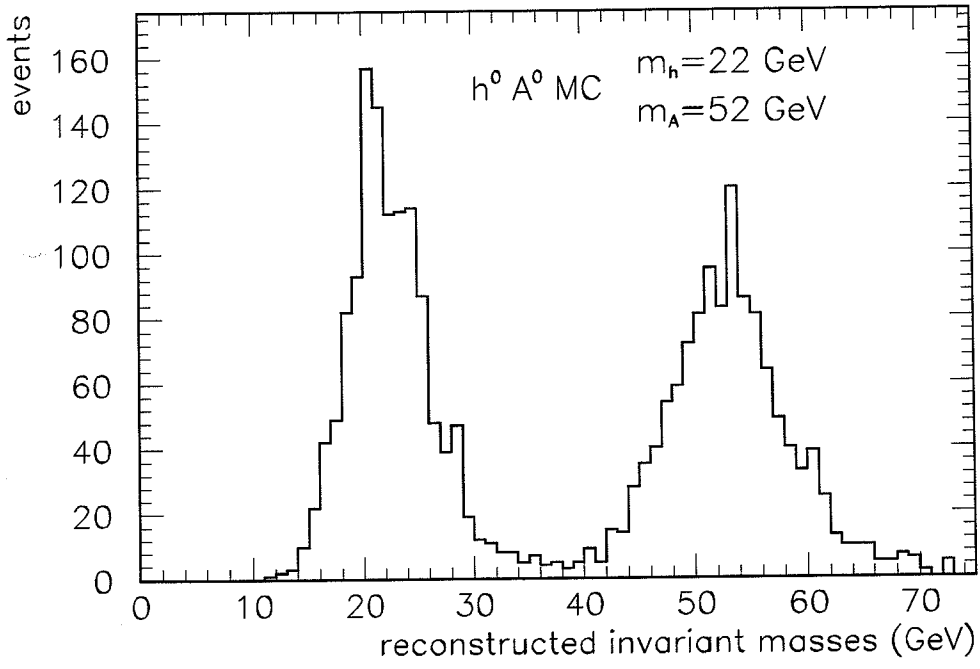

Figure 5.2: Reconstructed Higgs boson masses for a simulated (22 GeV,52 GeV) Higgs boson signal in the bbbb channel.

Figure 5.3 shows the χ^2-distributions for a (22 GeV, 52 GeV) signal, the $Z^0 \rightarrow q\bar{q}$ background and the data. As expected, the χ^2_{min} distribution for the signal

is steeper than for the background. Having selected the best jet-jet combination with minimum χ^2, events are rejected with $\chi^2_{min} > 2$. At this stage the jets coming from the decays of h^0 and A^0 are identified.

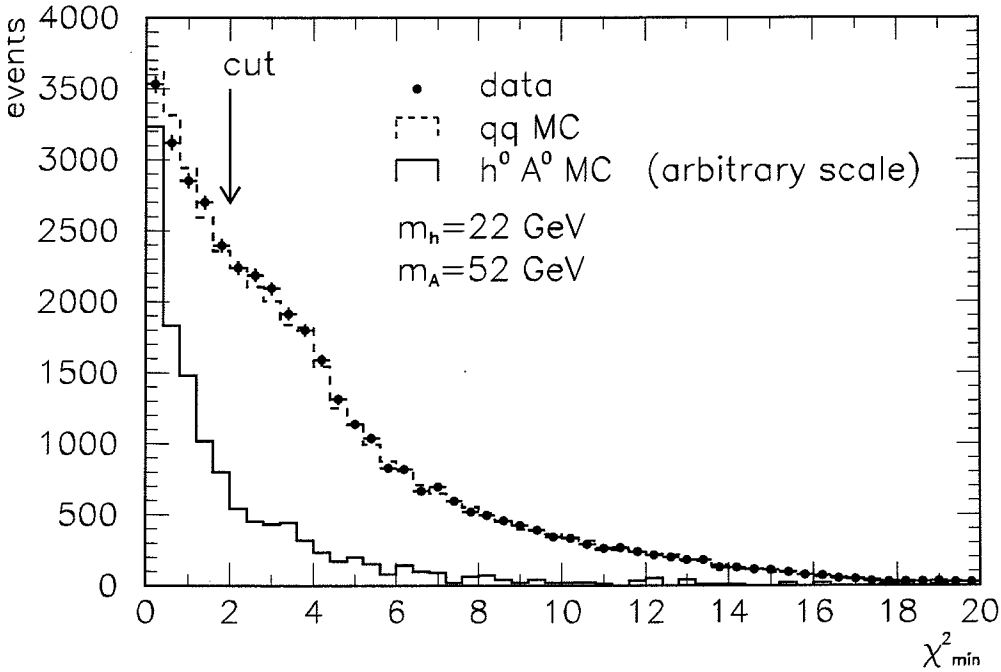

Figure 5.3: Distribution of χ^2_{min} for data, simulated background and Higgs boson signal in the bbbb channel. See text for a definition of χ^2_{min}.

Additional topological cuts are applied to reduce the $Z^0 \rightarrow q\bar{q}$ background. These cuts are optimized at simulated signal points (m_h,m_A) and subsequently parameterized as a function of (m_h,m_A). The cut values are then interpolated for any arbitrary point in the (m_h,m_A) plane. The variables used in this analysis are:

- The production angle, θ_p, of the h^0 and A^0 bosons defined as the angle between the Higgs boson direction and the beam axis in the laboratory. The $Z^0 \rightarrow h^0A^0$ events are expected to follow a $\sin^2\theta_p$ distribution whereas the $Z^0 \rightarrow q\bar{q}$ background events should have a $(1+\cos^2\theta_p)$ distribution.

- The decay angle, θ_d, defined as the angle between the direction of the jets with respect to the Higgs boson direction in the rest frame of the Higgs boson. The

signal distribution is expected to be flat, while for $Z^0 \to q\bar{q}$ background the distribution should be peaked at small angles due to gluon bremsstrahlung.

- The event thrust, T, which discriminates signal events for large Higgs boson masses against $Z^0 \to q\bar{q}$ background. Figure 5.4 shows the T-distribution for events with $m_h = 52$ GeV and $m_A = 22$ GeV Higgs boson masses after the χ^2_{min}, $\cos\theta_p$ and $\cos\theta_d$ cuts are applied. The signal is concentrated at smaller thrust values than the $Z^0 \to q\bar{q}$ background.

- The minimum angle between any jet-pair, θ^{jj}_{min}. The signal has a flatter $\cos\theta^{jj}_{min}$ distribution than the $Z^0 \to q\bar{q}$ background.

- The angle, ψ_{pl}, between the normal to the plane of the two jets from h^0 and the normal to the plane of the two jets from the A^0 decays: 4-jet events from QCD processes tend to have a smaller ψ_{pl} angles than the one for the signal events.

The values of the cuts used for each (m_h,m_A) signal simulated are given in Table 5.1.

bbbb Channel					
Masses (GeV)	$\lvert\cos\theta_p\rvert$	$\lvert\cos\theta_d\rvert$	T	$\lvert\cos\theta^{jj}_{min}\rvert$	$\lvert\cos\psi_{pl}\rvert$
m_h,m_A	$\leq$	$\leq$	$\leq$	$\leq$	$\leq$
22,22	0.6	0.8	0.9	0.8	1.0
22,32	0.75	0.8	0.84	0.65	0.95
22,42	0.7	0.8	0.76	0.60	0.95
22,52	0.75	0.8	0.79	0.60	0.95
22,62	0.5	0.8	0.82	1.0	0.80
32,32	0.9	0.7	0.78	0.5	1.0
32,42	1.0	0.7	0.78	0.5	1.0
32,52	0.8	0.7	0.78	1.0	0.8
42,42	0.8	0.7	0.78	1.0	0.8

Table 5.1: Values of topological cuts in the bbbb channel
Values of topological cuts applied to select $Z^0 \to h^0A^0 \to b\bar{b}b\bar{b}$ events at the various (m_h,m_A) values for which the signal Monte Carlo was generated.

The $Z^0 \to h^0A^0 \to b\bar{b}b\bar{b}$ signal is expected to have a larger number of leptons from inclusive semileptonic decays compared to 4-jet events from QCD background.

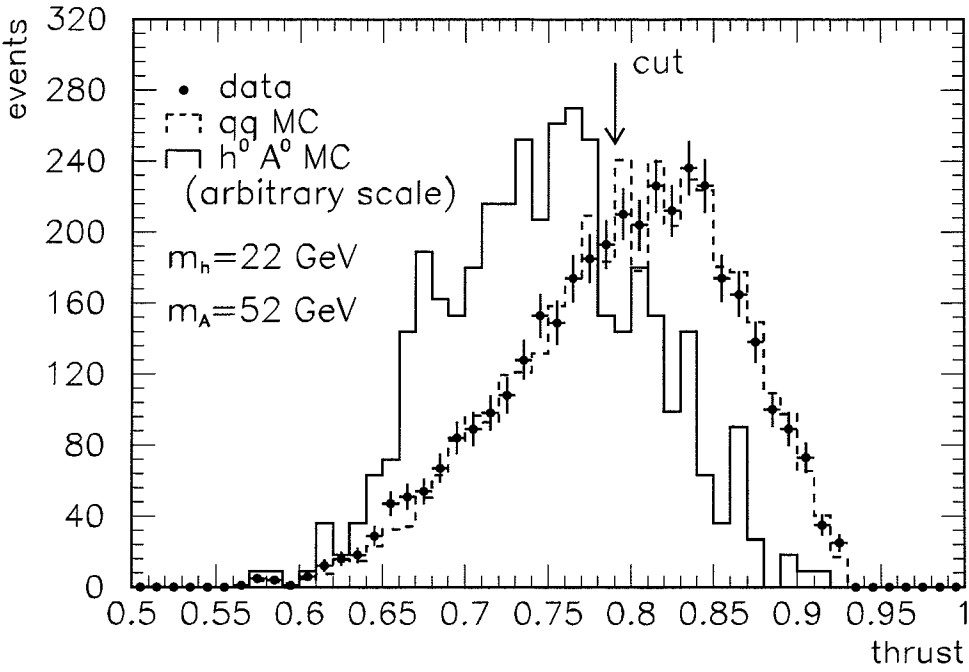

Figure 5.4: Thrust distribution for data, simulated background and Higgs boson signal in the bbbb channel.

Both electrons and muons are used in this analysis. A requirement is made of at least one lepton with high momentum ($\geq$ 3 GeV) and high p_T with respect to the nearest jet ($\geq$ 1.5 GeV). The quality cuts for the lepton selection as described in the inclusive lepton analyses [91] are imposed. For the electron sample the lateral shower profile, the BGO shower shape χ^2 and the azimuthal angle and energy–momentum matching between the TEC detector and the electromagnetic calorimeter are used. For the muon sample, a track reconstruction is required both in the muon chamber and in the TEC; the two measurements should match. The effects of the cuts, the expected signals, the background and the data are summarized in Table 5.2. All distributions of important cut quantities are shown in appendix A.

5.1.2 Results of the Search in the bbbb Channel

The numbers of surviving events in the simulated signal, in the $Z^0 \rightarrow q\bar{q}$ background and in the data are shown in Table 5.3 for the 1990 and 1991 runs.

bbbb Channel						
Selection Cuts m_h=m_A=32 GeV	Signal Acc. (%)	$Z^0 \to q\bar{q}$ Events	Data Events	Signal Acc. (%)	$Z^0 \to q\bar{q}$ Events	Data Events
	1991			**1990**		
			296k			116k
Preselection	84.9	39855	39480	87.0	16195	16782
$\chi^2 \leq 2$	60.8	12007	12264	60.4	4958	5220
$\lvert\cos\theta_p\rvert \leq 0.9$	60.0	11796	12042	59.6	4874	5131
$\lvert\cos\theta_d\rvert \leq 0.7$	31.1	1658	1820	32.1	651	713
$T \leq 0.78$	28.6	1113	1137	30.0	426	545
$\lvert\cos\theta^{jj}_{min}\rvert \leq 0.5$	26.6	782	846	26.1	301	336
incl. lepton	4.4	27	23	5.3	8.9	4

Table 5.2: Cuts, acceptances and corresponding numbers of data and background events for the different steps of the selection in the bbbb channel for a $m_h = m_A = 32$ GeV. Details of the preselection are given in the text. 1600 Higgs boson events are simulated for the 1991 data sample and 872 for the 1990 data sample.

bbbb Channel						
Masses (GeV)	Signal Acc. (%)	$Z^0 \to q\bar{q}$ Events	Data Events	Signal Acc. (%)	$Z^0 \to q\bar{q}$ Events	Data Events
m_h, m_A	**1991**			**1990**		
22,22	3.9	19	13	3.3	3	5
22,32	3.1	20	19	2.4	9	5
22,42	2.4	21	19	3.2	7	9
22,52	2.6	27	24	—	7	11
22,62	1.3	21	22	—	9	11
32,32	4.4	27	23	5.8	9	4
32,42	3.5	28	23	3.9	10	5
32,52	2.1	21	24	—	4	7
42,42	2.3	13	15	1.9	4	4

Table 5.3: Acceptances and numbers of data and background events after all cuts for various Higgs boson masses in the bbbb channel The $Z^0 \to q\bar{q}$ background is normalized to the data.

The systematic errors and their effects on the predicted signal acceptances for the $b\bar{b}b\bar{b}$ channel are given in Table 5.4. For the available signal Monte Carlo samples, the statistical error is about 15%. The resulting total uncertainty is estimated to be 27%, which is the amount by which the signal efficiency is reduced in order to obtain a 95% CL limit on the $Z^0 \rightarrow h^0A^0 \rightarrow b\bar{b}b\bar{b}$ branching ratio

$$\frac{\Gamma(Z^0 \rightarrow h^0A^0 \rightarrow b\bar{b}b\bar{b})}{\Gamma(Z^0 \rightarrow q\bar{q})} \tag{5.3}$$

as function of m_h and m_A. Figure 5.5 shows the regions in the (m_h,m_A) plane excluded at 95% CL for values of the branching ratio larger than or equal to 1×10^{-3} and 2×10^{-3}, respectively. Interpretations of these limits in the MSSM are discussed in Section 9.

bbbb Channel		
Selection Cuts $m_h = m_A = 32$ GeV	Variation	Acceptance Reduction (%)
Preselection	–	< 3
$N_J = 4$ or 5	20%	20
$\chi^2 \leq 2$	0.2	9
$\lvert\cos\theta_p\rvert \leq 0.9$	0.02	1.7
$\lvert\cos\theta_d\rvert < 0.7$	0.04	4.0
$T \leq 0.78$	0.01	5.0
$\lvert\cos\theta^{jj}_{min}\rvert \leq 0.5$	0.044	2.9
incl. leptons	5%	5
TOTAL		23

Table 5.4: Reduction of expected Higgs boson acceptance in the bbbb channel due to modeling of the detector response for each quantity used in the analysis. For continuous quantities the variation is taken as one standard deviation on the measured quantity and for discrete quantities as one standard deviation on the normalization of the event rate. The reductions are summed in quadrature.

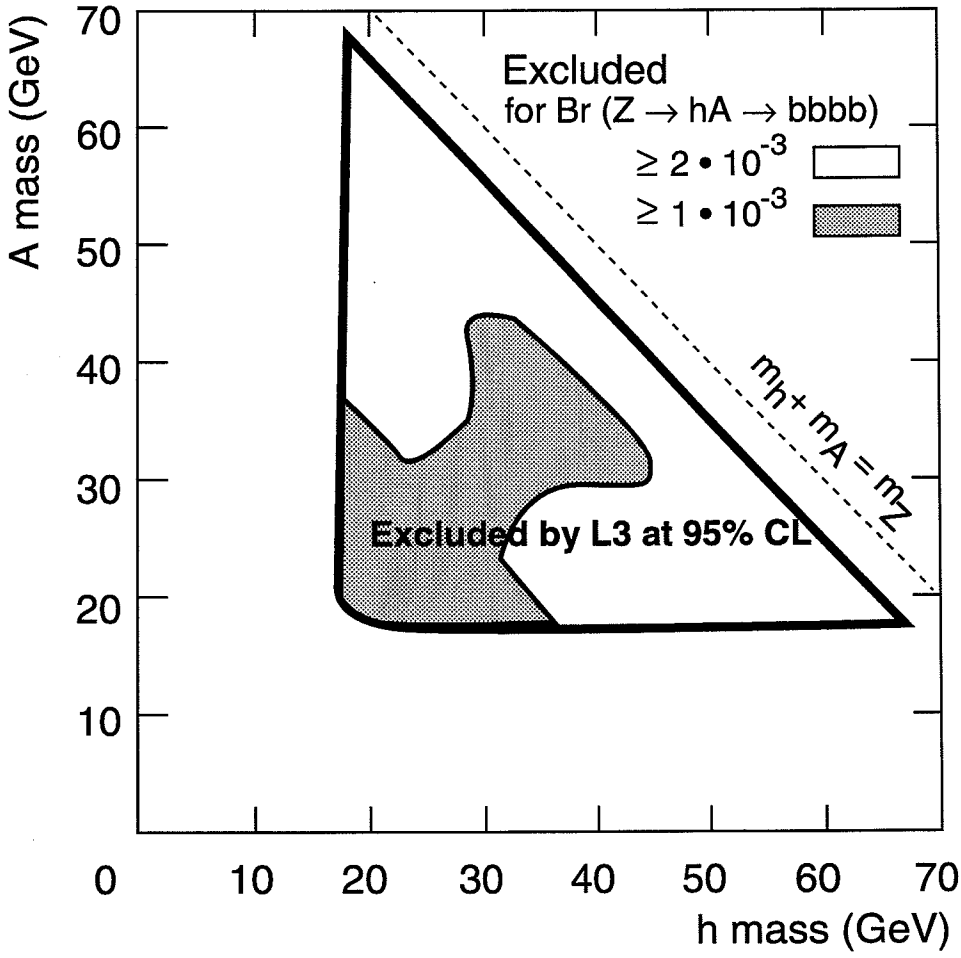

Figure 5.5: Regions of the (m_h,m_A) plane excluded at 95% CL for values of the branching ratio $\Gamma(Z^0 \to h^0 A^0 \to b\bar{b}b\bar{b})/\Gamma(Z^0 \to q\bar{q}) \geq 1 \times 10^{-3}$ (dark region), $\geq 2 \times 10^{-3}$ (region inside heavy contour line).

5.2 The Search in the $Z^0 \rightarrow h^0A^0 \rightarrow A^0A^0A^0 \rightarrow b\bar{b}b\bar{b}b\bar{b}$ Channel

A simulated Higgs boson event in this channel is shown in Figure 5.6. The process $Z^0 \rightarrow h^0A^0 \rightarrow A^0A^0A^0 \rightarrow b\bar{b}b\bar{b}b\bar{b}$ is possible if $m_h > 2m_A$. At the parton level one expects six jets in the event. However, the number of reconstructed jets can be different. A study of a simulated signal for (m_h,m_A) values (50, 22), (60, 22) and (60, 27) GeV shows that more than 80 % of the events led to $N_J \geq 5$ jets in the final state using the clustering algorithm described in section 3.6. The $Z^0 \rightarrow q\bar{q}$ background is normalized to the 5-and-more-jet-rate in the data.

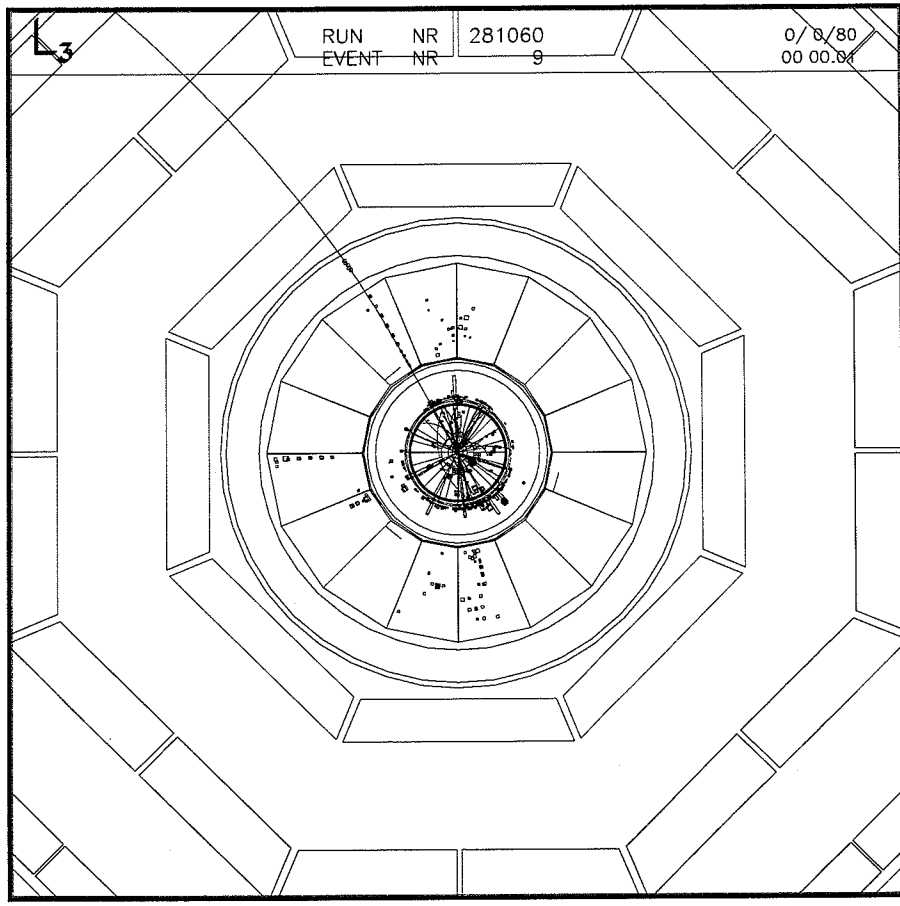

Figure 5.6: Simulated $Z^0 \rightarrow h^0A^0 \rightarrow A^0A^0A^0 \rightarrow b\bar{b}b\bar{b}b\bar{b}$ event after full detector simulation and reconstruction, shown in the plane perpendicular to the beam axis.

5.2.1 Selection Details

A cut of $T < 0.8$ is imposed. This requirement provides a very effective way of suppressing the QCD background: only about 2.1% of the background events and about 70% signal events survive the cut.

Since most of the events lead to only 5 jets in the final state, the reconstruction of the masses is not possible. The search strategy is therefore based on the reconstruction of two A^0 bosons of a specific mass. Following the procedure adopted for the 4-jet analysis, a mass-χ^2 is defined as to reconstruct the A^0 mass:

$$\chi^2_i = \frac{(m^{rec}_{A_1} - m_A)^2}{\sigma^2_{A_1}} + \frac{(m^{rec}_{A_2} - m_A)^2}{\sigma^2_{A_2}} \tag{5.4}$$

where i runs over six possible jet-pairing, $m^{rec}_{A_1}$ and $m^{rec}_{A_2}$ are reconstructed invariant masses of the jet-pairings and $\sigma_{A_{1,2}}$ are the corresponding mass resolutions. From a study of signal Monte Carlo events a resolution of 2.7 GeV is obtained in the mass range of interest (20 to 27 GeV). Combinations of $A^0{}_1 \to \mathrm{jet_i\ jet_j}$ and $A^0{}_2 \to \mathrm{jet_k\ jet_l}$ are then selected for which the χ^2 is minimum; events with $\chi^2_{\mathrm{min}} \geq 3$ are rejected.

Additional cuts are applied:

- $|\cos\theta_p| \leq 0.9$, where $\cos\theta_p$ is the production angle of A^0. Although only one A^0 is directly produced, a cut on the production angle of the two identified A^0 bosons distinguishes the expected signal from background.

- $|\cos\theta^{jj}_{min}| \leq 0.8$, where $\cos\theta^{jj}_{min}$ is the minimum angle between any two jets.

- $\sum \mathrm{M^{rec}_{jet}} \geq$ 28 GeV cut is applied, where $\sum \mathrm{M^{rec}_{jet}}$ is the sum of jet masses. The signal final state (consisting of 6 b-quarks) leads to higher values of the $\sum \mathrm{M^{rec}_{jet}}$ compared to the $Z^0 \to q\bar{q}$ background. Figure 5.7 shows the $\sum \mathrm{M^{rec}_{jet}}$ distributions for data, $Z^0 \to q\bar{q}$ background and for a (50 GeV, 22 GeV) simulated signal.

Finally, at least one semileptonic b decay (e or μ) is required with the same lepton characteristic as for the $Z^0 \to h^0A^0 \to b\bar{b}b\bar{b}$ final state. With six b-quarks in the final state the probability of observing a semi-leptonic decay of one of the b quarks is large. The effects of the cuts and the expected signal, background and data are summarized in Table 5.5. All distributions of important cut quantities are shown in appendix B.

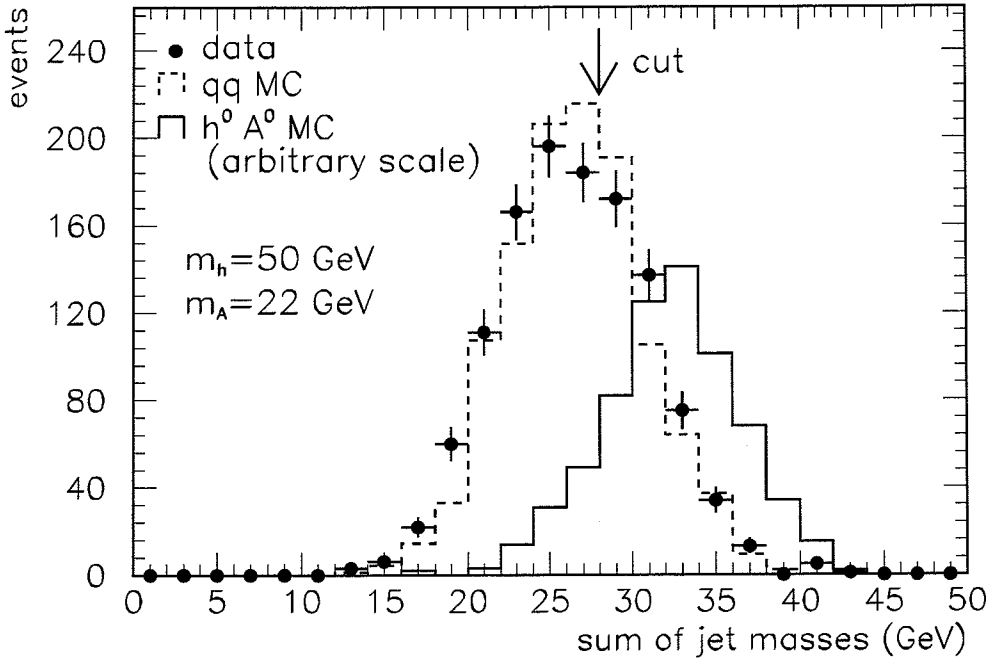

Figure 5.7: Distribution of the sum of jet masses for data, simulated background and Higgs boson signal in the bbbbbb channel.

bbbbbb Channel					
Selection Cuts $m_h = 60$ GeV, $m_A = 27$ GeV	Signal Acc. (%)	$Z^0 \to q\bar{q}$ Events	Data Events	$Z^0 \to q\bar{q}$ Events	Data Events
	1991			**1990**	
			296k		116k
Preselection	82.4	78287	58887	29018	25018
N_J, T	67.1	2907	2997	1328	1289
$\chi^2 \leq 3.0$	51.4	1786	1936	804	837
$\lvert\cos\theta_p\rvert \leq 0.9$	46.8	1535	1641	677	703
$\lvert\cos\theta_{min}^{jj}\rvert \geq 0.8$	38.4	983	1122	427	474
$\sum M_{jet}^{rec} \geq 28.$	34.3	376	452	187	198
incl. lepton	6.8	12	16	12	6

Table 5.5: Cuts, acceptances and corresponding numbers of data and background events for the different steps of the selection in the bbbbbb channel for $m_h = 60$ GeV, $m_A = 27$ GeV. Details of the preselection are given in the text. 1600 Higgs boson signal events are simulated.

5.2.2 Results of the Search in the bbbbbb Channel

After applying the above cuts on the simulated signal, the selection efficiency is found to be 6.3% in the (m_h,m_A) range of interest. The comparison between data events surviving the cuts and the QCD expectation is given in Table 5.6.

bbbbbb Channel								
m_A (GeV)	20	21	22	23	24	25	26	27
1990+1991 Data (Events)	18	21	20	22	19	17	18	22
$Z^0 \to q\bar{q}$ (Events)	25	26	29	25	22	22	23	24

Table 5.6: Numbers of data and background events after all cuts for various Higgs boson masses in the bbbbbb channel as a function of m_A. The selection is independent of m_h.

The systematic errors and their effects on the predicted signal acceptances for the $b\bar{b}b\bar{b}b\bar{b}$ channel are given in table 5.7.

bbbbbb Channel		
Selection Cuts $m_h = 60$ GeV, $m_A = 27$ GeV	Variation	Acceptance Reduction (%)
Preselection	–	< 3
$N_J = 5$ or 6	20%	20
$\chi^2 \leq 3$	0.4	8.0
$\lvert\cos\theta_p\rvert \leq 0.9$	0.04	5.5
$\lvert\cos\theta_{min}^{jj}\rvert < 0.8$	0.044	5.5
$\sum M_{jet}^{rec} \geq 28$ GeV	1.7	12
incl. leptons	5%	5
TOTAL		26

Table 5.7: Reduction of expected Higgs boson acceptance in the bbbbbb channel due to modeling of the detector response for each quantity used in the analysis. For continuous quantities the variation is taken as one standard deviation on the resolution in the measured quantity and for discrete quantities as one standard deviation on the normalization of the event rate. The reductions are summed in quadrature.

For the mass range $20 \leq m_A \leq 27$ GeV and $m_h > 2m_A$, model independent limits on the branching rate for the $Z^0 \to h^0A^0 \to A^0A^0A^0 \to b\bar{b}b\bar{b}b\bar{b}$ process are derived from the numbers of surviving events given in Table 5.6. For the available

signal Monte Carlo samples, the statistical error is about 11%. The resulting total uncertainty is estimated to be 28%, which is used to reduce the signal efficiency in order to obtain a 95% CL limit on the branching ratio: a limit at 95% CL is set:

$$\frac{\Gamma(Z^0 \to h^0 A^0 \to A^0 A^0 A^0 \to b\bar{b}b\bar{b}b\bar{b})}{\Gamma(Z^0 \to q\bar{q})} \leq 9.1 \times 10^{-4}. \quad (5.5)$$

5.3 The Search in the $Z^0 \to h^0 A^0 \to \tau^+\tau^- b\bar{b}$ Channel

A simulated Higgs boson event in this channel is shown in Figure 5.8. The events from $Z^0 \to h^0 A^0 \to \tau^+\tau^- b\bar{b}$ are characterized by an isolated pair of narrow jets, associated with a small number of tracks (2 in 74% and 4 in 25% of the tau pair final states) and a large amount of missing momentum, recoiling against two broad hadronic jets. The main background comes from hadronic Z^0 decays.

The analysis presented here concentrates on the identification and the mass reconstruction of the $\tau^+\tau^-$ pair. As a first step in the identification of the $\tau^+\tau^-$ pair, the event is divided into two hemispheres using the plane perpendicular to the thrust axis and counting the number of calorimetric clusters in each of them. The hemisphere with the lower number of clusters (hereafter referred to as the tau-hemisphere) should contain the $\tau^+\tau^-$ pair. In the tau-hemisphere, the calorimetric clusters are combined into jets using $y_{cut} = 0.001$; this allows the separation of two jets down to a mass of 2.9 GeV. In the hemisphere with the higher number of clusters (hereafter referred to as the jet hemisphere), a $y_{\rm cut}$ value of 0.02 is used. The identification of the $\tau^+\tau^-$ pair is made by requiring two narrow jets and two tracks with opposite charge. The invariant mass of the $\tau^+\tau^-$ pair is reconstructed and the $\tau^+\tau^-$ mass distribution scanned in different mass windows to search for an excess of events over the expected hadronic background.

5.3.1 Selection Details

The events have to pass a preselection similar to one used for the $b\bar{b}b\bar{b}$ channel:

$$E_{\parallel}/E_v < 0.40, \quad E_{\perp}/E_v < 0.60, \quad 0.4 < E_v/\sqrt{s} < 0.9, \quad |\cos\theta_T| < 0.7. \quad (5.6)$$

The cut on $\cos\theta_T$ selects events in the central region of the detector, enhancing the signal from $Z^0 \to h^0 A^0$, which has a $\sin^2\theta_T$ distribution, over the background from

$Z^0 \to q\bar{q}$ and $Z^0 \to \tau^+\tau^-$, which has a $(1+\cos^2\theta_T)$ distribution. For the mass region under investigation, the acceptance for the simulated $Z^0 \to h^0A^0 \to \tau^+\tau^-b\bar{b}$ events after these cuts is about 65%.

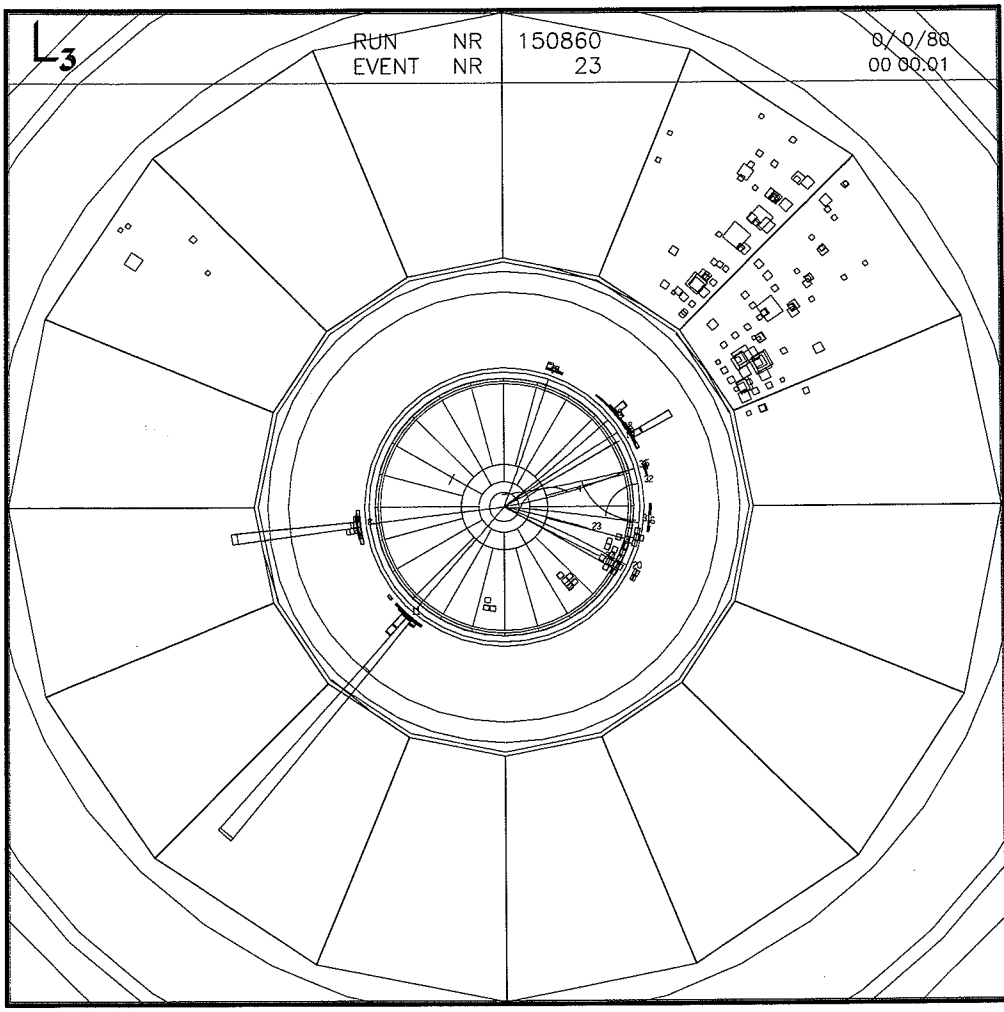

Figure 5.8: Simulated $Z^0 \to h^0A^0 \to \tau^+\tau^-b\bar{b}$ event after full detector simulation and reconstruction, shown in the plane perpendicular to the beam axis.

In order to reject low-multiplicity events ($Z^0 \to e^+e^-$, $\mu^+\mu^-$, $\tau^+\tau^-$) and to identify $\tau^+\tau^-$ pairs in the tau-hemisphere, the following cuts are applied:

- $N_{cl} \geq 15$, where N_{cl} is the number of calorimetric clusters,

- $N_J \geq 2$, where N_J is the number of broad jets in the jet hemisphere,
- $N_\tau = 2$, where N_τ is the number of narrow jets in the tau hemisphere with $0.5 \leq E_\tau \leq 30$ GeV, where E_τ is the narrow jet energy,
- $N_{tr} = 2$, where N_{tr} is the number of tracks in the tau hemisphere,
- $N_q = 0$, where N_q is the total charge in the tau hemisphere.

The distribution of the number of calorimetric clusters after the preselection is shown in Figure 5.9. The charged-track multiplicity is given in Figure 5.10 after the preselection and the first three cuts.

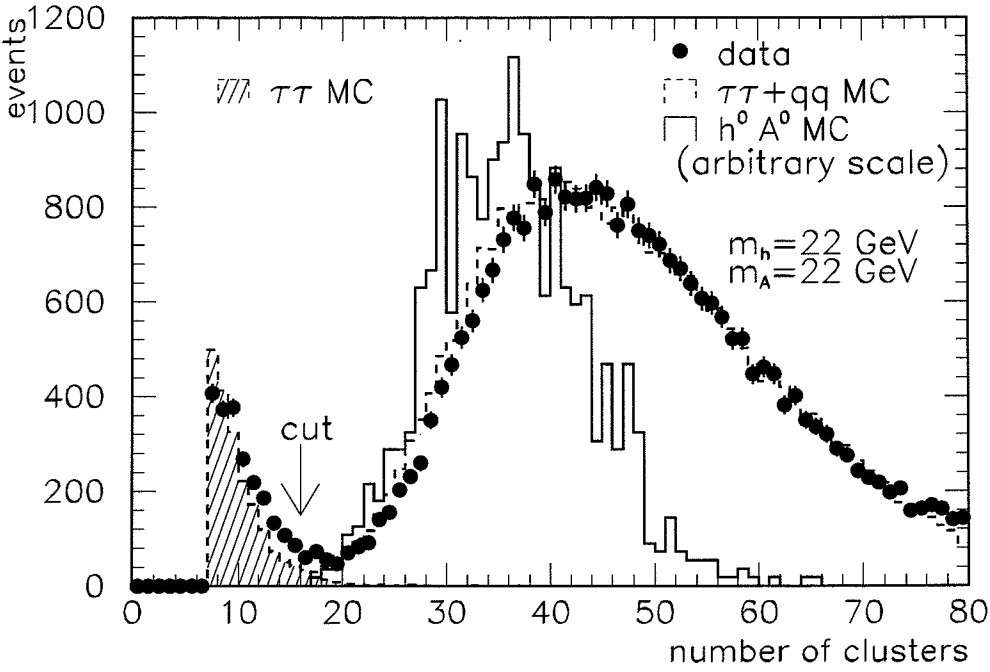

Figure 5.9: Distribution of the number of calorimetric clusters for data, background and simulated Higgs boson signal in the $\tau\tau$bb channel.

Finally, as described in the next section, the invariant mass of the identified $\tau^+\tau^-$ pair is reconstructed using the measured momenta of the two narrow jets and the missing momentum vector of the event.

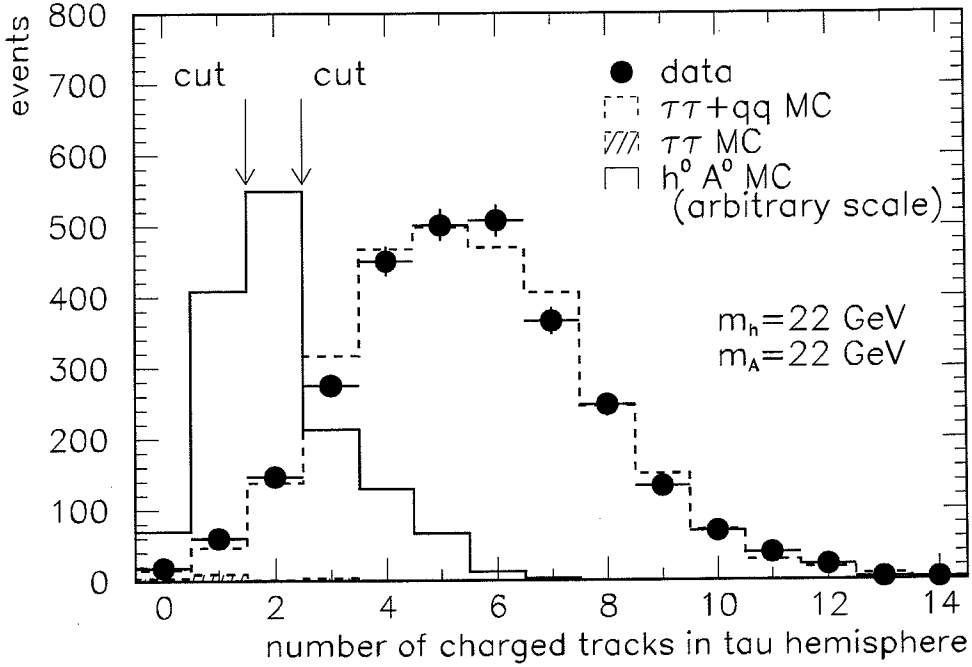

Figure 5.10: Distribution of the number of charged tracks in the tau hemisphere for data, background and simulated Higgs boson signal in the $\tau\tau$bb channel.

5.3.2 Mass Reconstruction of the τ-Pair

The reconstruction of the invariant mass of the τ-pair is based on the fact that, in spite of the presence of (one or two) neutrinos among the τ-decay products, the momentum of each of the two τ's can be fully reconstructed using the measured energy and direction of the visible τ-decay products and the missing momentum vector. If the masses of the particles from the τ-decay are small compared to their momenta, the direction of the τ's is, to a good approximation, the same as that of its observable decay products (either a tau-jet or an electron or a muon). If the two τ's are not back to back (in which case the reconstruction of the individual momenta of the two τ's is not possible), the missing momentum vector can be used to determine the momentum carried by the neutrinos from the decay of each of the two τ's, using the following relations:

$$P \cos\theta_{j_1 P} = p_{\nu_1} + p_{\nu_2} \cos\theta_{j_1 j_2},$$

$$P \sin\theta_{j_1 P} = p_{\nu_2} \sin\theta_{j_1 j_2}, \tag{5.7}$$

where P is the magnitude of the measured missing momentum vector $\mathbf{P}$, $\theta_{j_1 P}$ the angle between the missing momentum vector and one of the two τ-jets and $\theta_{j_1 j_2}$ the angle between the two τ-jets (see Figure 5.11).

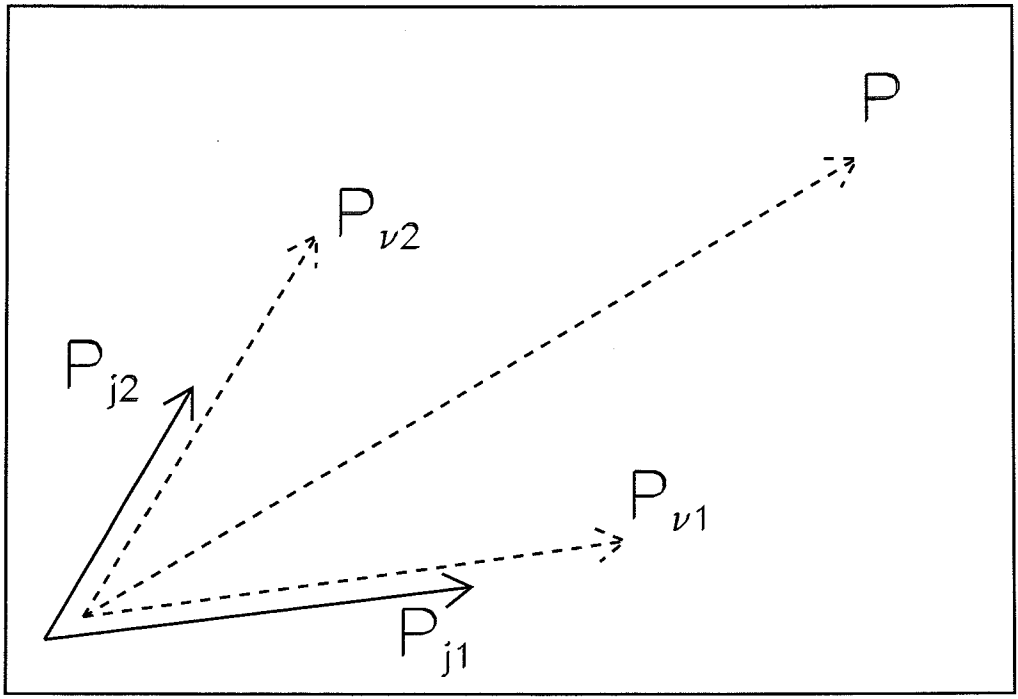

Figure 5.11: Schematic illustration of the reconstruction of the tau momenta $p_{\tau_{1,2}} = p_{j_{1,2}} + p_{\nu_{1,2}}$, using the direction of the tau jets $p_{j_{1,2}}$ and the missing energy vector $\mathbf{P}$.

Reconstruction of the tau momenta $p_{\tau_{1,2}} = p_{j_{1,2}} + p_{\nu_{1,2}}$, using the direction of the tau jets $p_{j_{1,2}}$ and the missing energy vector $\mathbf{P}$. The magnitudes p_{ν_1} and p_{ν_2} of the momenta carried by the neutrinos from the decay of the two τ's can be calculated from eq. (5.7), provided the two τ-jets are not collinear (*i.e.* if $\theta_{j_1 j_2} \neq 180°$). The τ-pair invariant mass is given by:

$$m_{\tau\tau} = [2 p_{\tau_1} p_{\tau_2} (1 - \cos\theta_{j_1 j_2})]^{1/2}, \tag{5.8}$$

in terms of the reconstructed τ-momenta $p_{\tau_{1,2}} = p_{j_{1,2}} + p_{\nu_{1,2}}$. Assuming that the two τ's come from the decay of the h^0, the h^0 mass resolution can be improved by

constraining the energy of the τ-pair $E_{\tau\tau} = p_{\tau_1} + p_{\tau_2}$ to the energy of the h^0 from $Z^0 \to h^0A^0$ decay:

$$E_h = \frac{1}{2} m_Z (1 - \frac{m_A^2 - m_h^2}{m_Z^2}). \tag{5.9}$$

For any (m_h,m_A) pair of mass values, the measured momenta of the two τ's multiplied by a factor $E_h/E_{\tau\tau}$ are used to calculate of the τ-pair invariant mass. The resulting mass distribution is compared to the background prediction and to the simulated signal for the (m_h,m_A) mass point under investigation. In Figure 5.12 this comparison is shown for $Z^0 \to h^0A^0$ events with $m_h = m_A = 22$ GeV. Events are kept if the τ-pair invariant mass, $m_{\tau\tau}$, is in the range $(m_h \pm \Delta m_h)$ with:

$$\begin{aligned} \Delta m_h &= 3 + 0.10 \times (m_h - 12) \quad \text{for} \quad m_h \geq 12 \text{ GeV}, \\ \Delta m_h &= 1 + 0.25 \times (m_h - 4) \quad \text{for} \quad m_h < 12 \text{ GeV}. \end{aligned} \tag{5.10}$$

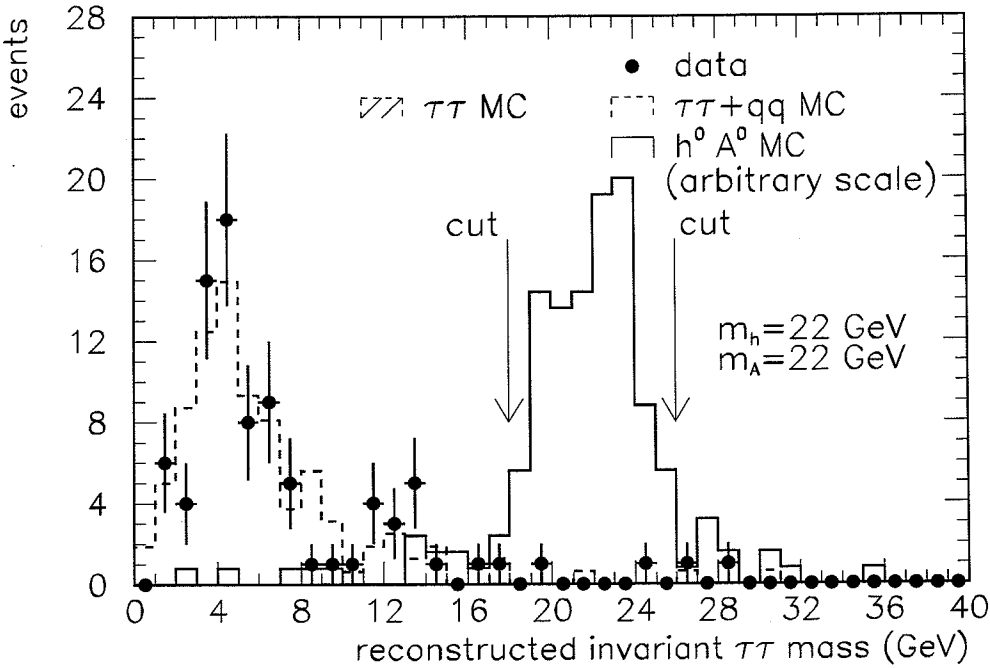

Figure 5.12: Distribution of the reconstructed invariant mass of $\tau^+\tau^-$ pairs for data, background and simulated Higgs boson signal in the $\tau\tau$bb channel.

In Table 5.8 all $\tau\tau$bb selection cuts and their effects on the data, the background and the simulated signal for $m_h = m_A = 22$ GeV and $m_h = m_A = 20$ GeV,

both for the 1991 and the 1990 detector configurations, are presented. For the Monte Carlo signal, 1500 and 1300 events were fully simulated in the 1991 and 1990 detector configurations, respectively. The 1991 data, $Z^0 \to q\bar{q}$ and $Z^0 \to \tau^+\tau^-$ simulated events correspond to 296k, 444k and 410k hadronic Z^0 decays, respectively. The 1990 data, $Z^0 \to q\bar{q}$ and $Z^0 \to \tau^+\tau^-$ simulated events correspond to 116k, 165k and 410k hadronic Z^0 decays, respectively. The $Z^0 \to q\bar{q}$ contribution is normalized to the data after preselection, taking the predicted $Z^0 \to \tau^+\tau^-$ contribution into account. All distributions of important cut quantities are shown in appendix C.

$\tau\tau$bb Channel				
Selection cuts	Signal Acc. (%)	$Z^0 \to q\bar{q}$ Events	$Z^0 \to \tau^+\tau^-$ Events	Data Events
	1991			
m_h=m_A=22 GeV				296K
Preselection	65.7	29379	2013	31392
$N_{cl} \geq 15$	65.7	29370	129	29326
$N_J \geq 2$	63.1	21506	43	21485
0.5 GeV $\leq E_\tau \leq$ 30 GeV	55.5	18504	30	18113
$N\tau$ =2	26.8	2861	17	2841
N_{tr} =2	12.6	137	1.4	146
N_q =0	10.7	84	1	87
18 GeV $\leq m_{\tau\tau} \leq$ 26 GeV	8.5	1.2	0	2
	1990			
m_h=m_A=20 GeV				116K
Preselection	72.1	15543	781	16324
$N_{cl} \geq 15$	72.1	15539	50	15551
$N_J \geq 2$	69.8	11400	17	11442
0.5 GeV $\leq E_\tau \leq$ 30 GeV	62.5	9607	12	9448
$N\tau$ =2	34.6	1259	7	1428
N_{tr} =2	13.5	86	0.3	101
N_q =0	10.8	46	0	67
16.2 GeV $\leq m_{\tau\tau} \leq$ 23.8 GeV	8.1	2	0	3

Table 5.8: Cuts, acceptances and corresponding numbers of data and background events for the different steps of the selection in the $\tau\tau$bb channel for m_h=m_A=22 GeV and for m_h=m_A=20 GeV for the 1991 and 1990 detector configurations, respectively. Details of the preselection are given in the text.

5.3.3 Results of the Search in the $\tau\tau$bb Channel

The $Z^0 \to h^0 A^0 \to \tau^+\tau^- b\bar{b}$ acceptances for several combinations of h^0 and A^0 masses compared to data and background are given in Table 5.9 for the 1991 and 1990 detector configurations.

$\tau\tau$bb Channel			
Masses (GeV) m_h, m_A	Signal Acceptance (%)	$Z^0 \to q\bar{q}, \tau^+\tau^-$ Events	Data Events
	1991		
4, 12	2.0	30	33
4, 22	2.9	31	33
4, 32	1.7	30	32
12, 12	6.2	12	15
12, 22	8.8	11	14
12, 32	5.3	8.8	14
12, 42	1.9	9.4	15
22, 22	8.5	1.2	2
22, 32	5.8	2.0	3
22, 42	1.0	2.0	3
	1990		
4, 11	2.1	14	12
11, 11	6.6	8	16
11, 25	6.3	7	15
20, 20	8.1	2	3
20, 25	5.8	2	2
30, 30	4.1	0	0

Table 5.9: Acceptances and numbers of data and background events after all cuts for various Higgs boson masses with $m_h \leq 30$ GeV in the $\tau\tau$bb channel

In the mass region for $m_h > 30$ GeV, we use the analysis developed for the Minimal Standard Model Higgs boson search [89] in the $h^0\tau^+\tau^-$ channel; this analysis was optimized for a Higgs of 55 GeV. The efficiencies resulting from this analysis are presented in Table 5.10 for a series of mass points. No data events pass the $\tau\tau$bb selection.

The predictions for the signal and the backgrounds are affected by a systematic uncertainty of 0.5% on the number of Z^0 hadronic decays used in the normalization and by a systematic uncertainty on the modeling of the detector response.

$\tau\tau$bb Channel	
Masses (GeV) m_h, m_A	Signal Acceptance (%)
32, 32	11.3
42, 12	20.0
42, 22	19.9
42, 42	11.0
52, 12	26.5
52, 22	21.6
52, 32	16.4
62, 12	23.2
62, 22	15.3

Table 5.10: Acceptances for various Higgs boson masses with $m_h > 30$ GeV in the $\tau\tau$bb channel. The selection for the search for Higgs boson bremsstrahlung in the $h^0\tau^+\tau^-$ channel is applied. No data event survives this selection.

The latter is estimated by varying the cuts over amounts equal to the error on the measured quantity. The main systematic errors affecting the predicted signal acceptances are listed in Table 5.11. For the available signal Monte Carlo samples, the statistical error lies between 10% and 30% depending on the signal acceptances. The resulting total uncertainty is used to reduce the signal efficiency in order to obtain a 95% CL limits on the $Z^0 \to h^0A^0 \to \tau^+\tau^-b\bar{b}$ branching ratio as function of the (m_h,m_A) masses.

The agreement between the measured distributions and those of known physics processes shows that there is no evidence in our data for the decay $Z^0 \to h^0A^0 \to \tau^+\tau^-b\bar{b}$. Thus upper limits for the branching ratio

$$\frac{\Gamma(Z^0 \to h^0A^0 \to \tau^+\tau^-b\bar{b})}{\Gamma(Z^0 \to q\bar{q})} \tag{5.11}$$

can be derived as function of m_h and m_A. Figure 5.13 shows the regions in the (m_h,m_A) plane excluded at 95% CL for values of the branching ratio larger or equal to 2×10^{-3}, 5×10^{-5} and 2×10^{-4}, respectively. The analysis described above has been performed for $h^0 \to \tau^+\tau^-$ and $A^0 \to b\bar{b}$. In the region $m_h > 30$ GeV the search for Higgs boson bremsstrahlung in the $h^0\tau^+\tau^-$ channel [89] is used.

$\tau\tau$bb Channel		
Selection Cuts m_h=m_A=22 GeV	Variation	Acceptance Reduction (%)
Preselection	–	< 3
$N_{cl} \geq 15$	1	< 1
$N_J \geq 2$	5%	5.0
$0.5 \leq E_\tau \leq 30$ GeV	11%	2.0
$N_\tau = 2$	5%	5.0
$N_{tr} = 2$	$< 3\%$	3.0
$N_q = 0$	$< 3\%$	3.0
18 GeV $\leq m_{\tau\tau} \leq 26$ GeV	$\sigma \pm 30\%$	9.7
TOTAL		13.0

Table 5.11: Reduction of expected Higgs boson acceptance in the $\tau\tau$bb channel due to modeling of the detector response for each quantity used in the analysis. For continuous quantities the variation is taken as one standard deviation on the measured quantity and for discrete quantities as one standard deviation on the normalization of the event rate. The reductions are summed in quadrature.

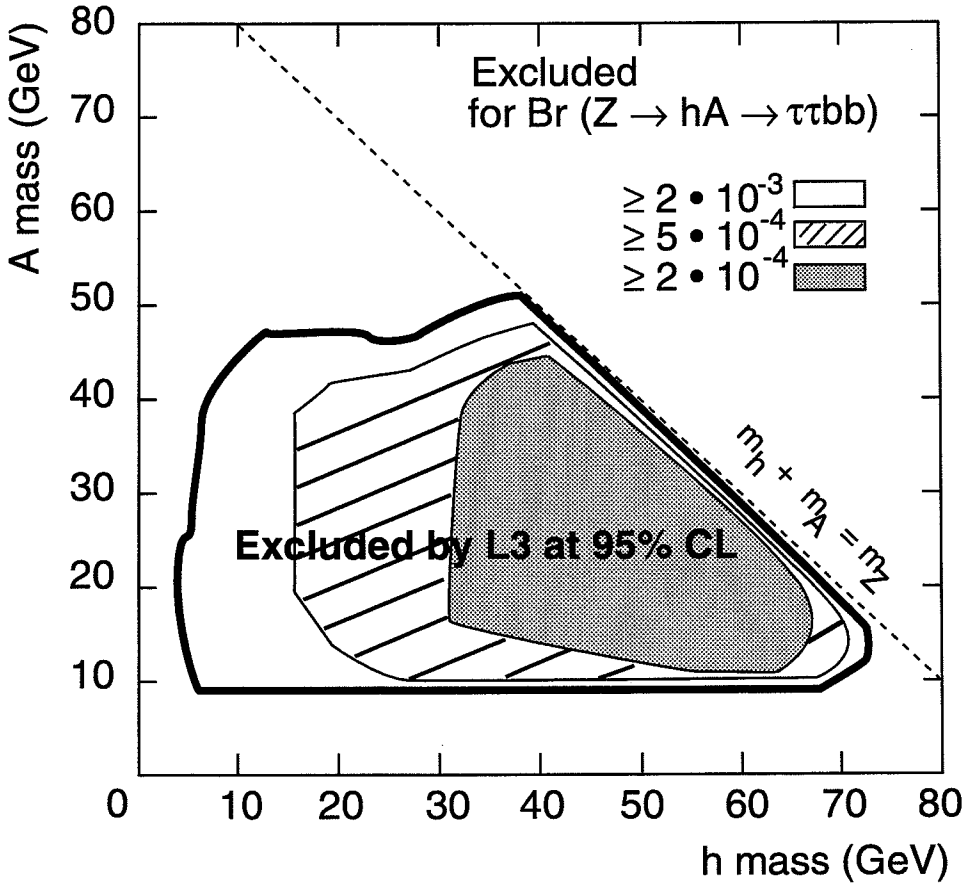

Figure 5.13: Regions of the (m_h,m_A) plane excluded at 95% CL for values of the branching ratio $\Gamma(Z^0 \to h^0A^0 \to \tau^+\tau^-b\bar{b})/\Gamma(Z^0 \to q\bar{q}) \geq 2 \times 10^{-4}$ (dark region), $\geq 5 \times 10^{-4}$ (hatched region) and $\geq 2 \times 10^{-3}$ (region inside heavy contour line). The analysis has been performed for $h^0 \to \tau^+\tau^-$ and $A^0 \to b\bar{b}$. The same efficiencies are obtained if h^0 and A^0 are interchanged, i.e. $h^0 \to b\bar{b}$, $A^0 \to \tau^+\tau^-$.

5.4 The Search in the $Z^0 \to h^0A^0 \to \tau^+\tau^-\tau^+\tau^-$ Channel

A simulated Higgs boson event in this channel is shown in Figure 5.14. The signature of a $Z^0 \to h^0A^0 \to \tau^+\tau^-\tau^+\tau^-$ event consists of 4 low-mass jets associated with a low number of charged tracks. Requiring small calorimetric activity in the event strongly reduces the $Z^0 \to q\bar{q}$ background. The additional requirement that there is one isolated pair of narrow jets associated with two tracks of opposite charge, reduces the background from $Z^0 \to \tau^+\tau^-$ decays. In fact, in such events a τ-jet can be split into two narrow jets, but the number of tracks associated with the jet pair is mostly 1 or 3 (the case of 2 tracks arises only as a result of detector inefficiencies). In the case of a real τ-pair the number of associated tracks is mostly 2. In the present search, again we adopt the method of dividing the event into two hemispheres, in order to select events with two well-separated pairs of jets. The hemisphere with the lower number of clusters (hereafter referred to as the low-multiplicity hemisphere) should contain the $\tau^+\tau^-$ pair with the smaller track multiplicity.

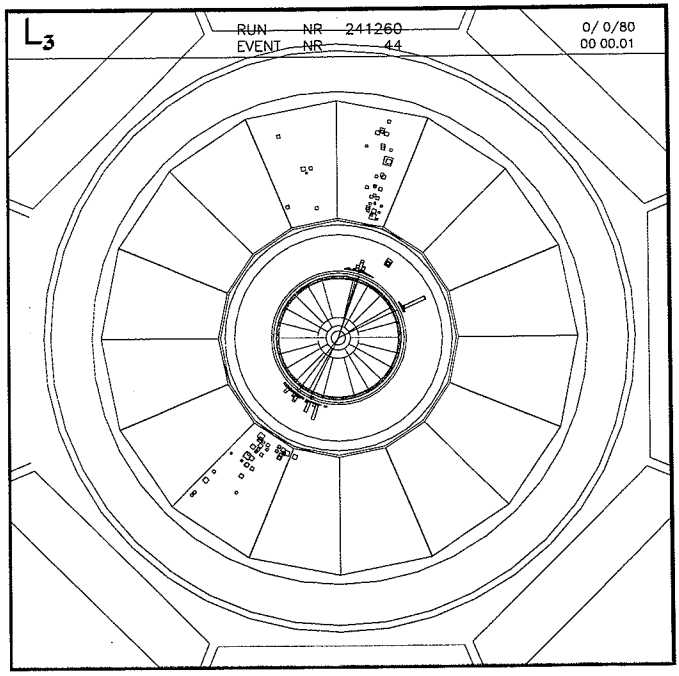

Figure 5.14: Simulated $Z^0 \to h^0A^0 \to \tau^+\tau^-\tau^+\tau^-$ event after full detector simulation and reconstruction, shown in the plane perpendicular to the beam axis.

5.4.1 Selection Details

The events have to pass the same preselection as for $\tau\tau$bb channel. Events with low calorimetric cluster multiplicity are selected in order to remove $Z^0 \to q\bar{q}$ background by requiring:

- $7 \leq N_{cl} \leq 20$.

At this stage of the selection, the data sample is dominated by low cluster multiplicity events ($Z^0 \to e^+e^-$, $\mu^+\mu^-$, $\tau^+\tau^-$). The acceptance for the simulated $Z^0 \to h^0A^0 \to \tau^+\tau^-\tau^+\tau^-$ events after these cuts is about 55%.

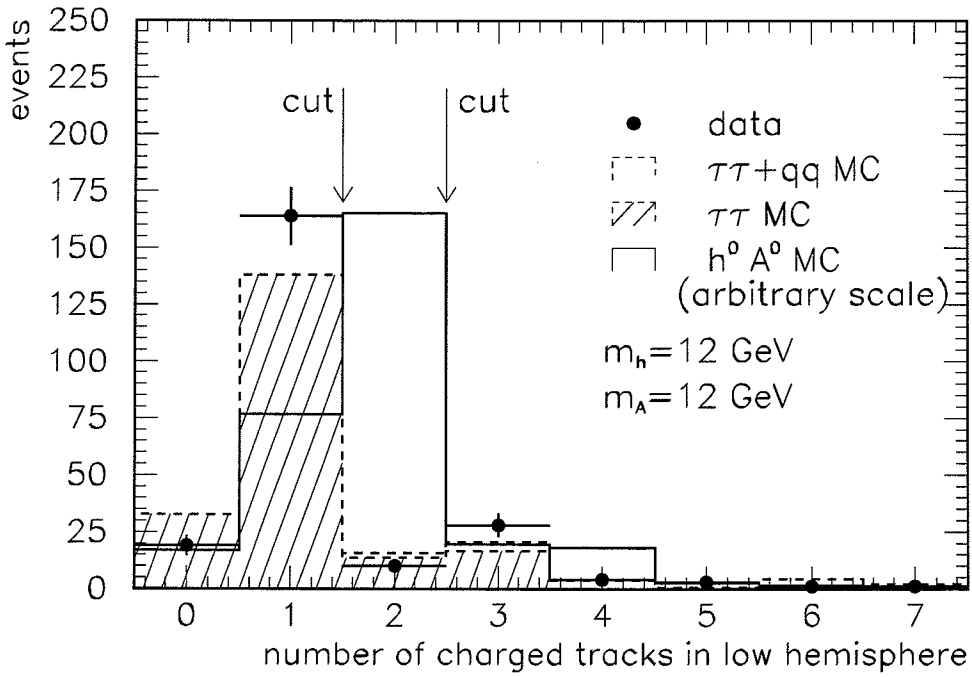

Figure 5.15: Distribution of the number of charged tracks in the low-multiplicity hemisphere for data, simulated background and Higgs boson signal in the $\tau\tau\tau\tau$ channel.

Events with 4 or 5 narrow jets and a two-prong final state for the τ-pair are selected by requiring:

- $N_\tau^l = 2$ and $N_\tau^h = 2$ or 3, where N_τ^l and N_τ^h refer to the number of narrow jets with 0.5 GeV $\leq E_\tau \leq$ 30 GeV in the low-multiplicity hemisphere and in the

high hemisphere respectively,

- $N_{tr} = 2$, where N_{tr} is the number of tracks in the low-multiplicity hemisphere. The distribution of the number of charged tracks in the low hemisphere after the previous cuts is shown in Figure 5.15.

- $N_q = 0$, where N_q is the total charge in the low-multiplicity hemisphere.

In Table 5.12 the $\tau\tau\tau\tau$ selection cuts and their effects on the data, the background and the simulated signal for $m_h = m_A = 12$ GeV and $m_h = m_A = 11$ GeV are presented for the 1991 and the 1990 detector configurations, respectively. All distributions of important cut quantities are shown in appendix D.

$\tau\tau\tau\tau$ Channel				
Selection cuts	Signal Acceptance (%)	$Z^0 \to q\bar{q}$ Events	$Z^0 \to \tau^+\tau^-$ Events	Data Events
	1991			
$m_h = m_A = 12$ GeV				296K
Preselection	55.1	29391	2005	31392
$7 \leq N_{cl} \leq 20$	51.4	182	1989	2455
0.5 GeV $\leq E_\tau \leq$ 30 GeV	31.1	49	470	628
$N_\tau^l = 2$ and N_τ^h=2 or 3	15.4	17	200	230
$N_{tr} = 2$	8.4	1.9	10	10
$N_q = 0$	8.0	1.2	7.2	7
	1990			
$m_h = m_A = 11$ GeV				116K
Preselection	42.7	15526	788	16324
$7 \leq N_{cl} \leq 20$	37.4	97	782	994
0.5 GeV $\leq E_\tau \leq$ 30 GeV	23.3	19	185	237
$N_\tau^l = 2$ and N_τ^h=2 or 3	12.6	5.3	79	96
$N_{tr} = 2$	7.1	0.7	5.4	7
$N_q = 0$	6.5	0.7	4.0	4

Table 5.12: Cuts, acceptances and corresponding numbers of data and background events for the different steps of the selection in the $\tau\tau\tau\tau$ channel] for $m_h = m_A = 12$ GeV and for $m_h = m_A = 11$ GeV for the 1991 and 1990 detector configurations, respectively. The details of the preselection are given in the text.

5.4.2 Results of the Search in the $\tau\tau\tau\tau$ Channel

The signal acceptances are given in Table 5.13. In the 1991 data sample 7 events survive the $\tau\tau\tau\tau$ selection and 8.4 are predicted from background processes. In the 1990 data sample 4 events are selected and 4.7 predicted as background. For the Monte Carlo signal, 1500 and 1300 events are fully simulated in the 1991 and the 1990 detector configuration, respectively.

$\tau\tau\tau\tau$ Channel	
Masses (GeV) m_h, m_A	Signal Acceptance (%)
1991	
4, 4	8.0
4, 12	8.3
4, 32	6.3
4, 42	4.5
4, 52	1.9
12, 12	8.0
12, 22	7.5
12, 32	7.0
12, 42	3.7
12, 52	1.9
22, 22	6.3
22, 42	2.5
32, 42	3.2
42, 42	4.9
1990	
4, 4	7.2
4, 11	6.9
11, 11	6.5

Table 5.13: Acceptances after all cuts for various Higgs boson masses in the $\tau\tau\tau\tau$ channel. No data event survives this selection.

The systematic errors affecting the predicted signal acceptances for the $\tau\tau\tau\tau$ channel are given in Table 5.14. Statistical errors on the signal predictions vary between 9% and 18%, depending on the (m_h,m_A) mass point, are taken into account.

The comparison between the data and the predictions for background shows no evidence for signal from $Z^0 \rightarrow h^0A^0 \rightarrow \tau^+\tau^-\tau^+\tau^-$ decay. Thus limits on the

$\tau\tau\tau\tau$ Channel		
Selection Cuts m_H=40 GeV	Variation	Acceptance Reduction (%)
Preselection	–	< 3
$N_{cl} \leq 15$	1	9
$0.5 \leq E_\tau \leq 30$ GeV	+0.5 GeV, −2 GeV	11
$N_\tau^l = 2$ $N_\tau^h = 2$ or 3	10%	10
$N_{tr} = 2$	< 3%	3
$N_q = 0$	< 3%	3
TOTAL		19

Table 5.14: Reduction of expected Higgs boson acceptance in the $\tau\tau\tau\tau$ channel due to modeling of the detector response for each quantity used in the analysis. For continuous quantities the variation is taken as one standard deviation on the measured quantity and for discrete quantities as one standard deviation on the normalization of the event rate. The reductions are summed in quadrature.

branching ratio

$$\frac{\Gamma(Z^0 \to h^0 A^0 \to \tau^+\tau^-\tau^+\tau^-)}{\Gamma(Z^0 \to q\bar{q})} \tag{5.12}$$

can be set as function of the h^0 and A^0 masses. Figure 5.16 shows the regions in the (m_h,m_A) plane excluded at 95% CL for values of the branching ratio larger or equal to 2×10^{-3}, 1×10^{-3} and 5×10^{-4}, respectively.

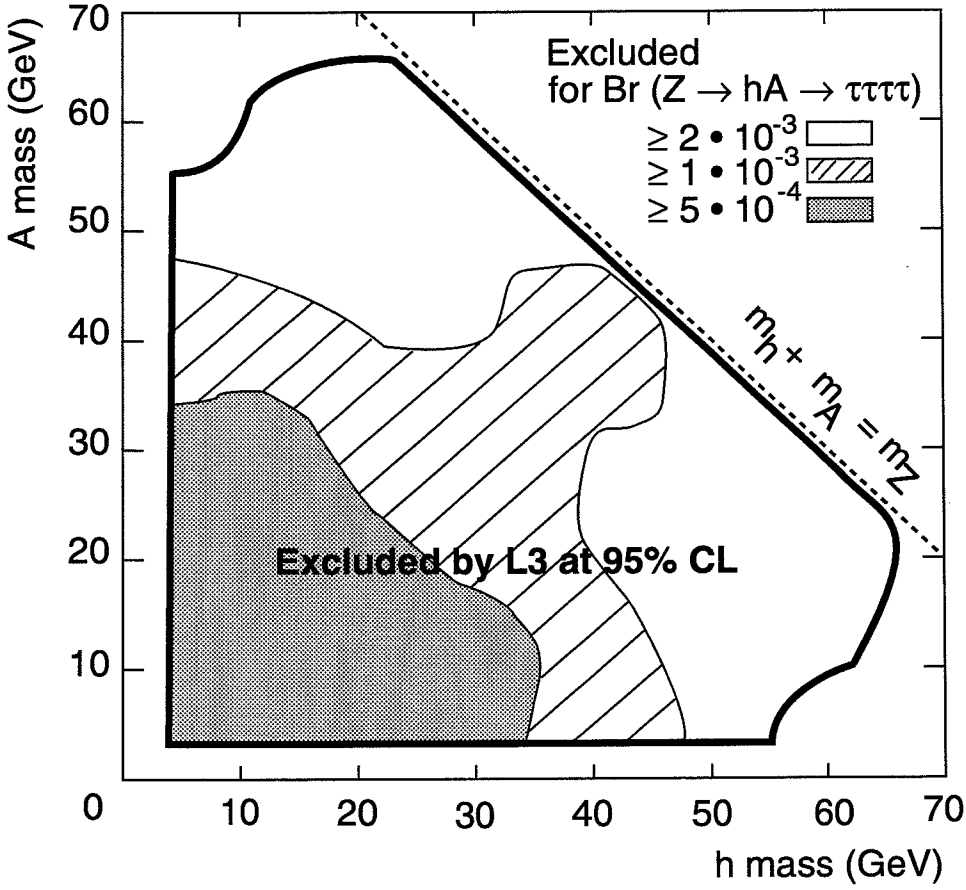

Figure 5.16: Regions of the (m_h,m_A) plane excluded at 95% CL for values of the branching ratio $\Gamma(Z^0 \to h^0A^0 \to \tau^+\tau^-\tau^+\tau^-)/\Gamma(Z^0 \to q\bar{q}) \geq 5 \times 10^{-4}$ (dark region), $\geq 1 \times 10^{-3}$ (hatched region) and $\geq 2 \times 10^{-3}$ (region inside heavy contour line).

Chapter 6

Searches for Charged Higgs Boson Pair-Production

Three signatures from charged Higgs boson pair-production in the channels cscs, cs$\tau\nu$ and $\tau\nu\tau\nu$ are searched for. A mass range between 20 GeV and the kinematic production threshold has been investigated. The mass region below 20 GeV had been excluded before the operation of the LEP accelerator [92].

6.1 The Search in the $Z^0 \rightarrow H^+H^- \rightarrow c\bar{s}\bar{c}s$ Channel

A simulated Higgs boson event in this channel is shown in Figure 6.1. The search for the $Z^0 \rightarrow H^+H^- \rightarrow c\bar{s}\bar{c}s$ process is made in the hadronic event sample. In order to improve the jet energy resolution, the total event energy is rescaled to the known LEP center-of-mass energy. Events with 4 and 5 jets (y_{cut}= 0.02) are selected. The 5 jet events are transformed into 4-jet events by combining the two jets with the minimum invariant mass. Since Higgs boson events are expected to be more spherical than standard Z^0 decays, the cut $T < 0.95$ is applied.

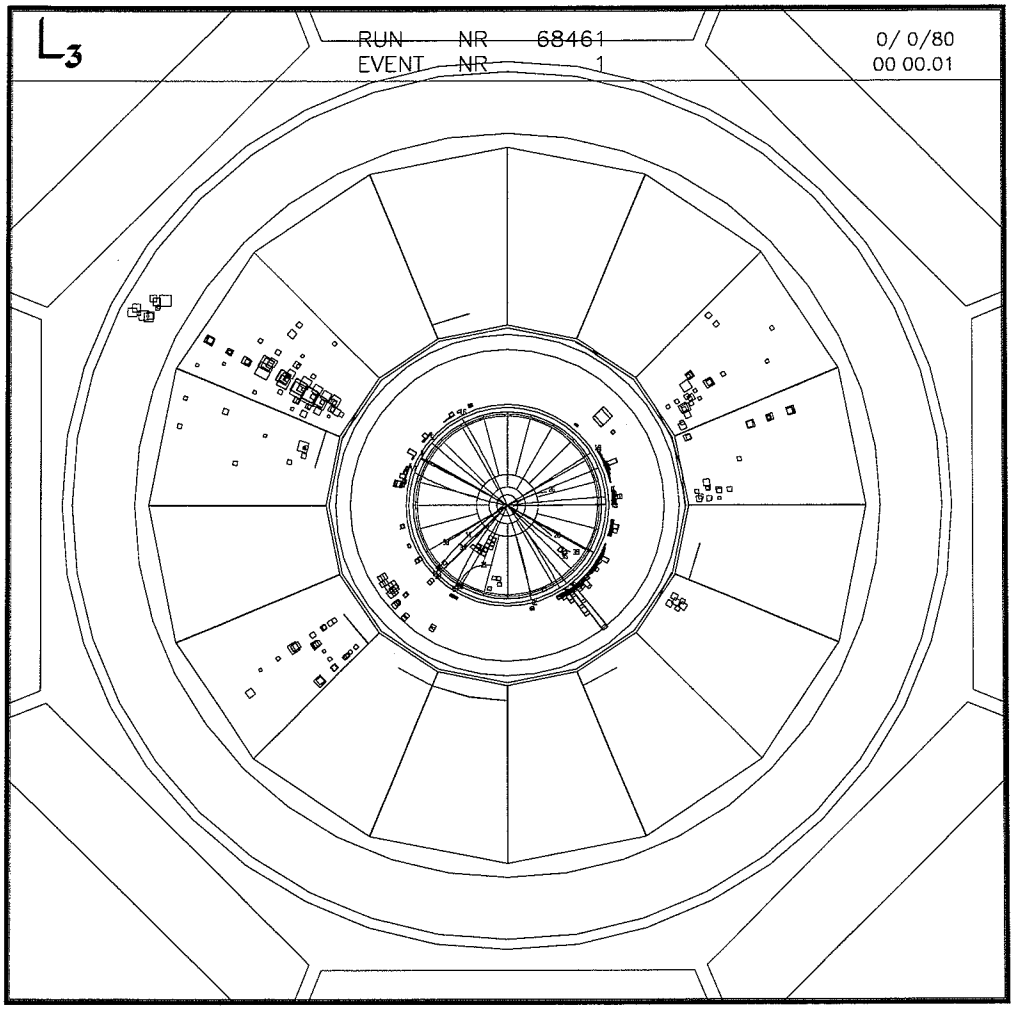

Figure 6.1: Simulated $Z^0 \rightarrow H^+H^- \rightarrow c\bar{s}\bar{c}s$ event after full detector simulation and reconstruction, shown in the plane perpendicular to the beam axis.

6.1.1 Selection Details

Cuts on the following variables are applied to search for the expected charged Higgs bosons. As an example the cuts and resolutions are given for a 40 GeV simulated Higgs boson signal:

- $\Delta m_{rec} = \mid m_{H^+}^{rec} - m_{H^-}^{rec} \mid$, where $m_{H^\pm}^{rec}$ are the reconstructed Higgs boson masses. The four jets can be combined into 2-jet pairs in three possible ways. In order

to select the combination most likely to come from charged Higgs boson production and decay, use is made of the fact that $m_{H^+} = m_{H^-}$. The combination with minimum Δm_{rec} is chosen and events with $\Delta m_{rec} \geq 6$ GeV are rejected.

- $|\cos\theta_p| \leq 0.5$ and $|\cos\theta_d| \leq 0.7$ are required and in order to exploit the back-to-back production of Higgs bosons it is required that $\Delta\cos\theta p \equiv |\cos\theta_p(H^+) + \cos\theta_p(H^-)| \leq 0.3$. The production angle and the decay angle distributions for data, $Z^0 \to q\bar{q}$ background and expected Higgs boson signal are shown in Figures 6.2 and 6.3, respectively. As expected, the signal θ_p distribution exhibits a clear $\sin^2\theta_p$ behavior and the $\cos\theta_d$ distribution is flat, whereas the data and $Z^0 \to q\bar{q}$ background distributions are peaked at large values in both variables.

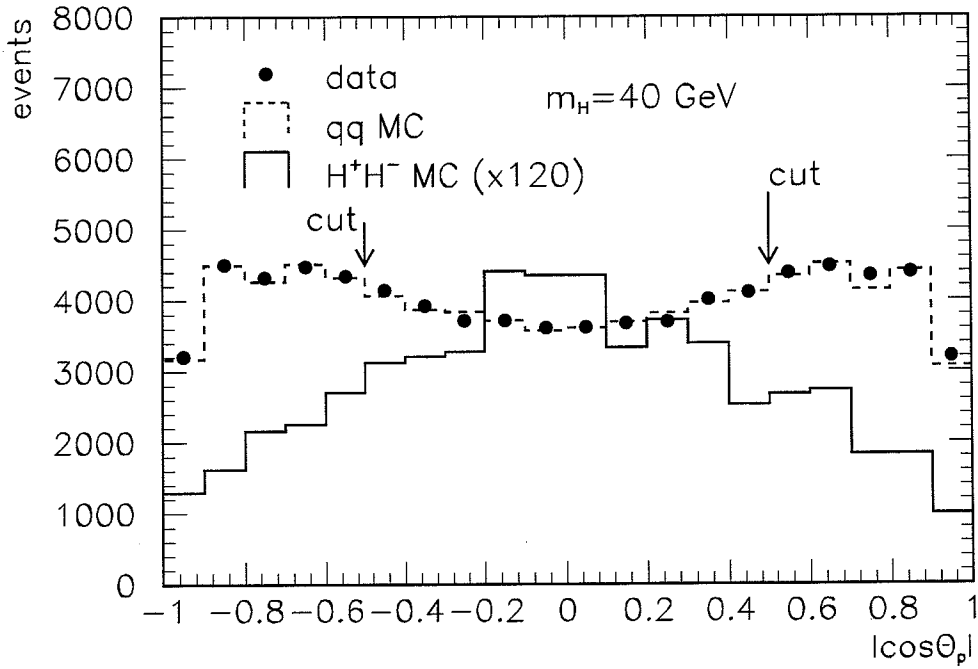

Figure 6.2: Distribution of the production angle for data, simulated background and Higgs boson signal in the cscs channel.

- $\psi_{pl} \geq 0.7$ rad is required, where ψ_{pl} is the angle between the $H^+ \to c\bar{s}$ decay plane and the $H^- \to \bar{c}s$ decay plane. For the signal the ψ_{pl} distribution is

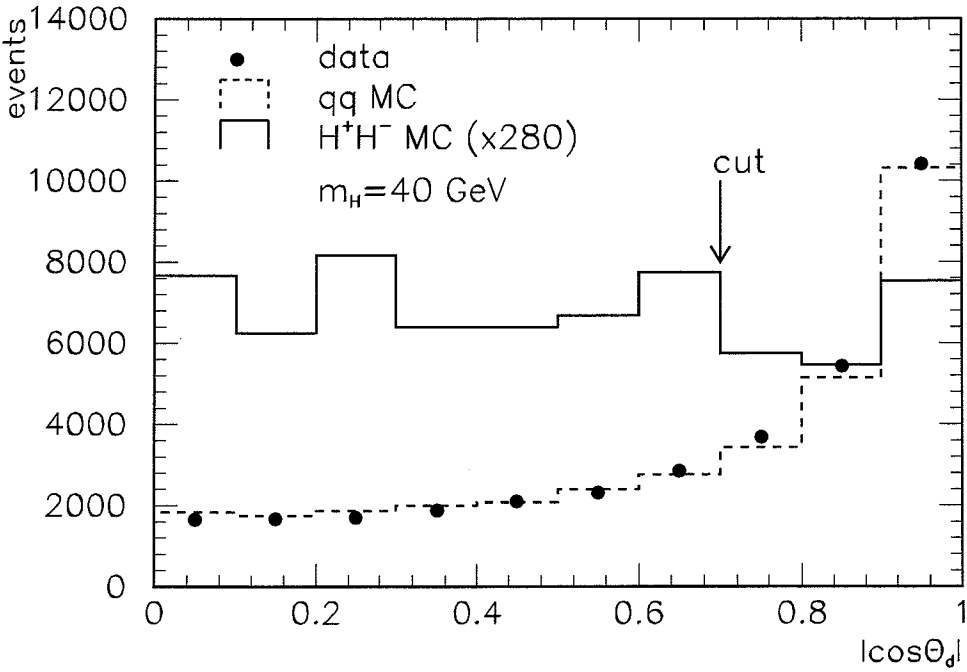

Figure 6.3: Distribution of the decay angle for data, simulated background and Higgs boson signal in the cscs channel.

expected to be flat whereas for the QCD background it is more peaked at small angles.

- Three mass-dependent cuts are applied on the variables $\sum M_{jet}^{rec}$, $E_{jet}^{max}/\sqrt{s}$ and $E_{jet}^{min}/\sqrt{s}$, where $\sum M_{jet}^{rec}$ is the sum of the jet masses, $E_{jet}^{max}/\sqrt{s}$, $E_{jet}^{min}/\sqrt{s}$ are the fractions of energies carried by the highest and lowest energy jets, respectively. In order to optimize the above cuts and determine the signal selection efficiency, 1600 signal events for $m_H = 20$, 30 and 40 GeV have been studied. The values of mass-dependent cuts are given in Table 6.1.

- To reduce the $Z \rightarrow b\bar{b}$ background, events with inclusive leptons (e or μ) as defined in the bbbb analysis, are rejected.

The percentages of surviving events with average reconstructed Higgs boson mass $m_H = 0.5 \times (m_{H^+}^{rec} + m_{H^-}^{rec})$ within 1 GeV of the generated Higgs boson mass are 3.8, 3.5 and 2.8% for $m_H = 20$, 30 and 40 GeV, respectively. The m_H distribution

cscs Channel			
Higgs mass (GeV)	20	30	40
$\sum M_{jet}^{rec}$ / GeV $\leq$	22	28	30
$E_{jet}^{max}/\sqrt{s} \leq$	0.39	0.38	0.34
$E_{jet}^{min}/\sqrt{s} \geq$	0.10	0.12	0.14

Table 6.1: Values of Higgs boson mass-dependent cuts applied in the cscs channel.

for the 40 GeV Higgs boson signal is shown in Figure 6.4. A mass resolution of 0.8 GeV is obtained, using the fact that both Higgs bosons must have the same mass and that the total visible energy must be the center-of-mass energy.

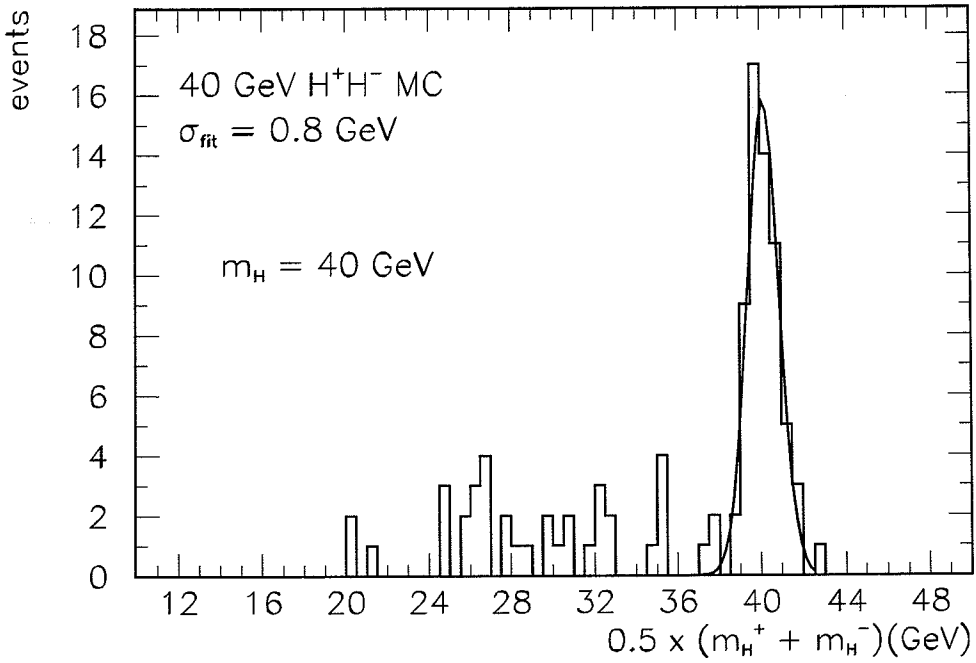

Figure 6.4: Expected mass resolution for a 40 GeV charged Higgs boson signal in the cscs channel.

Linearly interpolating the mass-dependent cuts, the number of surviving events in the data and $Z^0 \rightarrow q\bar{q}$ background are determined in the range $m_H = 20$ to 43 GeV at 0.5 GeV intervals. The distribution of the average reconstructed Higgs

boson mass, $0.5 \times (m_{H^+}^{rec} + m_{H^-}^{rec})$, is shown in Figure 6.5 together with the events expected from 40 GeV charged Higgs boson production after taking into account the selection efficiency (2.8%) at this mass value. The distributions of data and $Z^0 \rightarrow q\bar{q}$ background are in good agreement and the number of surviving events in a 1 GeV bin is about 10 over the entire mass range. In Table 6.2 the cscs selection cuts and their effects on data, background and signal for 40 GeV charged Higgs bosons are listed for the 1991 and 1990 detector configurations. All distributions of important cut quantities are shown in appendix E.

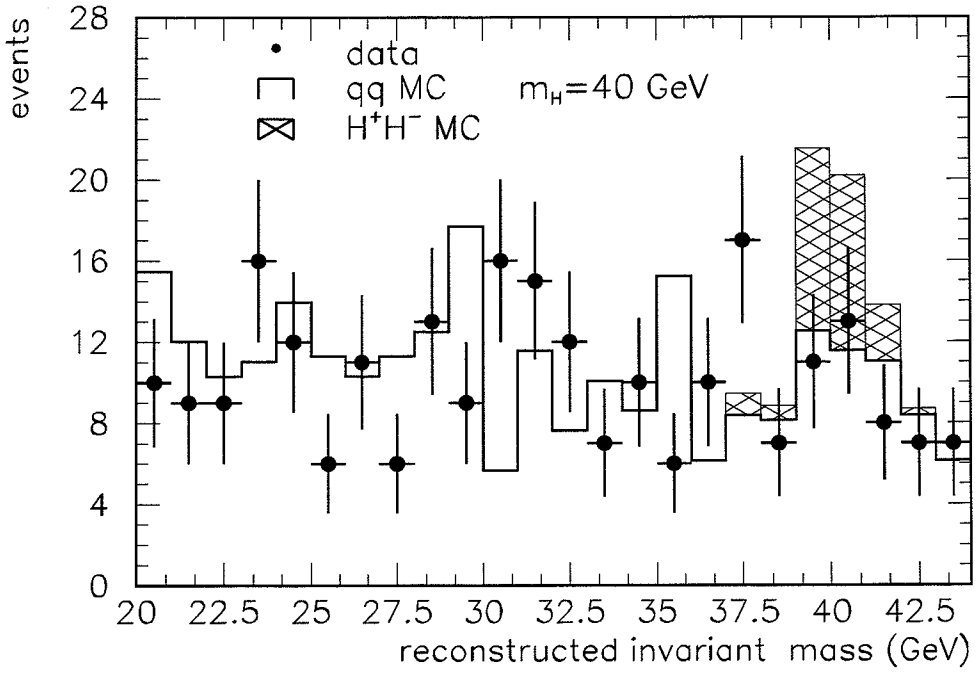

Figure 6.5: Reconstructed invariant mass of data, simulated background and Higgs boson signal in the cscs channel.

6.1.2 Results of the Search in the cscs Channel

The signal acceptances and a comparison between data and expected background events are given in Table 6.3. No signal has been found. The systematic errors and their effects on the predicted signal acceptances for the cscs channel are given in Table 6.4. A 33% error, including 12% statistical error, on the number

of expected events is taken into account in the evaluation of the excluded region. Figure 8.4 shows the excluded mass region as a function of the leptonic branching fraction and the charged Higgs boson mass.

cscs Channel			
Selection Cuts	Signal Acc.(%)	$Z^0 \rightarrow q\bar{q}$ Events	Data Events
	1991		
$m_H = 40$ GeV			296 k
Preselection	85.8	59569	59569
$\Delta m_{rec} \leq 6$ GeV	48.6	22152	29075
$\lvert\cos\theta_p\rvert \leq 0.5$	25.3	12790	12327
$\lvert\cos\theta_d\rvert \leq 0.7$	13.0	1608	1510
$\psi_{pl} \geq 0.7$ rad	8.2	742	790
$\sum M_{jet}^{rec} \leq 30$ GeV	6.0	575	554
$0.14 \leq E_{jet} \leq 0.34$	6.0	255	227
incl. lepton rejection	4.5	254	223
39 GeV $\leq m_H \leq$ 41 GeV	2.8	18	19
	1990		
$m_H = 40$ GeV			116k
Preselection	82.2	24947	24947
$\Delta m_{rec} \leq 6$ GeV	53.7	12283	12329
$\lvert\cos\theta_p\rvert \leq 0.5$	27.2	5239	5145
$\lvert\cos\theta_d\rvert \leq 0.7$	13.5	628	584
$\psi_{pl} \geq 0.7$ rad	8.7	301	295
$\sum M_{jet}^{rec} \leq 30$ GeV	8.7	215	198
$0.14 \leq E_{jet} \leq 0.34$	7.3	86	84
incl. lepton rejection	7.3	83	83
39 GeV $\leq m_H \leq$ 41 GeV	2.7	6	7

Table 6.2: Cuts, acceptances and corresponding numbers of data and background events for the different steps of the selection in the cscs channel for $m_H = 40$ GeV. Details of the preselection are described in the text.

cscs Channel						
m_H (GeV)	Signal Acc.(%)	$Z^0 \to q\bar{q}$ Events	Data Events	Signal Acc.(%)	$Z^0 \to q\bar{q}$ Events	Data Events
	1990			1991		
20	4.2	6	5	3.8	18	19
30	4.2	5	9	2.9	18	16
40	2.7	6	7	2.8	18	19

Table 6.3: Acceptances and numbers of data and background events after all cuts for various Higgs boson masses in the cscs channel.

cscs Channel		
Selection Cuts $m_H = 40$ GeV	Variation	Acceptance Reduction (%)
Preselection	–	< 3
$N_J = 4$ or 5	20%	20
$\Delta m_{rec} \leq 6$ GeV	0.5 GeV	5
$\lvert\cos\theta_p\rvert \leq 0.5$	0.04	7.2
$\lvert\cos\theta_d\rvert \leq 0.7$	0.04	5.8
$\psi_{pl} \geq 0.7$ rad	0.08	8.0
$\sum M_{jet}^{rec} \leq 30$ GeV	1 GeV	9.4
$E_{jet}^{max}/\sqrt{s} \leq 0.34$	0.01	7.1
$E_{jet}^{min}/\sqrt{s} \geq 0.14$	0.01	6.5
39 GeV $\leq m_H \leq$ 41 GeV	$\sigma \pm 30\%$	16
TOTAL		31

Table 6.4: Reduction of expected Higgs boson acceptance in the cscs channel due to modeling of the detector response for each quantity used in the analysis. For continuous quantities the variation is taken as one standard deviation on the measured quantity and for discrete quantities as one standard deviation on the normalization of the event rate. The reductions are summed in quadrature.

6.2 The Search in the $Z^0 \to H^+H^- \to cs\tau\nu$ Channel

A simulated Higgs boson event in this channel is shown in Figure 6.6. The signature for $Z^0 \to H^+H^- \to cs\tau\nu$ is one isolated tau and missing energy recoiling against a hadronic system. Signal events for different Higgs boson masses between 20 GeV and 44 GeV have been simulated. Background from $Z^0 \to q\bar{q}$ and $Z^0 \to \tau^+\tau^-$ have been studied. The description of the selection cuts and resolutions are given for the search for a 40 GeV Higgs boson signal.

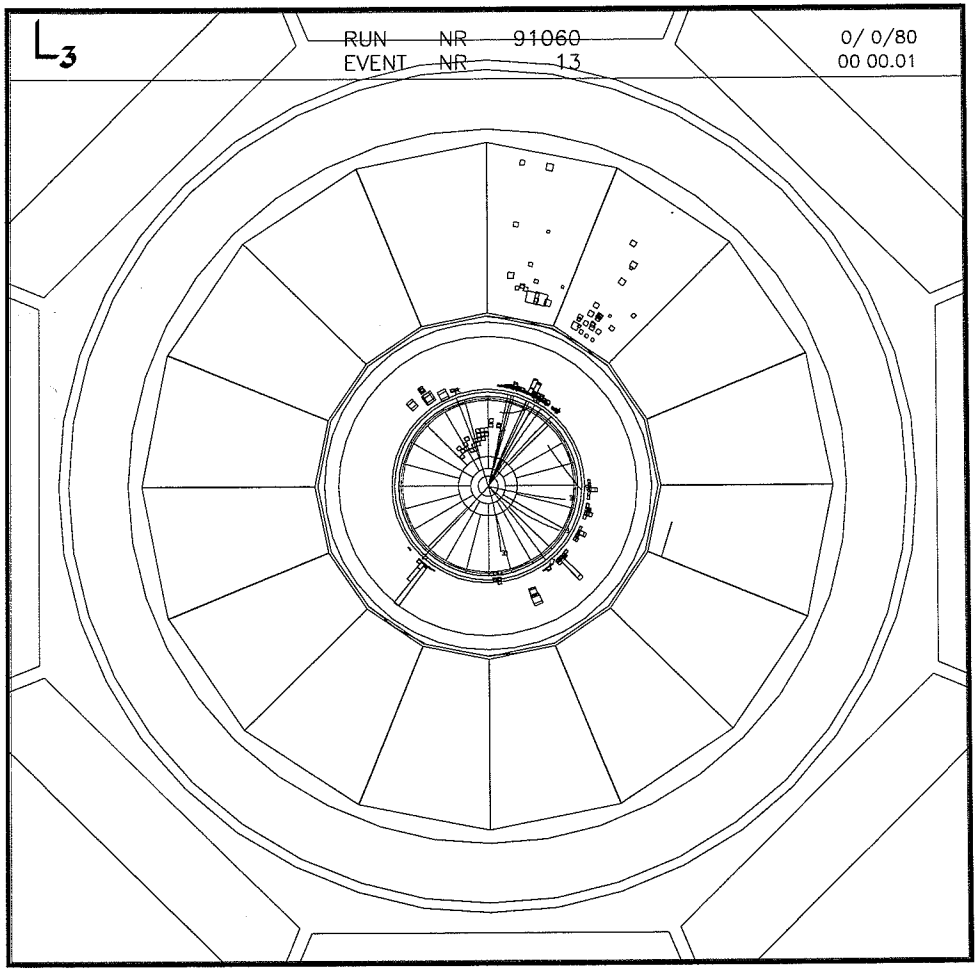

Figure 6.6: Simulated $Z^0 \to H^+H^- \to cs\tau\nu$ event after full detector simulation and reconstruction, shown in the plane perpendicular to the beam axis.

6.2.1 Selection Details

We require large calorimetric cluster multiplicity, $N_{\rm cl} \geq 20$ to remove pure leptonic events. Backgrounds from two-photon and beam-gas events are removed by requiring small longitudinal energy imbalance, $E_{\parallel}/E_v < 0.60$, the thrust axis not pointing along the beam axis, $|\cos\theta_T| < 0.9$ and the total calorimetric energy in a range expected for the signal, $0.4 < E_v/\sqrt{s} < 0.75$. The upper cut removes much of the hadronic background. A cut on the thrust, $T \leq 0.95$, removes 2-jet events. After this preselection, about 4000 events from $Z^0 \rightarrow q\bar{q}$ background survive, keeping an efficiency of about 70% for the signal. The main selection consists of the following cuts:

- $N_{\rm cl} \leq 30 + 0.5 \times m_{\rm H}/{\rm GeV}$. Expected signal events with smaller cluster multiplicity are preferentially selected and the $Z^0 \rightarrow q\bar{q}$ background is reduced by about 50%.

- $M \geq 0.2 + 0.0025 \times (m_{\rm H}/{\rm GeV} - 20)$. The event major, M, is defined as:

$$M = \max_{\vec{n}_{\rm M}} \frac{\sum_i |\vec{p}_i \times \vec{n}_{\rm M}|}{\sum_i |\vec{p}_i|} \tag{6.1}$$

  where the maximum is over all possible orientations of the axis $\vec{n}_{\rm M}$ perpendicular to the thrust axis. Only very spherical events pass this cut. The distribution of M is shown in Figure 6.7.

- One isolated tau in the event is required. Only one-prong tau decays are considered to reduce misidentification of low-multiplicity isolated hadronic jets from $Z^0 \rightarrow q\bar{q}$ background. Tau candidates are defined as isolated tracks with azimuthal angle $|\cos\theta| < 0.8$. We consider an inner cone of half angle 10° around the track and an outer cone of half angle θ_{is}. In the inner cone we require one track. The energy of the isolated tau candidate, E_τ, is the calorimetric energy deposited in this cone. The isolation angle, θ_{is}, is defined as the maximum half angle for which the ratio of energy deposited between the inner and outer cone does not exceed 6%. The distribution of the isolation angle is shown in Figure 6.8. Tau candidates must have $\theta_{is} \geq 40°$ and $2 \leq E_\tau \leq 25$ GeV. The low-energy cut reduces background from fluctuations in fragmentation. Low visible energy is likely for tau candidates in signal events since neutrinos are produced in both the tau production and decay.

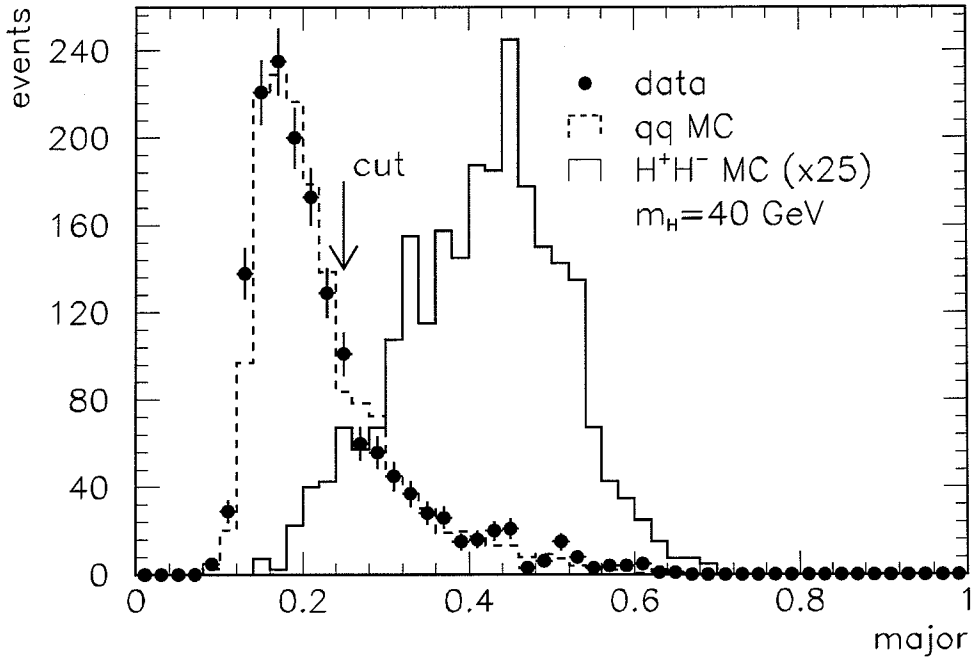

Figure 6.7: Major distribution for data, simulated background and Higgs boson signal in the $cs\tau\nu$ channel.

- $E_\perp/E_v > 0.01 \times (45 - m_{\mathrm{H}}/\mathrm{GeV})$ where $E_\perp$ is the momentum imbalance perpendicular to the thrust axis. The imbalance is due to the neutrinos in the decay products of the charged Higgs boson. For a heavy Higgs boson which decays almost at rest this cut becomes less efficient.

- $0.35 < E_h/\sqrt{s} < 0.60$ is required, where $E_h = E_v - E_\tau$. Then E_h is scaled to the beam energy (as expected for a charged Higgs boson signal) to calculate the invariant mass of the hadronic system. The reconstructed mass distribution is shown in Figure 6.9. An energy resolution of 1.5 GeV is obtained for a 40 GeV Higgs boson signal. The reconstructed mass has to be within 10 GeV of the expected Higgs boson mass for a 20 GeV Higgs boson and the tolerance decreases linearly to 5.2 GeV for a 44 GeV Higgs boson.

For the 1990 detector configuration identical cuts are applied except that the cut on N_{cl} is slightly different:

- $16 \leq N_{\mathrm{cl}} \leq 22 + 0.5 \times m_{\mathrm{H}}/\mathrm{GeV}$.

This change in the selection cut is due to the absence of BGO endcaps in 1990. Only a few data events survive, in agreement with the expected background. The selection efficiency for a 40 GeV Higgs boson is 13%. The cuts and their effects on data, background and signal for a 40 GeV Higgs boson signal are summarized in Table 6.5. All distributions of important cut quantities are shown in appendix F.

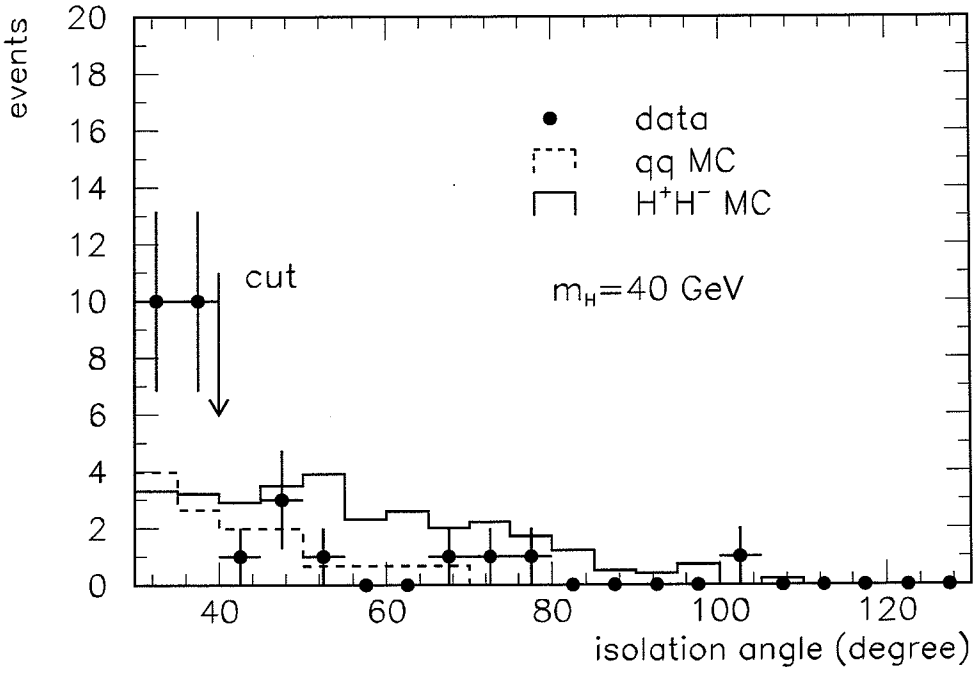

Figure 6.8: Distribution of the isolation angle for tau candidates for data, simulated background and Higgs boson signal in the cs$\tau\nu$ channel.

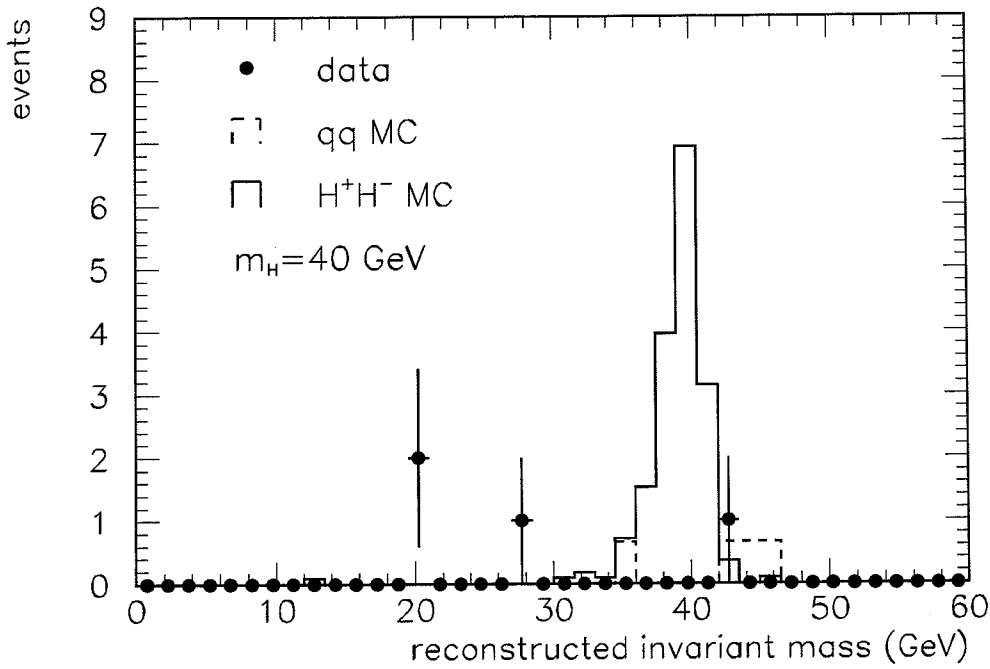

Figure 6.9: Distribution of the reconstructed invariant mass for data, simulated background and Higgs boson signal in the $cs\tau\nu$ channel.

6.2.2 Results of the Search in the $cs\tau\nu$ Channel

The signal acceptances and a comparison between data and expected background events are given in Table 6.6. The four remaining data events in the mass range 20 to 30 GeV are used to calculates constraints on the two-doublet Higgs boson model. The events have been scanned to determine their probable origins, with the conclusion that they are most likely fluctuations of the hadronic background.

In this mass range more than 700 charged Higgs boson events are expected. No indication of a signal has been found. The systematic errors and their effects on the predicted signal acceptances for the $cs\tau\nu$ channel are given in Table 6.7. A 14% error, including 8% statistical error, on the number of expected events is taken into account in the exclusion plot shown in Figure 8.4.

The systematic errors and their effects on the predicted signal acceptances for the $cs\tau\nu$ channel are given in Table 6.7.

$cs\tau\nu$ Channel			
Selection cuts	Signal Acc.(%)	$Z^0 \to q\bar{q}$ Events	Data Events
	1991		
$m_H = 40$ GeV			296k
Preselection	70.8	3843	3765
$N_{cl} \leq 50$	64.4	1574	1605
$M \geq 0.25$	60.5	426	420
1 isolated τ	15.5	6.6	9
$E_\perp > 0.05 \times E_v$	15.3	5.9	8
$0.35 < E_{had}/\sqrt{s} < 0.60$	12.7	2.6	4
34 GeV $< m_{had} <$ 46 GeV	12.5	2.6	1
	1990		
$m_H = 40$ GeV			116k
Preselection	72.5	2276	2559
$N_{cl} \leq 42$	69.3	1014	1115
$M \geq 0.25$	63.0	301	321
1 isolated τ	18.0	5.8	8
$E_\perp > 0.05 \times E_v$	17.8	3.8	6
$0.35 < E_{had}/\sqrt{s} < 0.60$	15.8	1.9	3
34 GeV $< m_{had} <$ 46 GeV	15.3	1.0	1

Table 6.5: Cuts, acceptances and corresponding numbers of data and background events for the different steps of the selection in the $cs\tau\nu$ channel for $m_H = 40$ GeV. The details of the preselection are described in the text.

$cs\tau\nu$ Channel						
m_H (Gev)	Signal Acc. (%)	$Z^0 \to q\bar{q}$ Events	Data Events	Signal Acc. (%)	$Z^0 \to q\bar{q}$ Events	Data Events
	1990			**1991**		
20	14.5%	0.0	1	14.0%	0.0	3
30	17.2%	0.0	1	16.9%	0.0	1
40	15.3%	1.0	1	12.5%	2.6	1
44	—	1.0	1	9.8%	1.4	1

Table 6.6: Acceptances and numbers of data and background events after all cuts for various Higgs boson masses in the $cs\tau\nu$ channel. Owing to the chosen bin size in the last cut, events can be selected at more than one listed mass value. A total of 7 events pass the selection.

$cs\tau\nu$ Channel		
Selection cuts $m_H = 40$ GeV	Variation	Acceptance Reduction (%)
Preselection	–	< 3
$N_{cl} \leq 50$	-1	2
$M \geq 0.25$	$+0.02$	2.8
1 isolated $\tau(40°)$	$3°$	4.6
$E_\perp/E_v > 0.05$	$+0.025$	8.3
$0.35 < E_h/\sqrt{s} < 0.60$	± 0.5 GeV	2.2
32 GeV $\leq m_{had} \leq$ 46 GeV	$\sigma \pm 30\%$	< 1
TOTAL		11

Table 6.7: Reduction of expected Higgs boson acceptance in the $cs\tau\nu$ channel due to modeling of the detector response for each quantity used in the analysis. For continuous quantities the variation is taken as one standard deviation on the measured quantity and for discrete quantities as one standard deviation on the normalization of the event rate. The reductions are summed in quadrature.

6.3 The Search in the $Z^0 \rightarrow H^+H^- \rightarrow \tau^+\nu\tau^-\bar{\nu}$ Channel

A simulated Higgs boson event in this channel is shown in Figure 6.10. The $Z^0 \rightarrow H^+H^- \rightarrow \tau^+\nu\tau^-\bar{\nu}$ events are characterized by a small particle multiplicity and large missing energy. For this channel, events from $Z^0 \rightarrow \tau^+\tau^-(\gamma)$, $Z^0 \rightarrow q\bar{q}$ and $e^+e^- \rightarrow e^+e^-f\bar{f}$ where both fermions are detected and the electron pair is lost in the beam pipe, are sources of background.

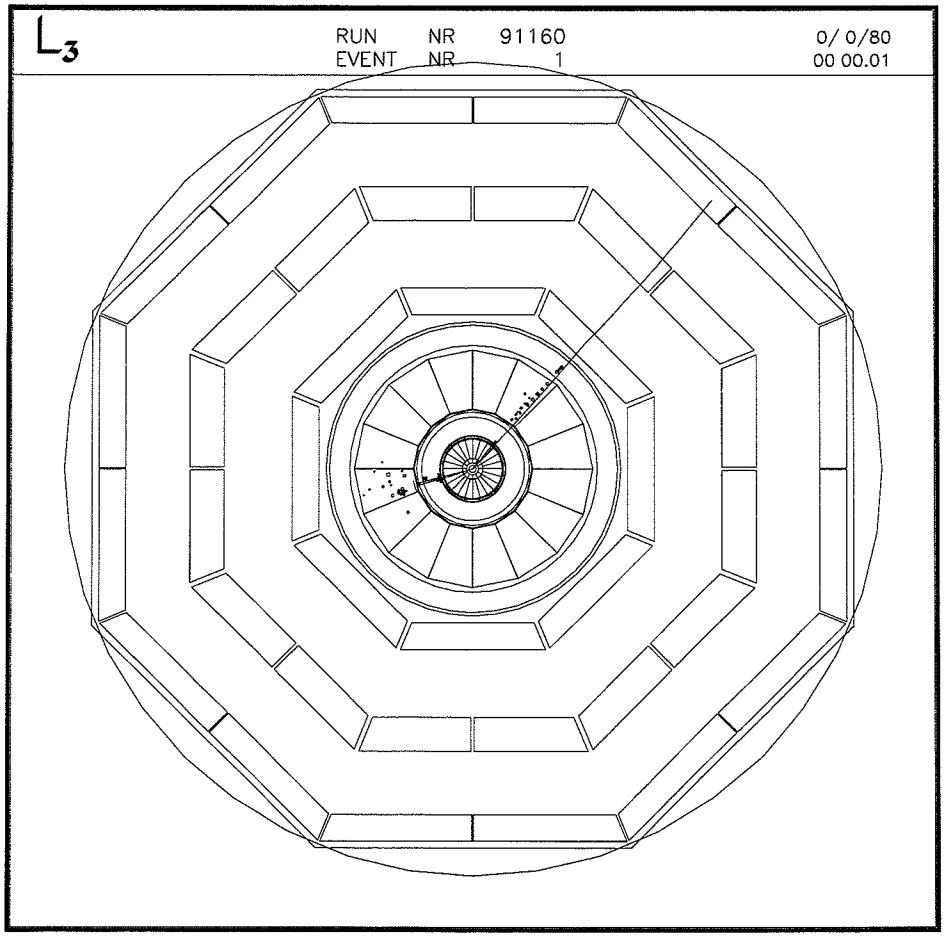

Figure 6.10: Simulated $Z^0 \rightarrow H^+H^- \rightarrow \tau^+\nu\tau^-\bar{\nu}$ event after full detector simulation and reconstruction, shown in the plane perpendicular to the beam axis.

6.3.1 Selection Details

Hadronic events are largely suppressed by requiring $N_{\rm cl} \leq 15$. In order to reject beam-gas and two-photon events with large energy deposit near the beam pipe, we require on the thrust axis $|\cos\theta_T| \leq 0.7$ and $E_\parallel/E_v < 0.5$. Each jet ($y_{\rm cut} = 0.02$) with azimuthal angle to the beam axis, $\theta_{\rm J}$, must fulfill $|\cos\theta_{\rm J}| \leq 0.93$. A lower cut on the calorimetric energy, $0.2 < E_v/\sqrt{s}$, removes most of the remaining $e^+e^- \to e^+e^-f\bar{f}$ events. In order to remove dimuon and Bhabha events, a cut on the visible energy (including the muon momenta) is applied: $E_v/\sqrt{s} < 0.8$. The remaining events have 2 or 3 jets. We require that at least two jets have an associated TEC track within a 50° half opening angle with the jet axis.

The following numbers correspond to the search for a 40 GeV Higgs boson signal. At this stage the signal efficiency is about 35% with about 3500 background events surviving. The remaining background consists of $Z^0 \to \tau^+\tau^-(\gamma)$ events. The trigger efficiency for signal events after the preselection cuts has been determined to be $\geq 99\%$. Further selection cuts are applied:

- $E_\perp/E_v > 0.2$, where $E_\perp$ is the perpendicular energy imbalance.
- $\theta_{123} < 2.8$ rad, where the variable θ_{123} is defined as: zero for one jet, θ_{12} for two jets, (where θ_{12} is the angle between jet_1 and jet_2), and $(\theta_{12} + \theta_{23} + \theta_{31})/2$ for three jets; is a measure of acolinearity and acoplanarity of the most energetic jets ($\theta_{123}=\pi$ if 3 jets are planar or 2 jets are collinear.) The $Z^0 \to \tau^+\tau^-$ background is substantially reduced while for the expected signal 28% selection efficiency is maintained. The θ_{123} distributions for data, background and signal are shown in Figure 6.11.

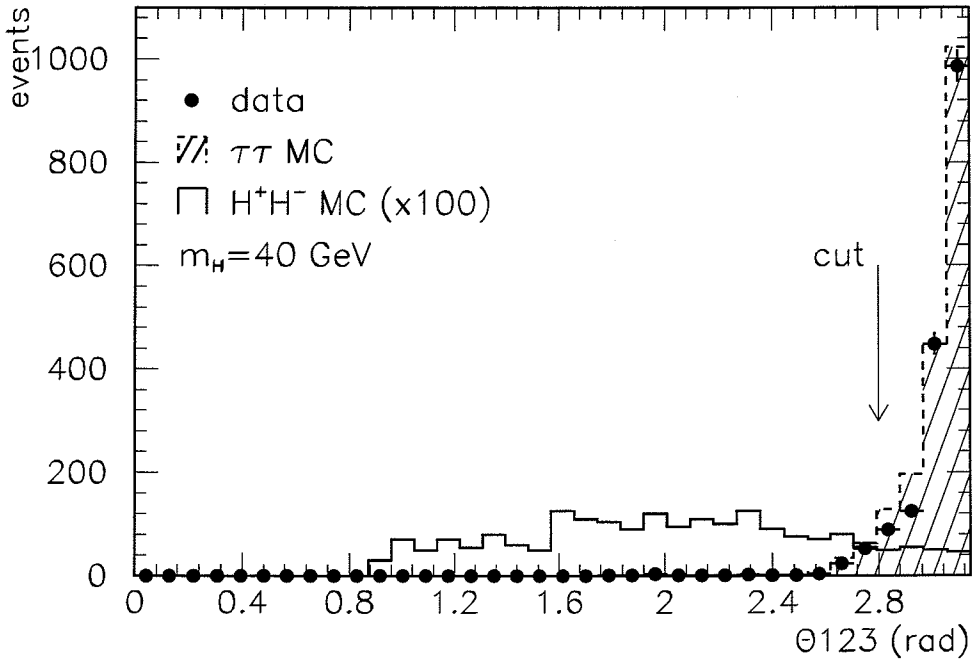

Figure 6.11: Distribution of θ_{123} for data, simulated background and Higgs boson signal in the $\tau\nu\tau\nu$ channel.

- $\theta_a < 2.8$ rad, where the acoplanarity angle, θ_a, is defined as the angular difference of the two most energetic jets in the plane perpendicular to the beam axis. It removes $e^+e^- \to \tau^+\tau^-(\gamma)$ events with a radiative photon where the photon is lost in the beam pipe. The distributions for data, background and signal are shown in Figure 6.12.

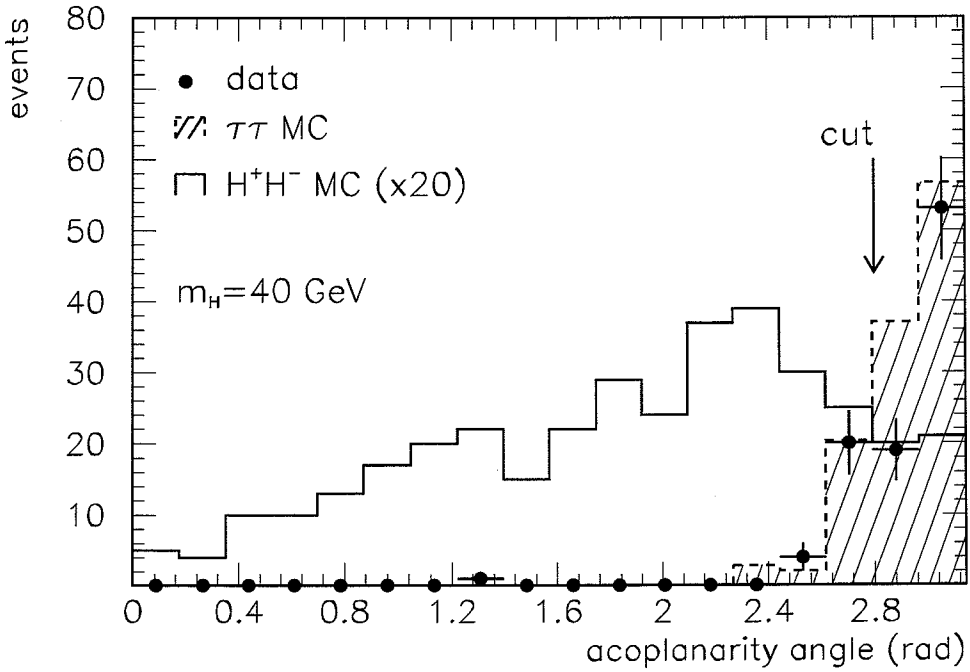

Figure 6.12: Acoplanarity angle distribution for data, simulated background and Higgs boson signal in the $\tau\nu\tau\nu$ channel.

- $M < 0.2$. This cut on the major, M, removes $Z^0 \to \tau^+\tau^-(\gamma)$ events in which the energy difference between the two taus is very large. Background events where one tau decays into an electron which travels in a direction opposite to the initial tau are rejected. The distributions in M for data, background and signal are shown in Figure 6.13.

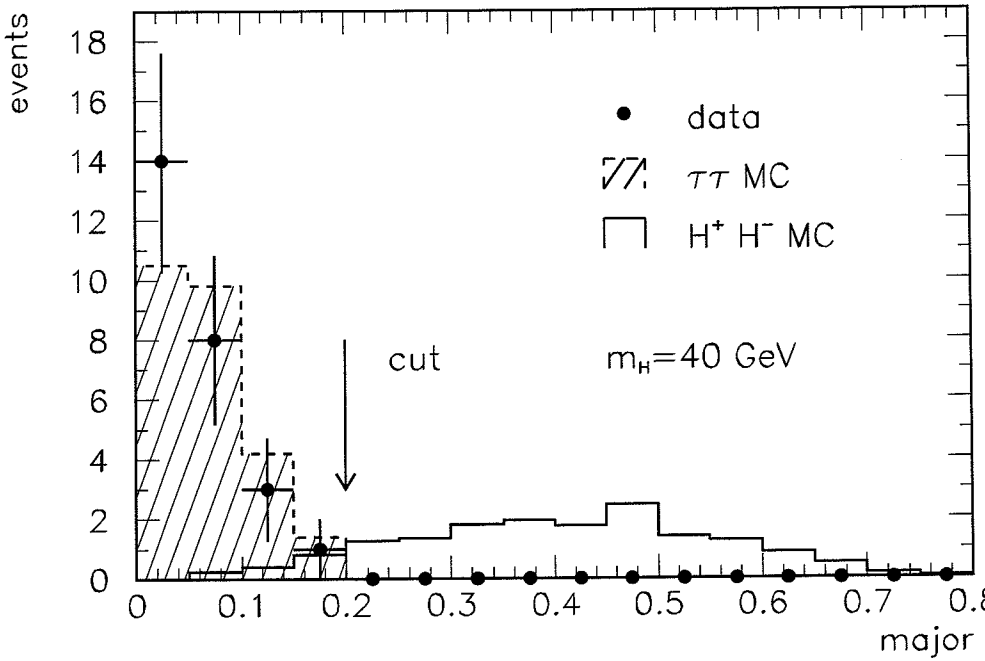

Figure 6.13: Major distribution for data, simulated background and Higgs boson signal in the $\tau\nu\tau\nu$ channel.

The cuts and their effects on data, background and signal for a 40 GeV Higgs boson signal are shown in Table 6.8. All distributions of important cut quantities are shown in appendix G.

$\tau\nu\tau\nu$ Channel			
Selection cuts	Signal Acc. (%)	$Z^0 \to \tau^+\tau^-$ Events	Data Events
	1991		
$m_H = 40$ GeV			296k
preselection	29.4	2821	2448
$E_\perp/E_v > 0.2$	27.0	1934	1753
$\theta_{123} < 2.8$ rad	24.2	119	97
$\theta_a < 2.8$ rad	21.6	26	26
$M \geq 0.2$	19.7	0	0
	1990		
$m_H = 40$ GeV			116k
preselection	30.8	1443	1750
$E_\perp/E_v > 0.2$	28.7	989	1219
$\theta_{123} < 2.8$ rad	25.2	60	51
$\theta_a < 2.8$ rad	22.2	13	9
$M < 0.2$	20.0	0	0

Table 6.8: Cuts, acceptances and corresponding numbers of data and background events for the different steps of the selection in the $\tau\nu\tau\nu$ channel for $m_H = 40$ GeV. Details of the preselection are described in the text.

6.3.2 Results of the Search in the $\tau\nu\tau\nu$ Channel

The signal acceptances are shown in Table 6.9 for different charged Higgs boson masses. No data events pass this selection. The systematic errors and their effects on the predicted signal acceptances for the $\tau\nu\tau\nu$ channel are given in Table 6.10. A 10% error, including 6% statistical error, on the number of expected events is taken into account in the exclusion plot shown in Figure 8.4.

$\tau\nu\tau\nu$ Channel		
m_H (GeV)	Signal Acceptance(%)	Signal Acceptance(%)
	1990	**1991**
20	11.8	10.1
30	18.3	16.1
40	20.0	19.7
44	—	19.5

Table 6.9: Acceptances after all cuts for various Higgs boson masses in the $\tau\nu\tau\nu$ channel No data event survives the selection.

$\tau\nu\tau\nu$ Channel		
Selection cuts $m_H = 40$ GeV	Variation	Acceptance Reduction (%)
Preselection	–	< 5
$E_\perp/E_v > 0.2$	0.03	2.9
$\theta_{123} < 2.8$ rad	0.09	2.9
$\theta_a < 2.8$ rad	0.04	2.2
$M < 0.2$	0.025	4.4
TOTAL		8.1

Table 6.10: Reduction of expected Higgs boson acceptance in the $\tau\nu\tau\nu$ channel due to modeling of the detector response for each quantity used in the analysis. For continuous quantities the variation is taken as one standard deviation on the measured quantity and for discrete quantities as one standard deviation on the normalization of the event rate. The reductions are summed in quadrature.

Chapter 7

Constraints from Z^0 Line-Shape Measurements

Severe limits on 'New Physics' beyond the Minimal Standard Model (MSM) can be set from precise measurements of the Z^0 parameters. A hypothetical Z^0 decay mode, $Z^0 \rightarrow X$, is constrained by measurements of a) the total Z^0 width, Γ_Z, b) the invisible Z^0 width, Γ_Z^{inv}, c) the hadronic peak cross section, σ_h^0, and d) the ratio of the hadronic and leptonic Z^0 decay width, R. Constraints on physics beyond the MSM are expressed as limits on $\Gamma_Z^X \equiv \Gamma(Z^0 \rightarrow X)$. These limits are based on the comparison of measured Z^0 parameter values with the limits set by the MSM.

In particular, limits set on Γ_Z^X can be used to constrain the existence of Higgs bosons in the two-doublet Higgs model, charginos and neutralinos in Supersymmetric models, heavy charged and neutral leptons.

This analysis uses the combined data of the four LEP experiments [93]. The Z^0 parameters are based on parameter fits of the Z^0 resonance, obtained by fitting the line-shape of the Z^0 decay into charged leptons and hadrons. In addition, recent results from 1991 data, presented at the Moriond conference for α_S and R [94], are included.

7.1 Measurement and Theory

Table 7.1 summarizes the measured values of Γ_Z, Γ_Z^{inv}, σ_h^0 and R. The upper and lower bounds on the measured values are given for a one-sided 95% CL[1]. The theoretical upper and lower bounds are obtained with ZFITTER [95] by varying the

[1]One-sided 95% CL are obtained by extending the 1 σ error to 1.64 σ, assuming Gaussian errors [93].

strong coupling constant, α_S, the top quark mass, $m_{\rm top}$, and the MSM Higgs boson mass, $m_{\rm h}$, independently within their 95% CL limits. The uncertainty in these values gives the dominant error on MSM predictions. The world average value of α_S has recently been improved: 0.123 ± 0.004 [94]. A lower top mass bound from the CDF collaboration [10] and an upper bound from LEP measurements [96] has been used. The lower mass limit of the Higgs boson in the MSM is based on 1990 data combined from the four LEP experiments [97]. Consistency arguments in the MSM result in an upper Higgs boson mass limit [98]. The limits on α_S, $m_{\rm top}$ and $m_{\rm h}$ are:

$$0.117 < \alpha_S < 0.129, \quad 91 < m_{\rm top} < 175 \text{ GeV}, \quad 57 < m_{\rm h} < 1000 \text{ GeV}. \tag{7.1}$$

The central values of the Minimal Standard Model predictions are arithmetic means of the obtained upper and lower limits.

Parameter	Measurement			Theory		
	Mean Value	Lower Bound	Upper Bound	Lower Bound	Upper Bound	Mean Value
$\Gamma_{\rm Z}$ (MeV)	2487 ± 10	2471	2503	2469	2509	2489
$\Gamma_{\rm inv}$ (MeV)	498 ± 8	485	511	498	503	501
$\sigma^0_{\rm had}$ (nb)	41.33 ± 0.23	40.96	41.70	41.37	41.50	41.44
R	20.89 ± 0.13	20.68	21.10	20.57	20.70	20.64

Table 7.1: Experimental and theoretical values of Z^0 line-shape parameters. Lower and upper limits are given in the Minimal Standard Model, for the parameter ranges: $0.117 < \alpha_S < 0.129$, $91 < m_{\rm top} < 175$ GeV, $57 < m_{\rm h} < 1000$ GeV.

7.2 Setting the Limits

In order to obtain conservative limits on $\Gamma_{\rm Z}^{\rm X}$, the differences between the upper and lower limits, each at 95% CL, are taken. If a shift in the mean values of the measured and predicted values decreases the difference, the shift is added to the interval between upper and lower limit. Table 7.2 summarizes the values obtained.

For later use, let the decay ratios of X be defined as:

$$x_j \equiv \frac{\Gamma(\mathrm{X} \to \mathrm{j})}{\Gamma_{\rm Z}^{\rm X}}, \tag{7.2}$$

	Diff.+Shift	Sum
$(\delta\Gamma_Z)_{max}$ (MeV)	$34+2$	36
$(\delta\Gamma_Z^{inv})_{max}$ (MeV)	$13+3$	16
$(\delta\sigma_h)_{min}$ (nb)	$-0.54+0$	-0.54
$(\delta R)_{max}$	$0.53+0$	0.53
$(\delta R)_{max}$	$-0.02-0.25$	-0.27

Table 7.2: Differences between experimental and theoretical line-shape parameter values. For details see text.

where $j = h, l, i$ for hadrons (h), leptons (l) and invisible particles (i). In this definition, $x_h + x_l + x_i = 1$. Also, let the hadronic and leptonic branching ratios of the Z^0 be defined as:

$$B_k \equiv \frac{\Gamma(Z^0 \to k)}{\Gamma_Z}, \qquad k = h, l. \tag{7.3}$$

Limits from Γ_Z: The limit on Γ_Z^X from Γ_Z is given by:

$$\Gamma_Z^X \leq (\delta\Gamma_Z)_{max} = 36 \text{ MeV}. \tag{7.4}$$

Limits from Γ_Z^{inv}: The limit on Γ_Z^X from Γ_Z^{inv} is given by:

$$x_i\Gamma_Z^X \leq (\delta\Gamma_Z^{inv})_{max} = 16 \text{ MeV}. \tag{7.5}$$

Limits from σ_h^0: The peak cross section, σ_h^0, is defined as:

$$\sigma_h^0 \equiv \frac{12\pi}{m_Z{}^2}\frac{\Gamma_l\Gamma_h}{\Gamma_Z{}^2}. \tag{7.6}$$

The measured σ_h^0 can be directly compared with the theoretical prediction, since QED effects (a 30% reduction), which depend on details of the four LEP detectors and on event selection criteria, have been multiplied out in the given experimental results [93].

The contribution of a non-MSM Z^0 decay channel, X, implies a change of σ_h^0:

$$\delta\sigma_h^0 = \frac{12\pi}{m_Z{}^2}\Gamma_l\frac{\Gamma_h + x_h\Gamma_Z^X}{(\Gamma_Z + \Gamma_Z^X)^2} \approx \sigma_h^0\frac{\Gamma_Z^X}{\Gamma_Z}\left(\frac{x_h}{B_h} - 2\right), \tag{7.7}$$

where the approximation is valid when $\Gamma_Z^X \ll \Gamma_Z$. The σ_h^0 change is negative and independent of the hadronic or leptonic branching fraction of X, thus the allowed maximum of Γ_Z^X is obtained for the minimum of $\delta\sigma_h^0$:

$$\Gamma_Z^X \leq \frac{(\delta\sigma_h^0)_{min}}{\sigma_h^0}\Gamma_Z\left(\frac{x_h}{B_h} - 2\right)^{-1}. \tag{7.8}$$

If X decays purely hadronically ($x_h = 1$), $\Gamma_Z^X < 57$ MeV, and if $x_h = 0$, a more stringent limit is obtained: $\Gamma_Z^X < 16$ MeV.

Limits from R: The ratio, R, between hadronic and leptonic Z^0 decays is defined as:

$$R \equiv \frac{B_h}{B_l}. \tag{7.9}$$

A contribution from X changes this ratio:

$$\delta R = \frac{B_h + x_h}{B_l + x_l} - \frac{B_h}{\frac{1}{3}B_l} \approx R(\frac{x_h}{B_h} - \frac{x_l}{3B_l}), \tag{7.10}$$

where the approximation is valid when $\Gamma_Z^X \ll \Gamma_Z$. The resulting limit on Γ_Z is given by:

$$\Gamma_Z^X \leq \frac{\delta R}{R}\Gamma_Z(\frac{x_h}{B_h} - \frac{x_l}{3B_l})^{-1}. \tag{7.11}$$

If $x_h = 1$ and $x_l = 0$, the maximum of δR leads to $\Gamma_Z^X \leq 44$ MeV; for $x_h = 0$ and $x_l = 1$ the minimum of δR results in $\Gamma_Z^X \leq 3.2$ MeV.

The Γ_Z^X limits are summarized in Table 7.3. The limit obtained from Γ_Z is independent of the decay branching fractions of X. The limit from Γ_Z^{inv} constrains only invisible decay modes of X. Constraints on Γ_Z^X from σ_h^0 are given for cases where X decays hadronically and leptonically, and limits from R are shown for X decaying into hadrons and charged leptons.

Origin	X Decay Modes	Γ_Z^X Limit (MeV)	BR($Z^0 \to X$) Limit (%)
Γ_Z	any	36	1.5
Γ_Z^{inv}	invisible	16	0.65
σ_h^0	hadronic	57	2.3
σ_h^0	leptonic	16	0.65
R	hadronic	44	1.8
R	charged lep.	3.2	0.13

Table 7.3: Limits on non-Standard Model Z^0 decays. Limits on Γ_Z^X for X decaying into any, invisible, hadronic and leptonic channels and the corresponding limits on BR($Z^0 \to X$) (in %) are summarized.

The most severe constraints on X can be set with charged leptonic decay modes. Also, tight constraints are obtained for leptonic X decays. This limit is more general and as tight as the limit on X decaying into invisible particles. The limit

on X for an unspecified decay mode is more constrained than the limit obtained for purely hadronic decays of X, making the latter limits obsolete.

Chapter 8

Interpretation in the Two-Doublet Higgs Model

8.1 Constraints from Higgs Boson Bremsstrahlung Searches

The limits on the $Z^0 \to h^0 Z^{0*}$ branching ratio (section 4) are interpreted as a limit on the $\sin^2(\beta-\alpha)$ parameter of the general two-doublet Higgs model. An upper limit on $\sin^2(\beta-\alpha)$ is given by: $\sin^2_{\max}(\beta-\alpha) = \Gamma(Z^0 \to h^0 Z^{0*})/\Gamma(Z^0 \to q\bar{q}) \times N_{SM}$, where N_{SM} is number of expected Higgs boson events in the Minimal Standard Model (equation 1.23). Figure 8.1 shows the limit on $\sin^2(\beta-\alpha)$ as a function of m_h.

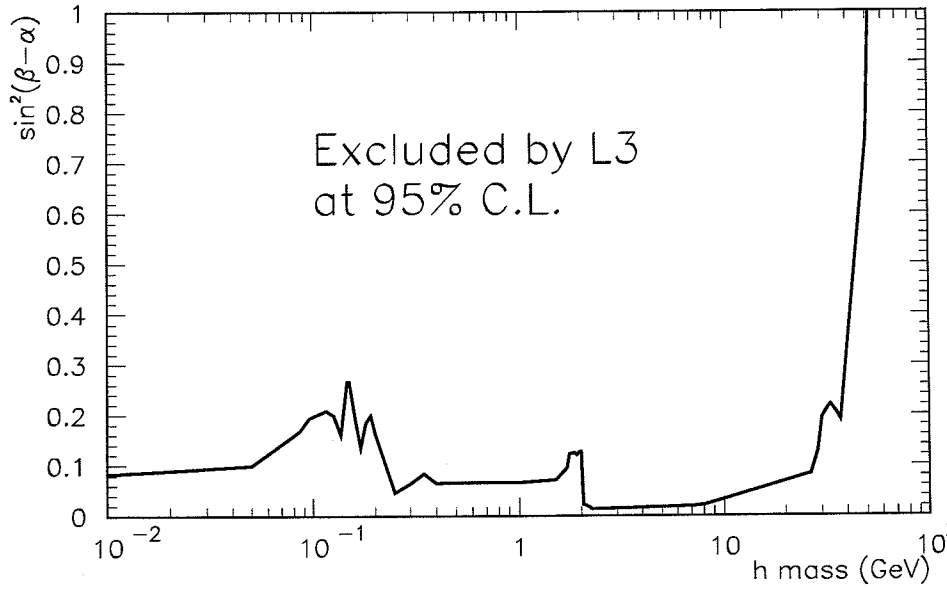

Figure 8.1: Limit on $\sin^2(\beta-\alpha)$ of the two-doublet Higgs model obtained by Higgs boson bremsstrahlung searches.

8.2 Constraints from Z^0 Line-Shape Measurements

In the general two-doublet Higgs model, the contribution to the total Z^0 width from a possible $Z^0 \rightarrow h^0A^0$ decay is known. The upper limit on the contribution from new physics to the Z^0 width , $\Gamma_Z^X < 36$ MeV (section 7), is used. The constraint on Γ_Z^X gives a limit on $\cos^2(\beta-\alpha)$ as function of m_h and m_A by converting eq. 1.36:

$$\cos^2_{max}(\beta-\alpha) = \tfrac{1}{2}\Gamma_Z^X/\Gamma(Z^0 \rightarrow \nu\bar{\nu})\lambda^{3/2}(\frac{m_h^2}{m_Z^2}, \frac{m_A^2}{m_Z^2}), \tag{8.1}$$

where $\lambda(a,b) = (1-a-b)^2 - 4ab$, $\Gamma(Z^0 \rightarrow \nu\bar{\nu}) = 166 \pm 2.7$ MeV [99]. Figure 8.2 shows the excluded range of $\cos^2(\beta-\alpha)$ as a function of m_h for $m_A = 20$ GeV.

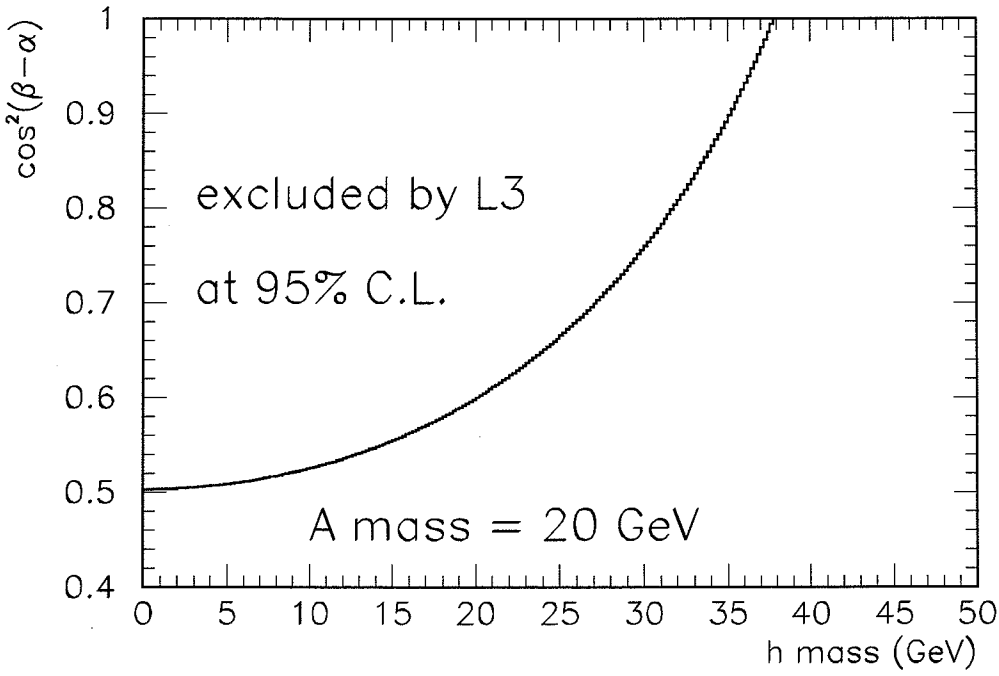

Figure 8.2: Limit on $\cos^2(\beta-\alpha)$ of the two-doublet Higgs model as a function of m_h for $m_A = 20$ GeV. The limit at 95% CL is based on constraints from the precision line-shape measurements on non-standard Z^0 decays from the reaction $Z^0 \rightarrow h^0A^0$.

8.3 Excluded Region in the (m_h,m_A) Plane

Using the upper limit on $\sin^2(\beta-\alpha)$ from bremsstrahlung searches and the upper limit on $\cos^2(\beta-\alpha)$, i.e., a lower limit on $\sin^2(\beta-\alpha)$, from line-shape constraints, a region in the (m_h,m_A) plane is excluded where the two limits are inconsistent with each other. The excluded (m_h,m_A) region is shown in Figure 8.3.

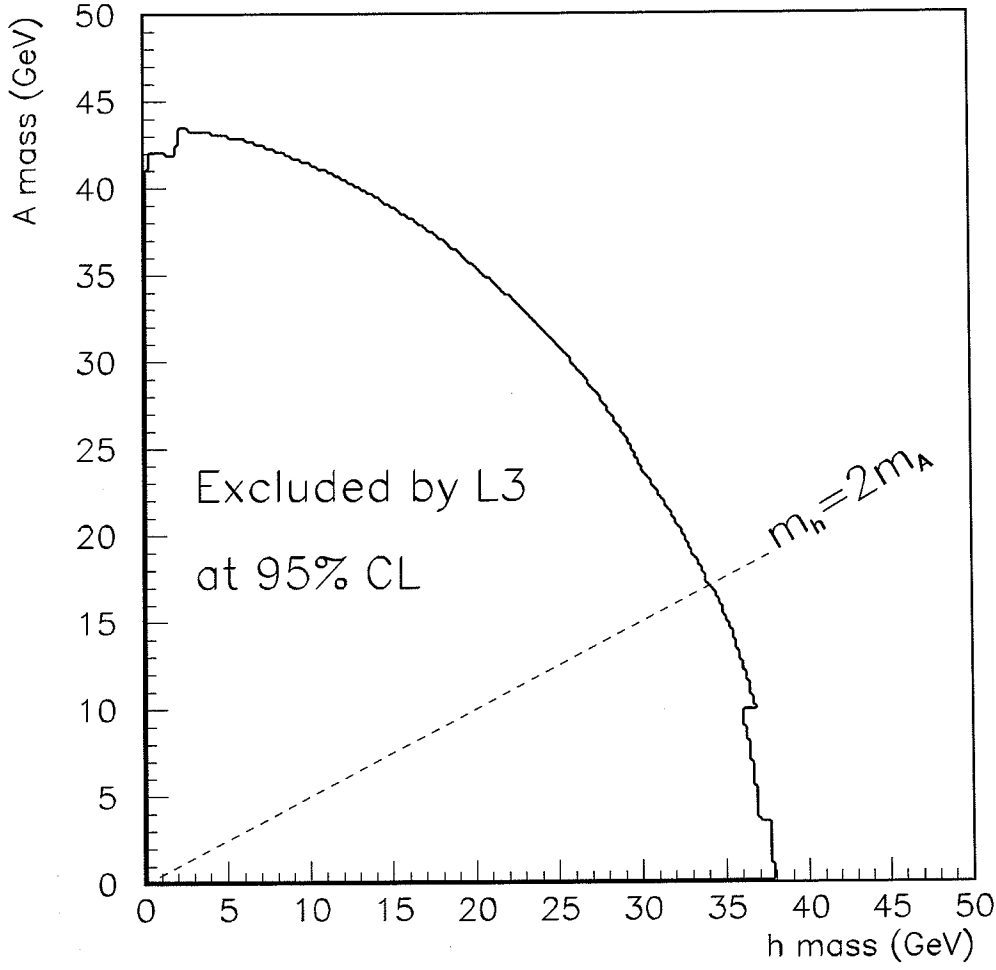

Figure 8.3: Regions of the (m_h,m_A) plane excluded in the two-doublet Higgs model. These are obtained by combining Higgs boson bremsstrahlung searches with limit from Z^0 line-shape measurements.

8.4 Combined Limit on Charged Higgs Boson Pair-Production

By combining the results in the three decay channels (cscs, cs$\tau\nu$ and $\tau\nu\tau\nu$), a lower limit on the Higgs boson mass of 41 GeV, independent of the Higgs boson decay mode, is set. In order to smooth the exclusion line in the cscs channel, the average of data and background is used over three neighboring mass points. Figure 8.4 shows the excluded regions for the cscs, cs$\tau\nu$ and $\tau\nu\tau\nu$ channel, separately as a function of the charged Higgs boson mass and the leptonic Higgs boson branching ratio R_l (eq. 1.41). In addition, the combined limit is shown.

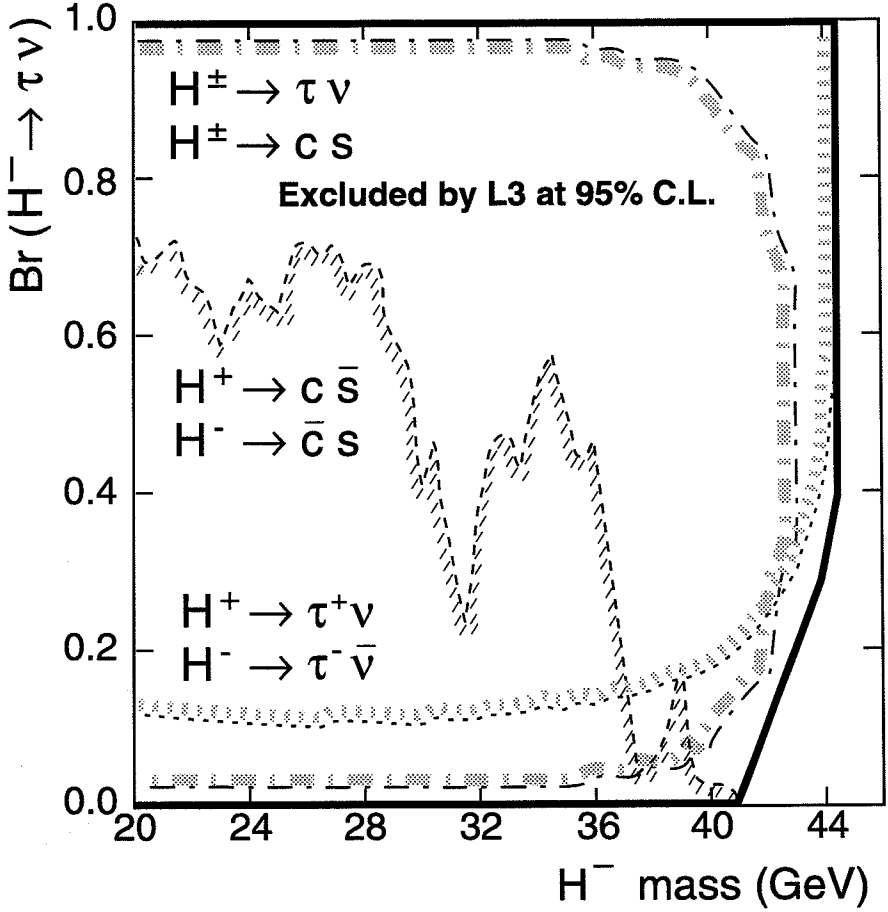

Figure 8.4: Lower limits on charged Higgs boson masses in the two-doublet Higgs model as a function of the charged Higgs boson mass and the leptonic Higgs boson branching fraction. The thick black line gives the combined excluded region.

Chapter 9

Interpretation in the Minimal Supersymmetric Standard Model

The direct searches in the neutral Higgs boson production channels are combined with limits from the Z^0 line-shape constraint in order to exclude regions in the (m_h,m_A) plane of the MSSM. The important implications of radiative corrections on the Higgs boson phenomenology were discussed in section 1.6.

A given mass point in the (m_h,m_A) plane is excluded if, for all allowed values of the ϵ parameter, eq. (1.68), the model fails at least one of the searches for neutral Higgs boson pair-production or is excluded by the searches for Higgs boson bremsstrahlung or by the constraint from the Z^0 line-shape limit. Figure 9.1 shows the excluded mass region in the (m_h,m_A) plane at 95% CL. The region $m_h \approx 50$ GeV, $m_A < 10$ GeV is not excluded, since in this region the tau pair with small invariant mass is almost undetectable in the hadronic system with large invariant mass.

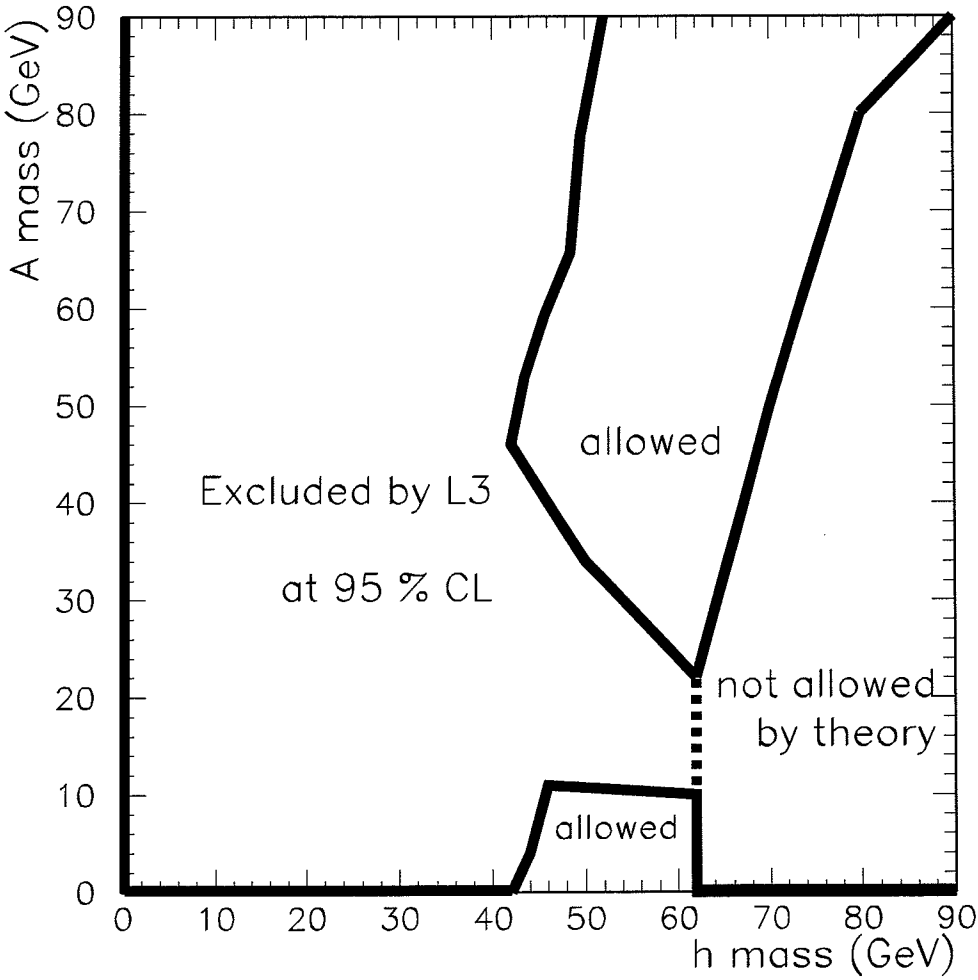

Figure 9.1: Regions of the (m_{h},m_{A}) plane excluded (95% CL) in the Minimal Supersymmetric Standard Model.

Chapter 10

Comparison of LEP Results

During three years of data-taking, the LEP experiments ALEPH, DELPHI, L3 and OPAL have performed intense searches for the neutral and charged Higgs bosons expected in extensions of the Minimal Standard Model [100, 101, 102, 103]. The interest in non-minimal Higgs searches by the LEP experiments is manifested by their large number of publications in this field. This comparison of their results includes their latest results: ALEPH [104], DELPHI [105], L3 [106], OPAL [107]. The L3 results are those of this thesis. A comparative study of the LEP results is given in [20]. All four LEP experiments have searched for singly and pair-produced Higgs bosons with the following results:

- Model-independent limits on bremsstrahlung-produced Higgs boson are set by L3 and OPAL. Comparable expected Higgs selection efficiencies were obtained and similar Higgs signatures were investigated. The L3 searches are more sensitive because the results are based on about three times more data (1990 and 1991 data-taking) than the OPAL results (1990 data only).

- In addition, L3 and OPAL present their pair-produced Higgs search results as model-independent limits on the Higgs boson branching ratio. For the same exclusion branching ratio, L3 excludes a much larger region. This is due to larger statistics and higher selection efficiency in the hadronic Higgs boson decay channels.

- All experiments use the limits obtained from searches for Higgs boson bremsstrahlung and combine them with the constraint from the Z^0 line-shape measurement. The resulting excluded (m_h,m_A) mass range is very similar because of similar detection efficiencies in the high Higgs boson mass range and similar limits from the line-shape measurements.

- Also, all four experiments set similar limits on the mass of the charged Higgs boson. These limits are close to the kinematic production threshold of the LEP beam energy.

- In the interpretation of the Minimal Supersymmetric extension of the Standard Model, ALEPH and L3 exclude almost the entire kinematically allowed mass region. L3 does not exclude a small region around the mass point $m_{\mathrm{h}} = 55$ GeV and $m_{\mathrm{A}} = 5$ as discussed earlier. For about $m_{\mathrm{h}} > 45$ GeV, OPAL does not exclude an extended mass region. The mass region excluded by DELPHI is not presented independently of the unknown amount of radiative correction and therefore cannot be compared with the other limits.

Chapter 11

Conclusions

No indication of Higgs bosons of non-minimal Higgs models has been found. Internal notes and publications which summarize the development of this work are given in [108]. The following limits on Higgs boson production from a study of Z^0 decays are obtained:

- An upper limit on the branching ratio of Higgs boson bremsstrahlung of 3×10^{-5} to 2×10^{-4} is set depending on the Higgs boson mass in the mass range 0 to 60 GeV (see Figure 4.1).

- For pair-produced neutral Higgs bosons, a search of the dominant decay channels yields limits on allowed h^0 and A^0 mass ranges, even for small branching ratios up to 2×10^{-4} (see Figures 5.5, 5.13 and 5.16).

- In the two-doublet Higgs model, the limit obtained from Higgs boson bremsstrahlung searches, as expressed as an upper limit on $\sin^2(\beta - \alpha)$, is about 0.1 for Higgs boson masses up to about 30 GeV (see Figure 8.1).

- Limits on the non-standard contributions to the Z^0 width, as well as a direct search for Higgs boson bremsstrahlung (including $h^0 \rightarrow A^0 A^0$ decays), exclude the region $m_h{}^2 + m_A{}^2 \leq (40 \text{ GeV})^2$ in the framework of the two-doublet Higgs model (see Figure 8.3).

- For charged Higgs bosons of the two-doublet Higgs model, a lower limit of 41 GeV is obtained at 95% CL independent of the Higgs decay modes (see Figure 8.4).

- The interpretation of the results in the context of the Minimal Supersymmetric extension of the Standard Model includes radiative corrections. Nearly the

entire (m_h,m_A) mass region, which is kinematically allowed at present LEP energies, is excluded (see Figure 9.1).

What can be expected in the future? First, more luminosity will allow an increase in sensitivity of any signal. Negative searches would tighten the limits on $\sin^2(\beta - \alpha)$ and the excluded region in the (m_h,m_A) parameter range of the two-doublet model. An extension in the m_h direction of the (m_h,m_A) parameter space is hardly possible, since LEP-I has almost reached its sensitivity limit for the search of the bremsstrahlung-produced Higgs boson in the Minimal Standard Model. In the searches for pair-produced Higgs bosons, more data will lead to a higher sensitivity. However, in hadronic decay channels, irreducible QCD-type events already create a significant background to the expected Higgs boson signals. The search for charged Higgs bosons of the general two-doublet model and searches for neutral pair-produced Higgs bosons in the MSSM have almost reached the kinematic limit. In the framework of the MSSM, the most elegant and promising extension of the Standard Model, the lightest Higgs boson has a mass less than about 130 GeV. Therefore, a major breakthrough for neutral or charged non-minimal Higgs boson searches may well occur at the higher center-of-mass energy which will be available at LEP200.

Appendices

The appendices contain the distributions of important preselection and all final selection cut variables for the searches in the seven pair-produced Higgs channels for 1990 and 1991 detector configurations, separately. First, for a general overview, a table lists the cut and the corresponding figure numbers and a figure summarizes the reduction of acceptances and the corresponding numbers of data and background events after a cut is applied. Then, preselection and final selection distributions are shown. The expected distributions of the Higgs signals are shown as histograms. The distributions for data are presented as dots with statistical error bars. Background from $Z^0 \to q\bar{q}$ and $Z^0 \to \tau^+\tau^-$ are shown as histograms, where the $Z^0 \to \tau^+\tau^-$ background is hatched.

Appendix A

Distributions for the $Z^0 \longrightarrow h^0A^0 \longrightarrow b\bar{b}b\bar{b}$ Search

Cut numbers and corresponding figure numbers are listed in table A.1. Figure A.1 gives an overview of the expected signal acceptances and numbers of data and background events after a cut is applied.

	bbbb Channel (32 GeV, 32 Gev)	
Cut#	Selection cuts	Fig#
1	$N_J = 4 \text{ or } 5$	–
2	$\chi^2 \leq 2$	A.7
3	$\lvert\cos\theta_p\rvert \leq 0.9$	A.8
4	$\lvert\cos\theta_d\rvert \leq 0.7$	A.9
5	$T \leq 0.78$	A.10
6	$\lvert\cos\theta^{\text{jj}}_{\text{min}}\rvert \leq 0.5$	A.11
7	incl. leptons	–

Table A.1: Cut number and corresponding figure number in the bbbb channel.

A.1 Preselection in the bbbb Channel

Figures A.2 to A.5 show distributions of cut variables for the preselection.

A.2 Final Selection in the bbbb Channel

Figures A.7 to A.11 show distributions of cut variables for the final selection. The last selection cut, requiring an inclusive lepton, is discrete and not shown.

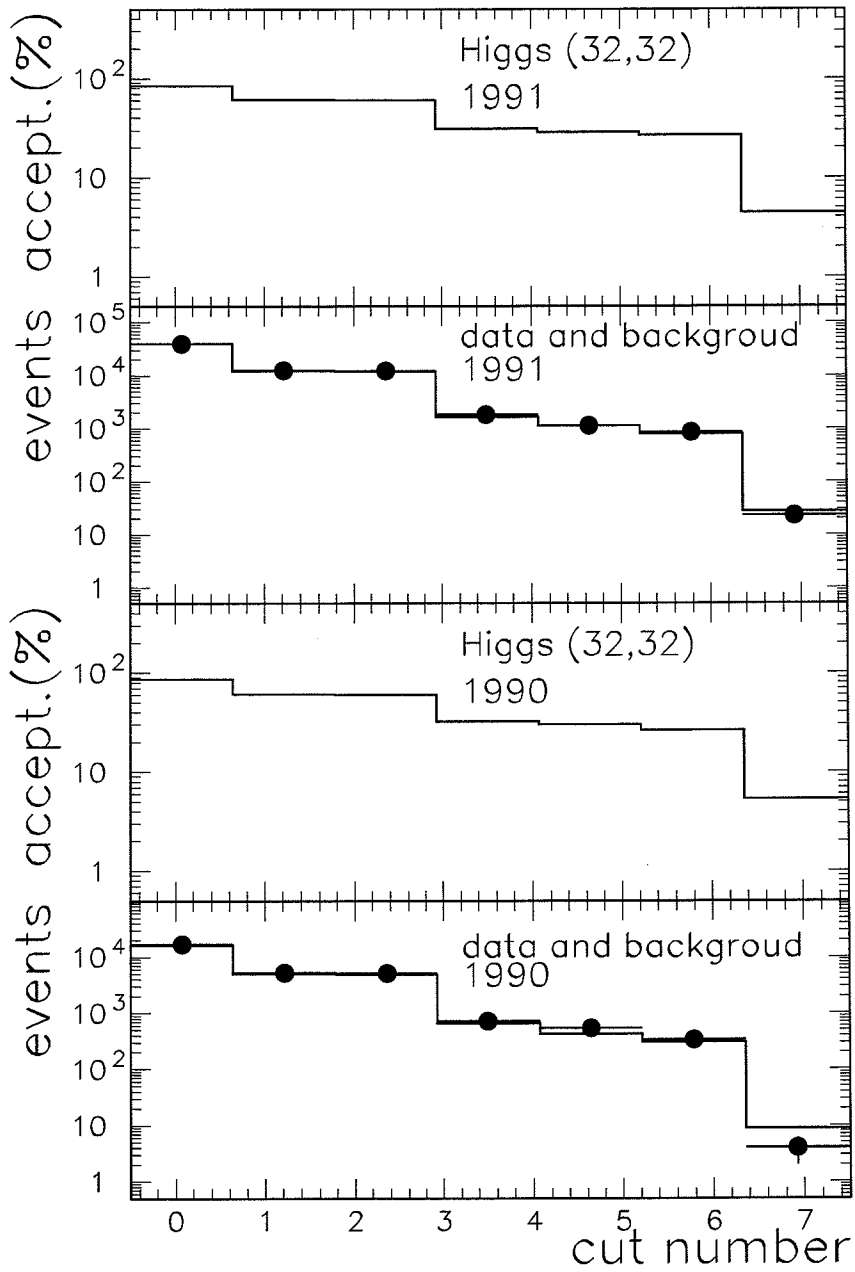

Figure A.1: Acceptances and numbers of data and background events after a cut is applied in the bbbb channel. Bin 0 corresponds to the preselection.

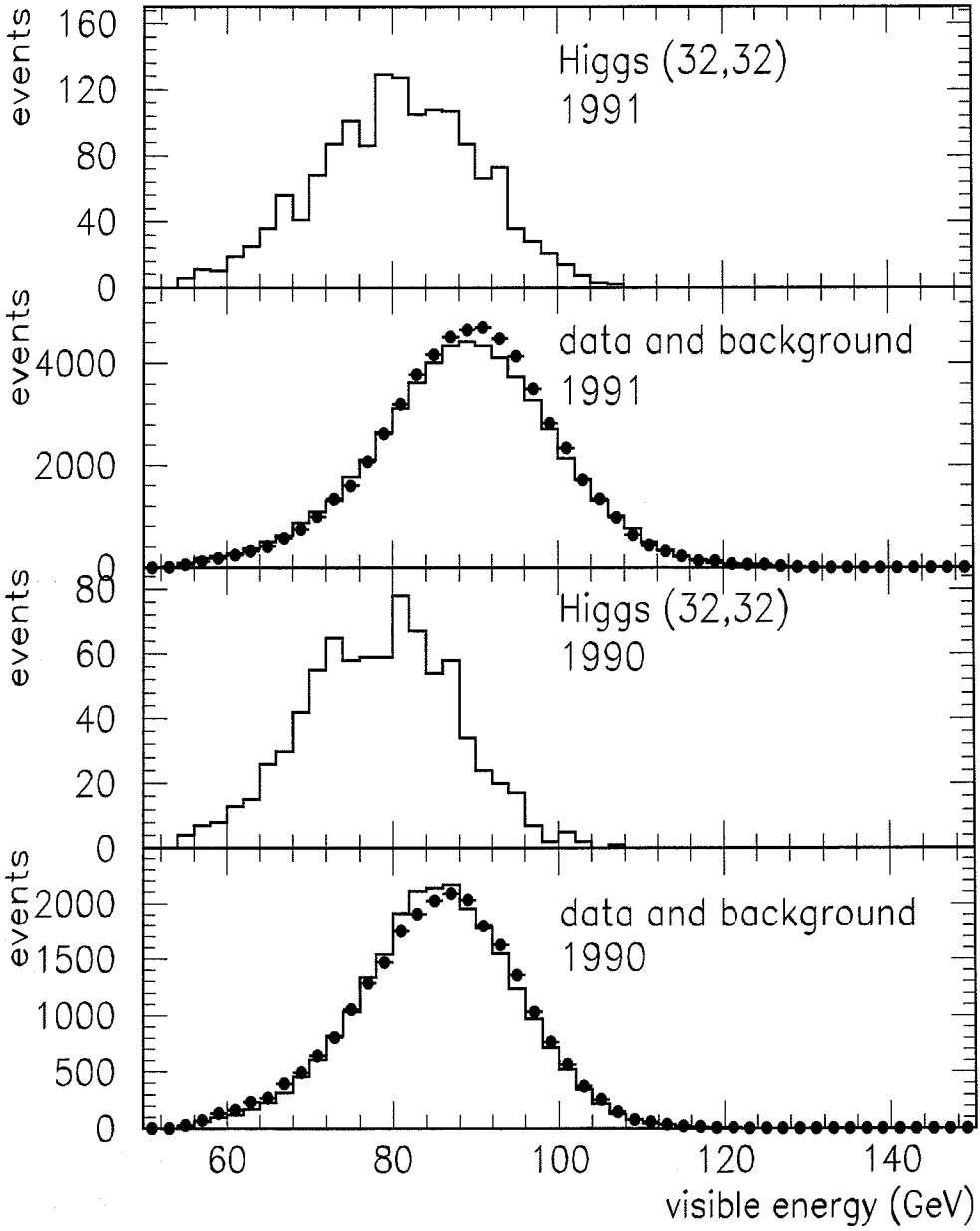

Figure A.2: Distribution of the visible energy in the bbbb channel.

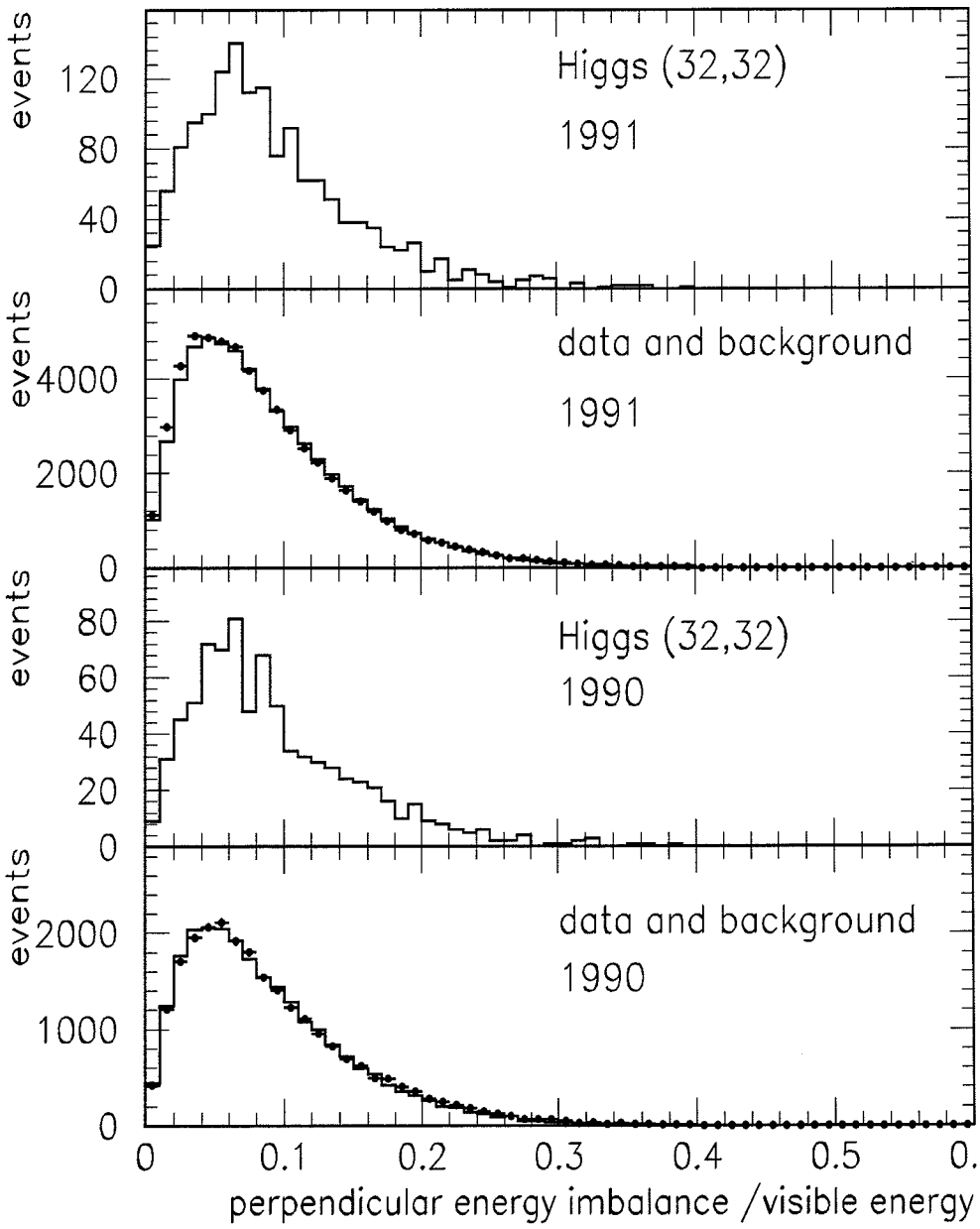

Figure A.3: Distribution of the perpendicular energy imbalance in the bbbb channel.

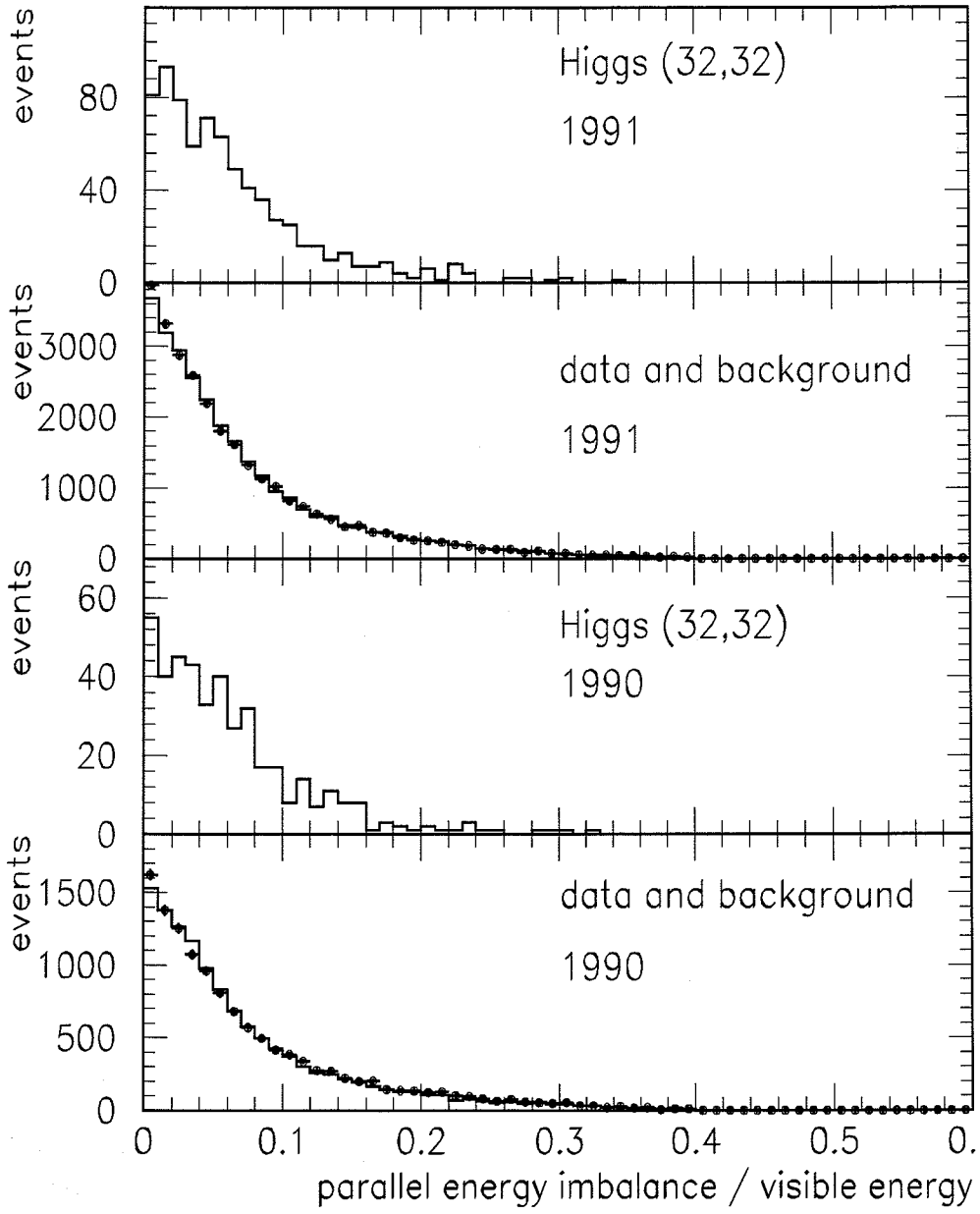

Figure A.4: Distribution of the parallel energy imbalance in the bbbb channel.

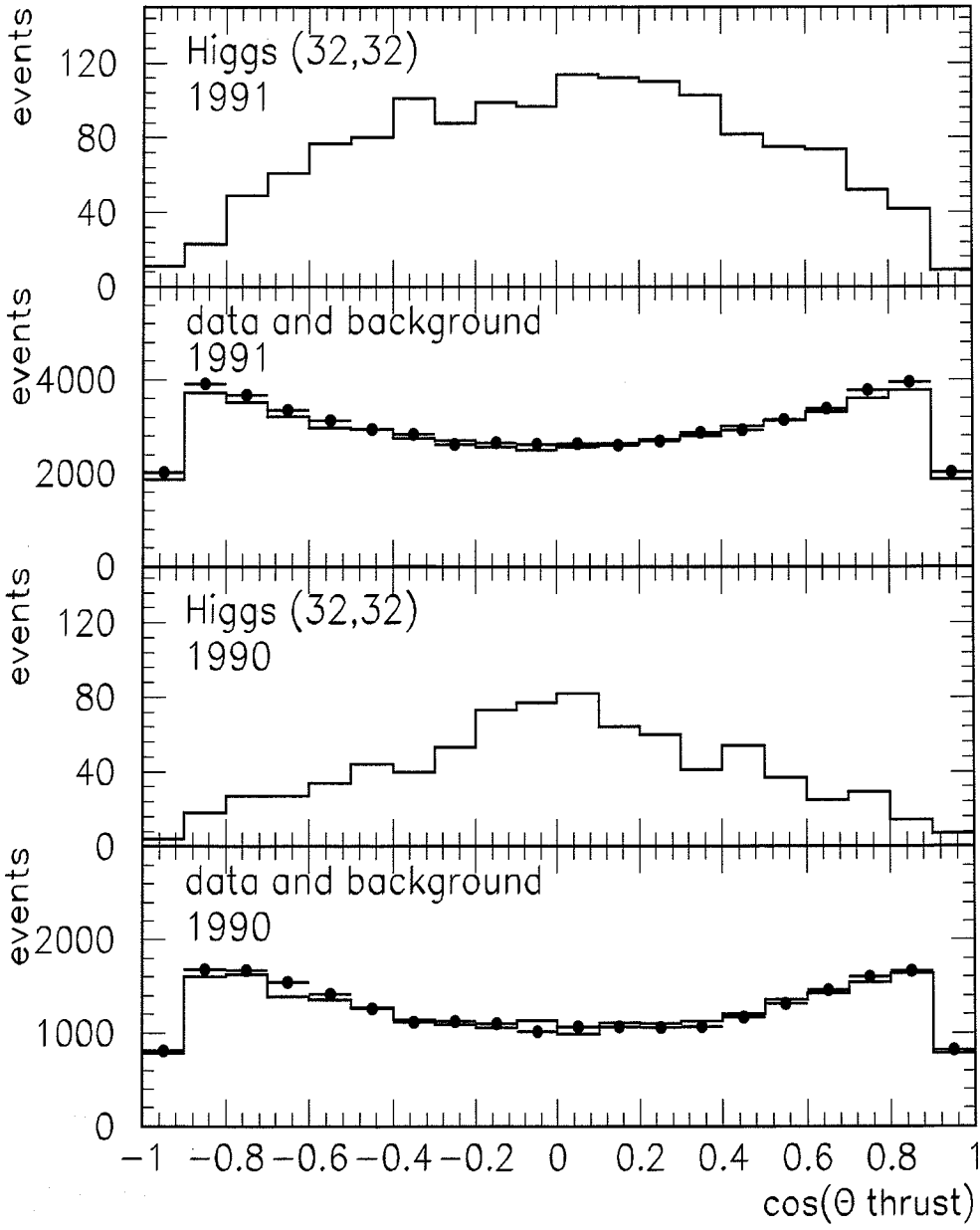

Figure A.5: Distribution of the thrust angle in the bbbb channel.

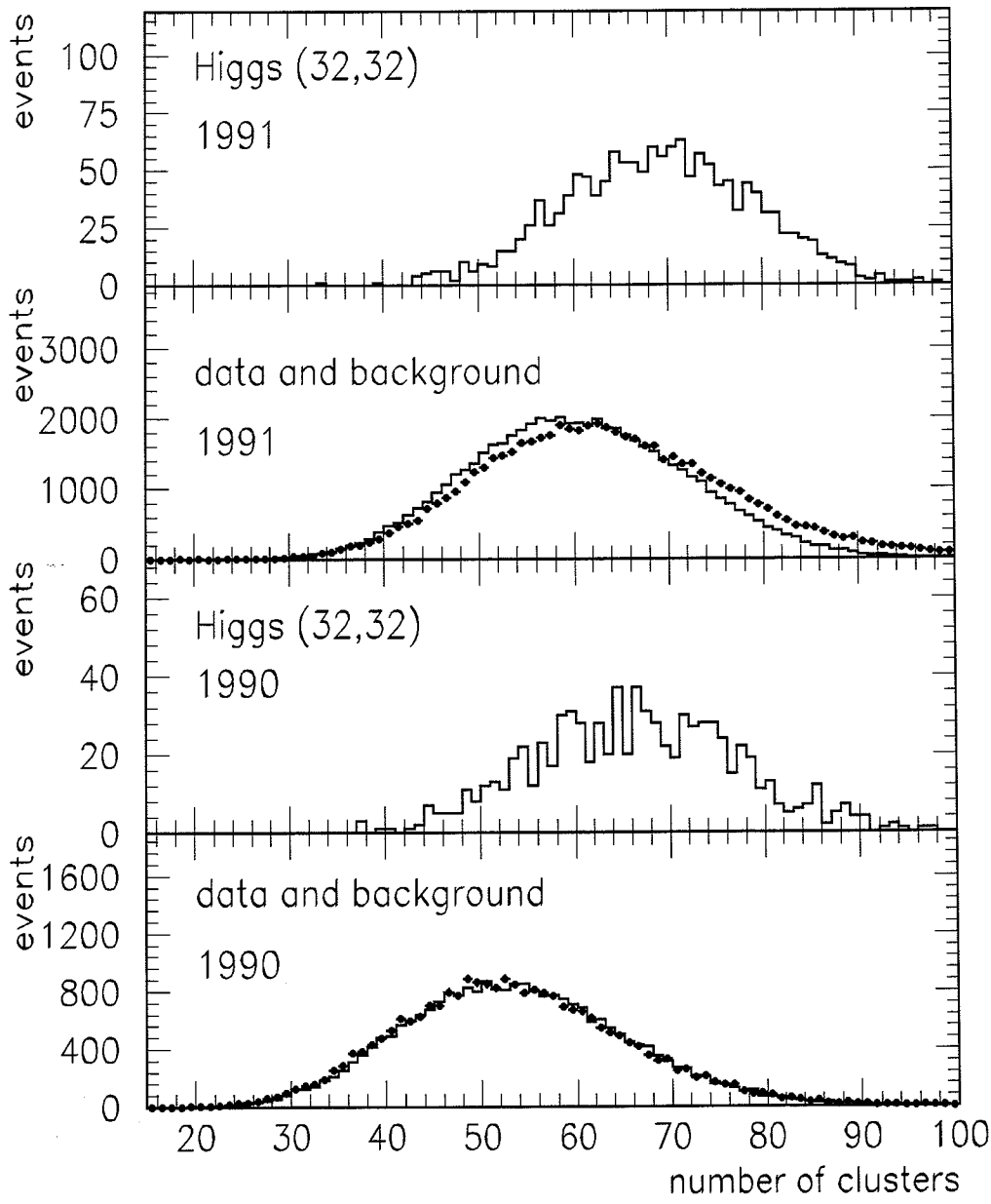

Figure A.6: Distribution of the number of calorimetric clusters in the bbbb channel.

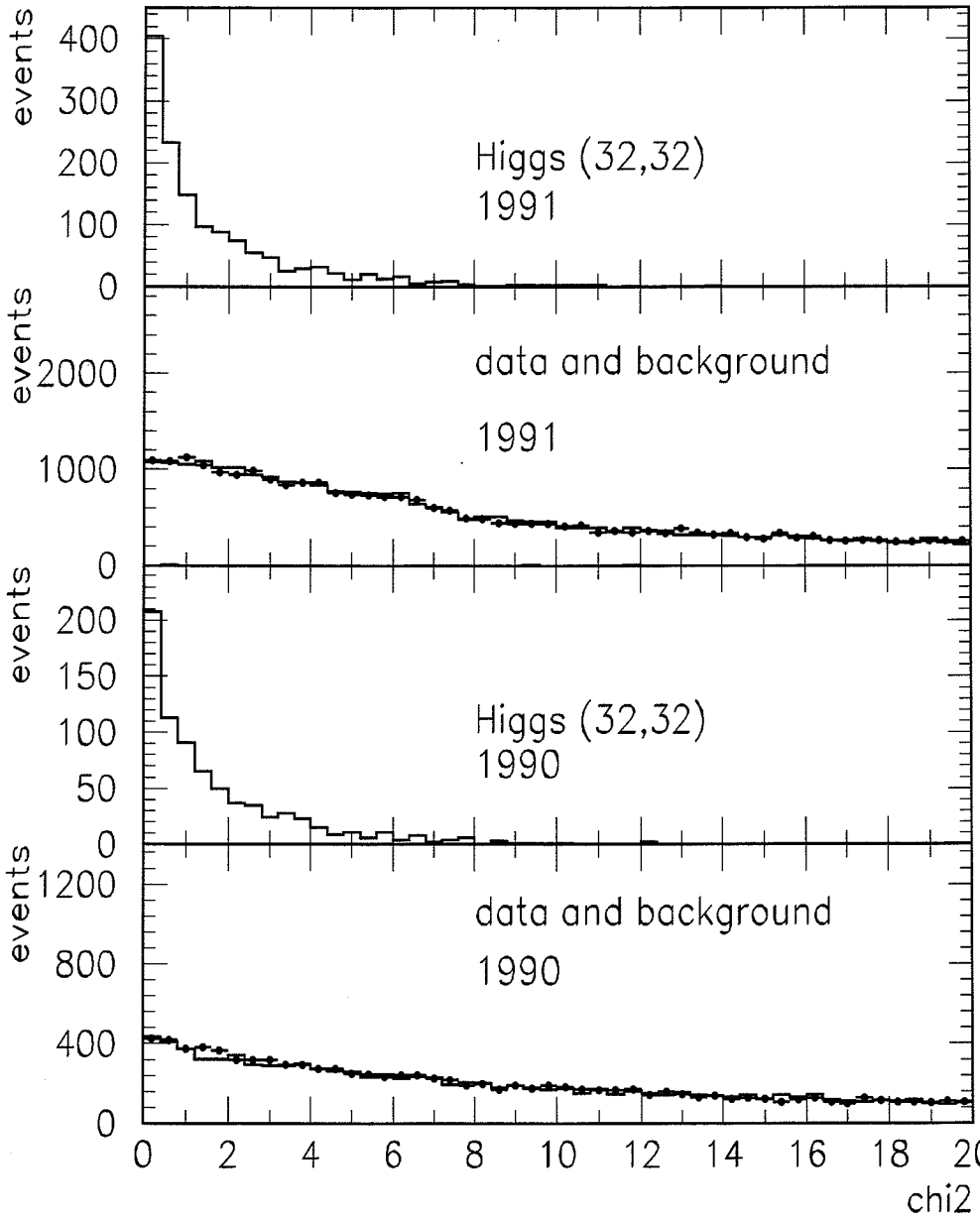

Figure A.7: Distribution of χ^2_{min} in the bbbb channel.

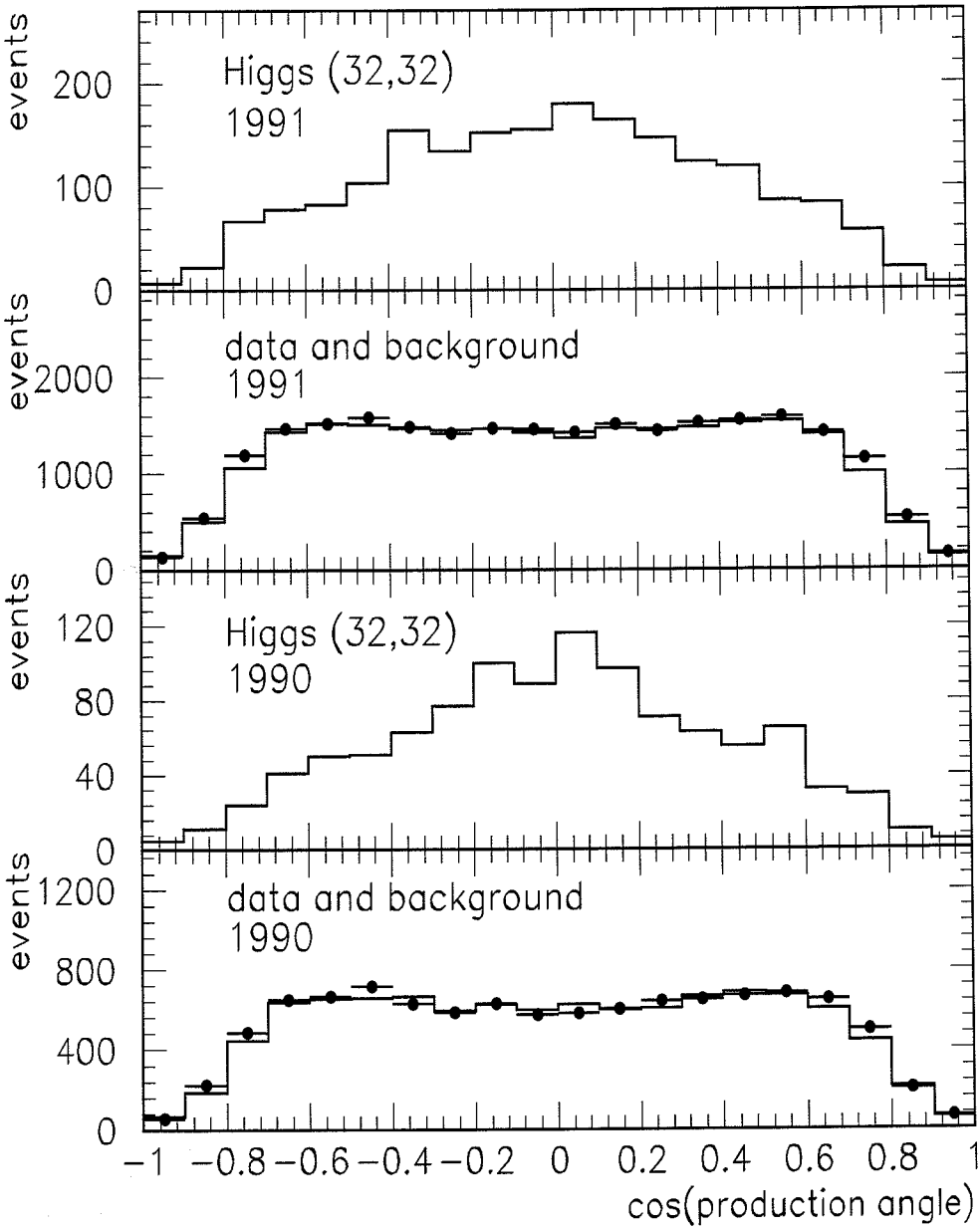

Figure A.8: Distribution of the production angle in the bbbb channel.

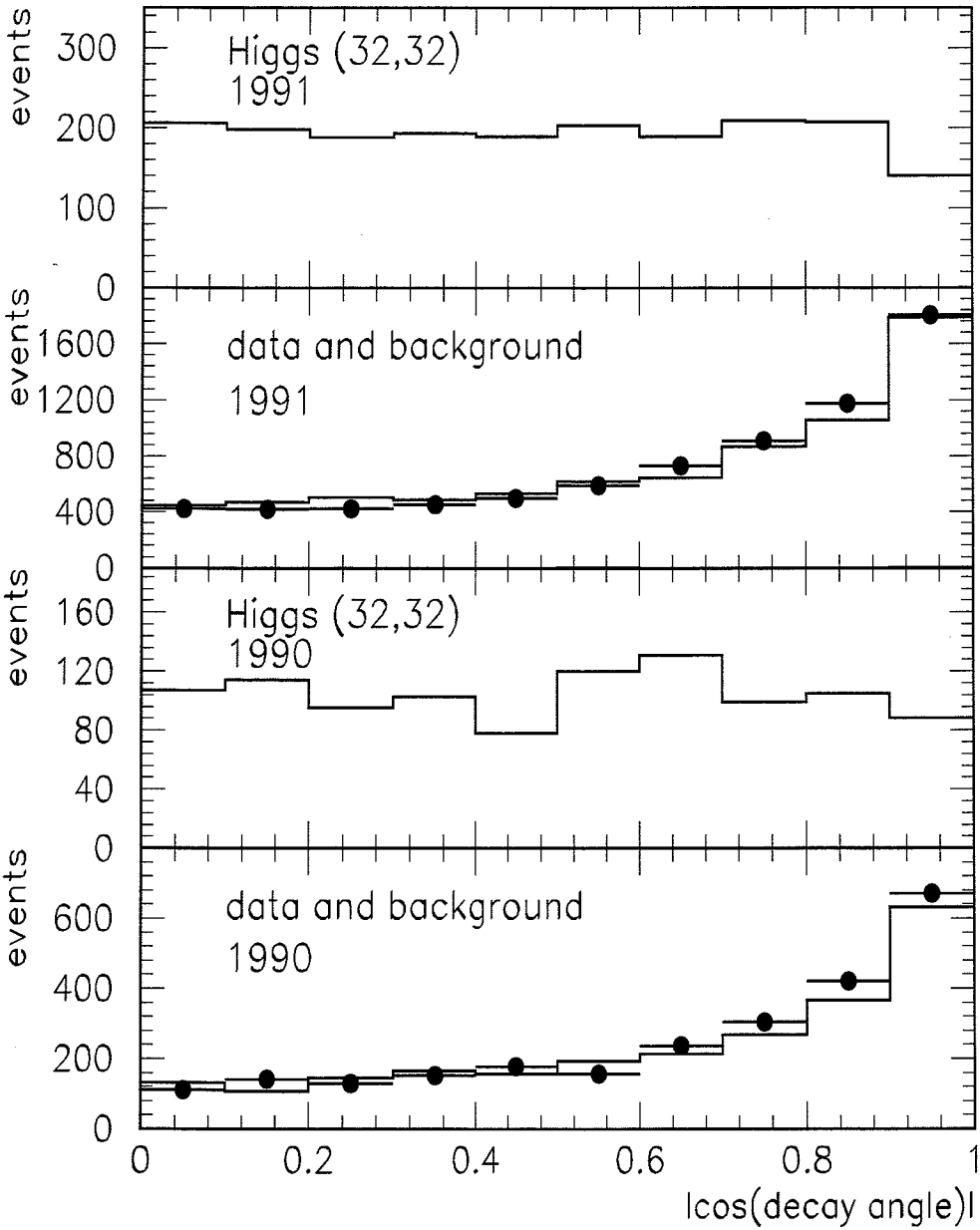

Figure A.9: Distribution of the decay angle in the bbbb channel.

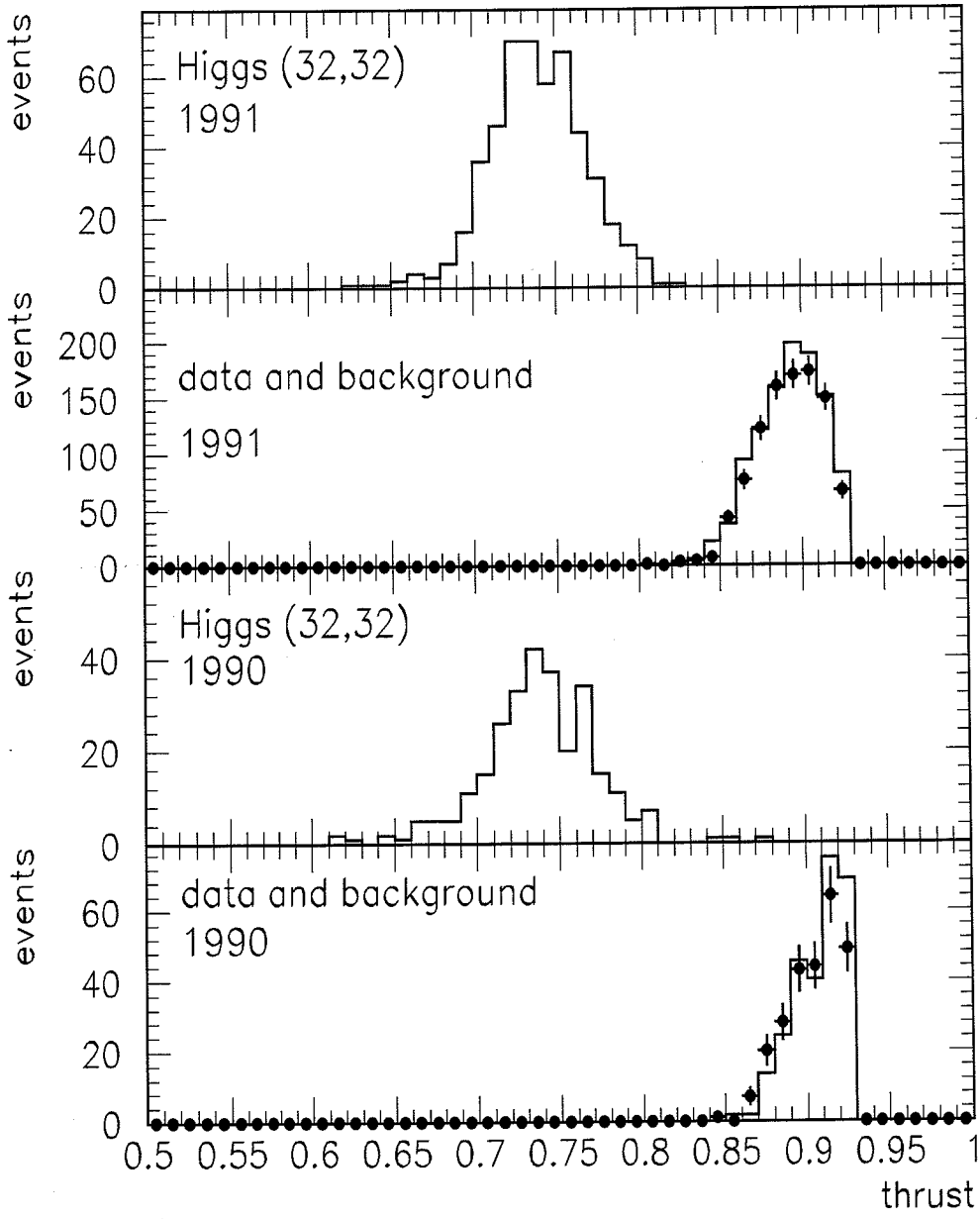

Figure A.10: Distribution of the thrust in the bbbb channel.

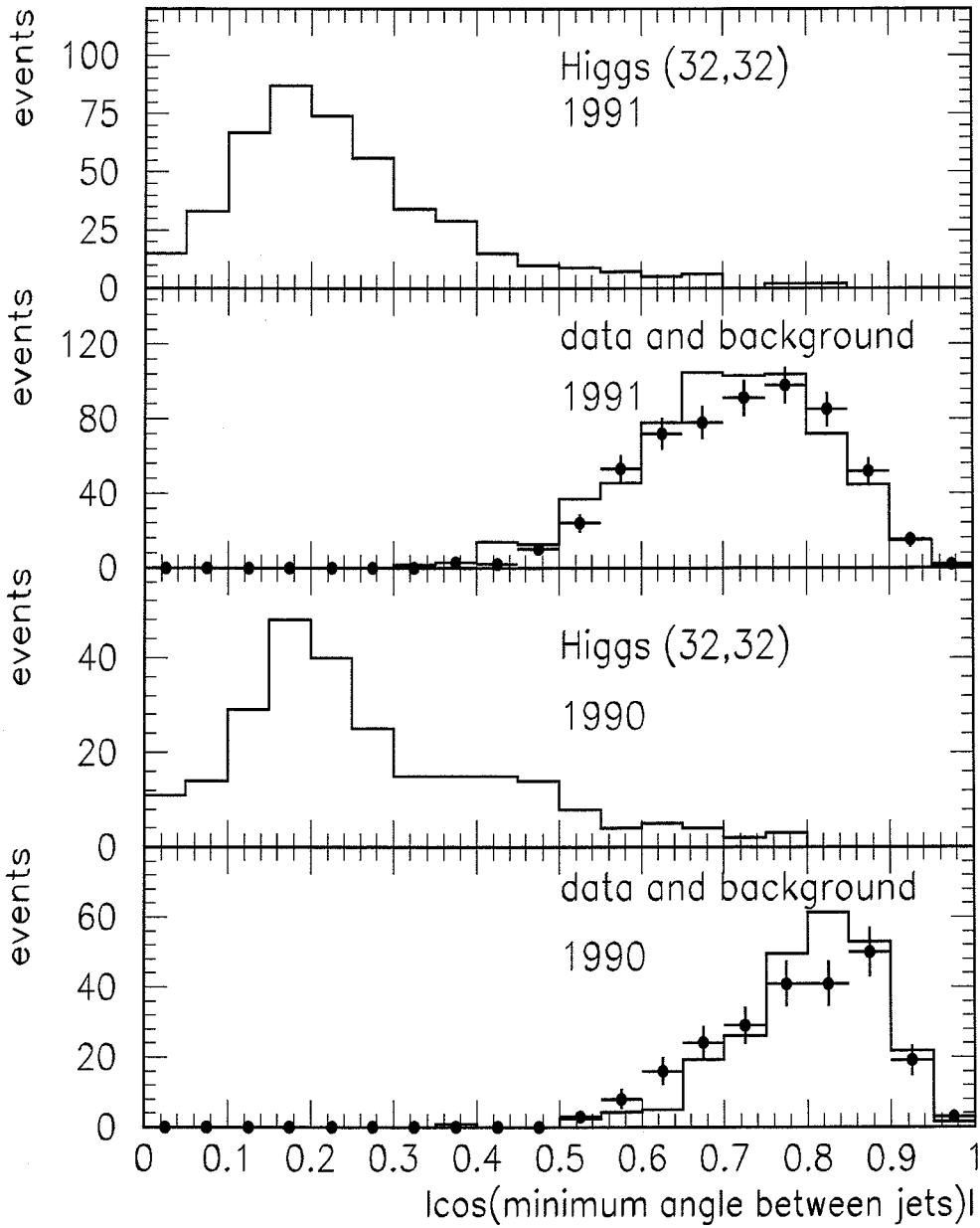

Figure A.11: Distribution of the minimum angle between jets in the bbbb channel.

Appendix B

Distributions for the $Z^0 \rightarrow h^0A^0 \rightarrow A^0A^0A^0 \rightarrow b\bar{b}b\bar{b}b\bar{b}$ Search

Cut numbers and corresponding figure numbers are listed in table B.1. Figure B.1 gives an overview of the expected signal acceptances and numbers of data and background events after a cut is applied.

	bbbbbb Channel (50 GeV, 22 GeV)	
Cut#	Selection cuts	Fig#
1	$N_J = 5 \text{ or } 6$	–
2	$T \leq 0.78$	B.2
3	$\chi^2 \leq 3$	B.3
4	$\lvert\cos\theta_p\rvert \leq 0.7$	B.4
5	$\lvert\cos\theta^{\text{jj}}_{\text{min}}\rvert \leq 0.5$	B.5
6	$\sum \text{M}^{\text{rec}}_{\text{jet}} \geq 30$ GeV	B.6
7	incl. leptons	–

Table B.1: Cut number and corresponding figure number in the bbbbbb channel.

B.1 Preselection in the bbbbbb Channel

The same preselection as in the bbbb channel is applied.

B.2 Final Selection in the bbbbbb Channel

Figures B.2 to B.6 show distributions of cut variables for the final selection. The last selection cut, requiring an inclusive lepton, is discrete and not shown.

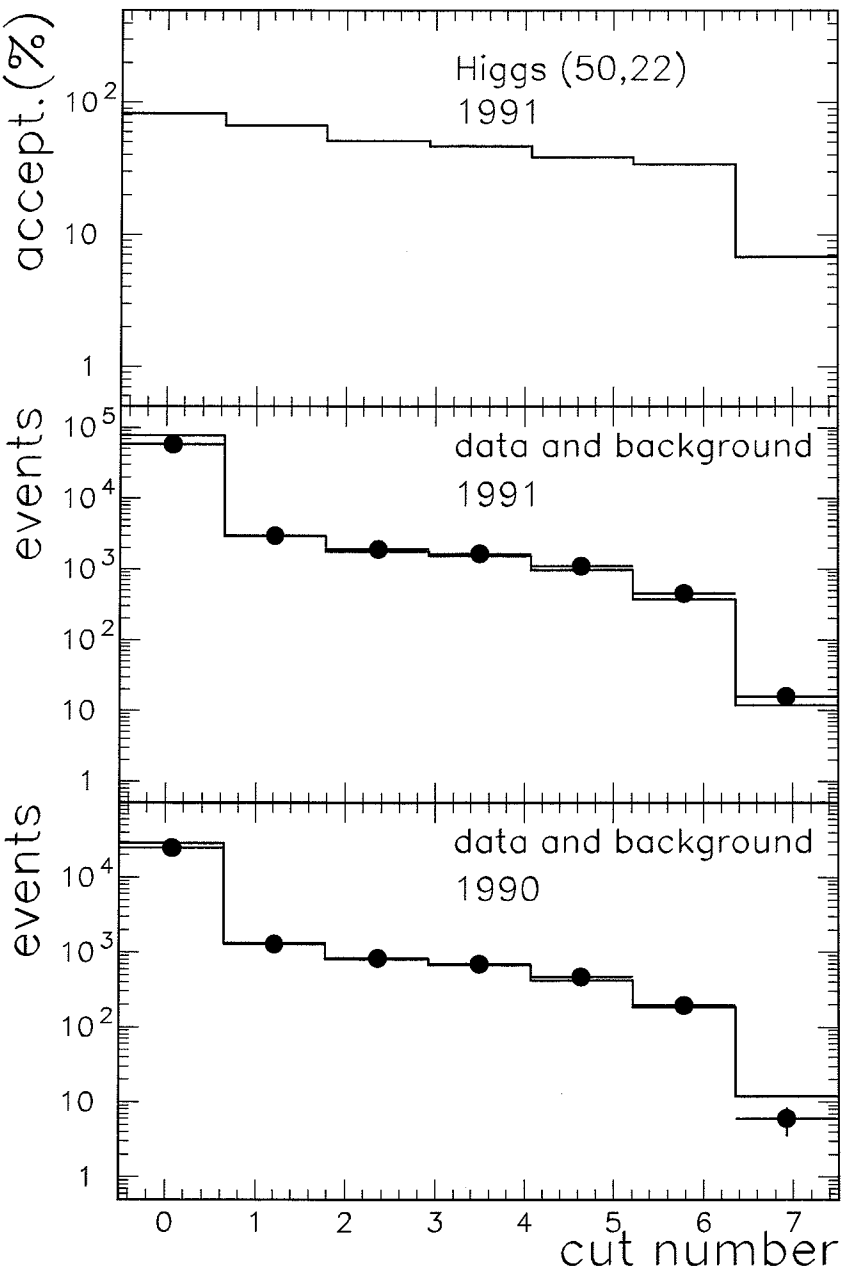

Figure B.1: Acceptances and numbers of data and background events after a cut is applied in the bbbbbb channel. Bin 0 corresponds to the preselection.

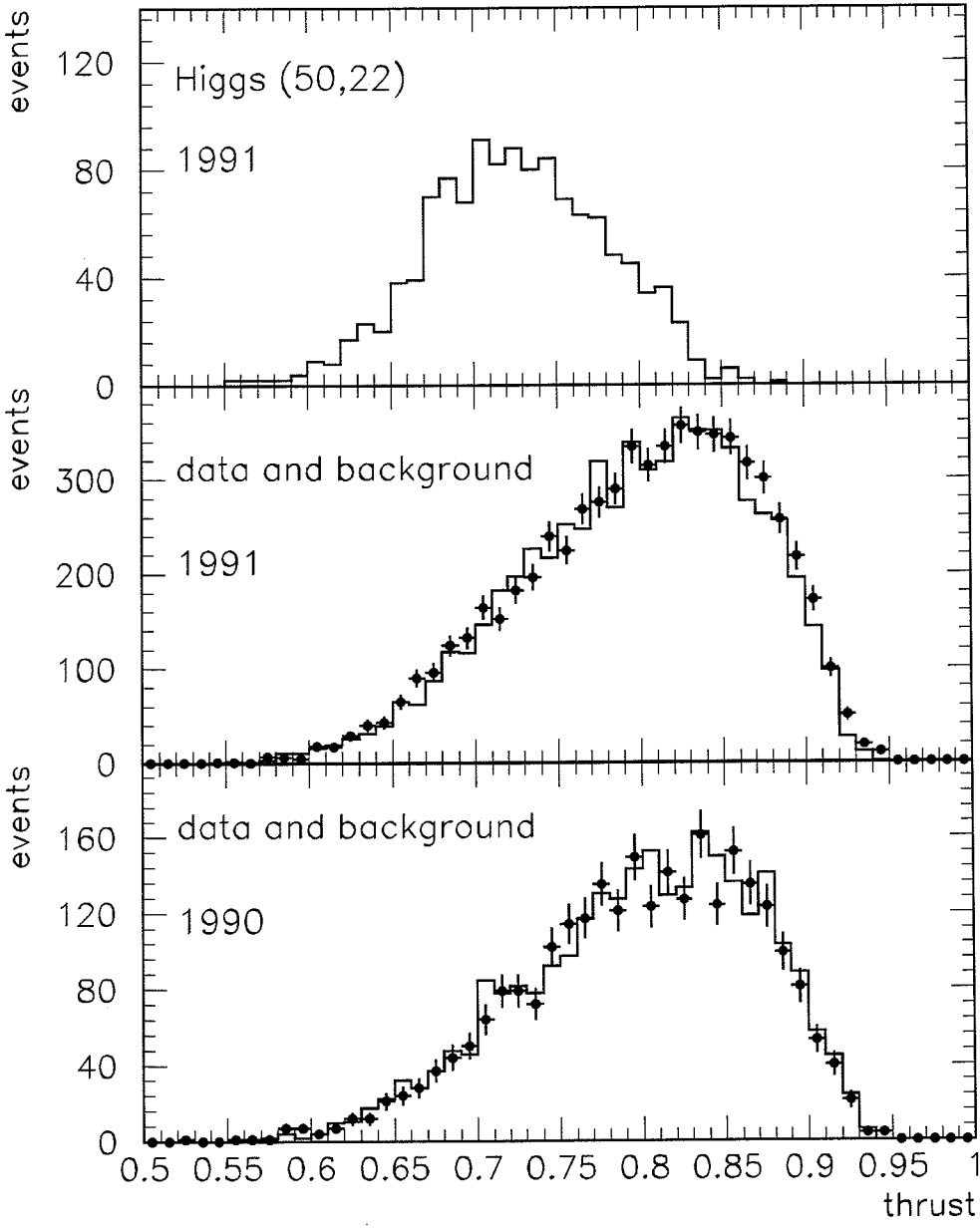

Figure B.2: Distribution of the thrust in the bbbbbb channel.

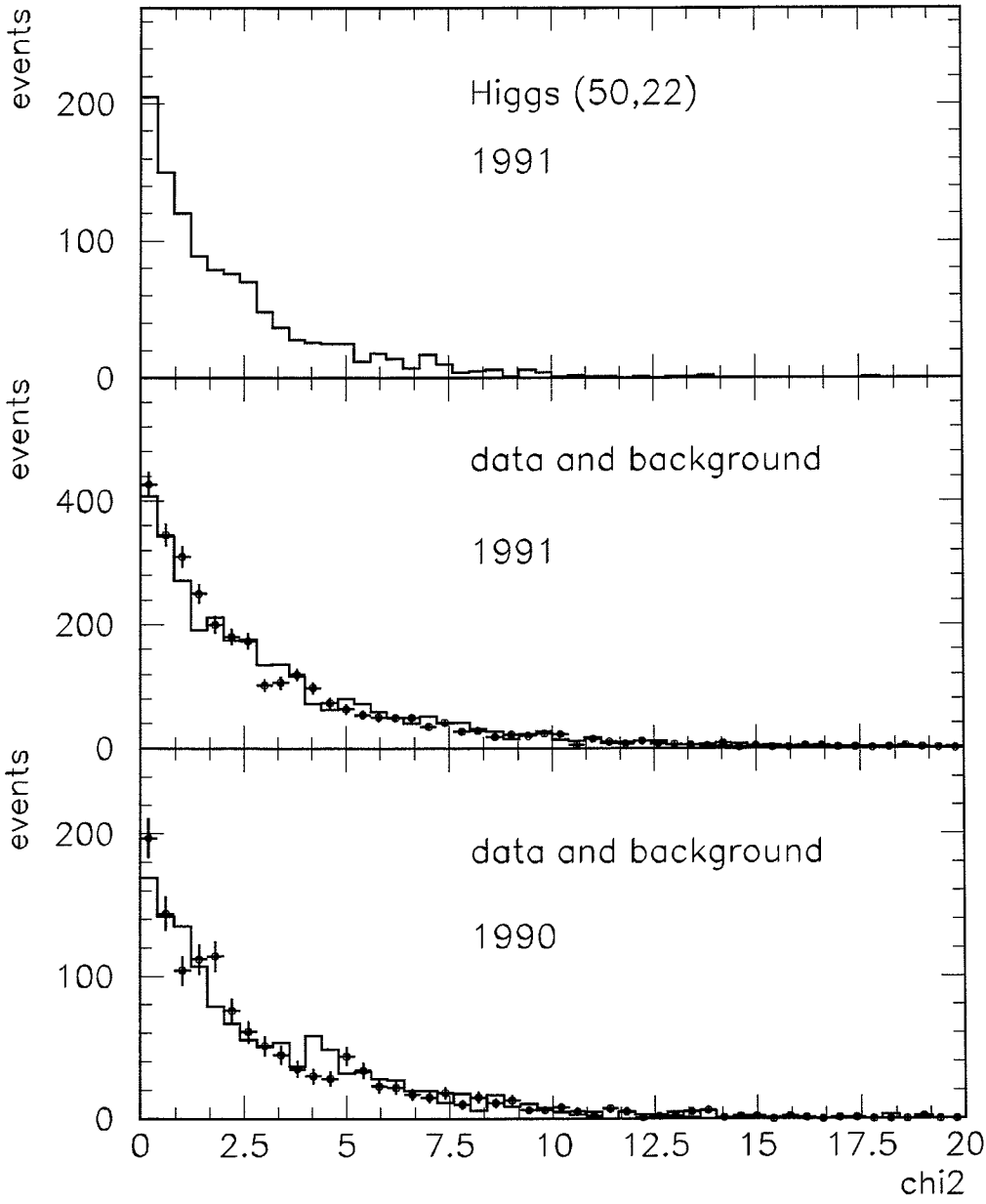

Figure B.3: Distribution of χ^2_{min} in the bbbbbb channel.

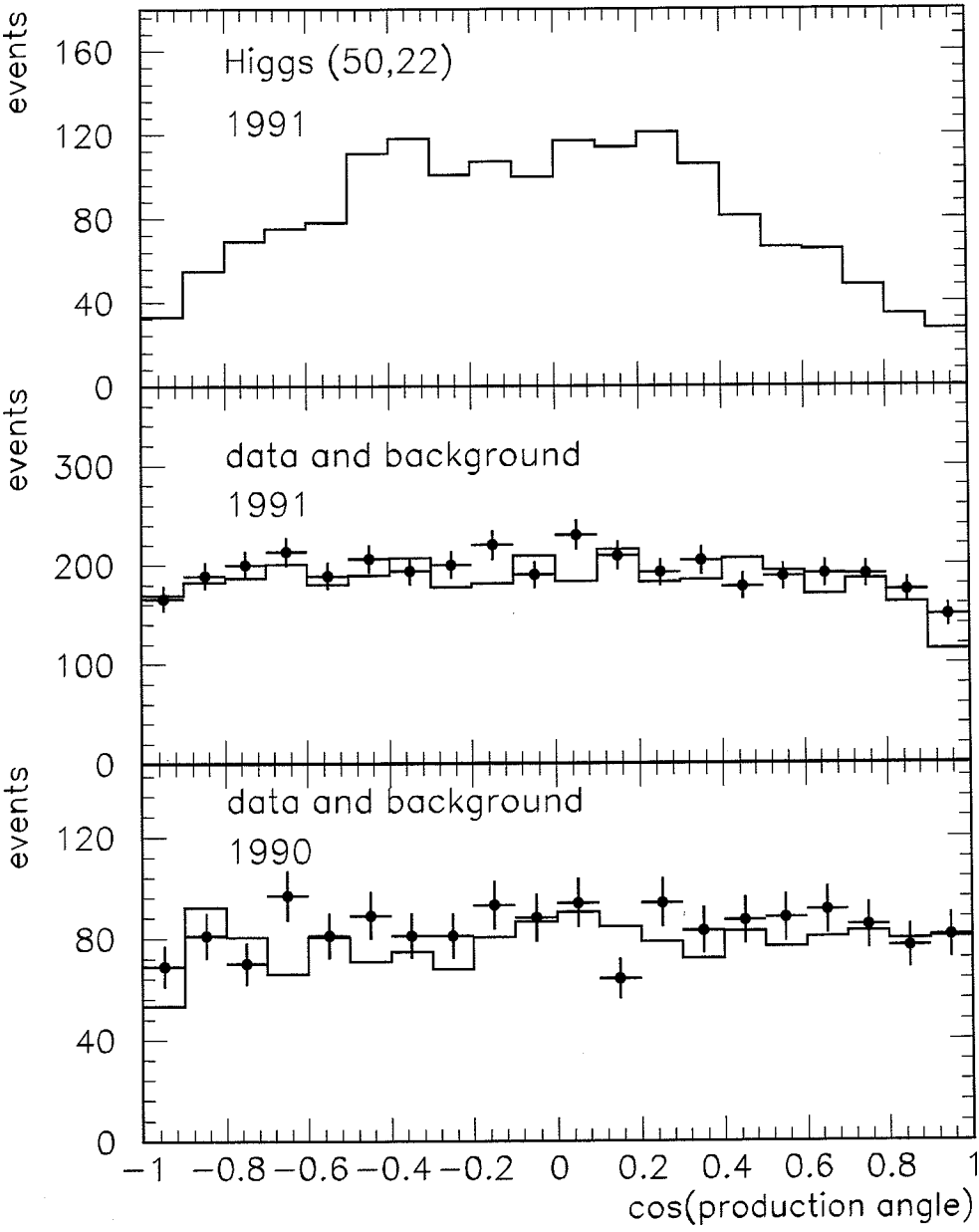

Figure B.4: Distribution of the production angle in the bbbbbb channel.

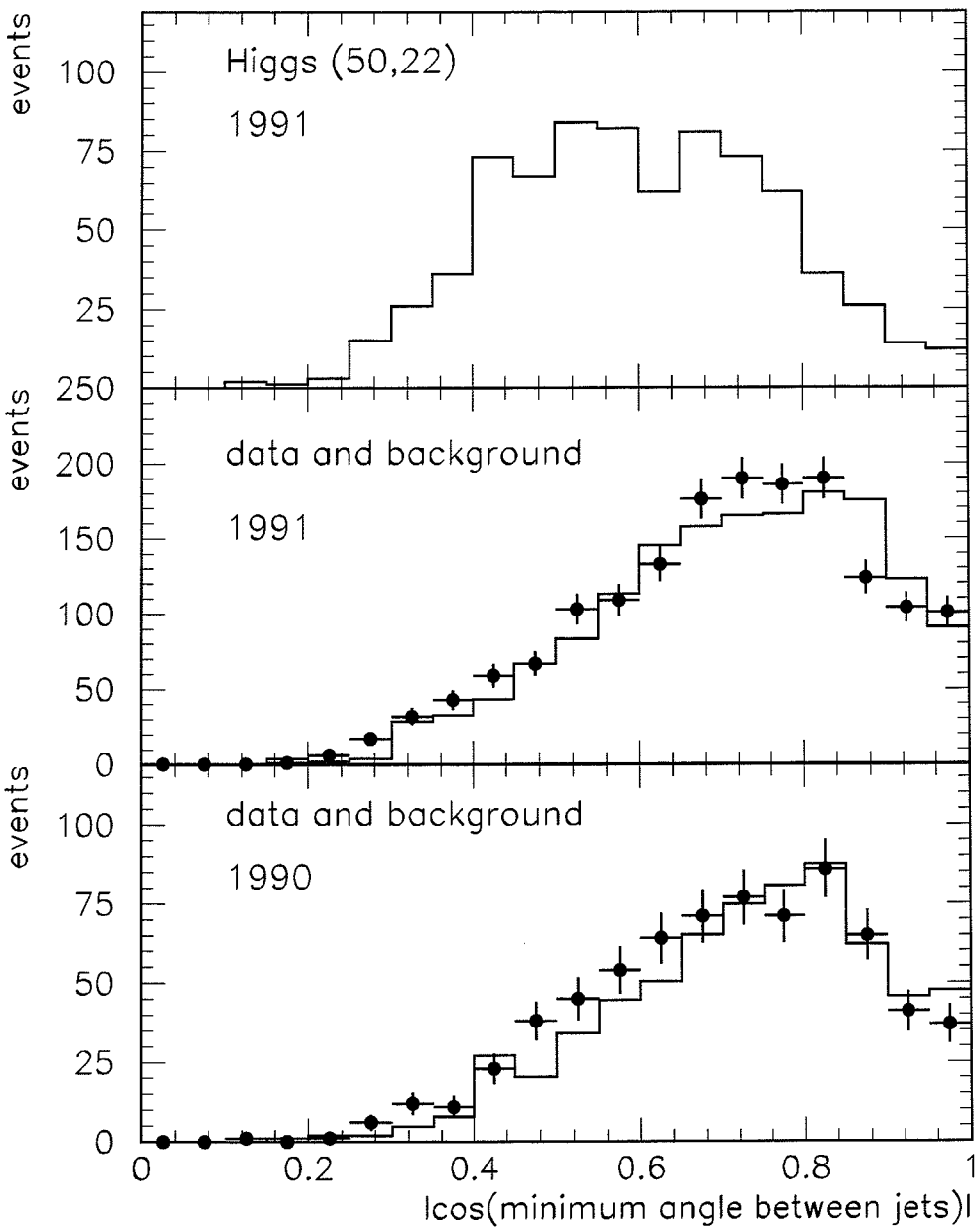

Figure B.5: Distribution of the minimum angle between jets in the bbbbbb channel.

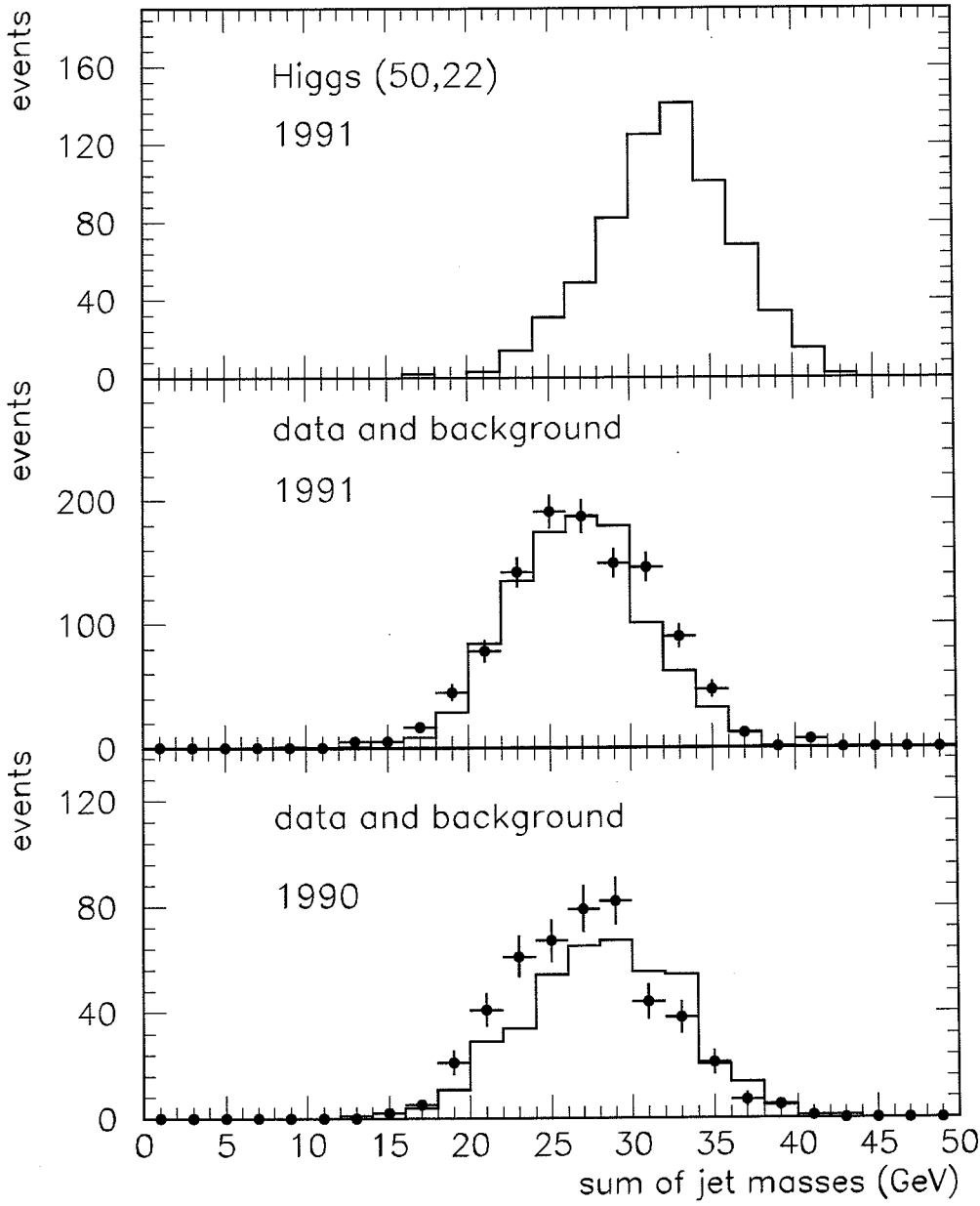

Figure B.6: Distribution of the sum of jet masses in the bbbbbb channel.

Appendix C

Distributions for the $Z^0 \longrightarrow h^0A^0 \longrightarrow \tau^+\tau^-b\bar{b}$ Search

Cut numbers and corresponding figure numbers are listed in table C.1. Figure C.1 gives an overview of the expected signal acceptances and numbers of data and background events after a cut is applied.

	$\tau\tau$bb Channel (22 GeV, 22 GeV)	
Cut#	Selection cuts	Fig#
1	$N_{cl} \geq 15$	C.6
2	$N_J \geq 2$	C.7
3	30 GeV $\geq E_\tau^{max}$	C.8
4	0.5 GeV $\leq E_\tau^{min}$	C.9
5	$N_\tau = 2$	C.10
6	$N_{tr} = 2$	C.11
7	$N_q = 0$	C.12
8	18 GeV $\leq m_{\tau\tau} \leq$ 26 GeV	C.13

Table C.1: Cut number and corresponding figure number in the $\tau\tau$bb channel.

C.1 Preselection in the $\tau\tau$bb Channel

Figures C.2 to C.5 show distributions of cut variables for the preselection.

C.2 Final Selection in the $\tau\tau$bb Channel

Figures C.6 to C.17 show distributions of cut variables for the final selection. Figures C.13, C.14, C.15, C.16 and C.17 belong to the last selection cut.

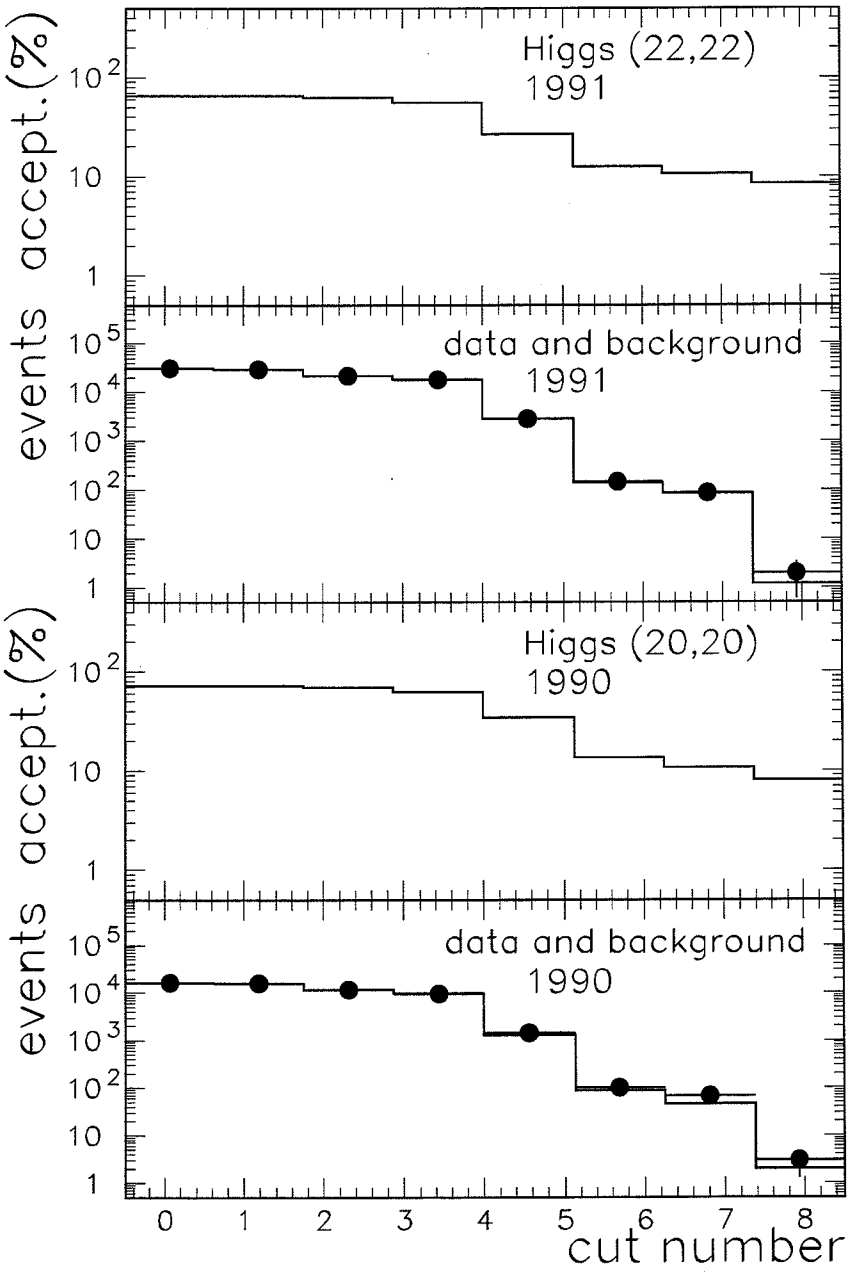

Figure C.1: Acceptances and numbers of data and background events after a cut is applied in the $\tau\tau$bb channel. Bin 0 corresponds to the preselection.

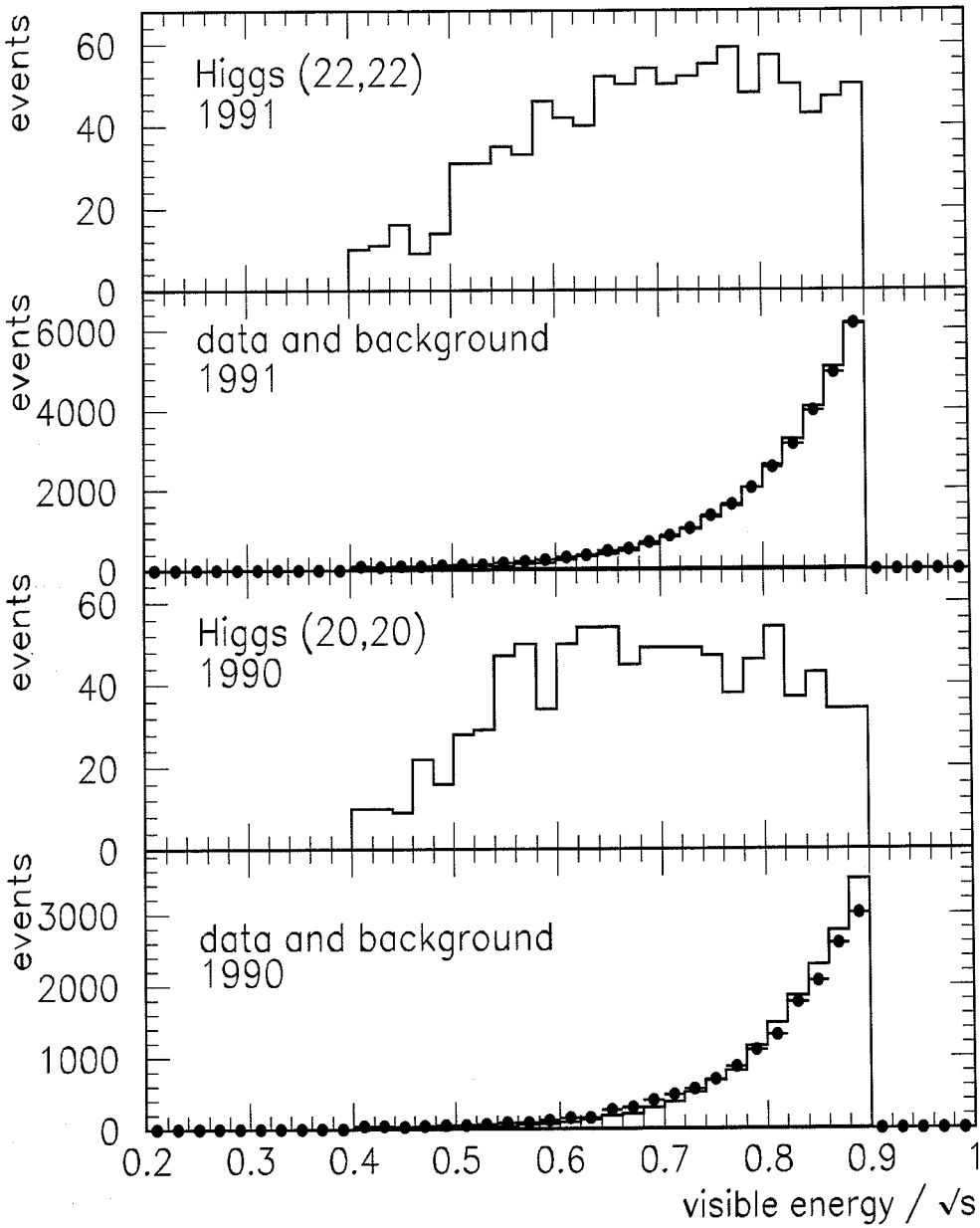

Figure C.2: Distribution of the visible energy in the $\tau\tau$bb channel.

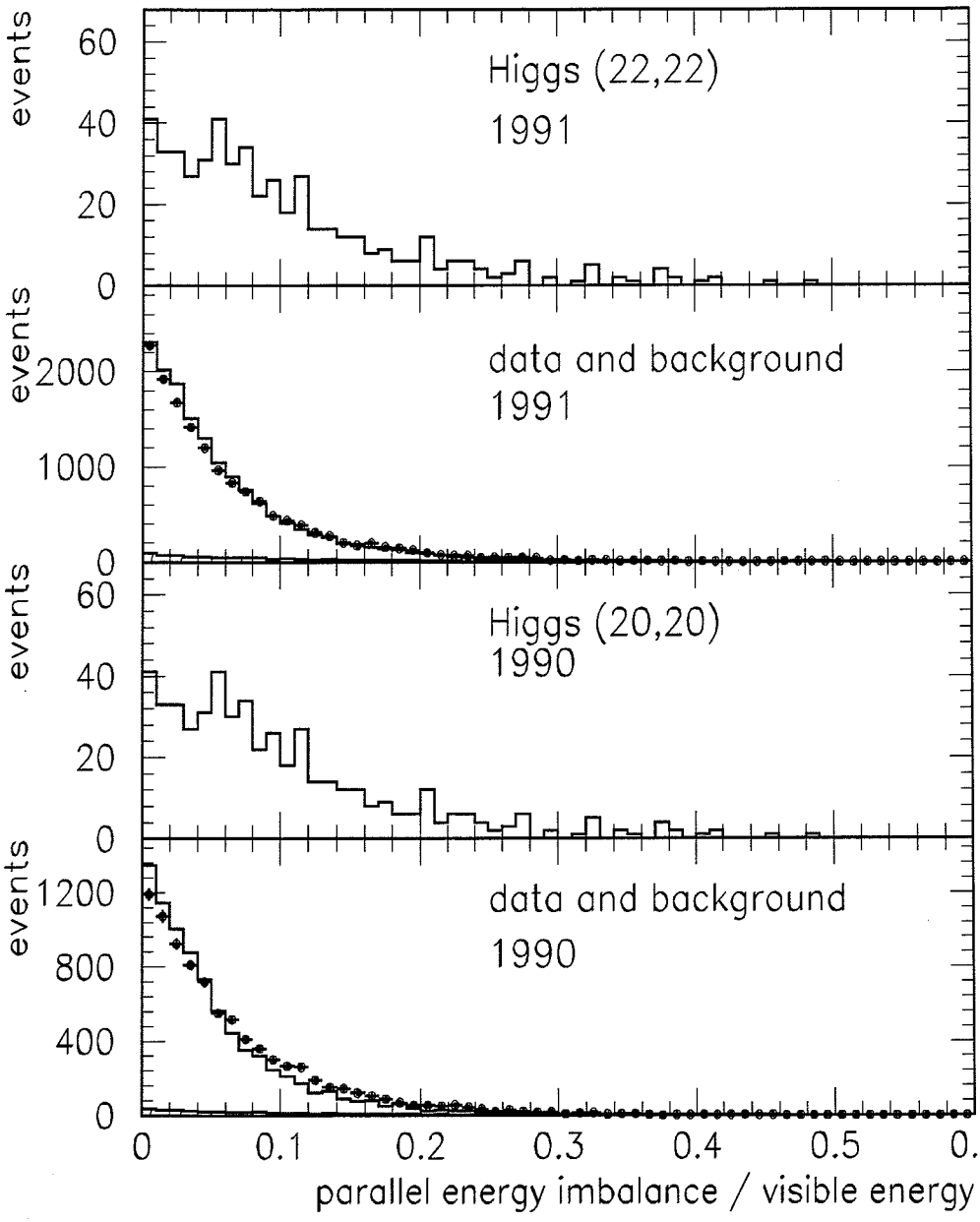

Figure C.3: Distribution of the parallel energy imbalance in the $\tau\tau$bb channel.

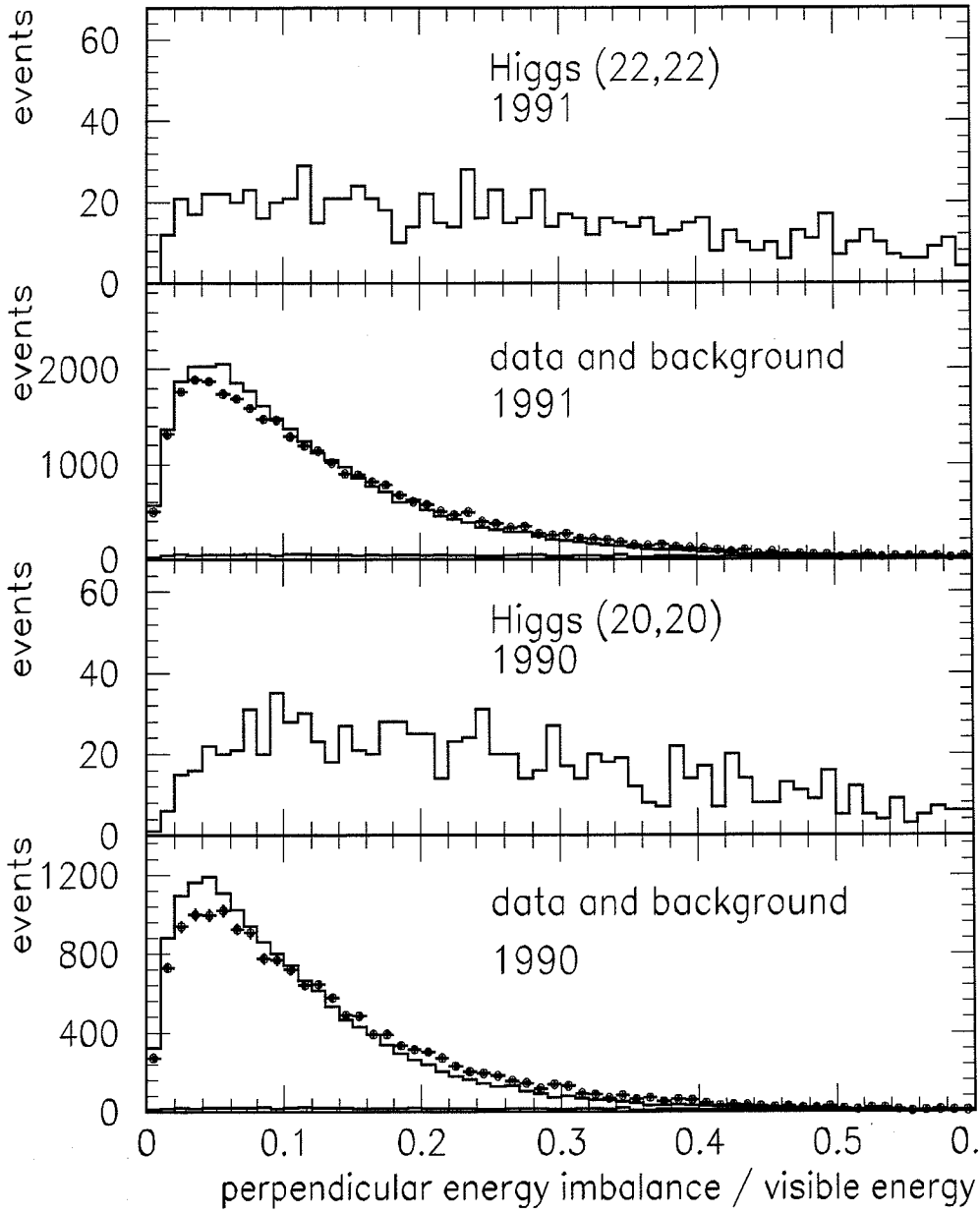

Figure C.4: Distribution of the perpendicular energy imbalance in the $\tau\tau$bb channel.

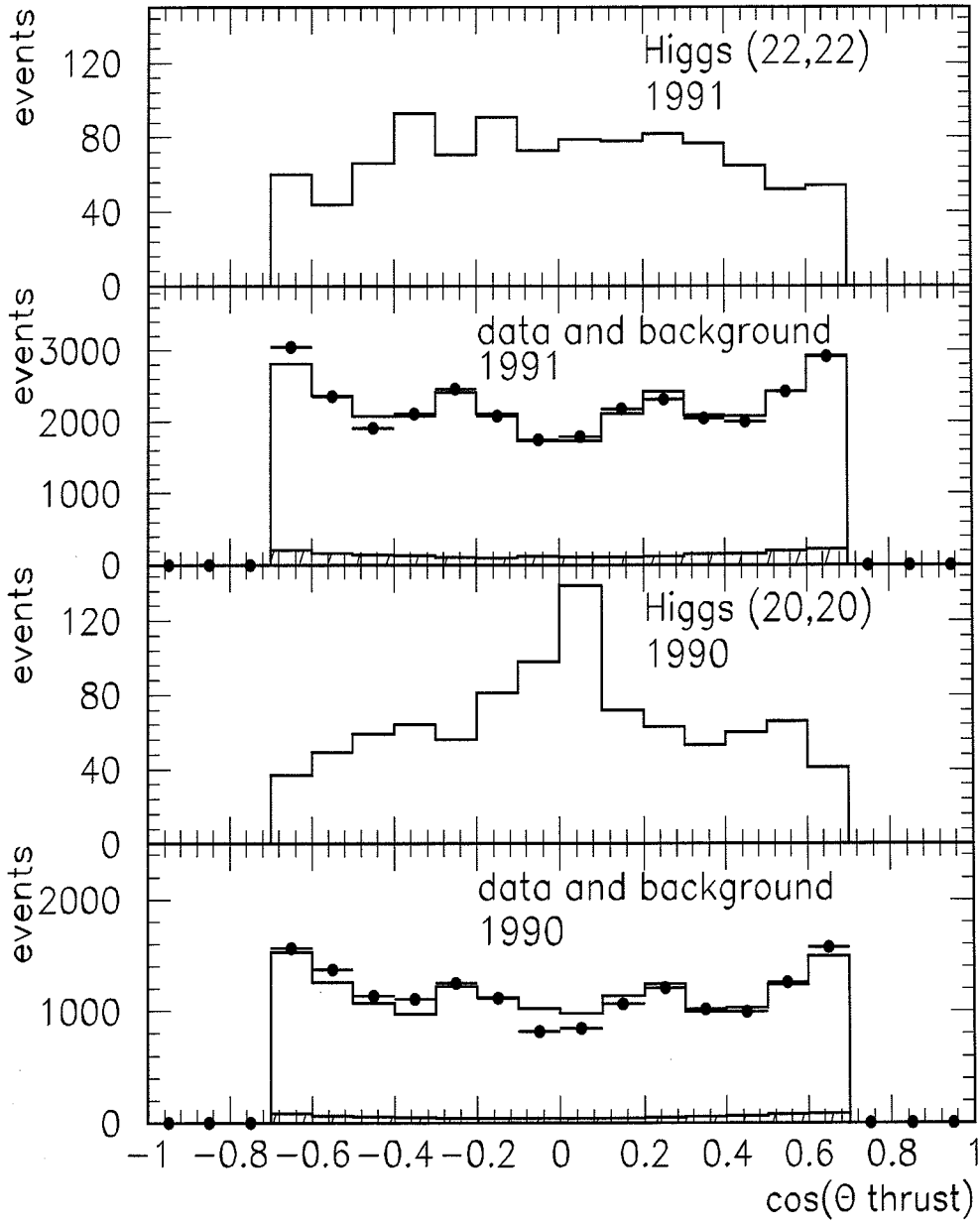

Figure C.5: Distribution of the thrust angle in the $\tau\tau$bb channel.

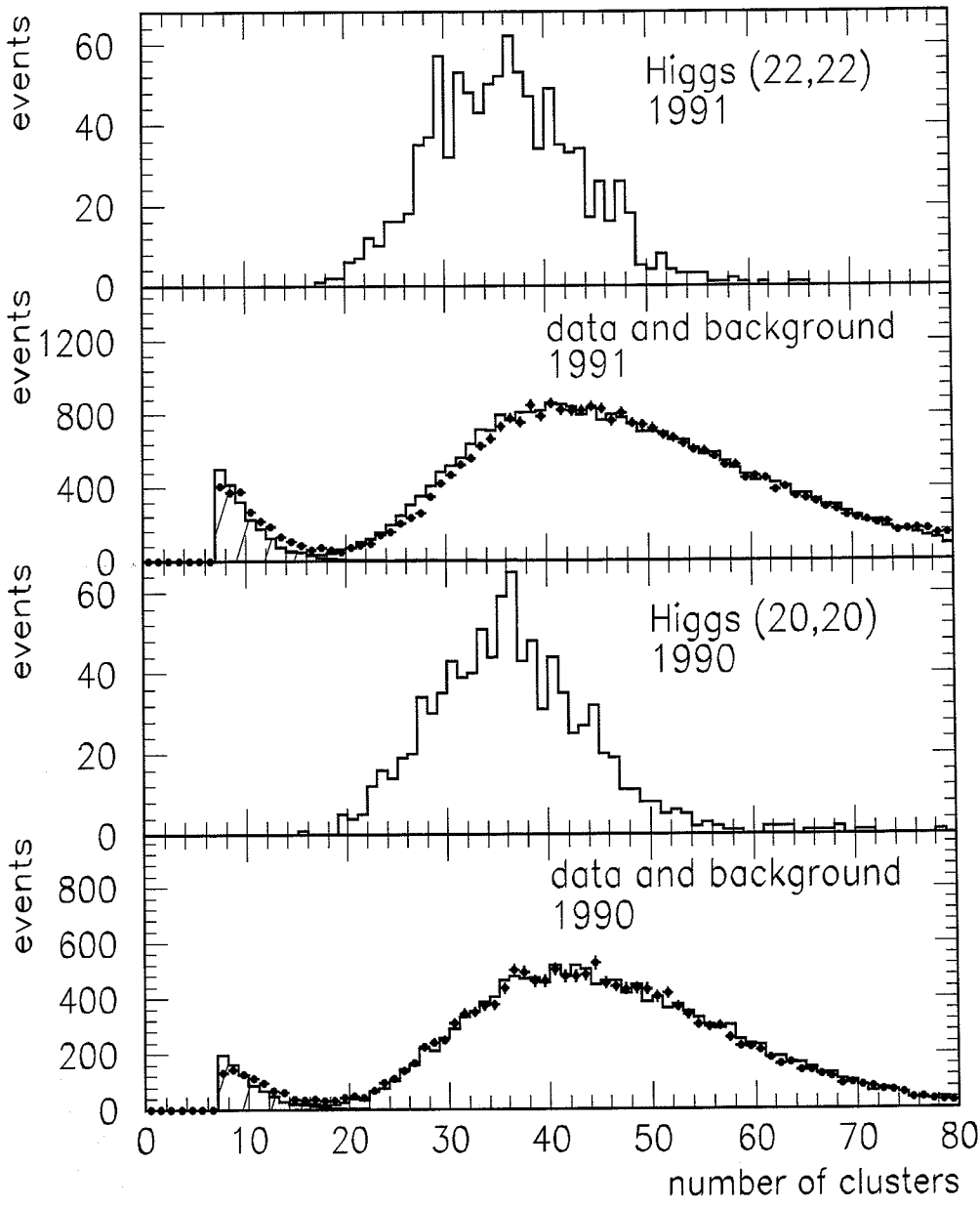

Figure C.6: Distribution of the number of calorimetric clusters in the $\tau\tau$bb channel.

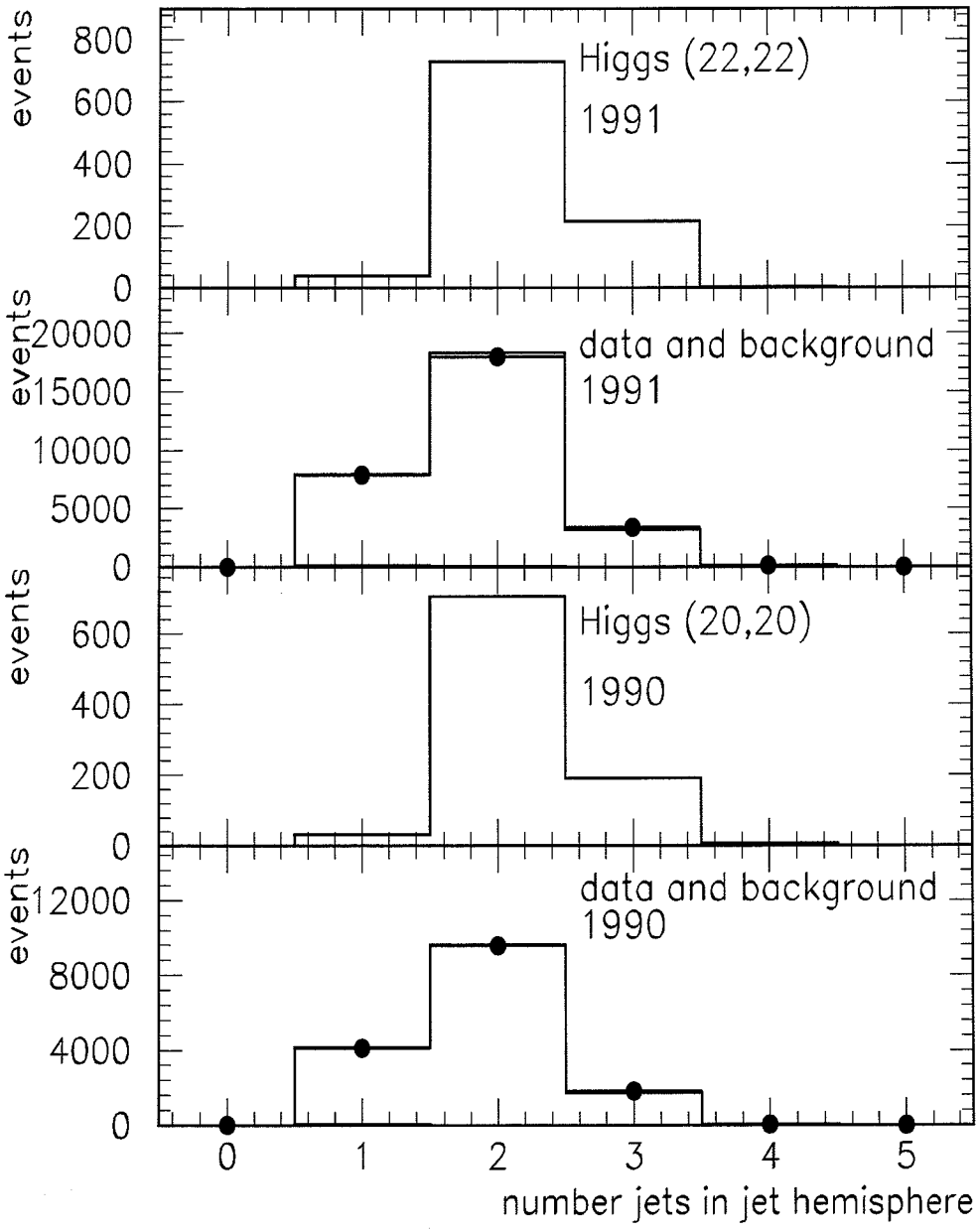

Figure C.7: Distribution of the number of wide jets in the jet hemisphere in the $\tau\tau$bb channel.

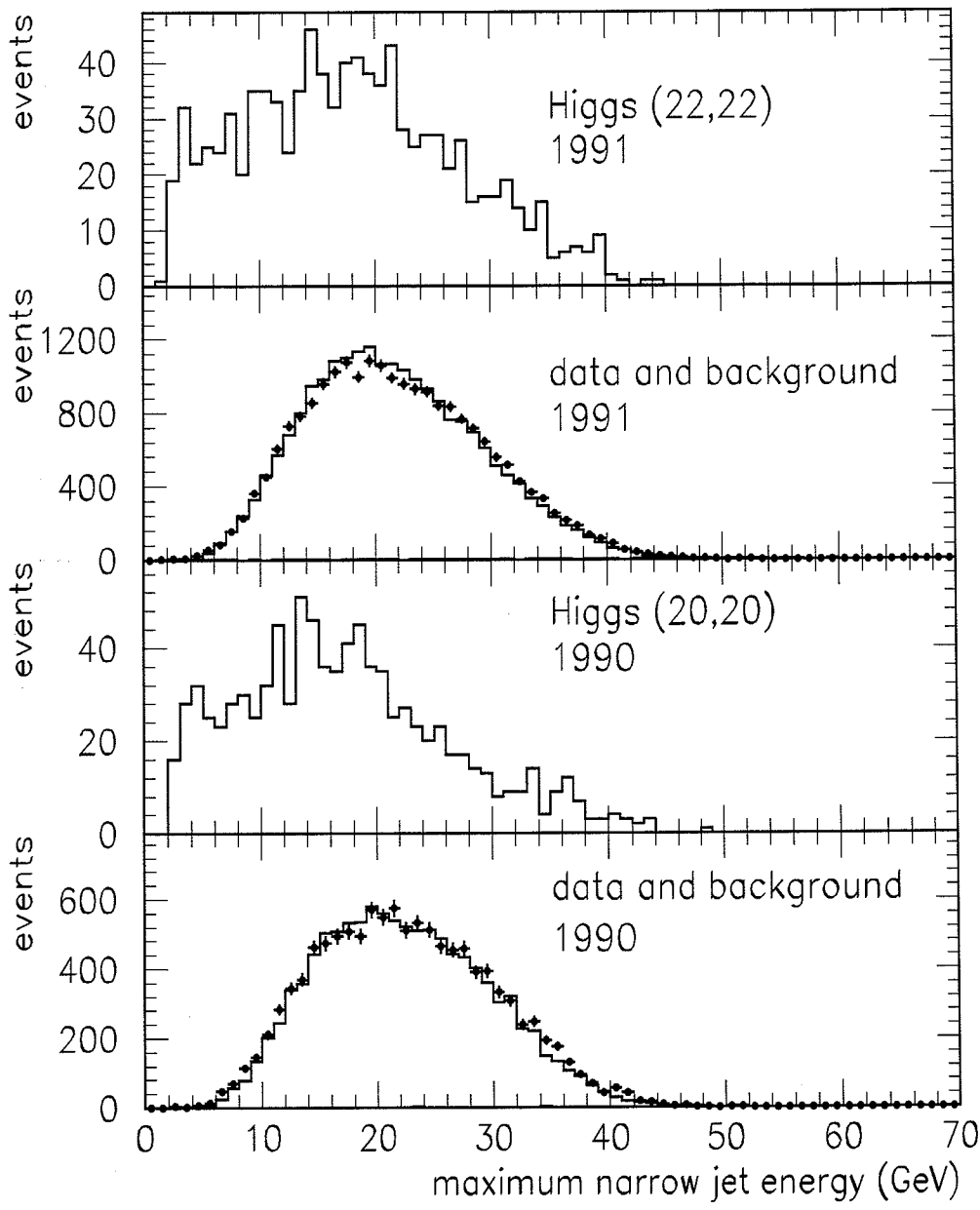

Figure C.8: Distribution of the maximum energy of narrow jets in the tau hemisphere in the $\tau\tau$bb channel.

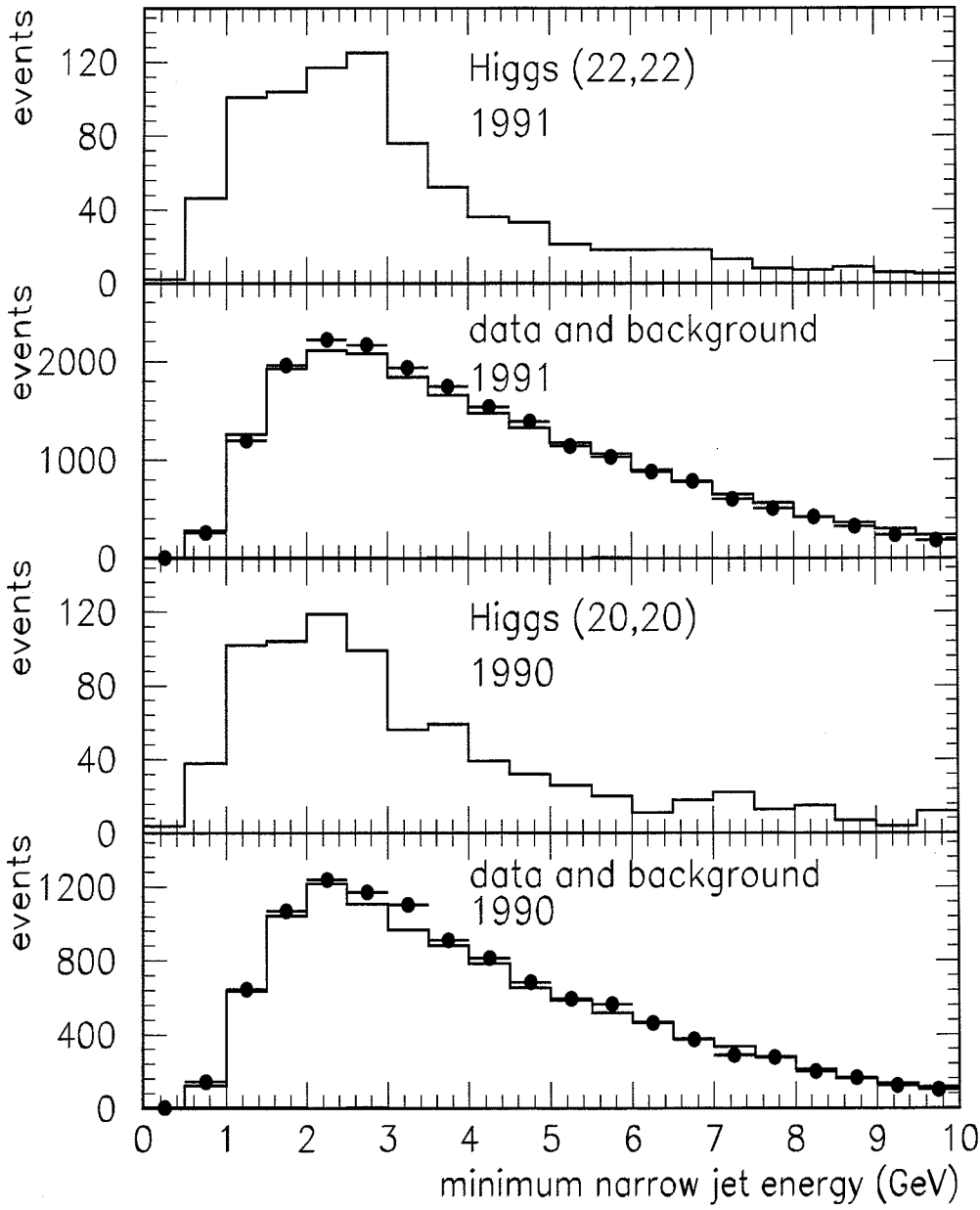

Figure C.9: Distribution of the minimum energy of narrow jets in the tau hemisphere in the $\tau\tau$bb channel.

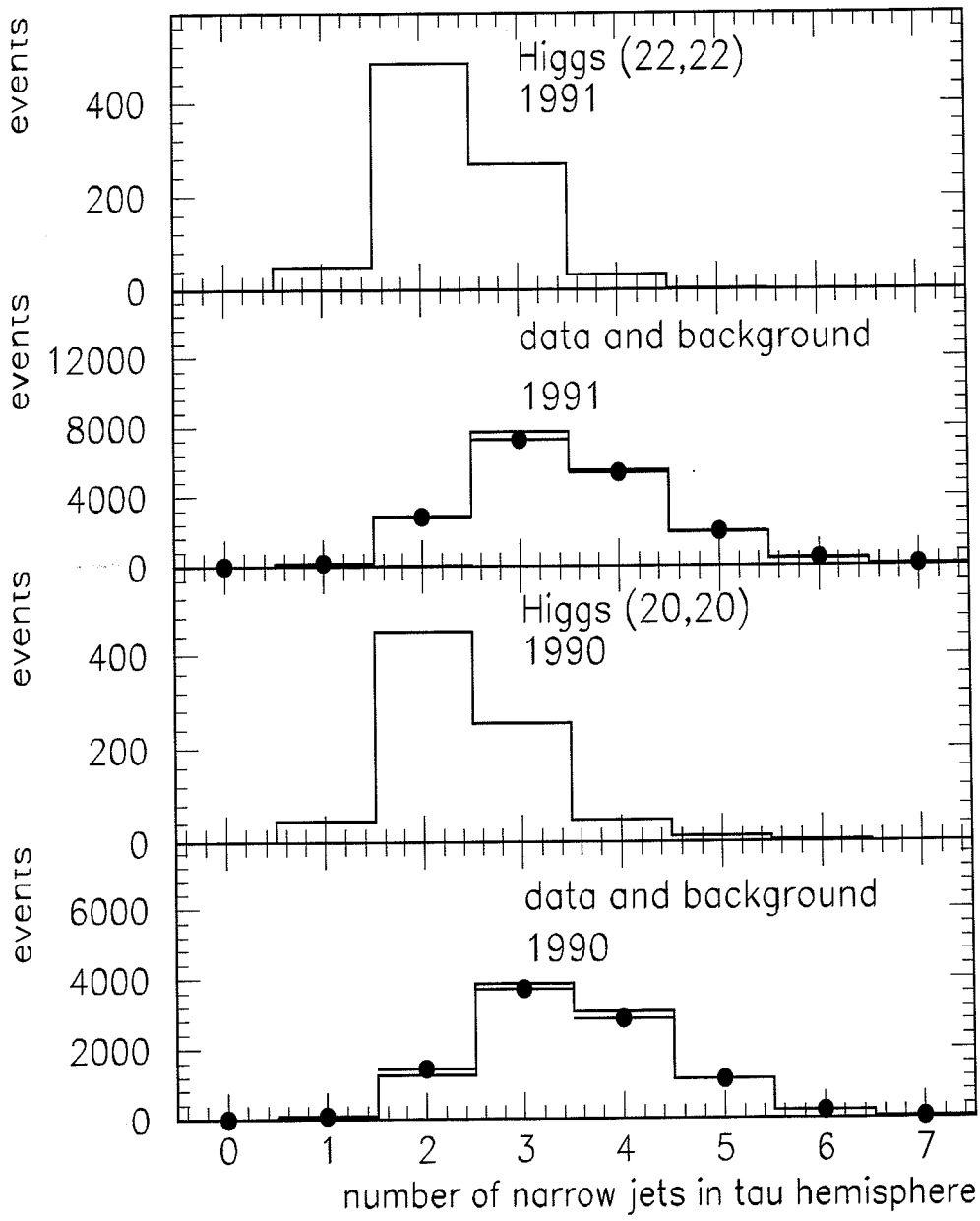

Figure C.10: Distribution of the number of narrow jets with energy above 0.5 GeV and below 30 GeV in the tau hemisphere in the $\tau\tau$bb channel.

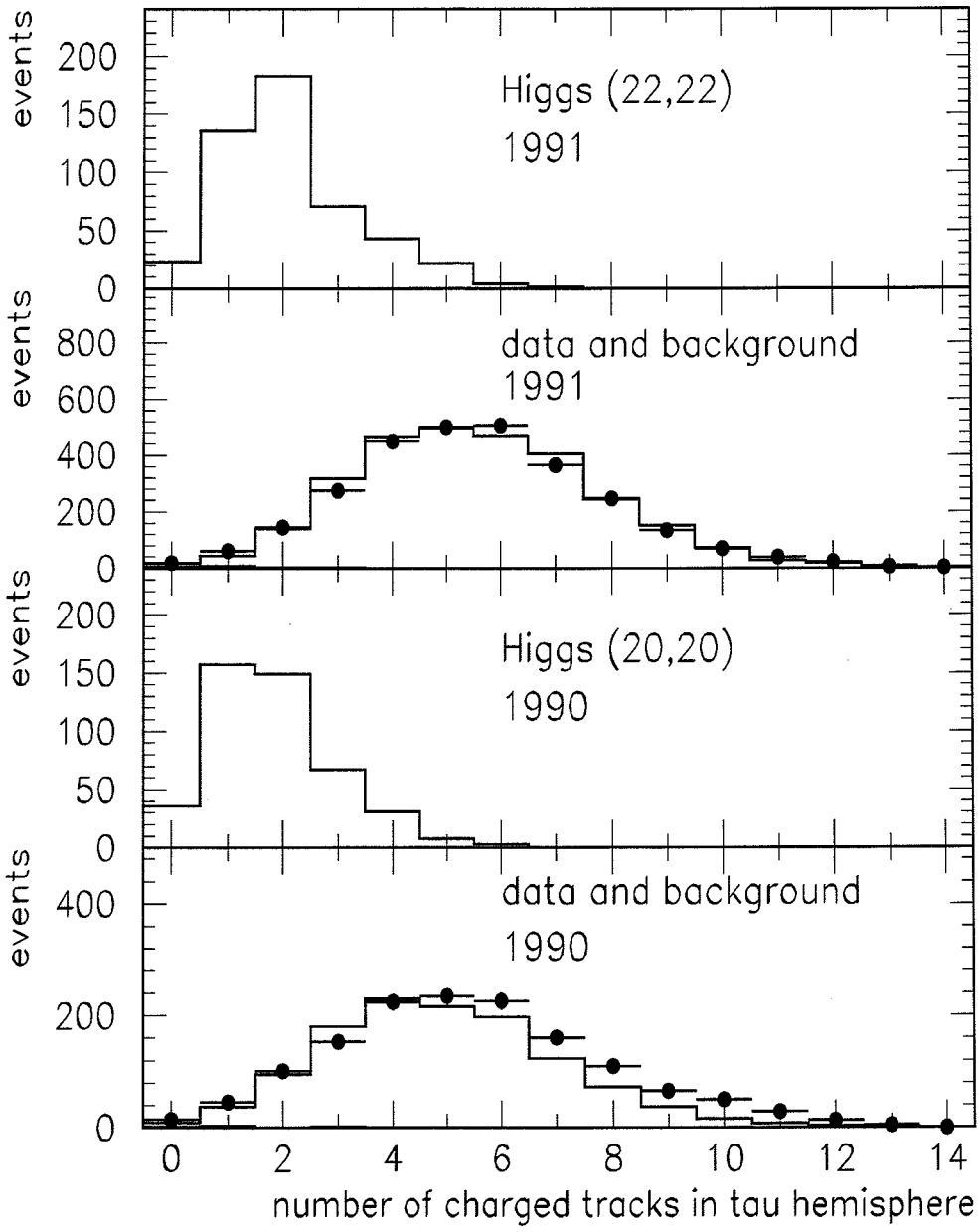

Figure C.11: Distribution of the number of charged tracks in the tau hemisphere in the $\tau\tau$bb channel.

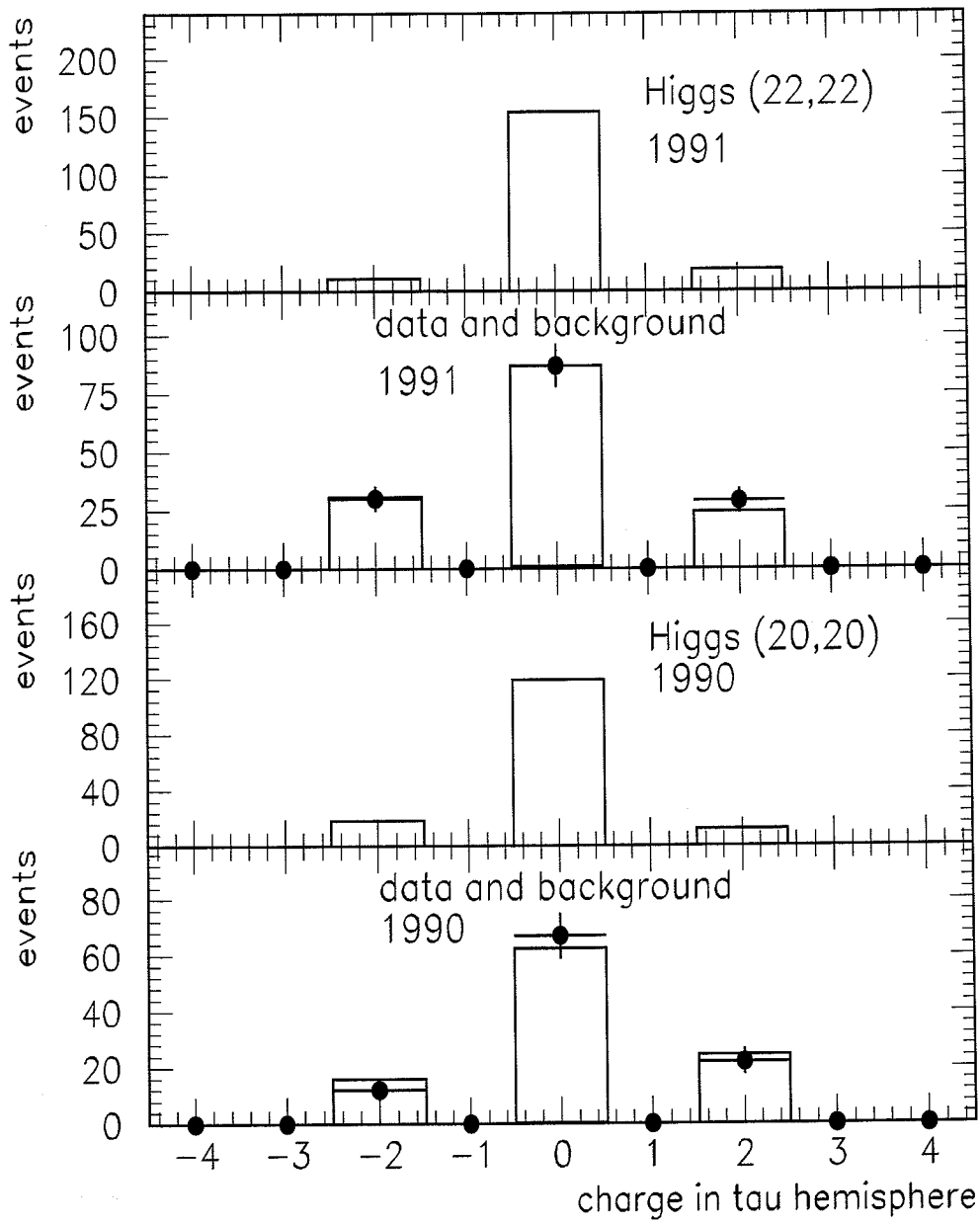

Figure C.12: Distribution of the total charge in the tau hemisphere for events with exactly two tracks in this hemisphere in the $\tau\tau$bb channel.

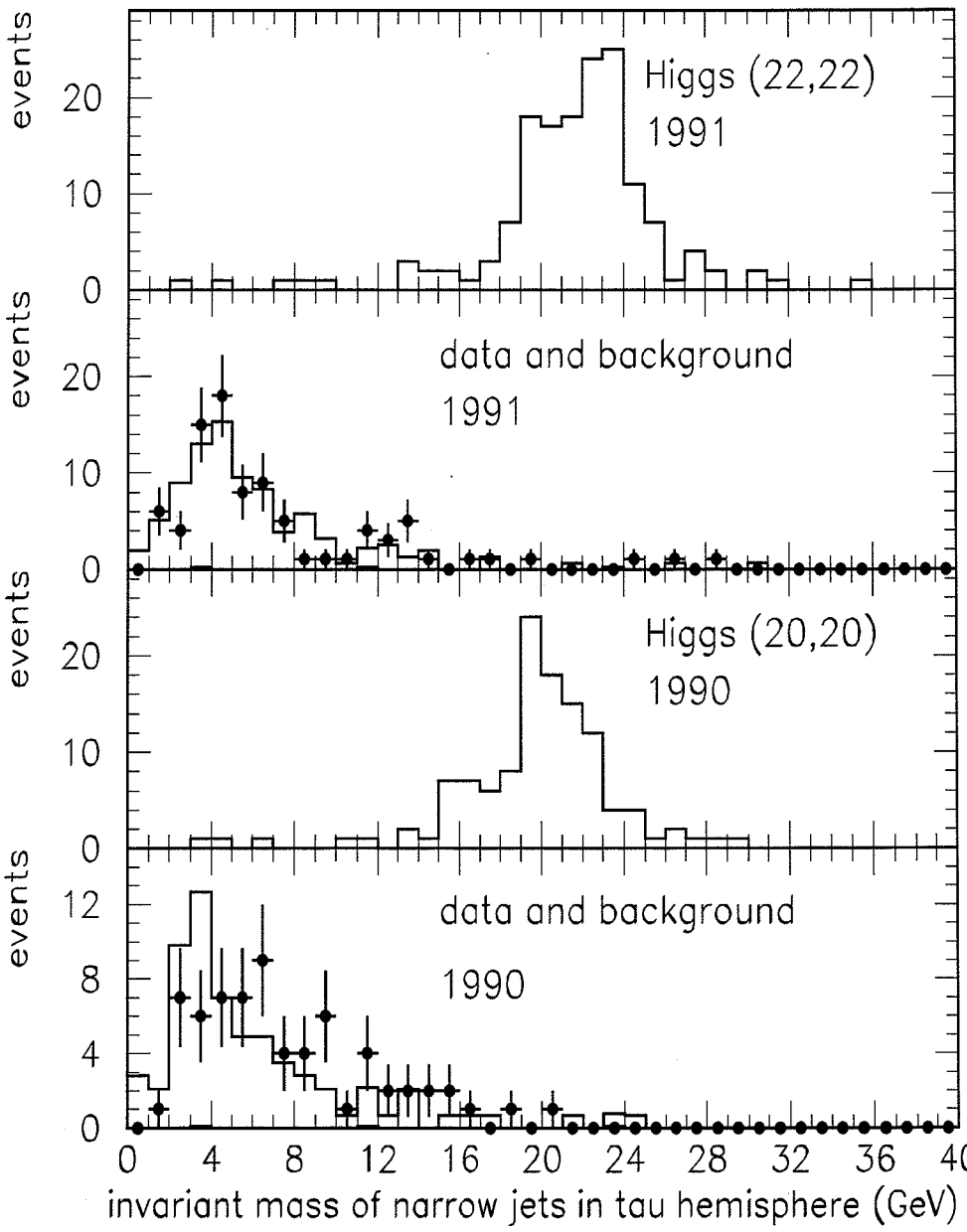

Figure C.13: Distribution of the reconstructed invariant mass of $\tau^+\tau^-$ pairs in the $\tau\tau$bb channel.

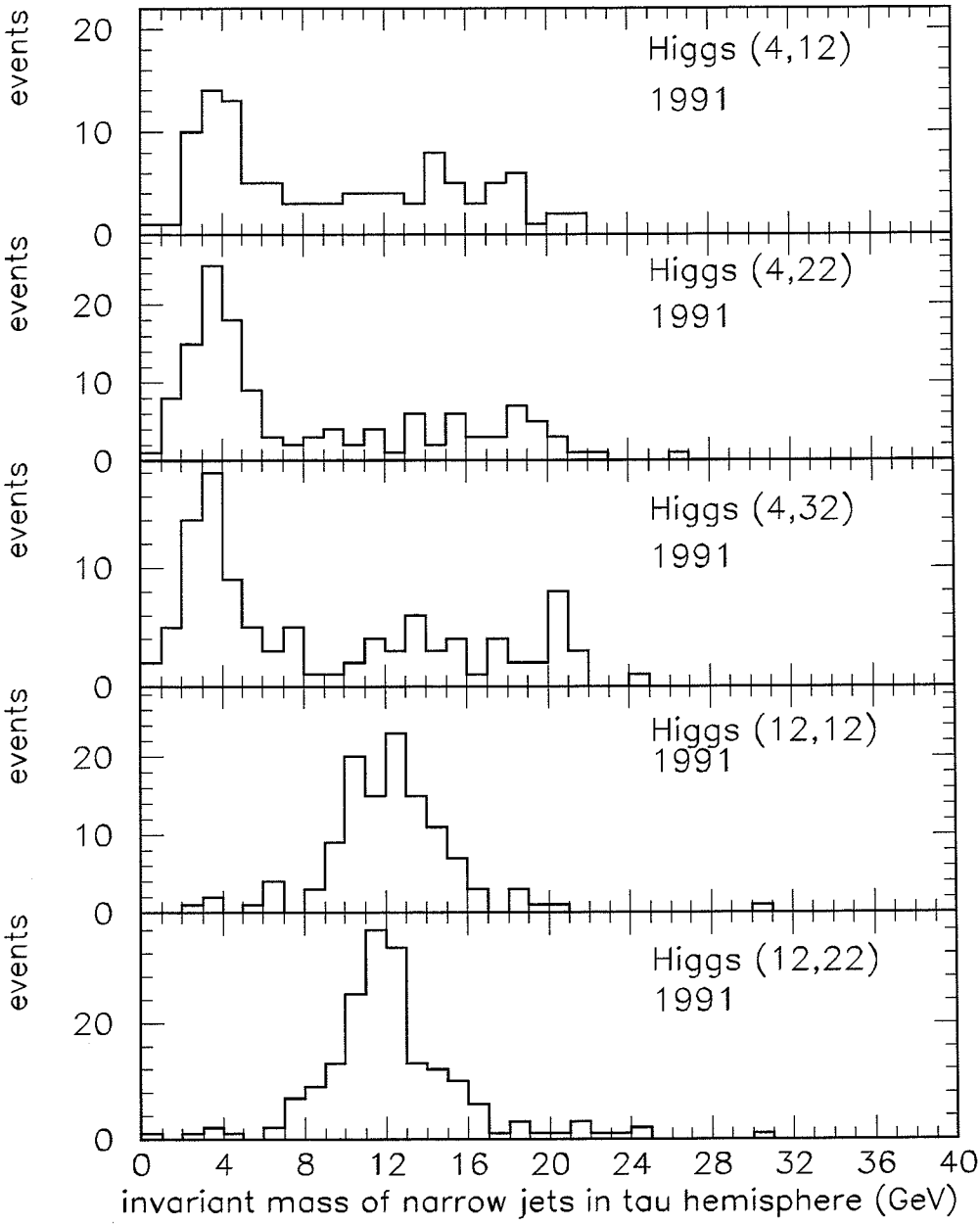

Figure C.14: Distribution of the reconstructed invariant mass of $\tau^+\tau^-$ pairs for various Higgs mass combinations in the $\tau\tau$bb channel.

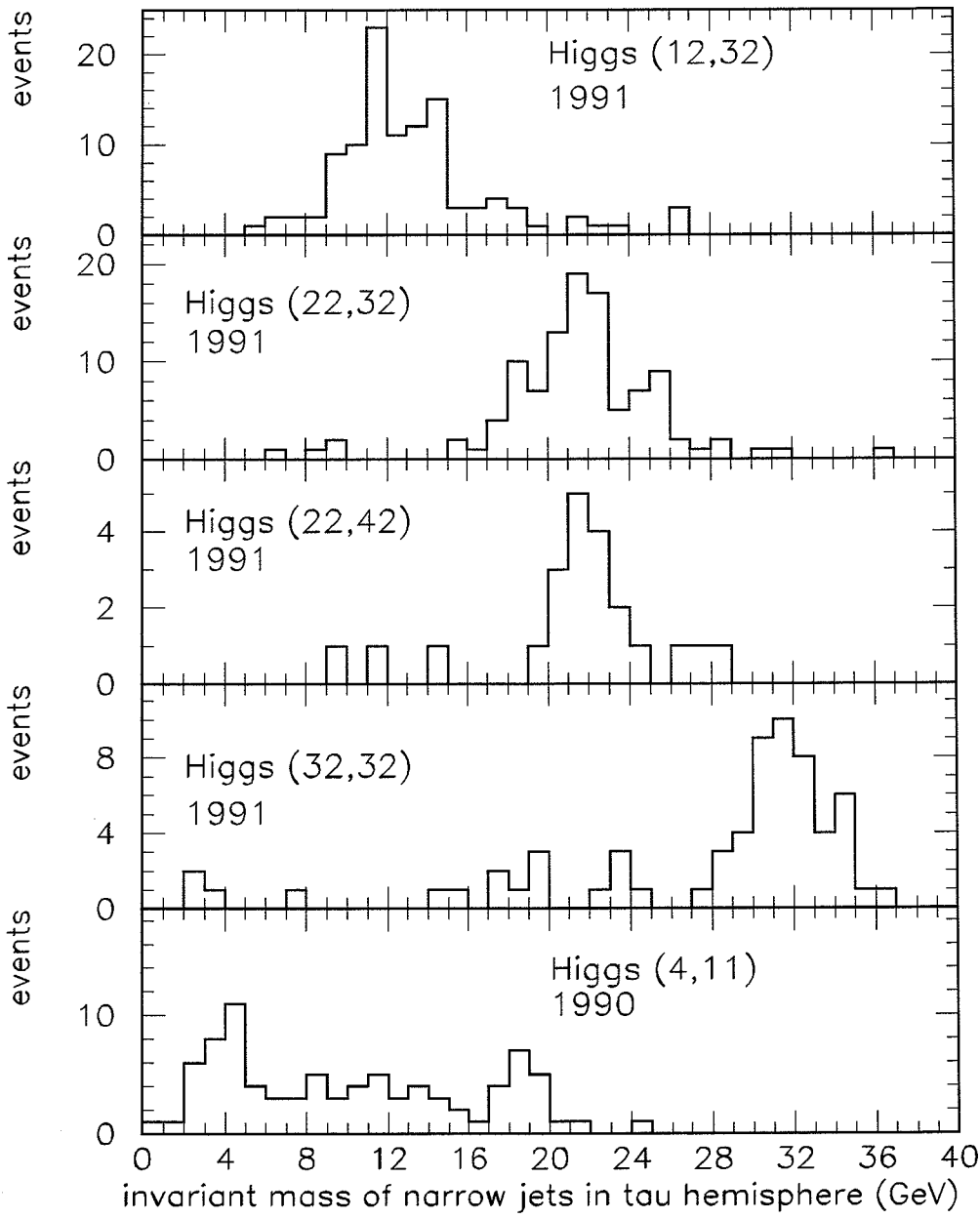

Figure C.15: Distribution of the reconstructed invariant mass of $\tau^+\tau^-$ pairs for various Higgs mass combinations in the $\tau\tau$bb channel.

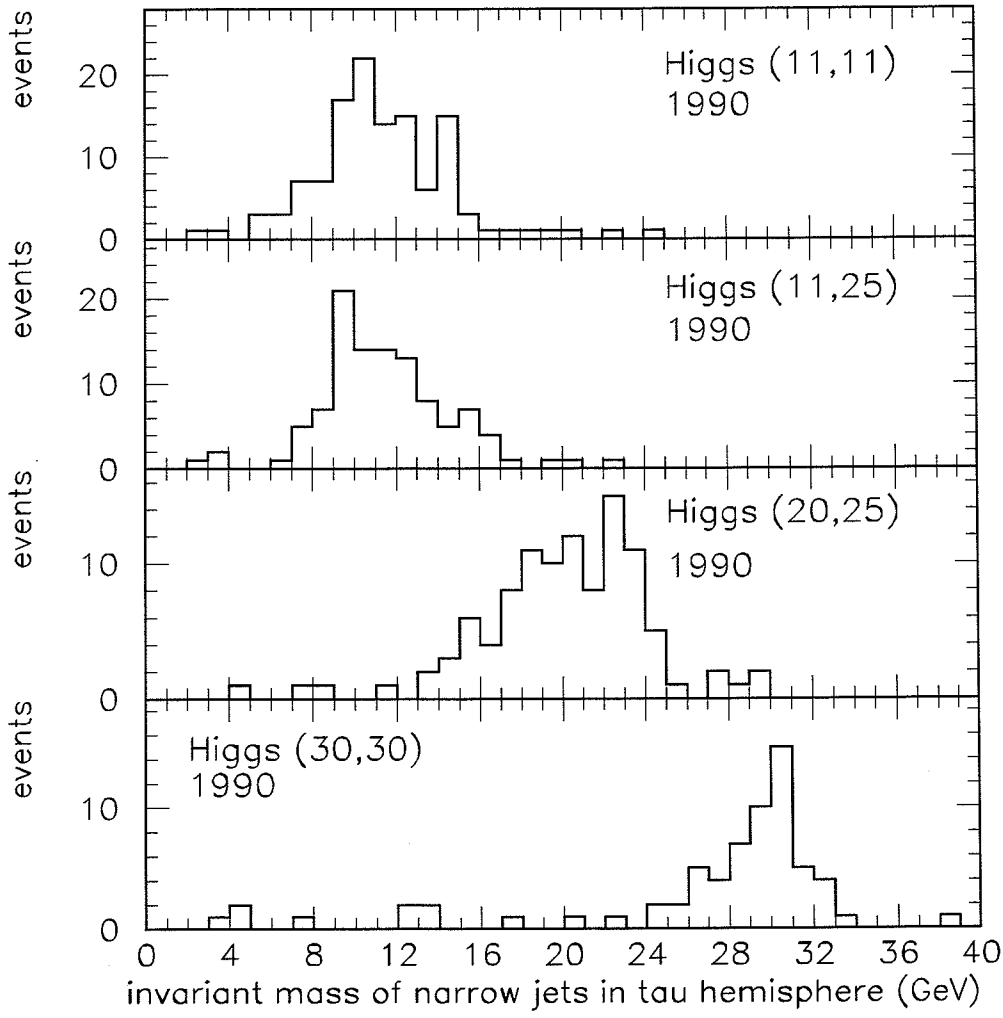

Figure C.16: Distribution of the reconstructed invariant mass of $\tau^+\tau^-$ pairs for various Higgs mass combinations in the $\tau\tau$bb channel.

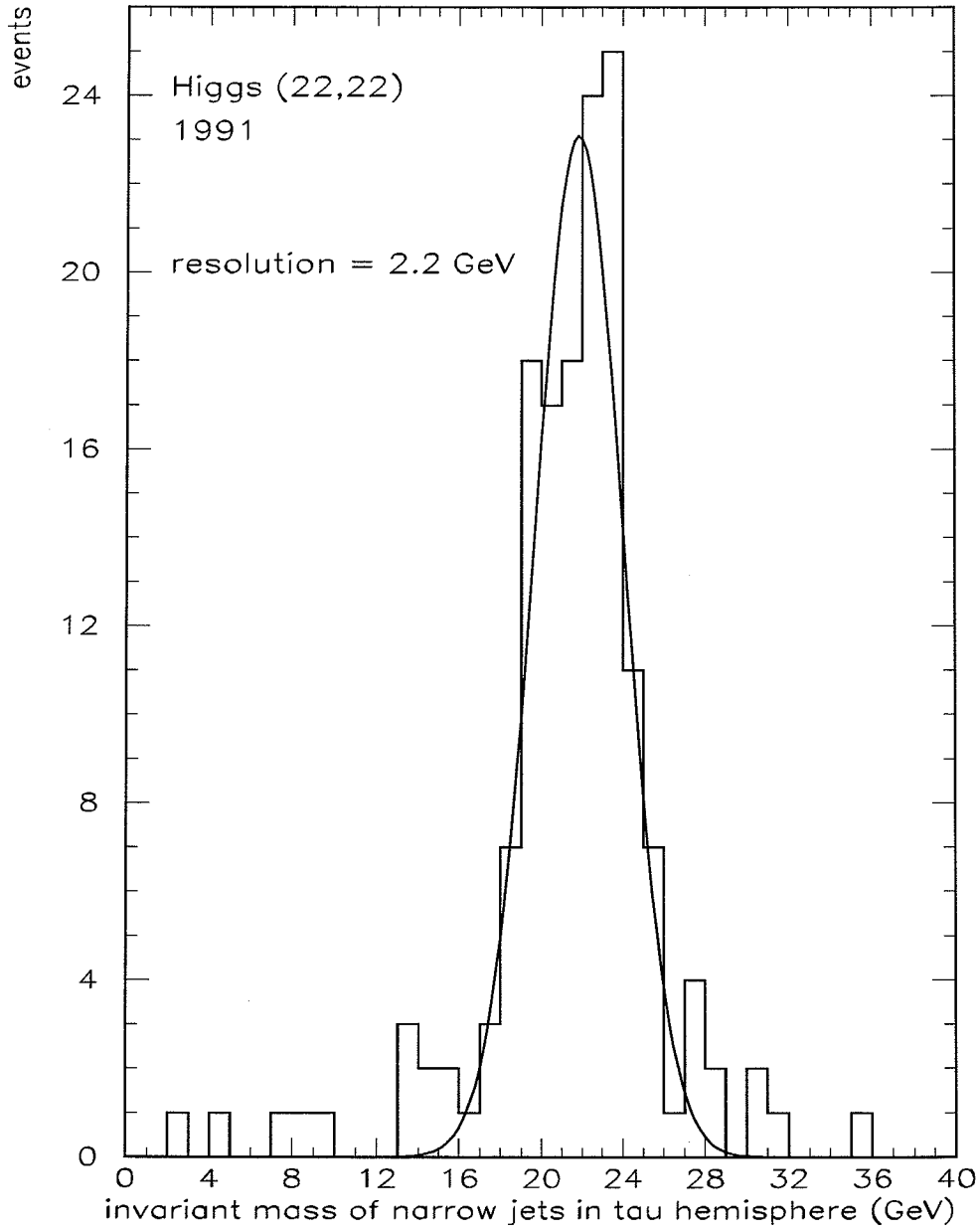

Figure C.17: Resolution of the reconstructed invariant mass of $\tau^+\tau^-$ pairs for $m_{\mathrm{h}} = 22$ GeV and $m_{\mathrm{A}} = 22$ GeV in the $\tau\tau$bb channel.

Appendix D

Distributions for the $Z^0 \rightarrow h^0A^0 \rightarrow \tau^+\tau^-\tau^+\tau^-$ Search

Cut numbers and corresponding figure numbers are listed in table D.1. Figure D.1 gives an overview of the expected signal acceptances and numbers of data and background events after a cut is applied.

	$\tau\tau\tau\tau$ Channel (12 GeV, 12 GeV)	
Cut#	Selection cuts	Fig#
1	$N_{cl} \leq 15$	D.3
2	30 GeV $\geq E_\tau^{\max}$	D.4
3	0.5 GeV $\leq E_\tau^{\min}$	D.5
4	$N_\tau^l = 2$ $N_\tau^h = 2$ or 3	D.6
5	$N_{tr} = 2$	D.7
6	$N_q = 0$	D.8

Table D.1: Cut number and corresponding figure number in the $\tau\tau\tau\tau$ channel.

D.1 Preselection in the $\tau\tau\tau\tau$ Channel

The same preselection as for the $\tau\tau$bb channel is applied. The expected $\tau\tau\tau\tau$ signal has lower energy as compared to the $\tau\tau$bb signal as shown in Figure D.2

D.2 Final Selection in the $\tau\tau\tau\tau$ Channel

Figures D.3 to D.8 show distributions of cut variables for the final selection.

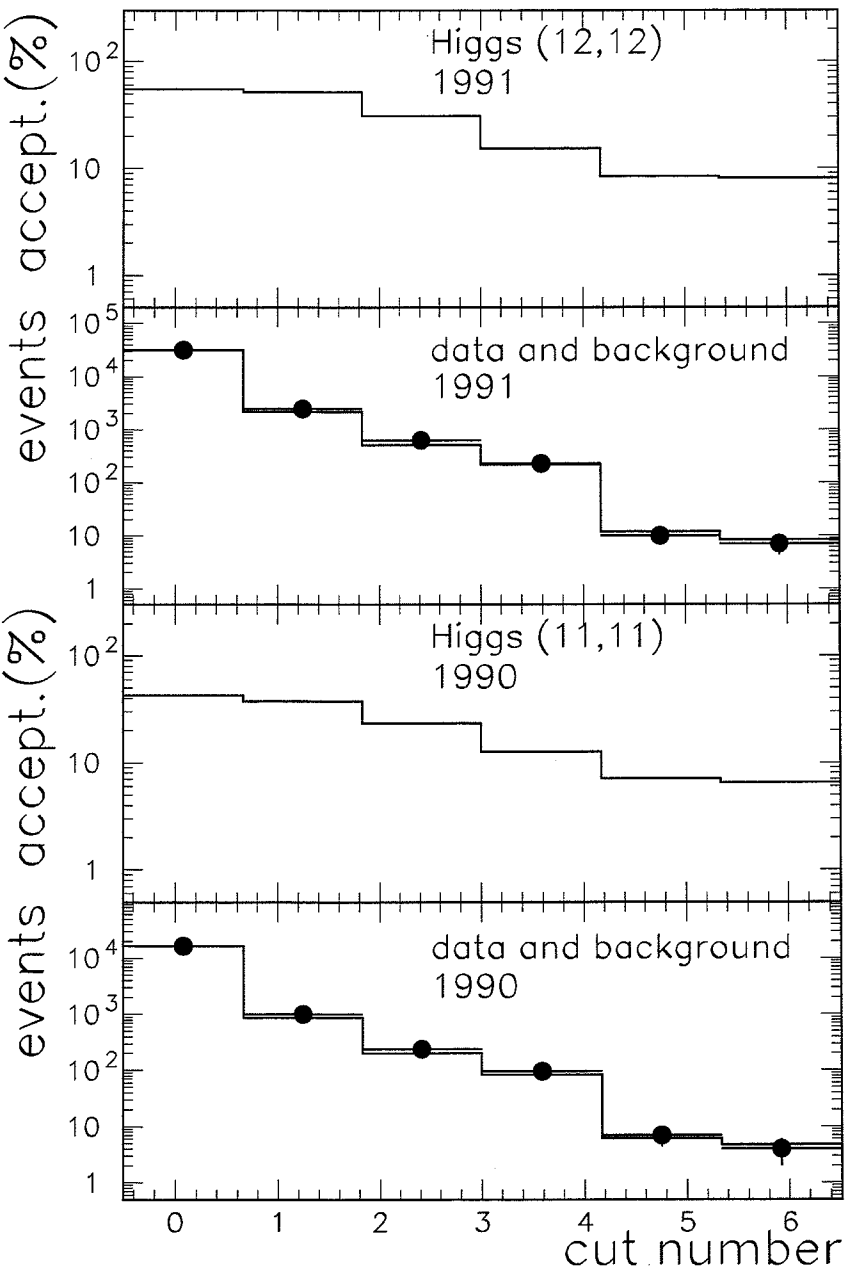

Figure D.1: Acceptances and numbers of data and background events after a cut is applied in the $\tau\tau\tau\tau$ channel. Bin 0 corresponds to the preselection.

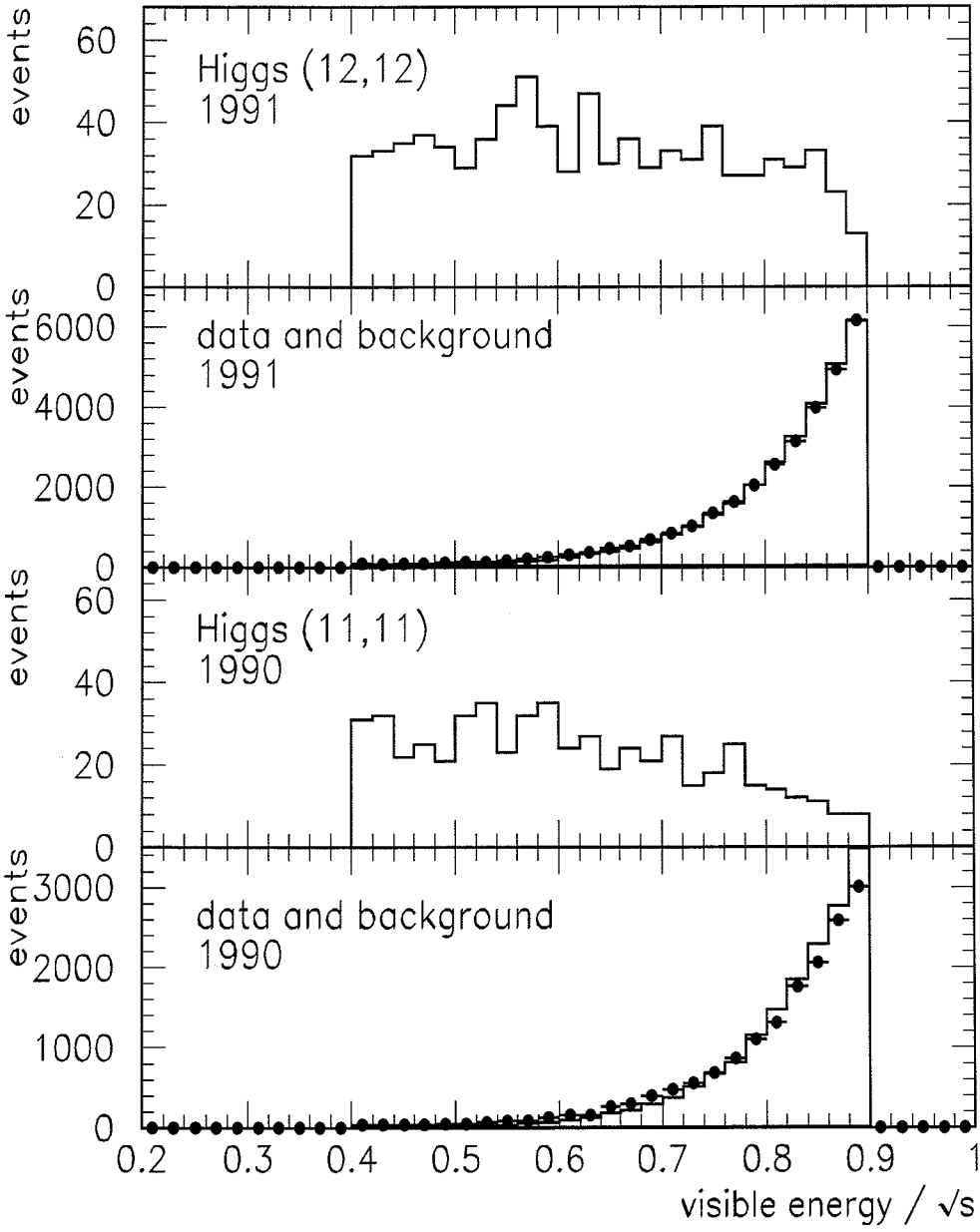

Figure D.2: Distribution of the visible energy in the $\tau\tau\tau\tau$ channel.

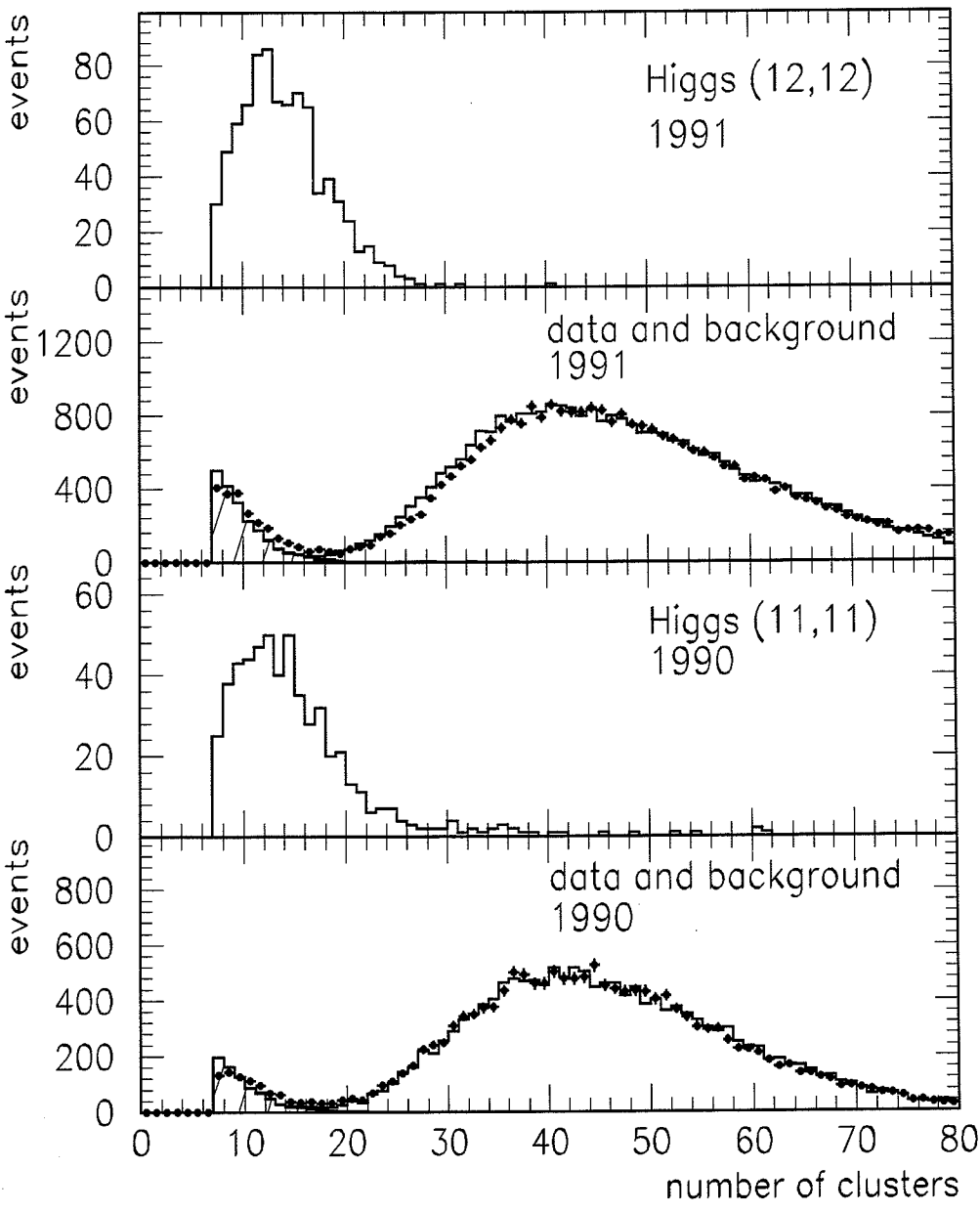

Figure D.3: Distribution of the number of calorimetric clusters in the $\tau\tau\tau\tau$ channel.

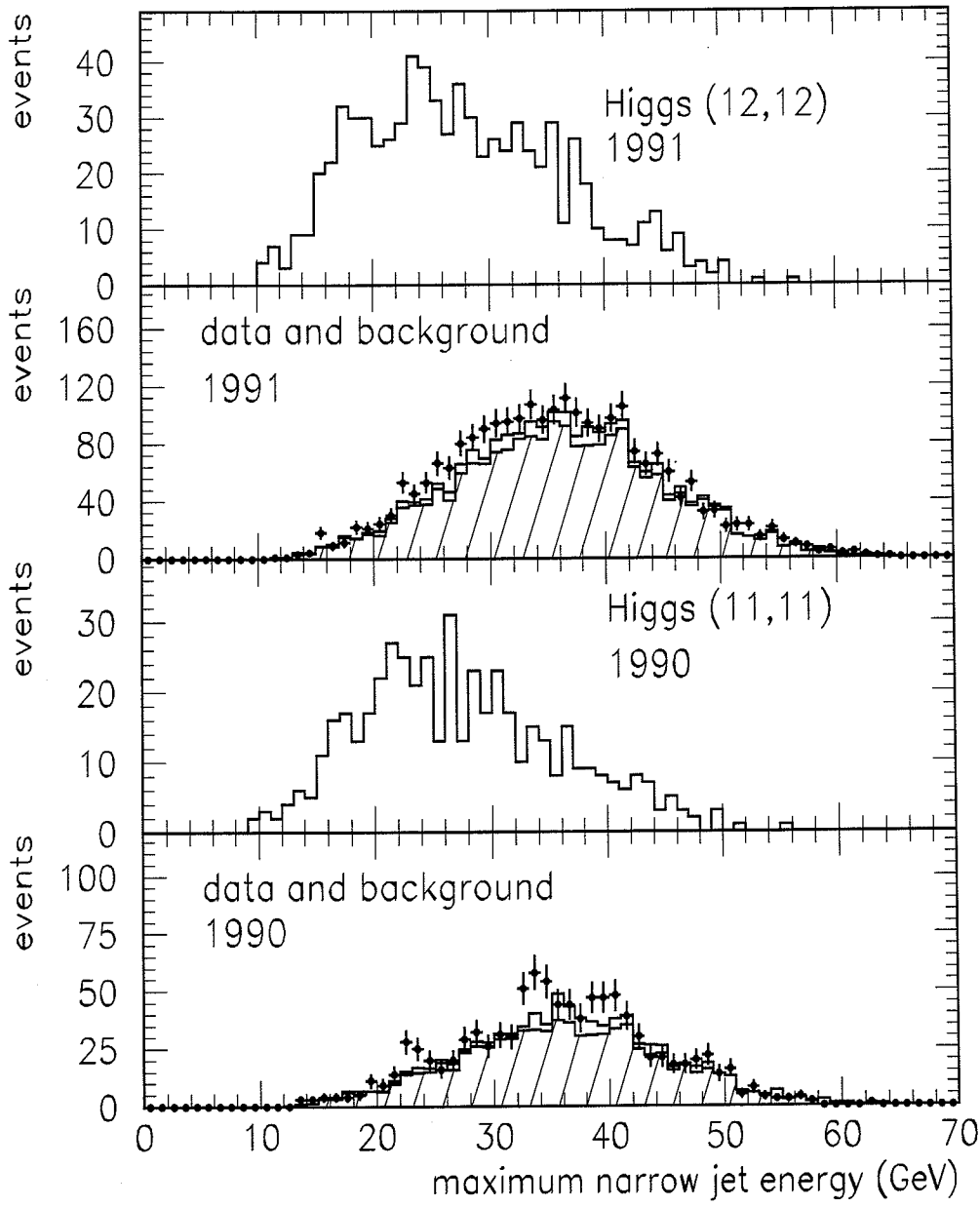

Figure D.4: Distribution of the maximum energy of the narrow jets in the $\tau\tau\tau\tau$ channel.

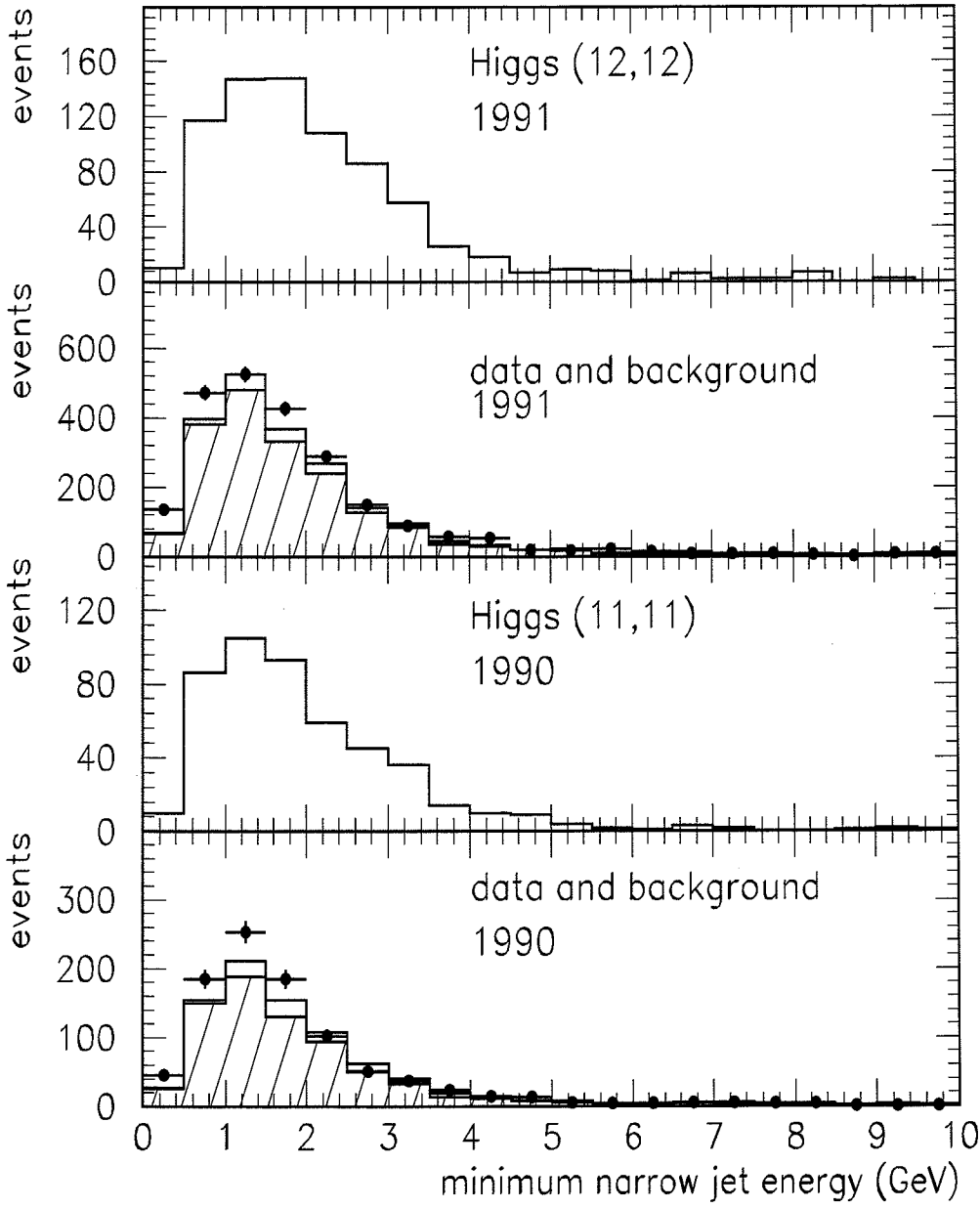

Figure D.5: Distribution of the minimum energy of the narrow jets in the $\tau\tau\tau\tau$ channel.

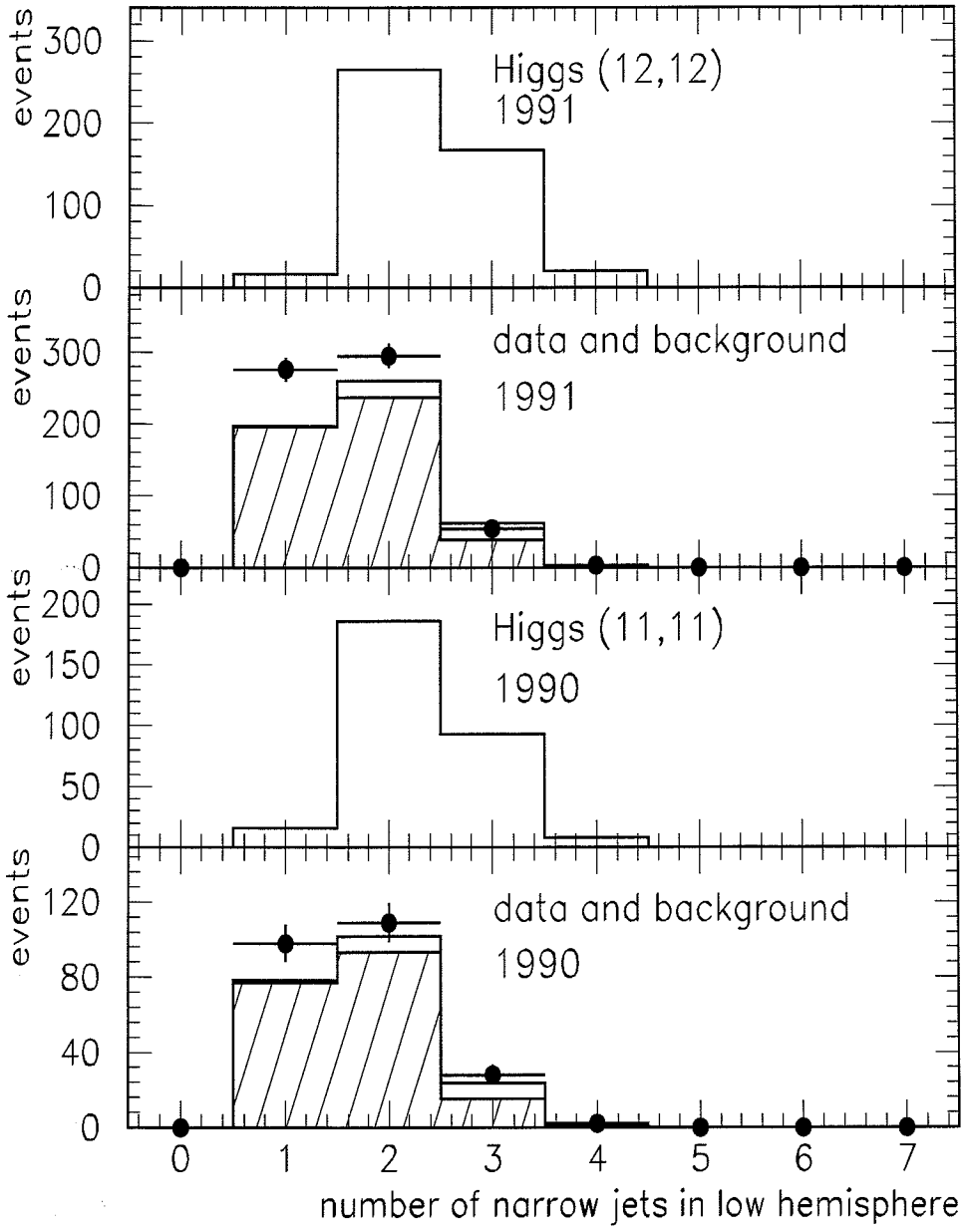

Figure D.6: Distribution of the number of narrow jets in the low hemispheres in the $\tau\tau\tau\tau$ channel.

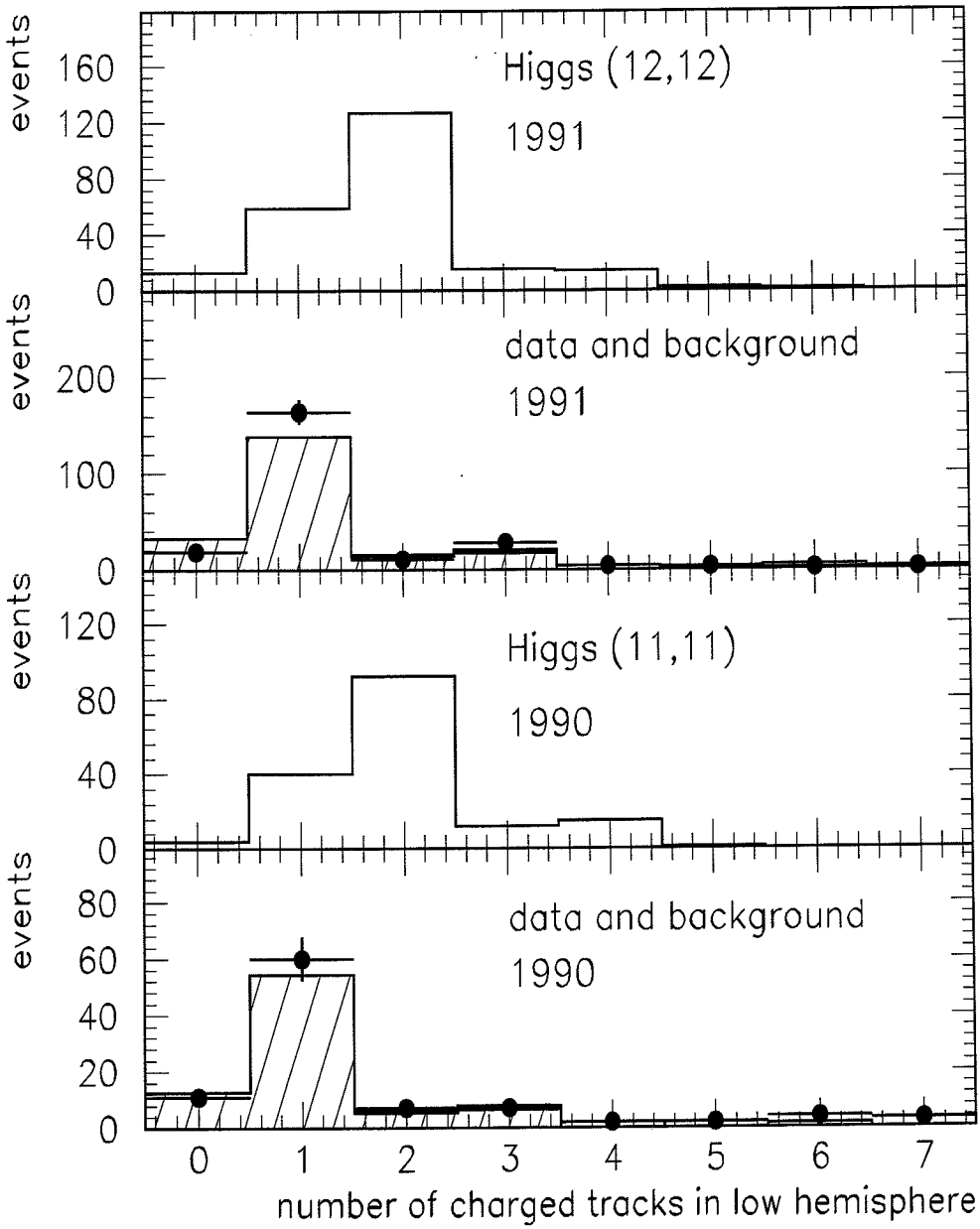

Figure D.7: Distribution of the number of charged tracks in the low hemisphere in the $\tau\tau\tau\tau$ channel.

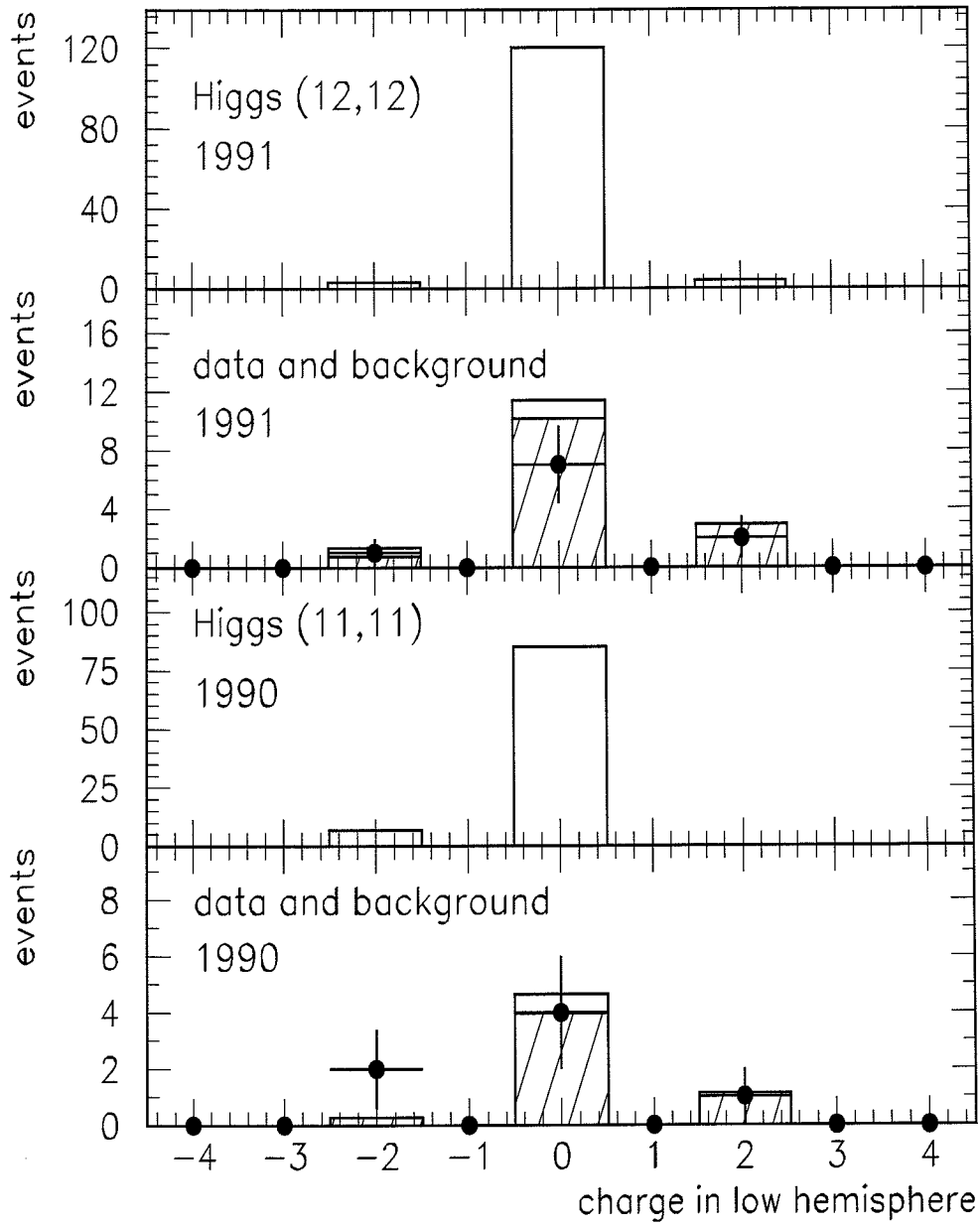

Figure D.8: Distribution of the total charge in the tau hemisphere in the $\tau\tau\tau\tau$ channel.

Appendix E

Distributions for the $Z^0 \rightarrow H^+H^- \rightarrow c\bar{s}\bar{c}s$ Search

Cut numbers and corresponding figure numbers are listed in table E.1. Figure E.1 gives an overview of the expected signal acceptances and numbers of data and background events after a cut is applied.

	cscs Channel $m_{\mathrm{H}} = 40$ GeV	
Cut#	Selection cuts	Fig#
1	$N_J = 4 \text{ or } 5$	–
2	$\Delta \mathrm{m_{rec}} \leq 6$ GeV	E.2
3	$\lvert \cos\theta_p \rvert \leq 0.5$	E.3
4	$\lvert \cos\theta_d \rvert \leq 0.7$	E.4
5	$\Delta \cos\theta p \leq 0.3$	E.5
6	$\psi_{pl} \geq 0.7$ rad	E.6
7	$\sum \mathrm{M_{jet}^{rec}} \geq 30$ GeV	E.7
8	$\mathrm{E_{jet}^{max}}/\sqrt{\mathrm{s}} \leq 0.34$	E.8
8	$\mathrm{E_{jet}^{min}}/\sqrt{\mathrm{s}} \geq 0.14$	E.9
9	39 GeV $\leq m_H \leq$ 41 GeV	E.10

Table E.1: Cut number and corresponding figure number in the cscs channel.

E.1 Preselection in the cscs Channel

The same preselection as for the bbbb channel is applied.

E.2 Final Selection in the cscs Channel

Figures E.2 to E.12 show distributions of cut variables for the final selection. Figures E.10, E.11, E.12 belong to the same selection cut.

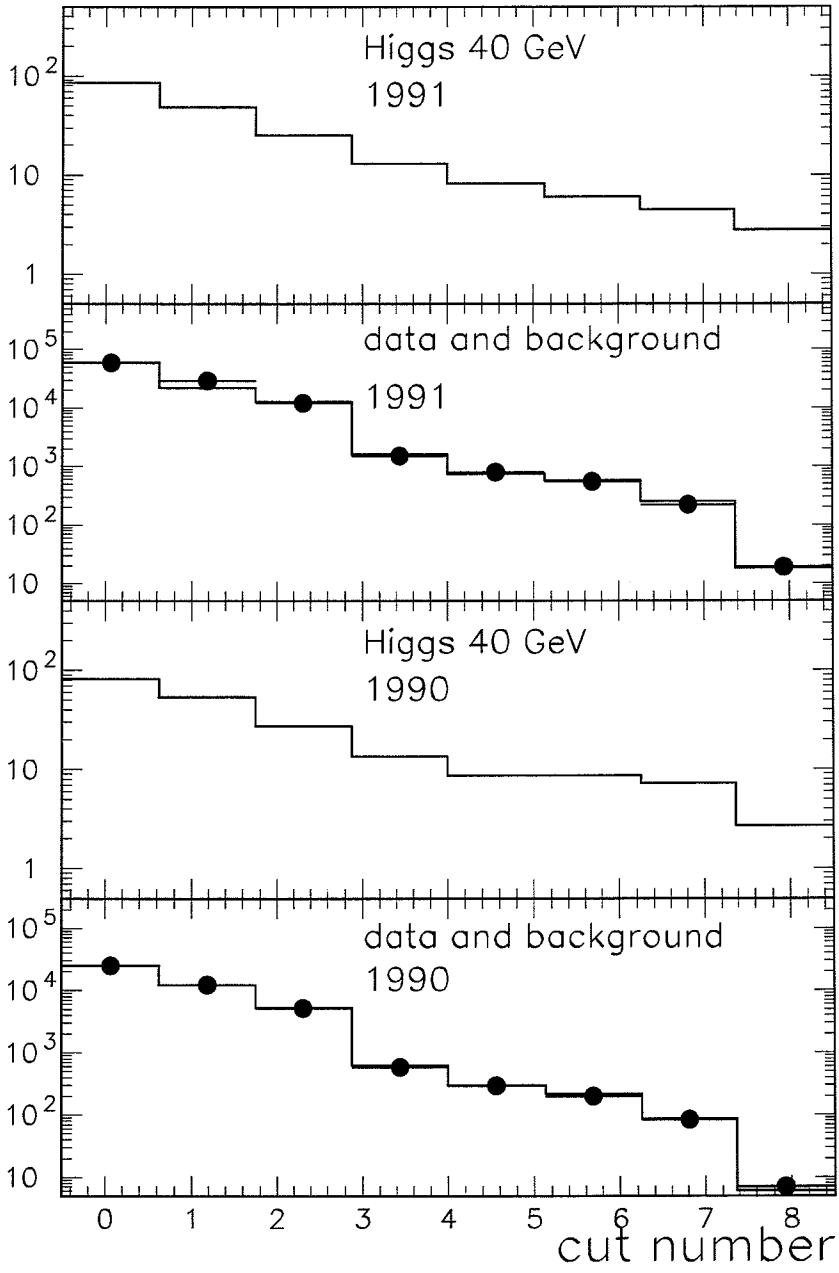

Figure E.1: Acceptances and numbers of data and background events after a cut is applied in the cscs channel. Bin 0 corresponds to the preselection.

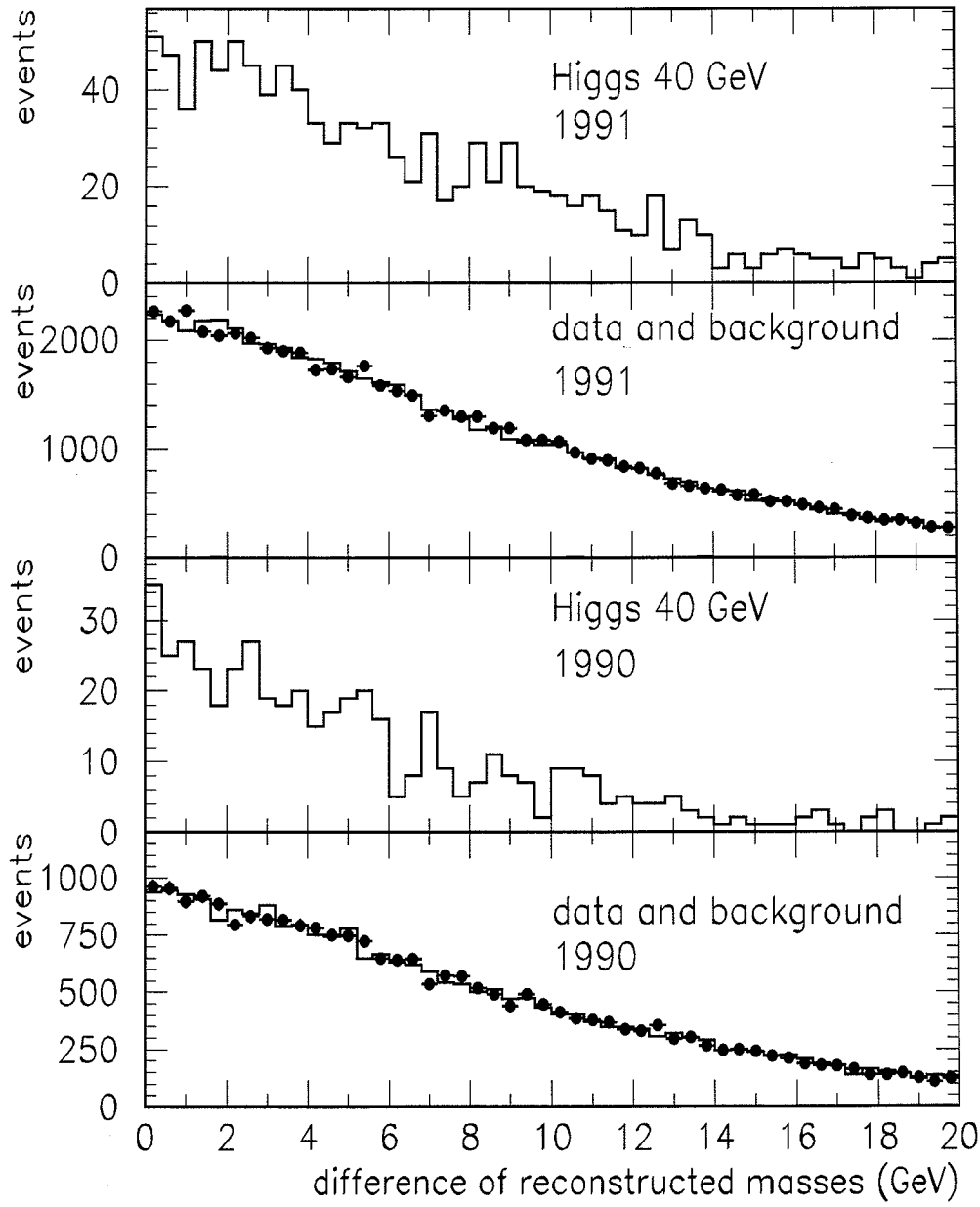

Figure E.2: Distribution of the difference between reconstructed invariant masses in the cscs channel.

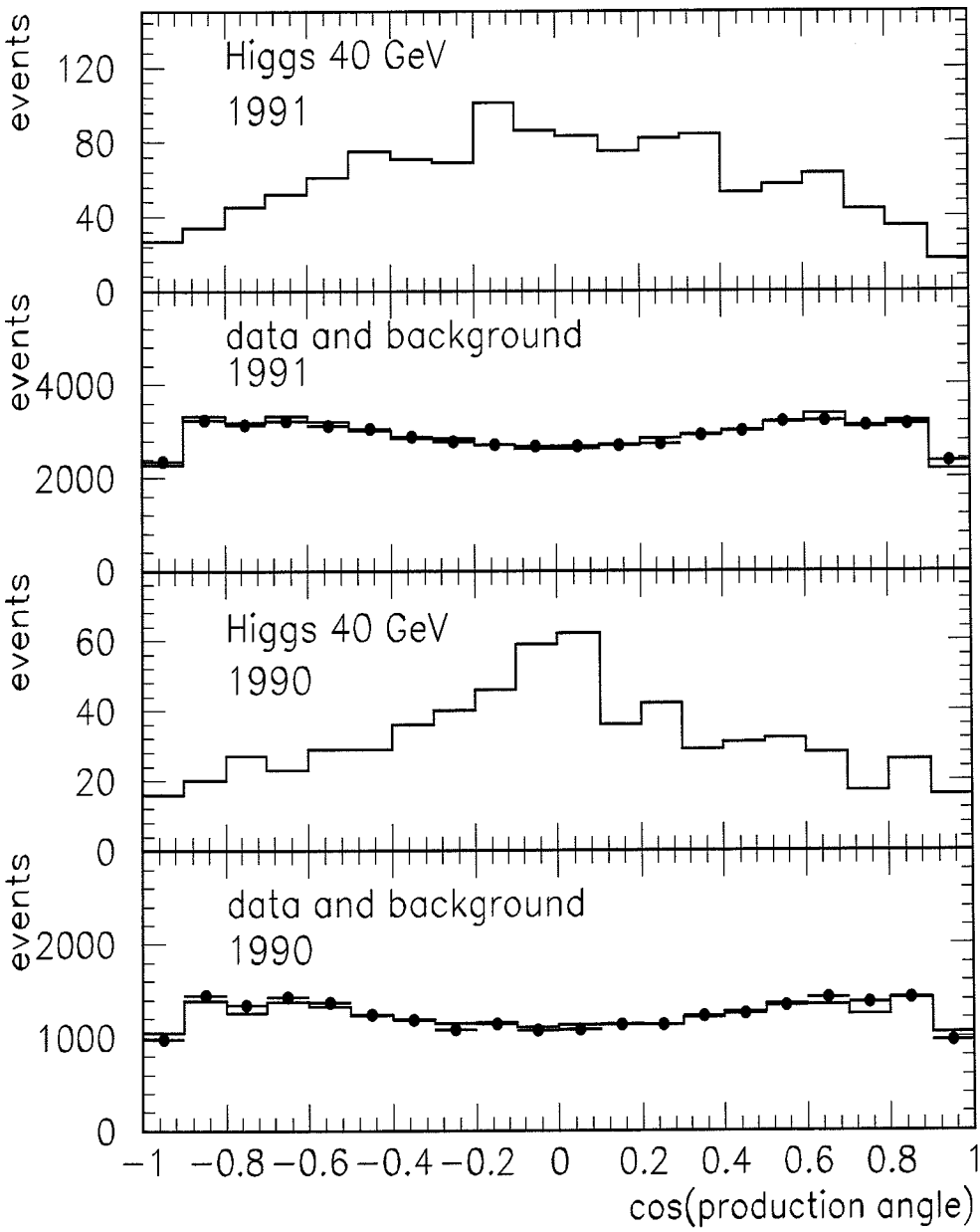

Figure E.3: Distribution of the production angle in the cscs channel.

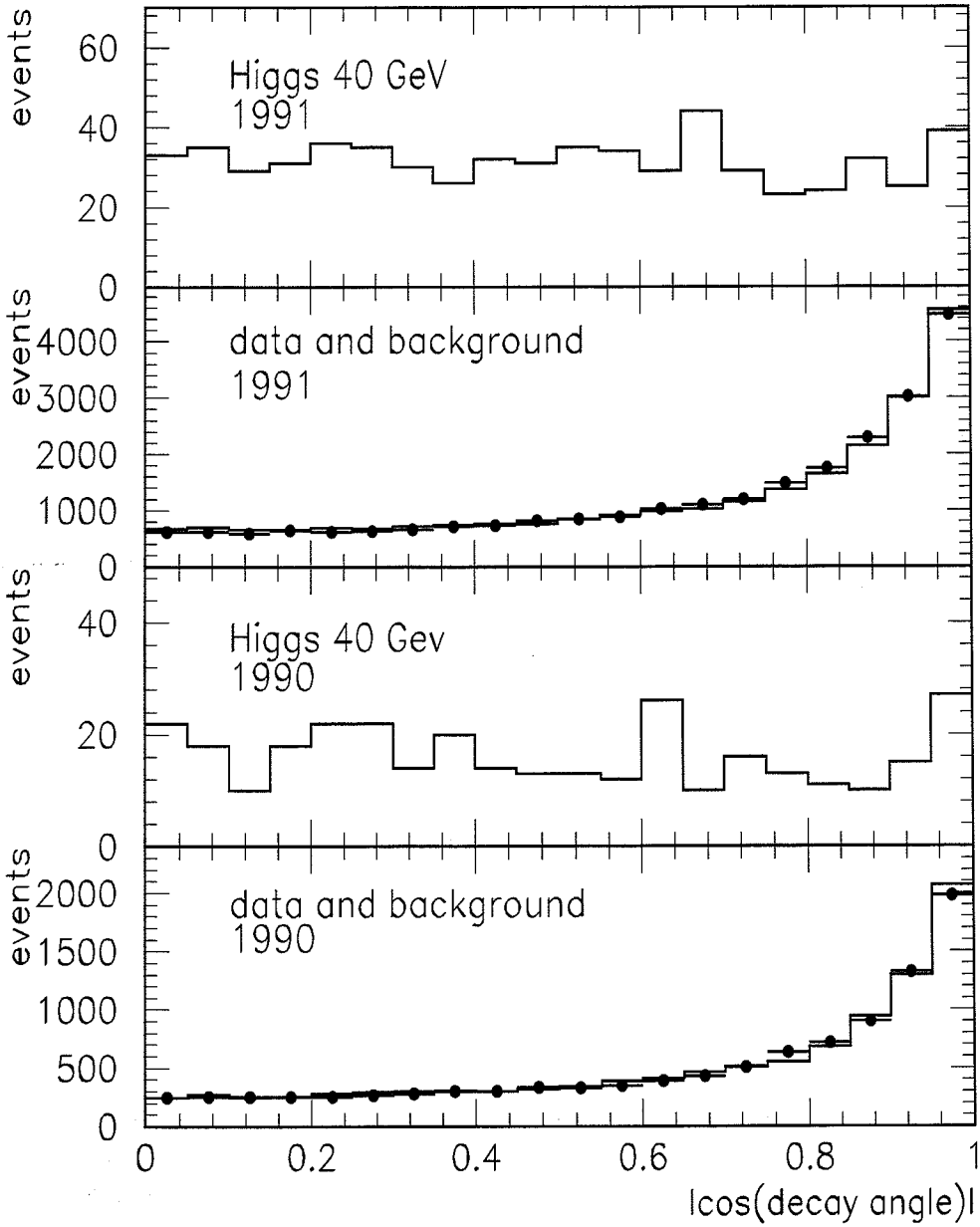

Figure E.4: Distribution of the decay angle in the cscs channel.

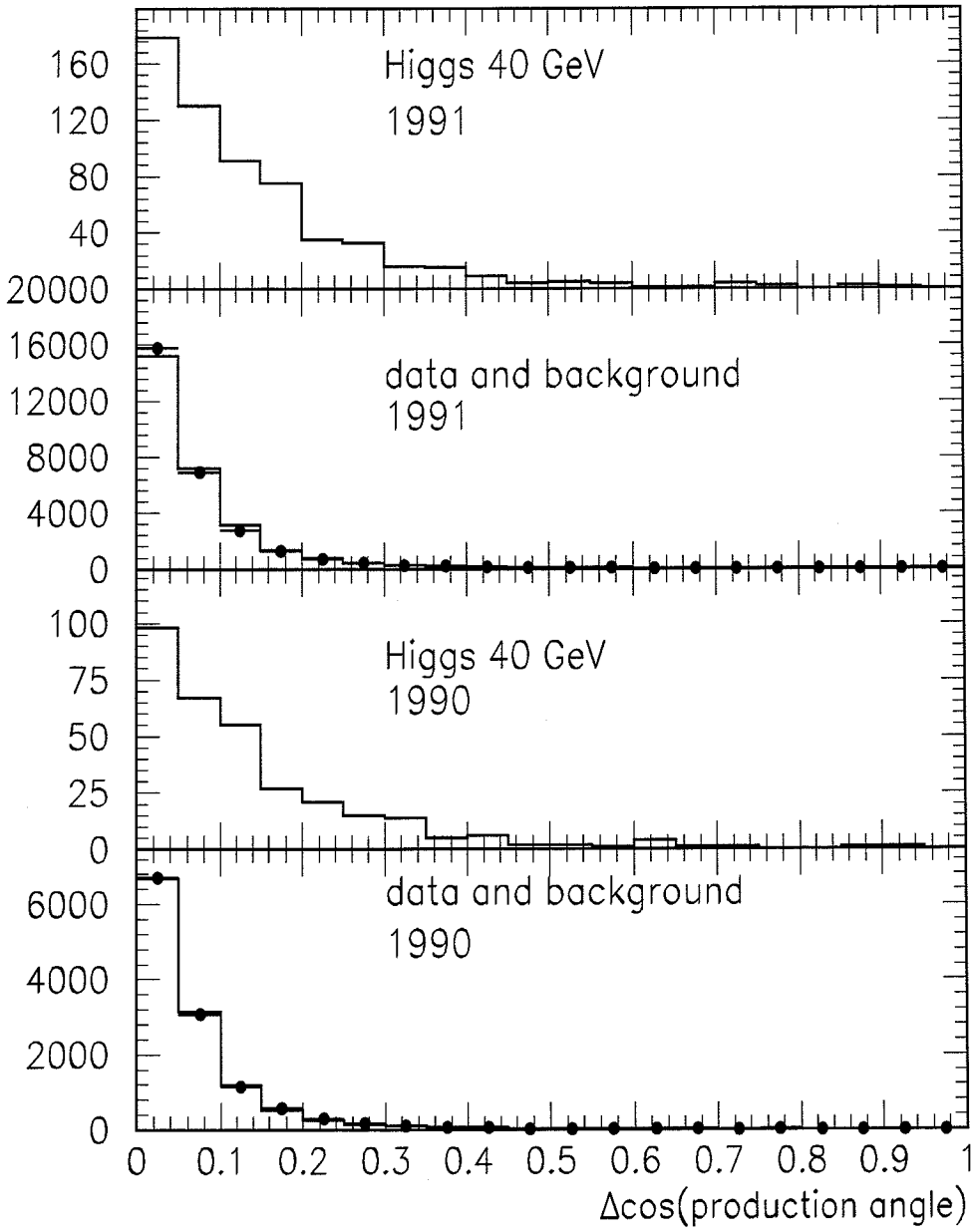

Figure E.5: Distribution of the difference between production angles in the cscs channel.

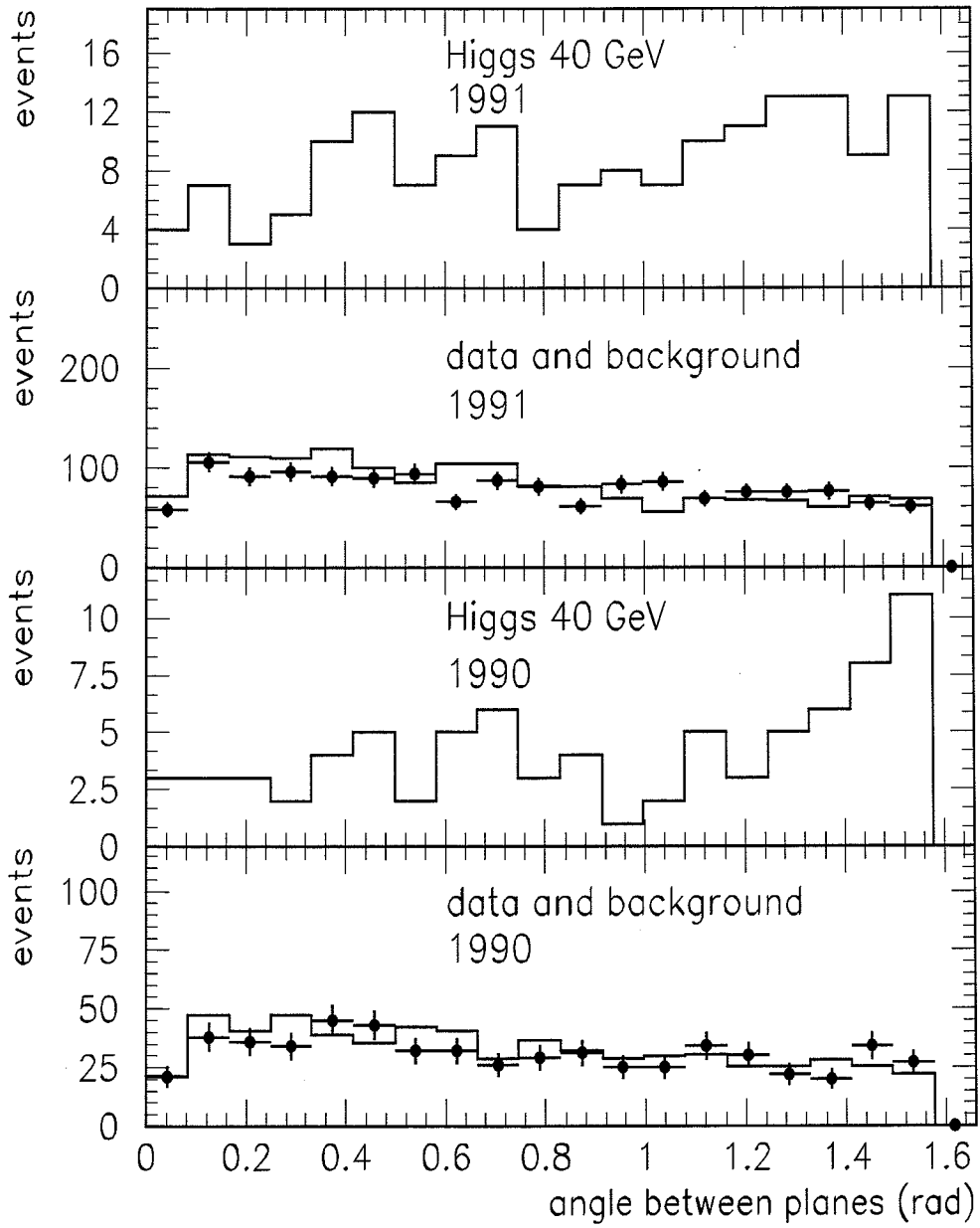

Figure E.6: Distribution of the angle between reconstructed Higgs planes in the cscs channel.

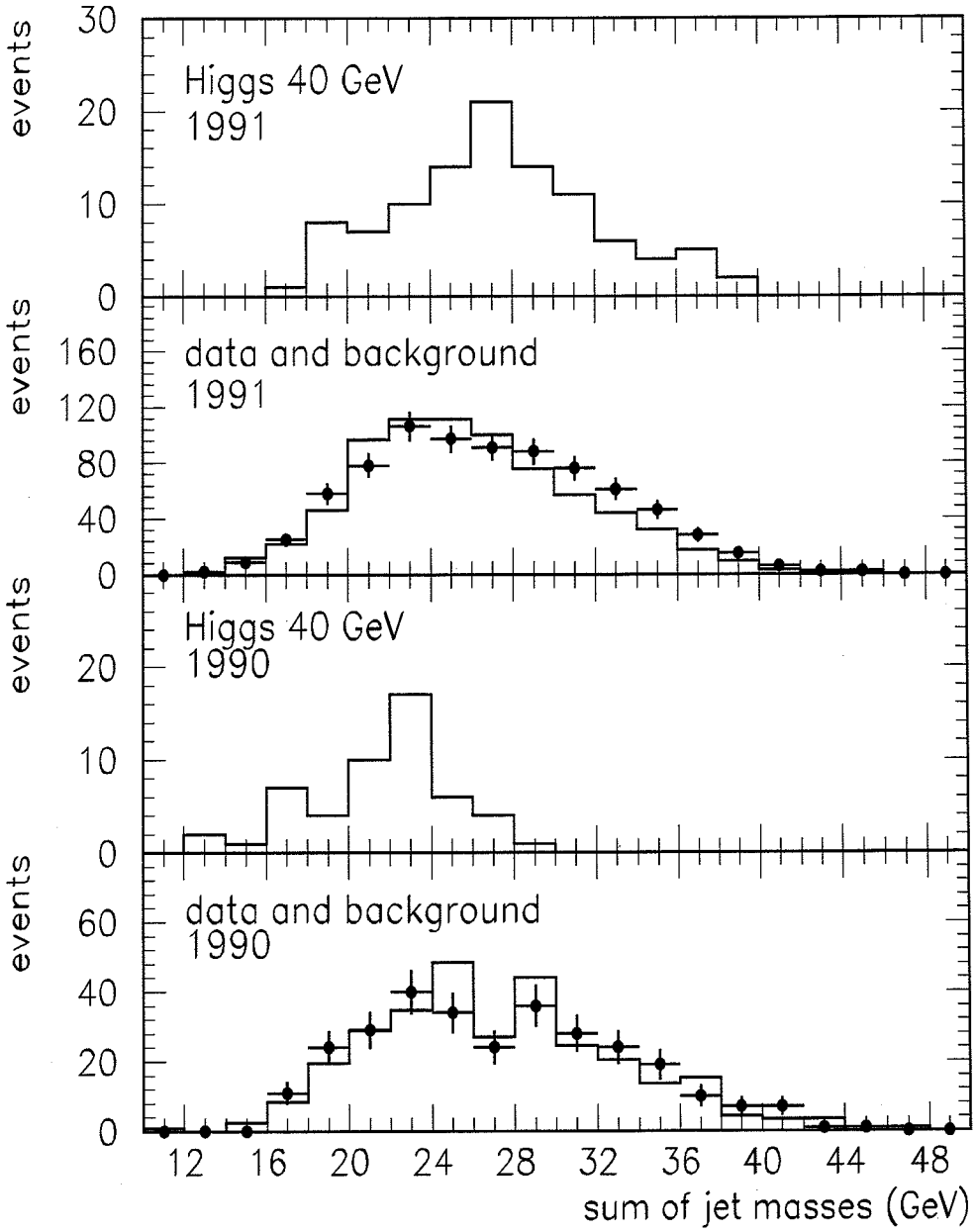

Figure E.7: Distribution of the sum of jet masses in the cscs channel.

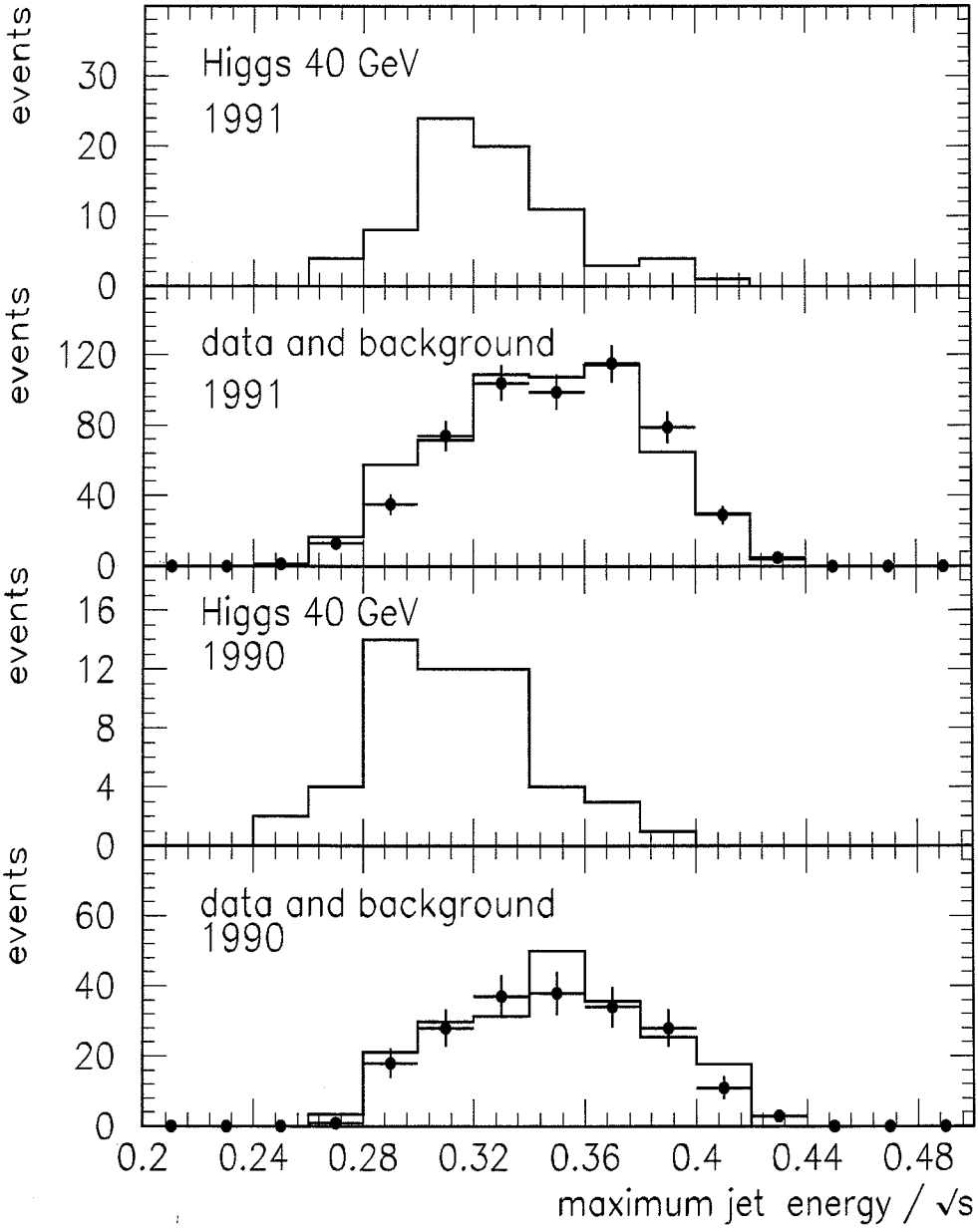

Figure E.8: Distribution of the maximum jet energy in the cscs channel.

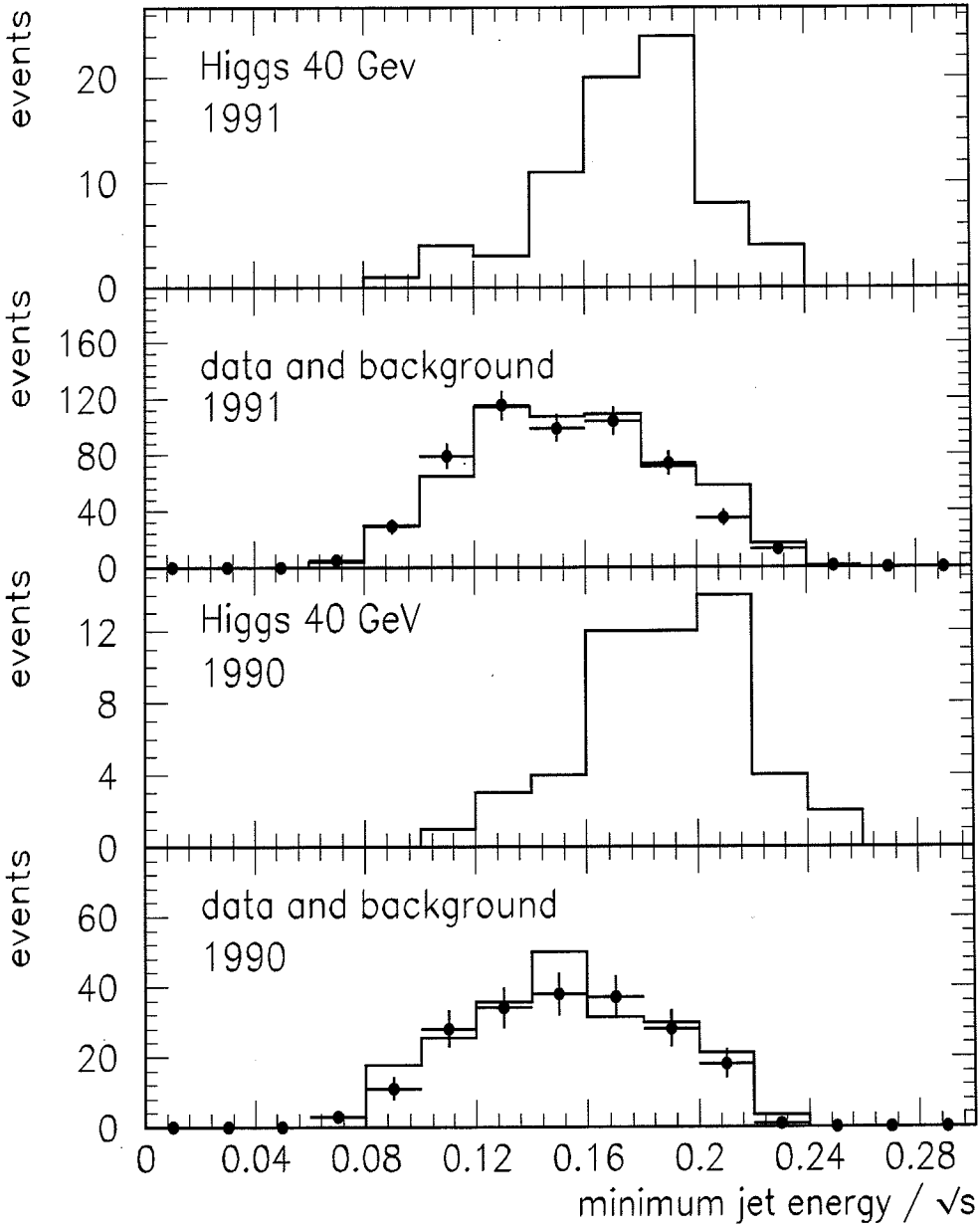

Figure E.9: Distribution of the minimum jet energy in the cscs channel.

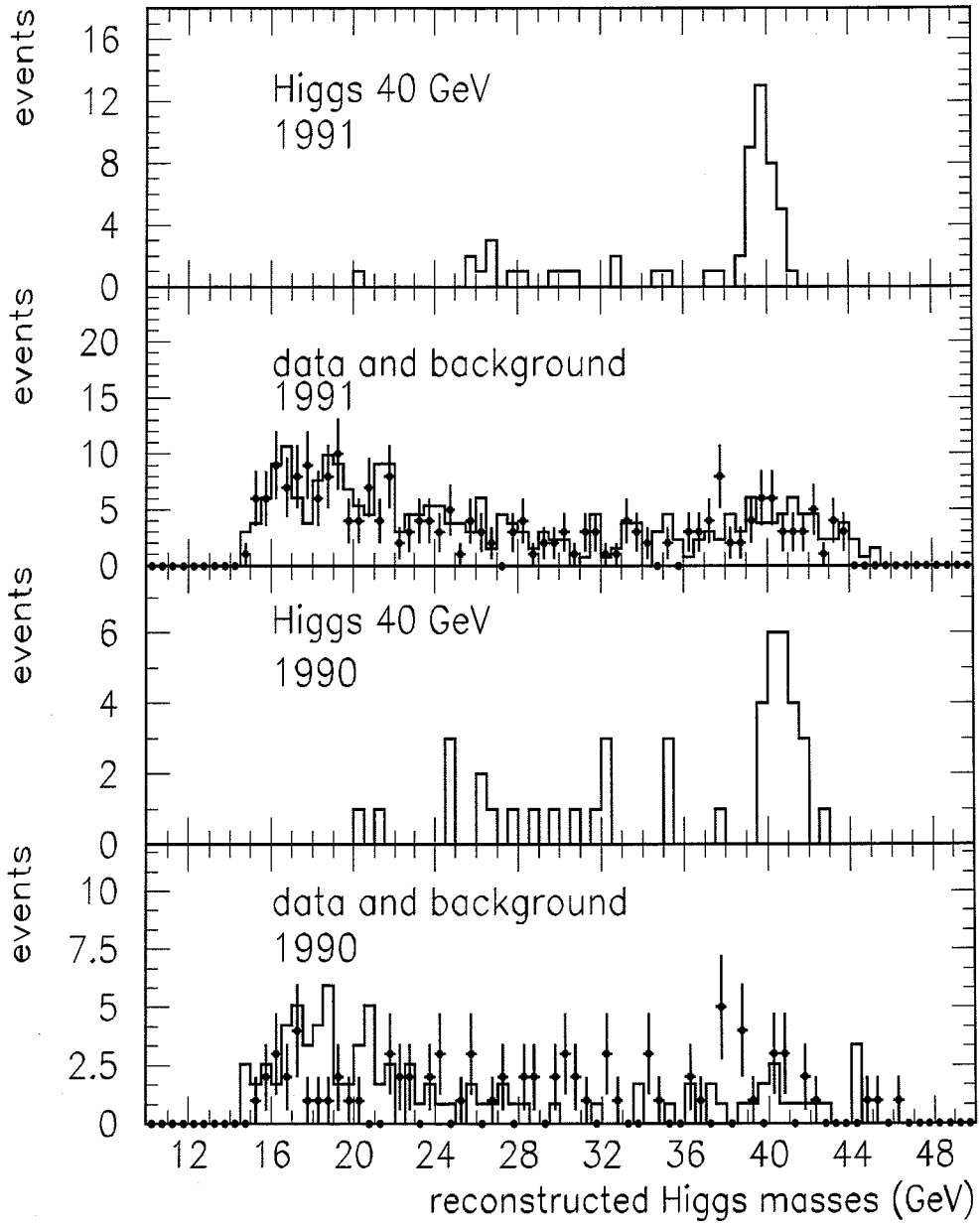

Figure E.10: Distribution of the reconstructed invariant mass in the cscs channel.

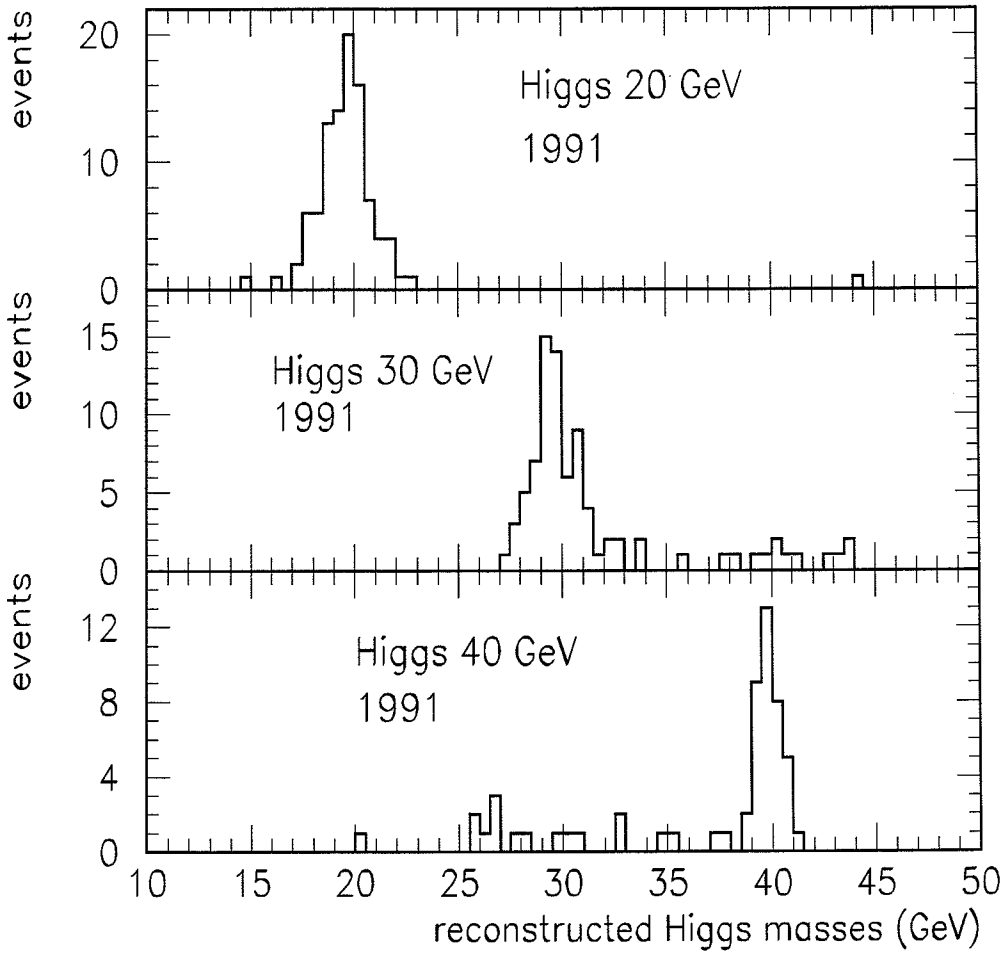

Figure E.11: Distribution of the reconstructed invariant mass (1991 Higgs simulations) in the cscs channel.

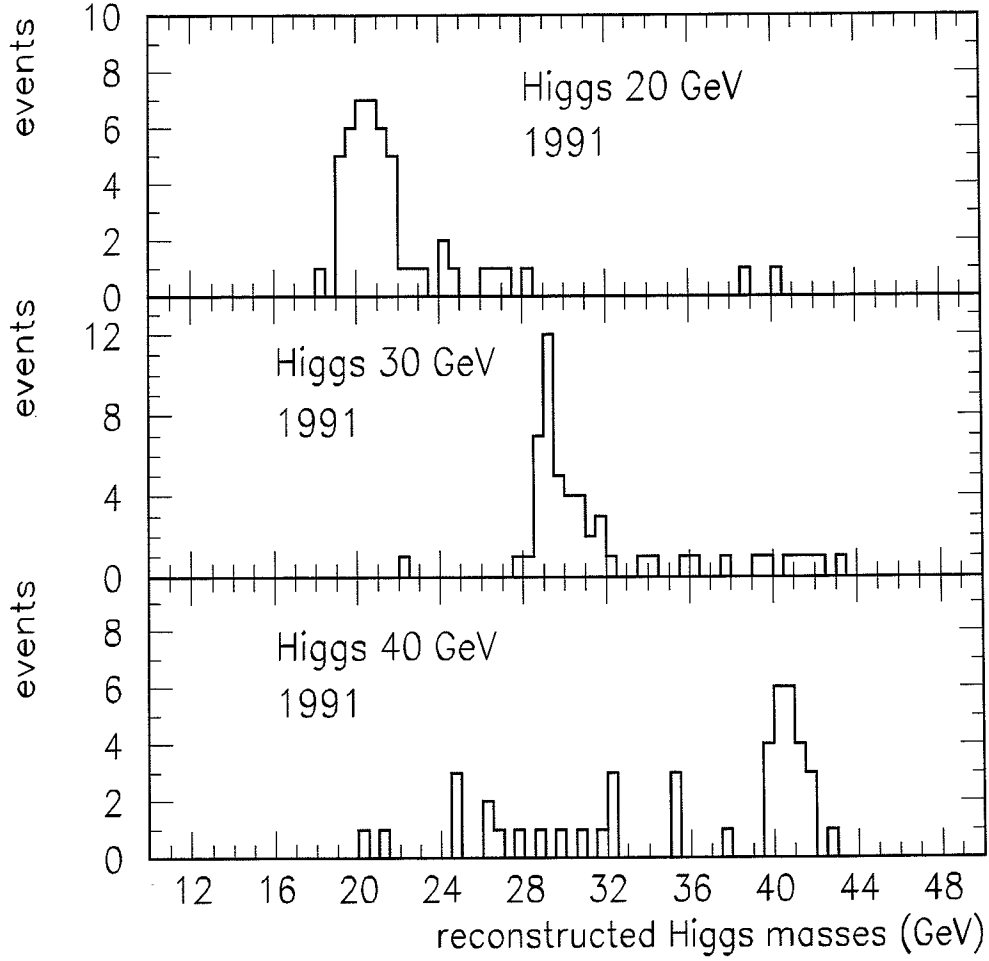

Figure E.12: Distribution of the reconstructed invariant mass (1990 Higgs simulations) in the cscs channel.

Appendix F

Distributions for the $Z^0 \rightarrow H^+H^- \rightarrow cs\tau\nu$ Search

Cut numbers and corresponding figure numbers are listed in table F.1. Figure F.1 gives an overview of the expected signal acceptances and numbers of data and background events after a cut is applied.

	cs$\tau\nu$ Channel $m_{\mathrm{H}} = 40$ GeV	
Cut#	Selection cuts	Fig#
1	$N_{cl} \leq 50$	F.5
2	$M \geq 0.25$	F.6
3	1 isolated τ with isol. angle $\geq 40°$	F.7
4	$E_{\perp}/E_v \geq 0.25$	F.8
5	$0.35 \leq E_h/\sqrt{s} \leq 0.60$	F.9
6	32 GeV $\leq m_{had} \leq$ 46 GeV	F.10

Table F.1: Cut number and corresponding figure number in the cs$\tau\nu$ channel.

F.1 Preselection in the cs$\tau\nu$ Channel

Figures F.2 to F.4 show distributions of cut variables for the preselection.

F.2 Final Selection in the cs$\tau\nu$ Channel

Figures F.5 to F.12 show distributions of cut variables for the final selection. Figures F.10 to F.12 belong to the last selection cut.

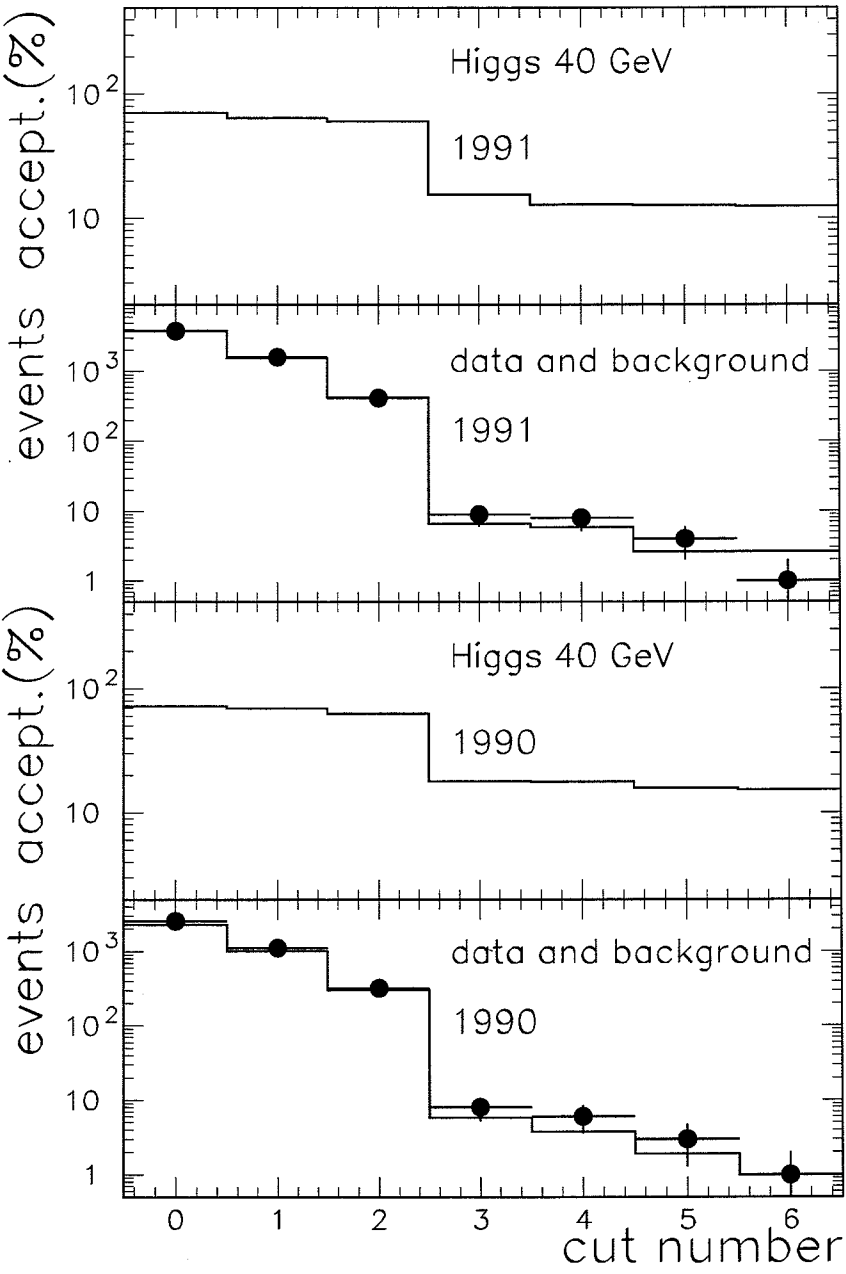

Figure F.1: Acceptances and numbers of data and background events after a cut is applied in the cs$\tau\nu$ channel. Bin 0 corresponds to the preselection.

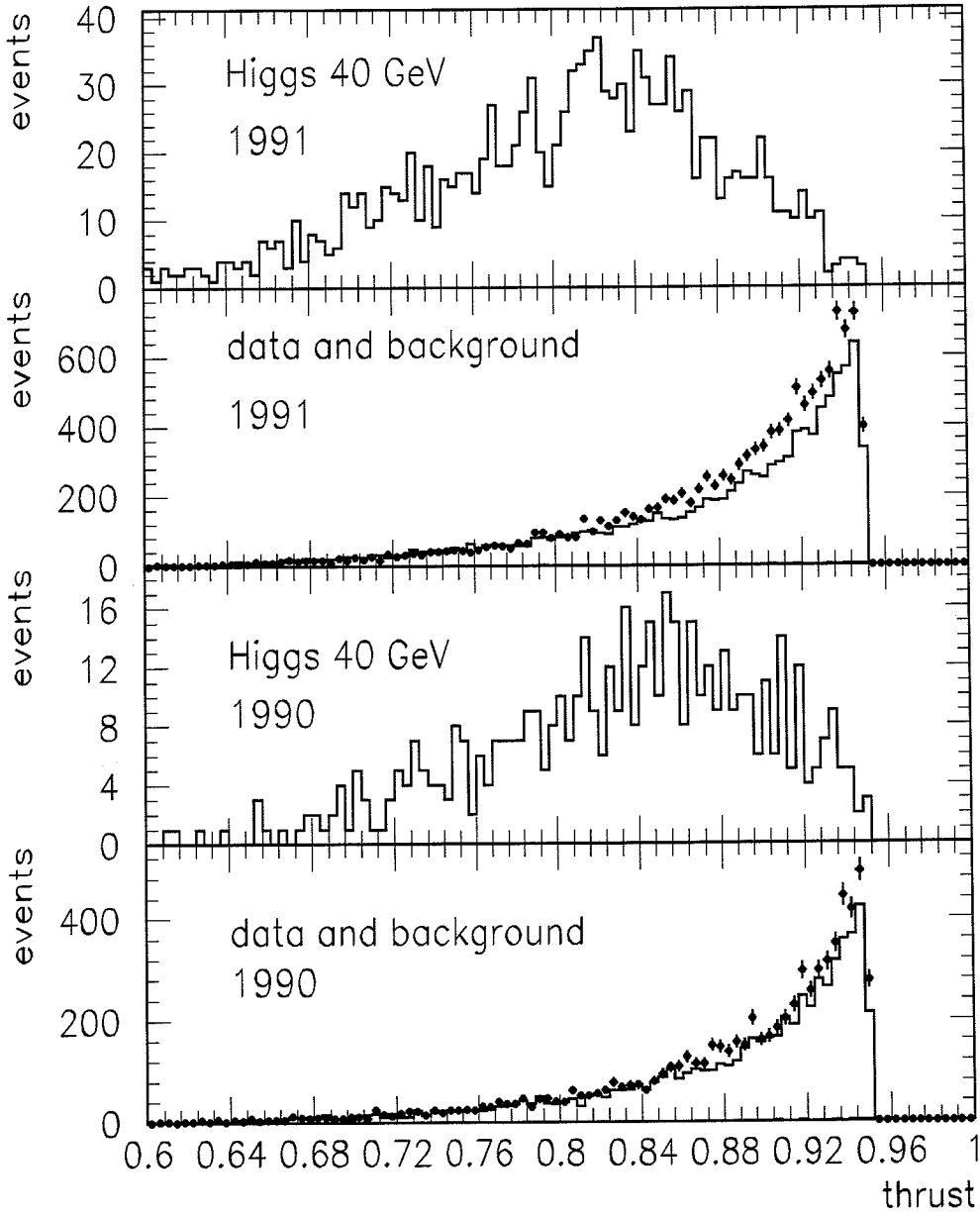

Figure F.2: Distribution of the thrust in the cs$\tau\nu$ channel.

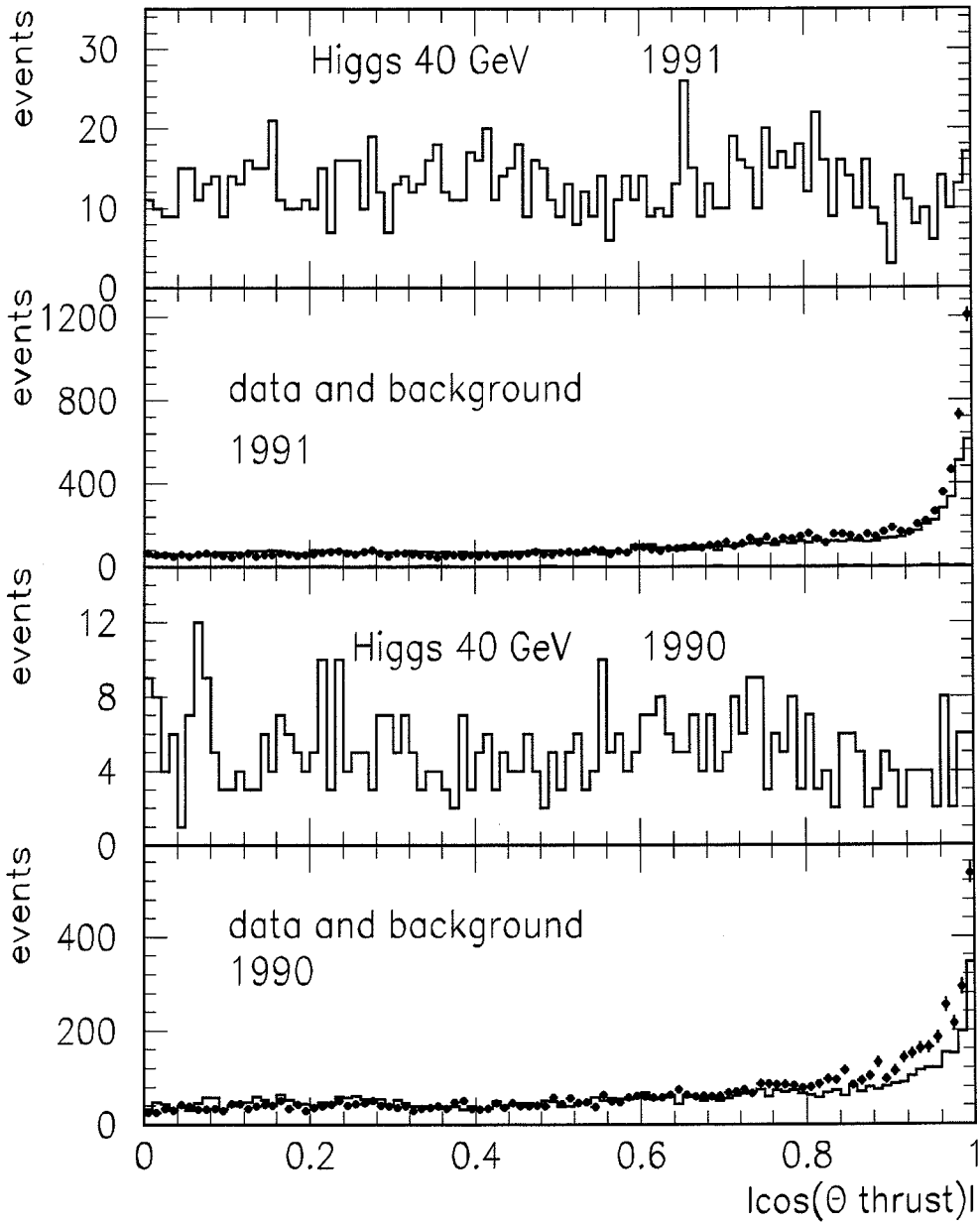

Figure F.3: Distribution of the thrust angle in the cs$\tau\nu$ channel.

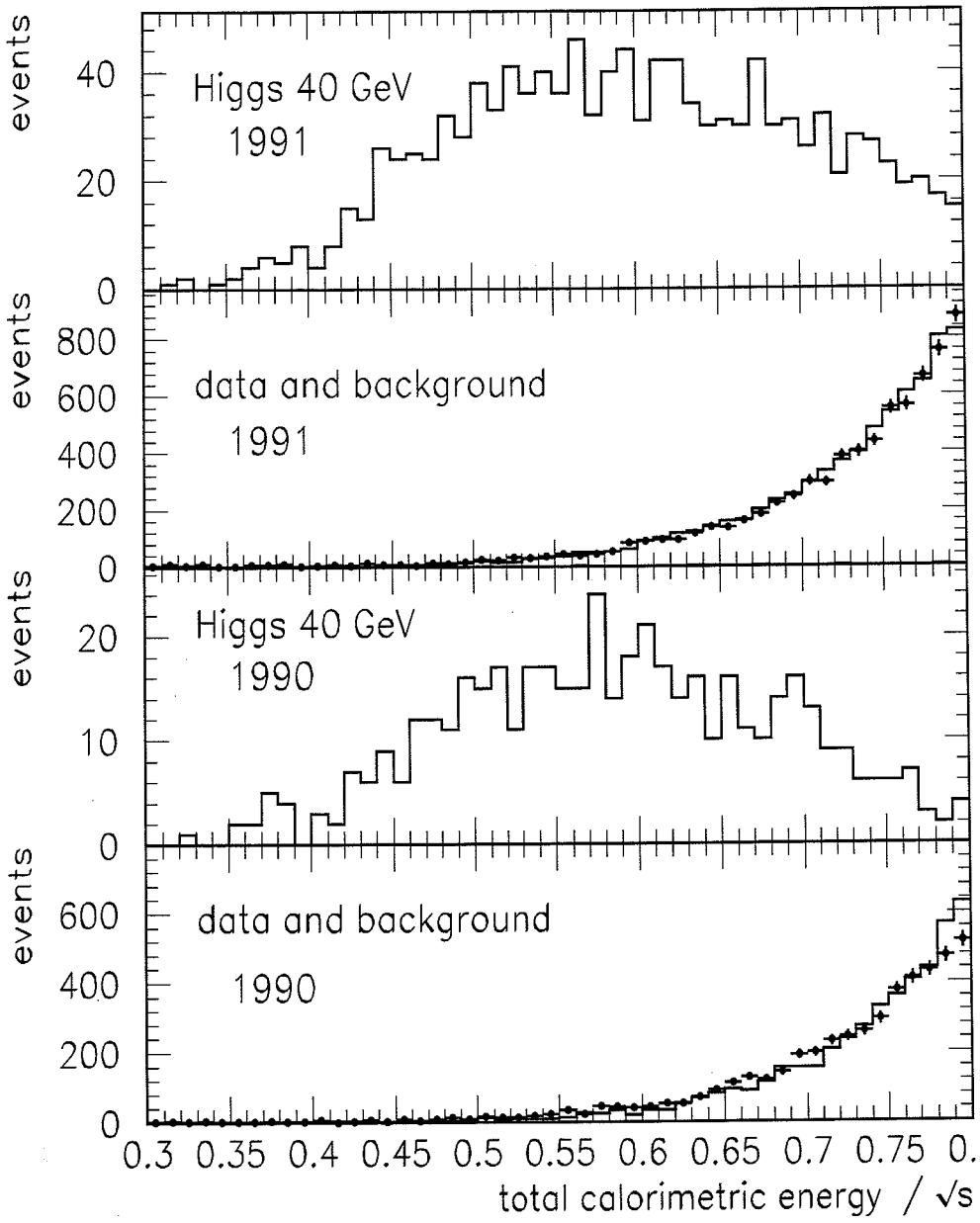

Figure F.4: Distribution of the calorimetric energy in the cs$\tau\nu$ channel.

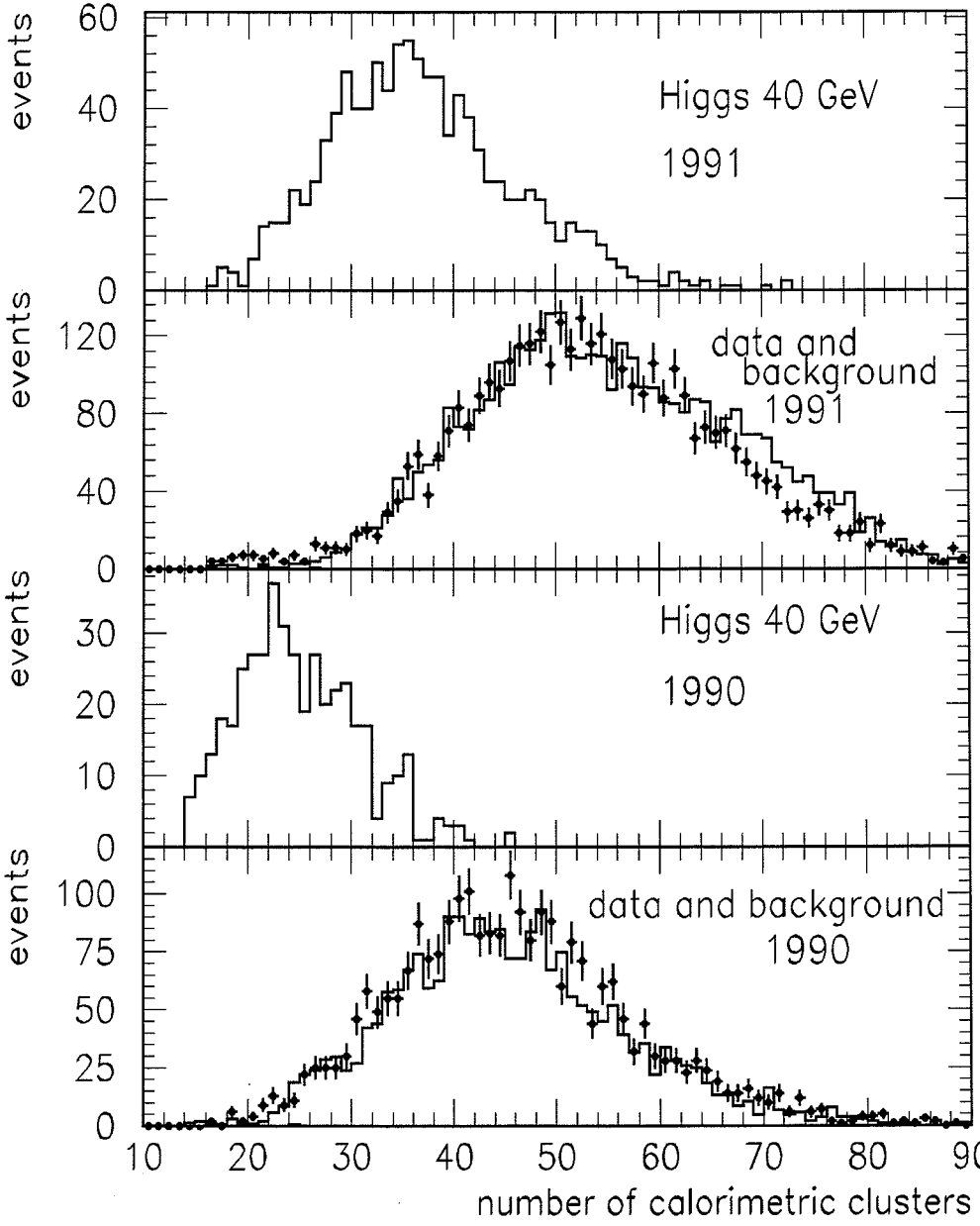

Figure F.5: Distribution of the number of calorimetric clusters in the cs$\tau\nu$ channel.

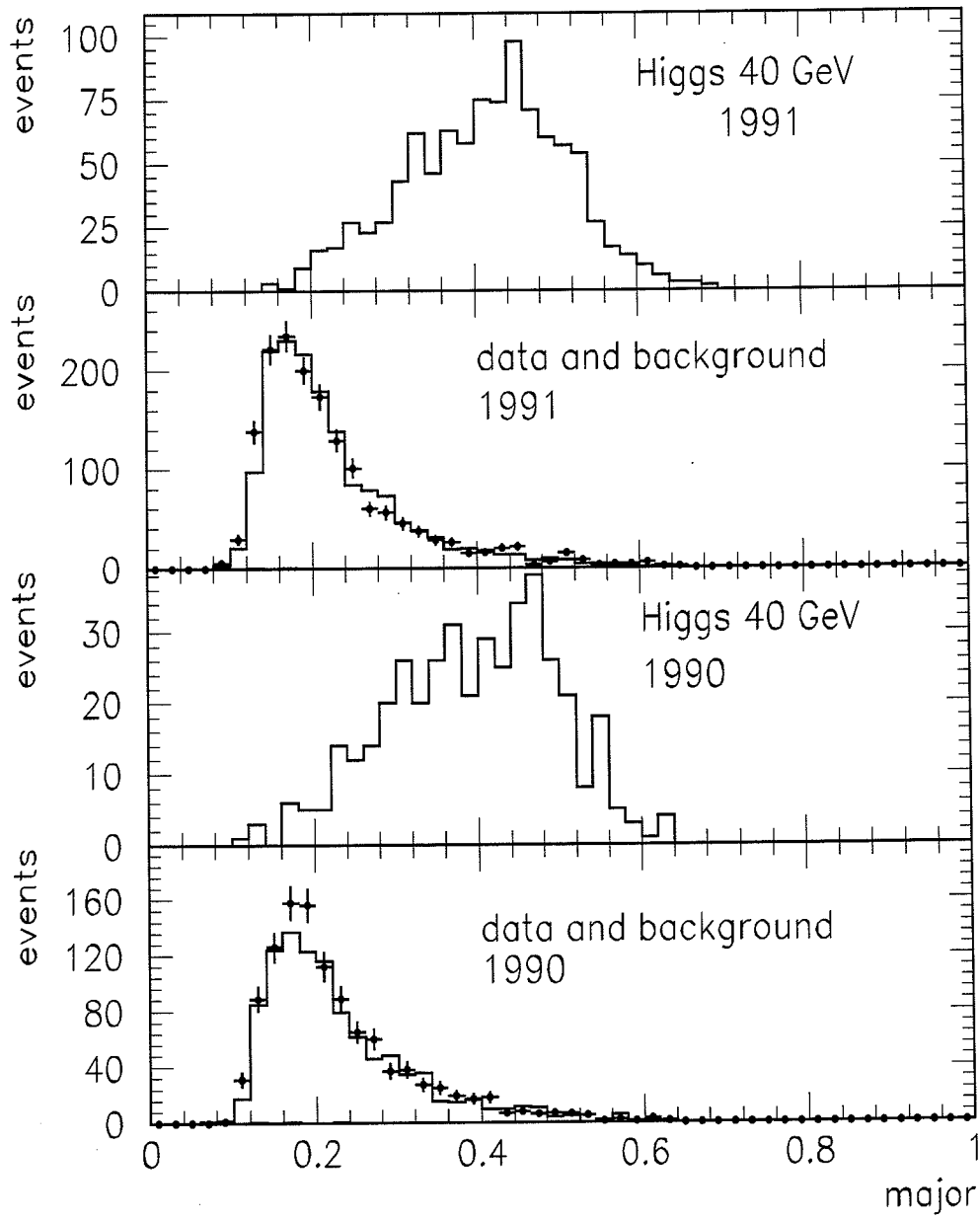

Figure F.6: Distribution of the major in the cs$\tau\nu$ channel.

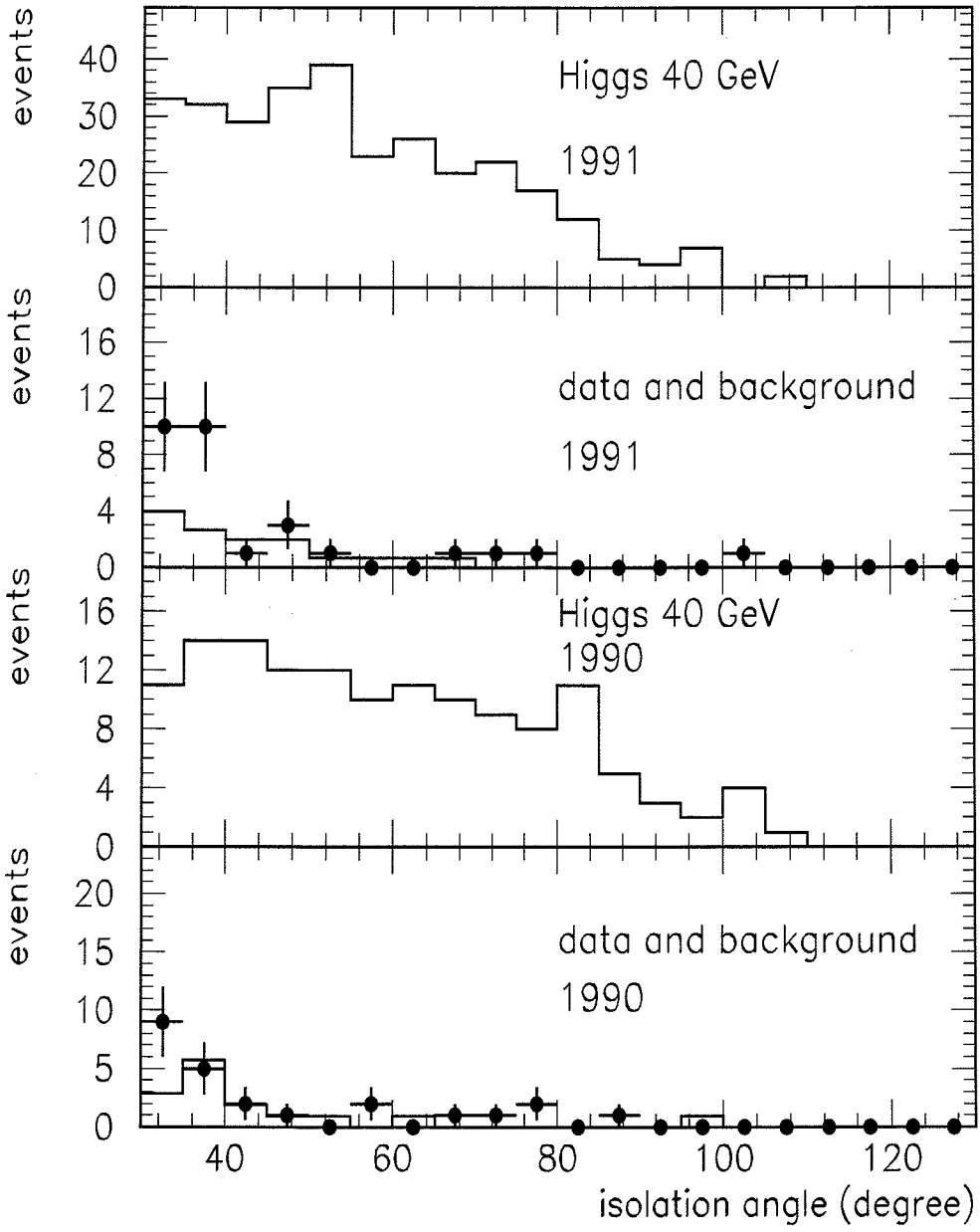

Figure F.7: Distribution of the isolation angle in the cs$\tau\nu$ channel.

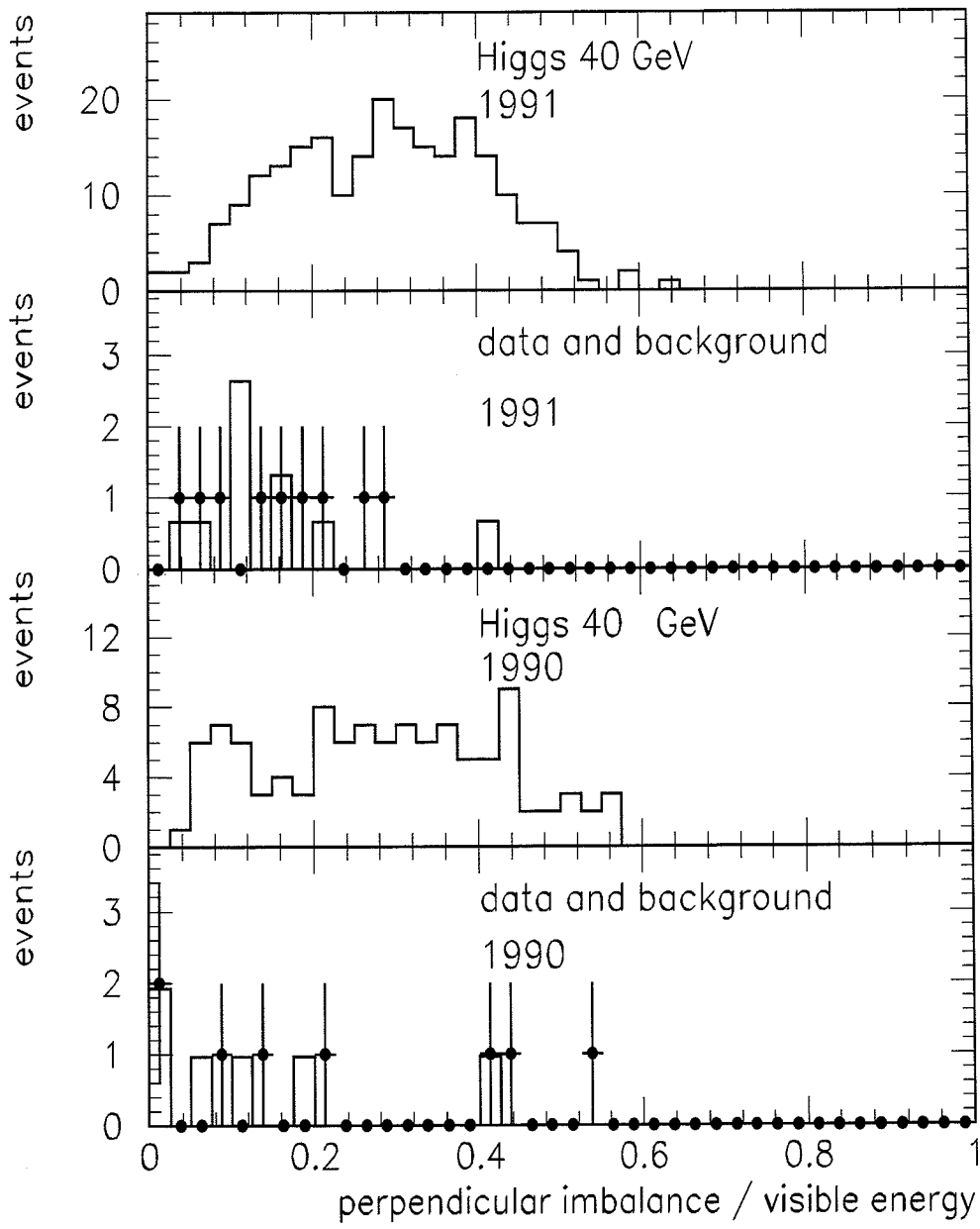

Figure F.8: Distribution of the perpendicular energy imbalance in the cs$\tau\nu$ channel.

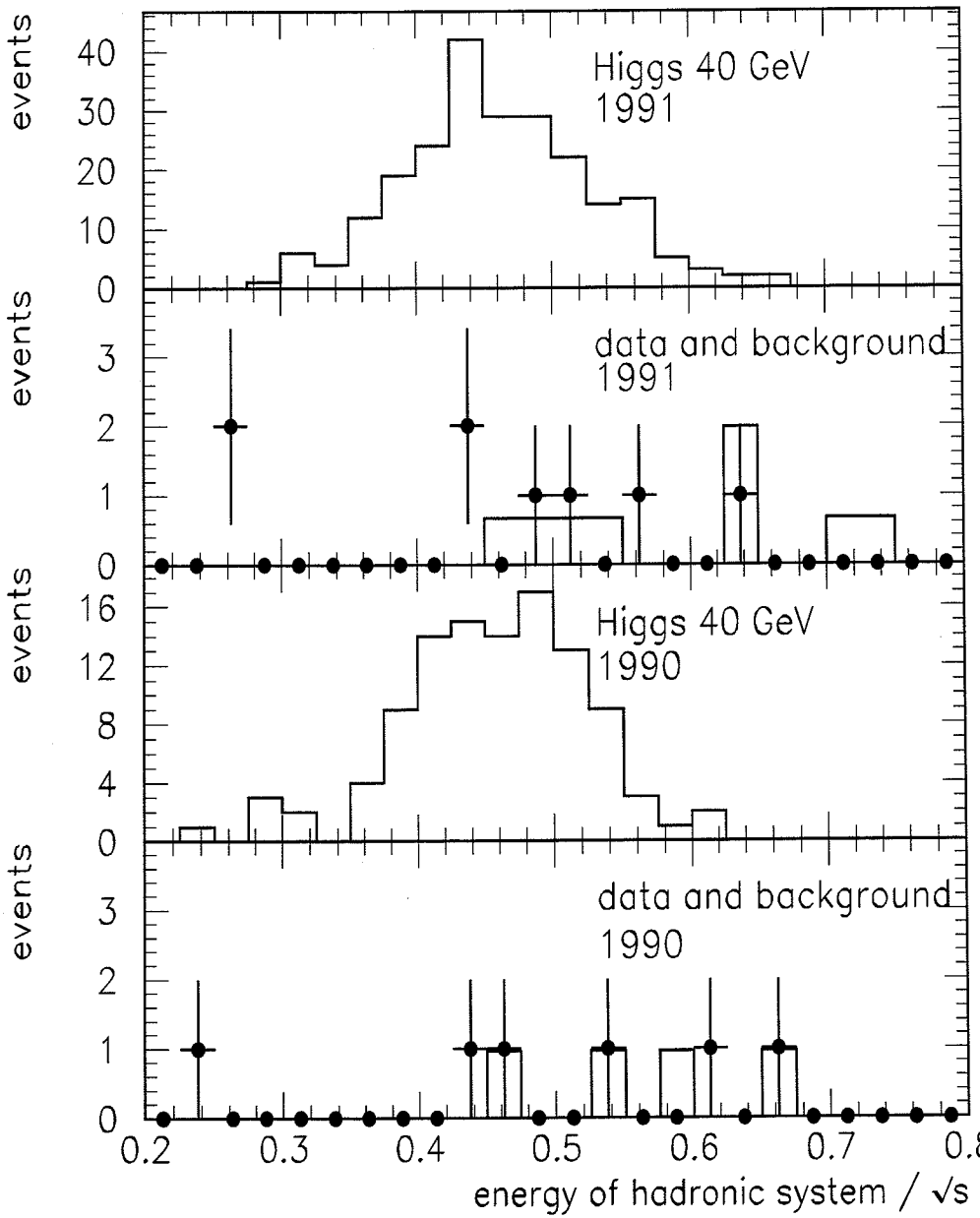

Figure F.9: Distribution of the calorimetric energy (tau energy subtracted) in the cs$\tau\nu$ channel.

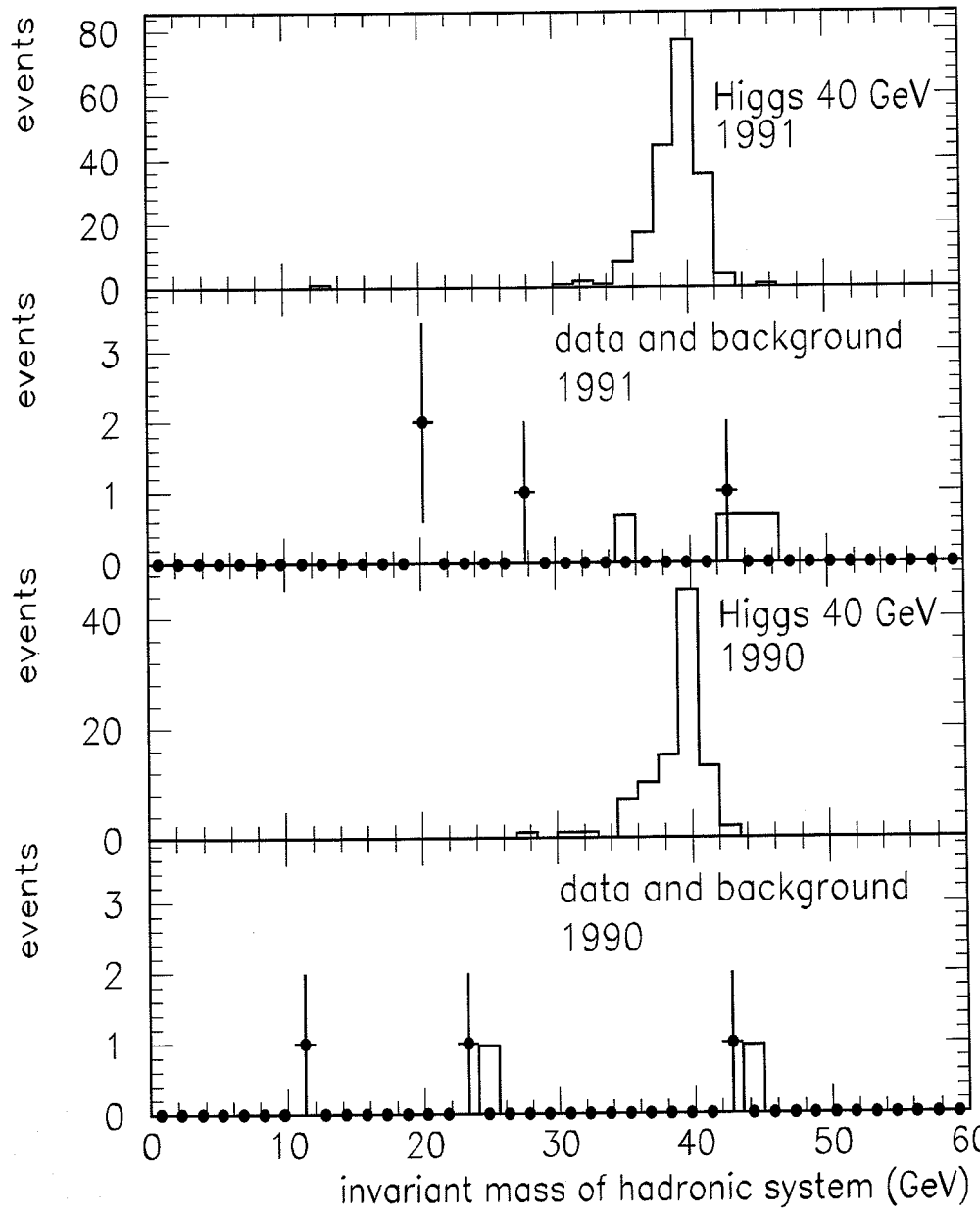

Figure F.10: Distribution of the reconstructed invariant mass in the cs$\tau\nu$ channel.

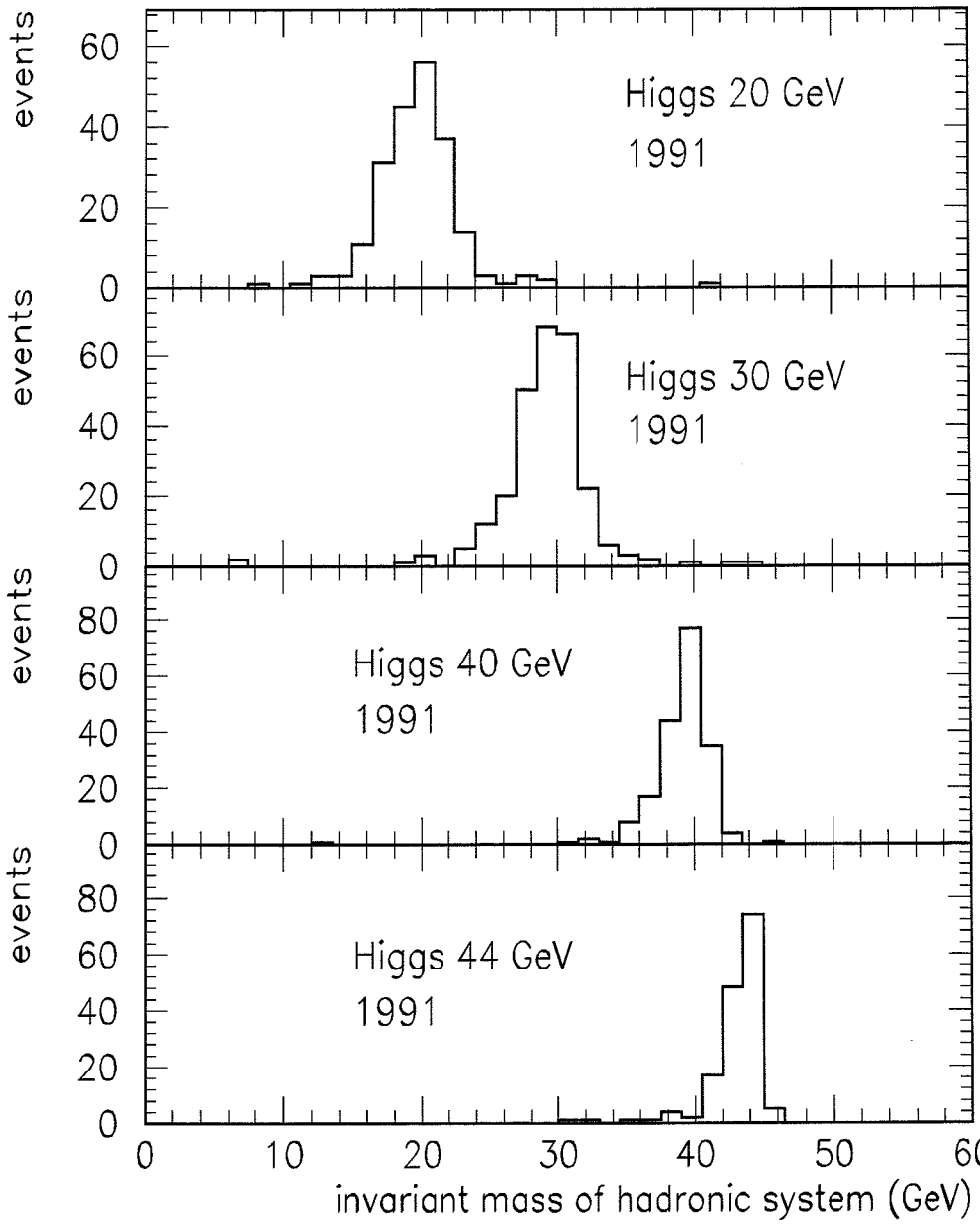

Figure F.11: Distribution of the reconstructed invariant mass (1991 Higgs simulations) in the cs$\tau\nu$ channel.

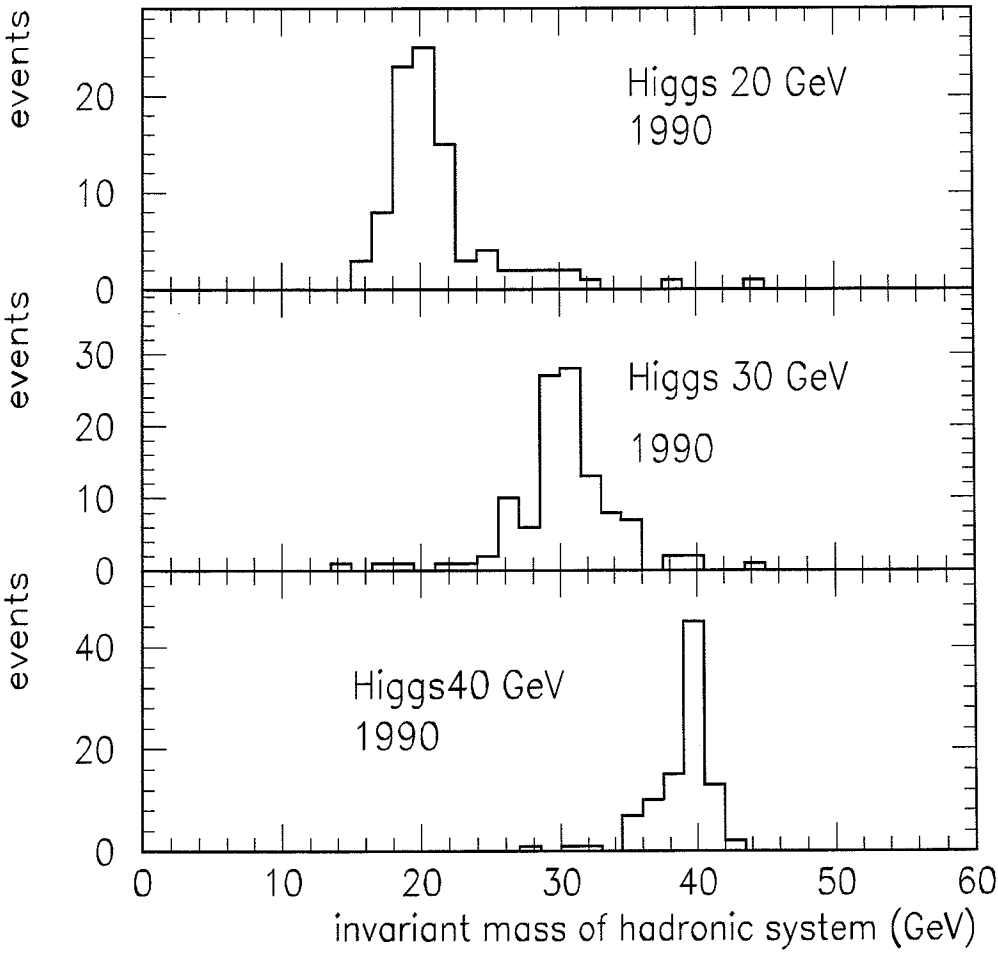

Figure F.12: Distribution of the reconstructed invariant mass (1990 Higgs simulations) in the cs$\tau\nu$ channel.

Appendix G

Distributions for the $Z^0 \to H^+H^- \to \tau^+\nu\tau^-\bar{\nu}$ Search

Cut numbers and corresponding figure numbers are listed in table G.1. Figure G.1 gives an overview of the expected signal acceptances and numbers of data and background events after a cut is applied.

	$\tau\nu\tau\nu$ **Channel** $m_H = 40$ GeV	
Cut#	Selection cuts	Fig#
1	$E_\perp/E_v > 0.2$	G.6
2	$\theta_{123} < 2.8$ rad	G.7
3	$\theta_a < 2.8$ rad	G.8
4	$M < 0.2$	G.9

Table G.1: Cut number and corresponding figure number in the cs$\tau\nu$ channel.

G.1 Preselection in the $\tau\nu\tau\nu$ Channel

Figures G.2 to G.5 show distributions of cut variables for the preselection.

G.2 Final Selection in the $\tau\nu\tau\nu$ Channel

Figures G.6 to G.9 show distributions of cut variables for the final selection.

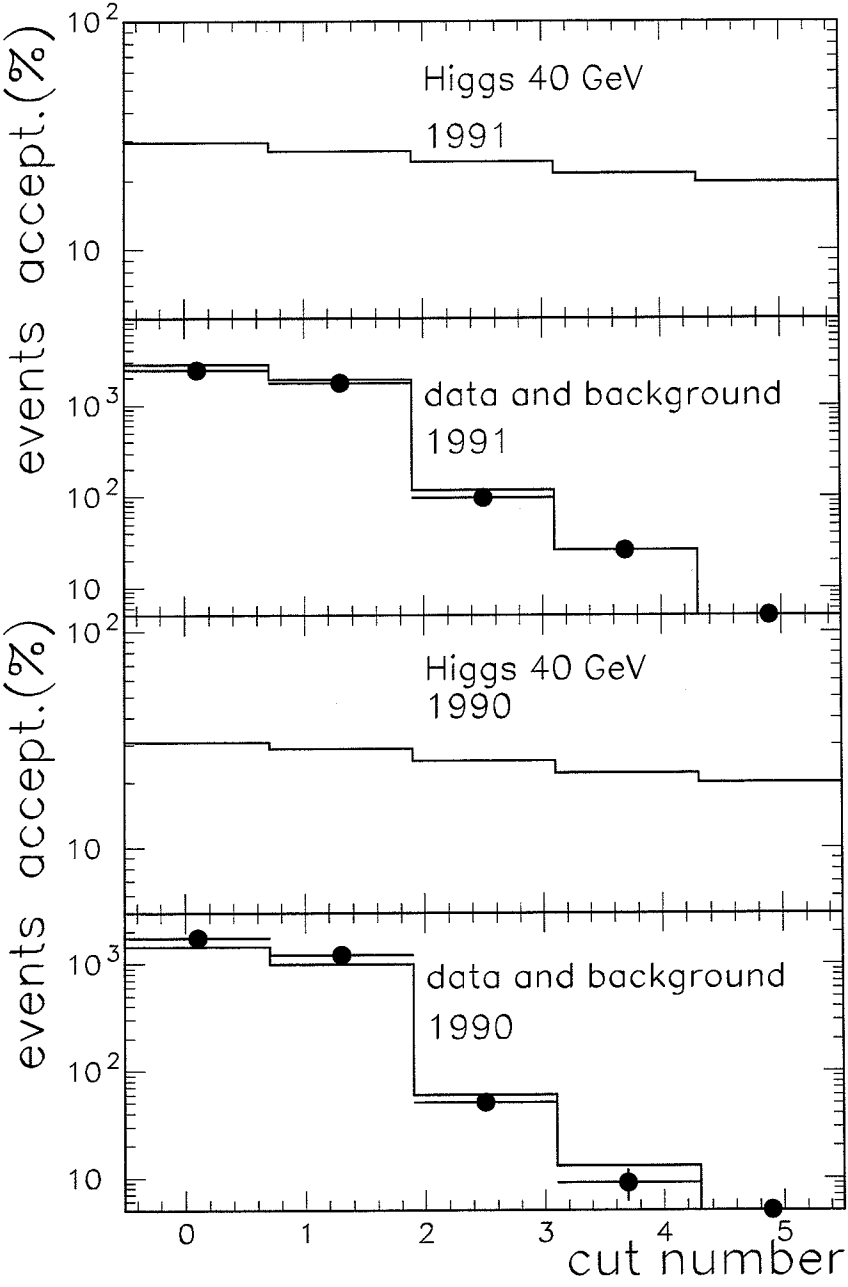

Figure G.1: Acceptances and numbers of data and background events after a cut is applied in the $\tau\nu\tau\nu$ channel. Bin 0 corresponds to the preselection.

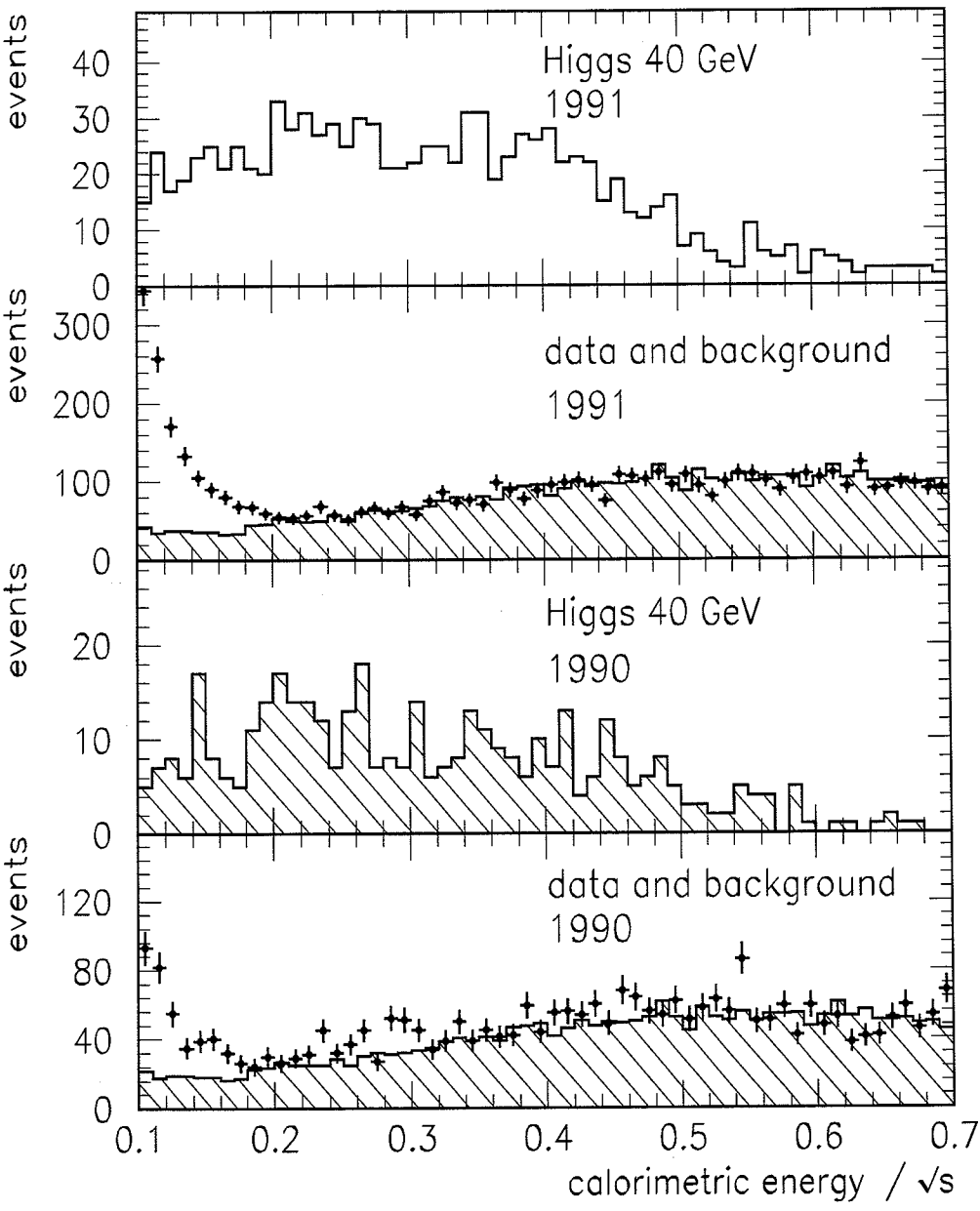

Figure G.2: Distribution of the total calorimetric energy in the $\tau\nu\tau\nu$ channel.

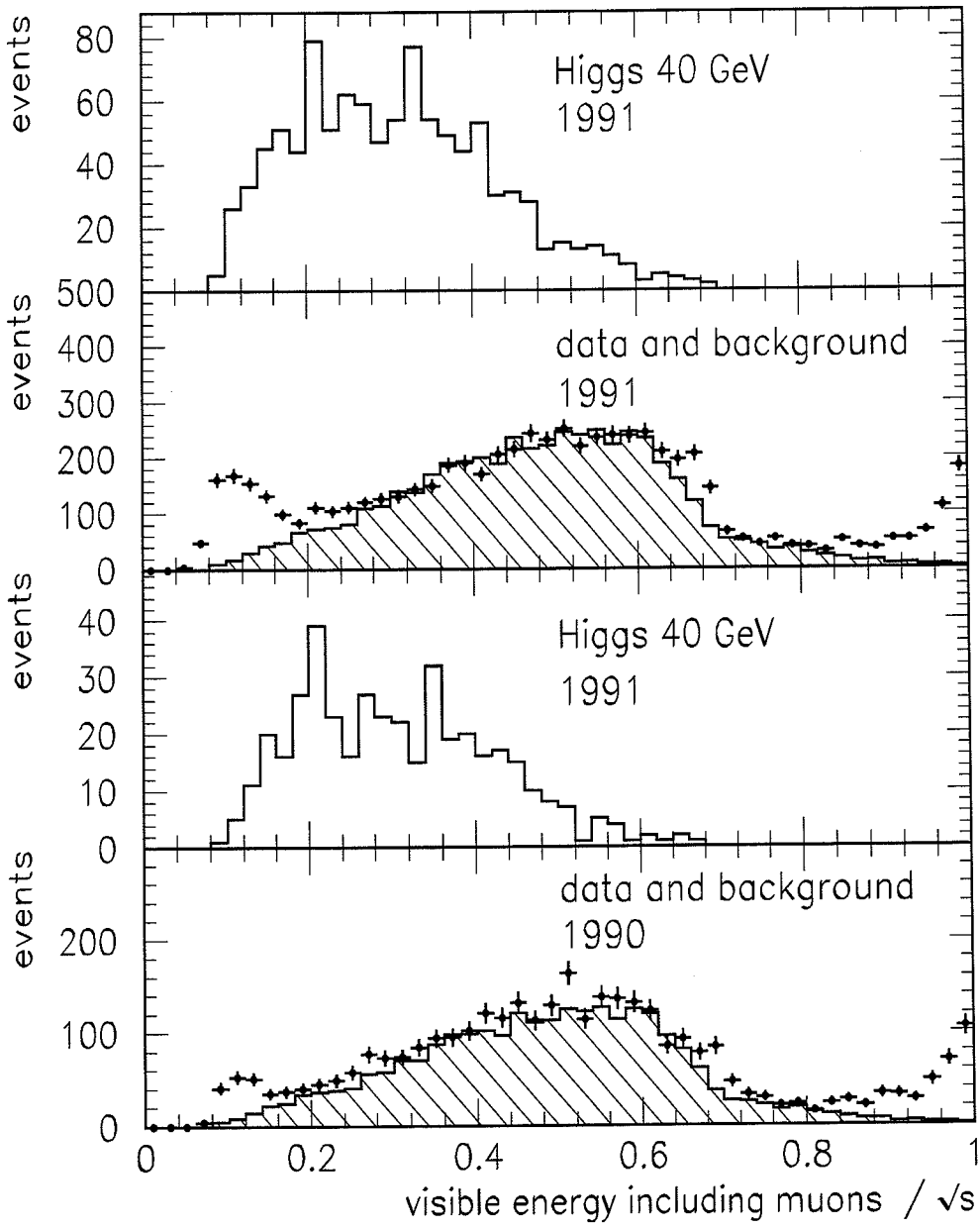

Figure G.3: Distribution of the visible energy in the $\tau\nu\tau\nu$ channel.

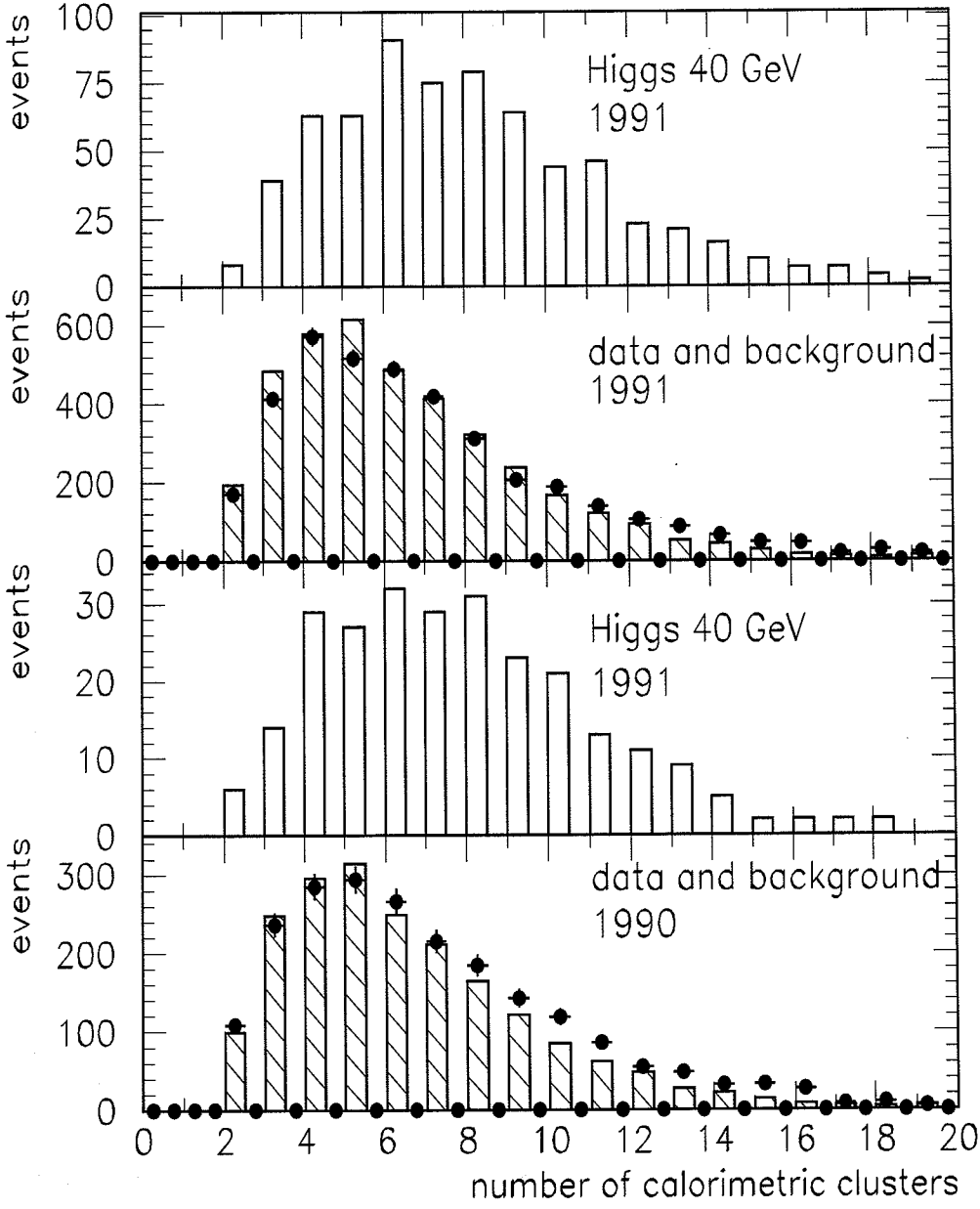

Figure G.4: Distribution of the number of calorimetric cluster in the $\tau\nu\tau\nu$ channel.

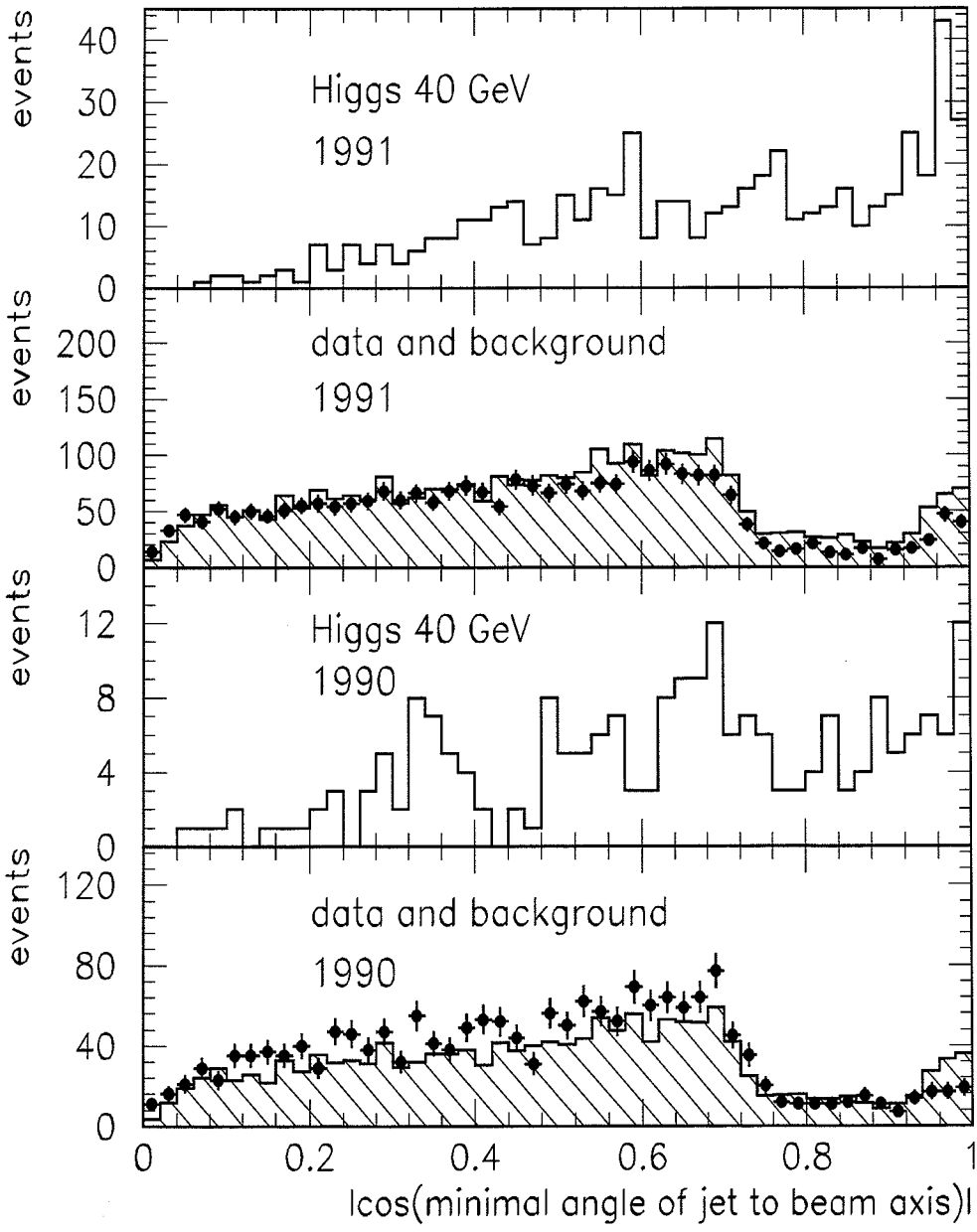

Figure G.5: Distribution of the minimum azimuthal jet angle (after $|\cos\theta_T| \leq 0.7$ cut) in the $\tau\nu\tau\nu$ channel.

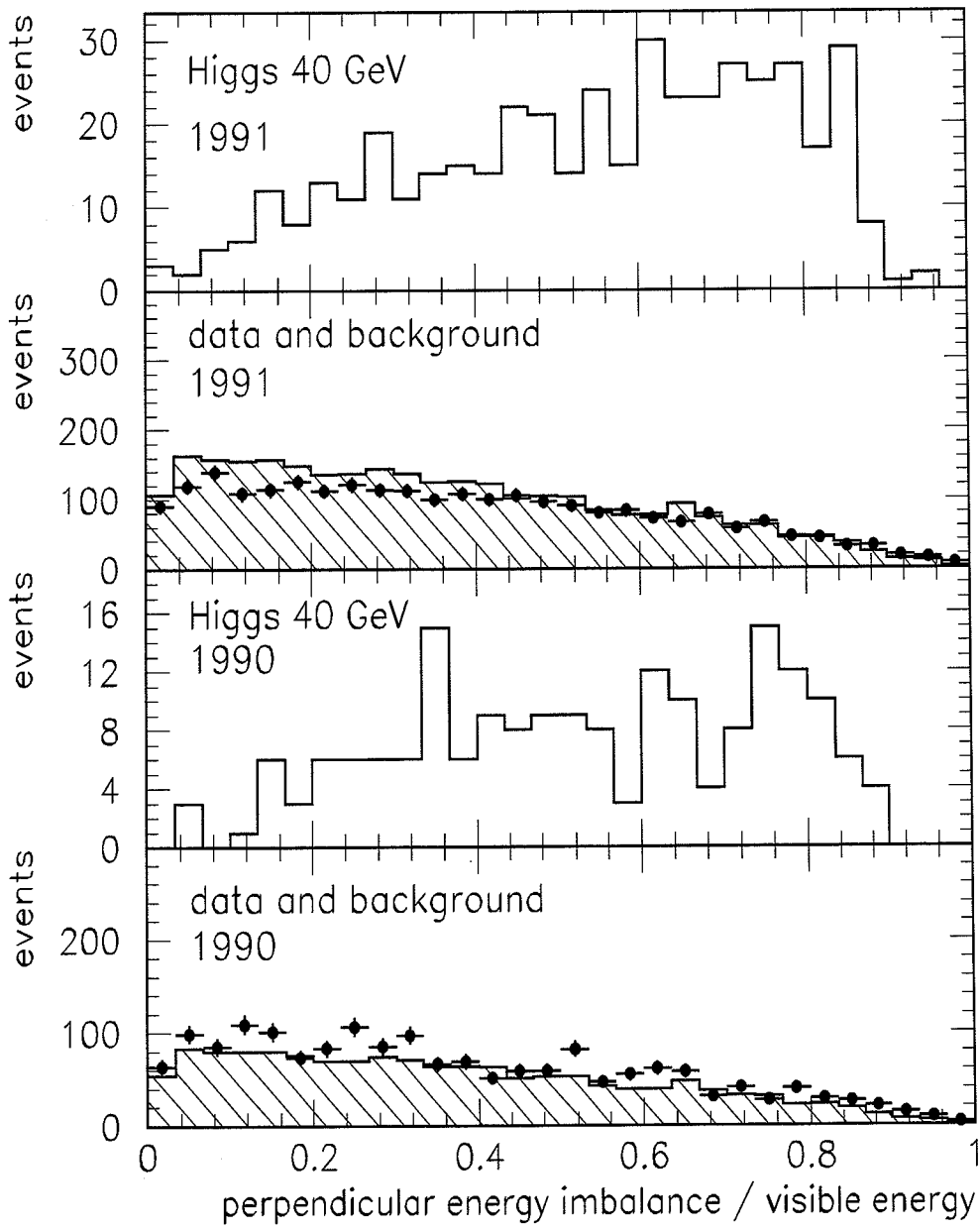

Figure G.6: Distribution of the perpendicular energy imbalance in the $\tau\nu\tau\nu$ channel.

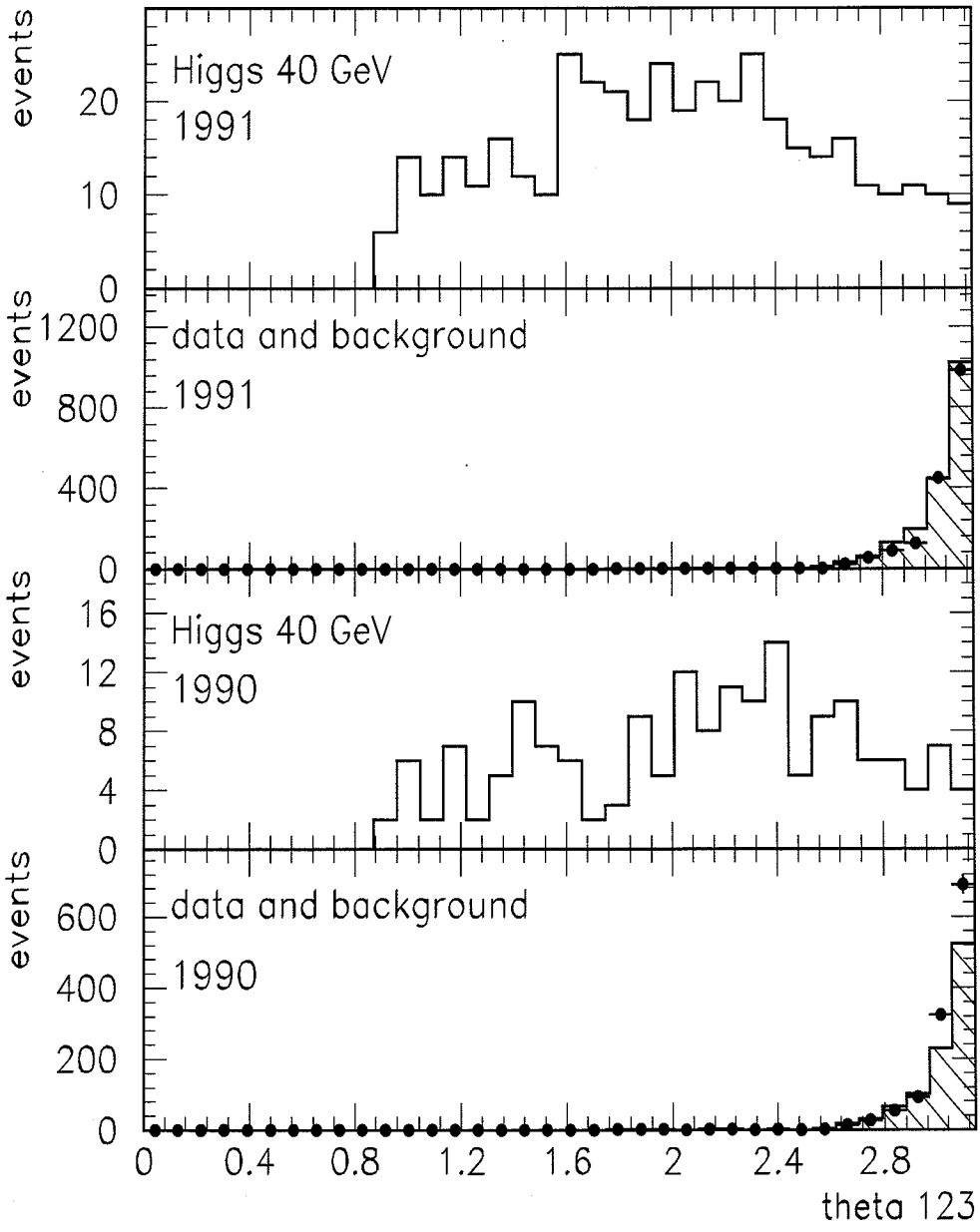

Figure G.7: Distribution of θ_{123} in the $\tau\nu\tau\nu$ channel.

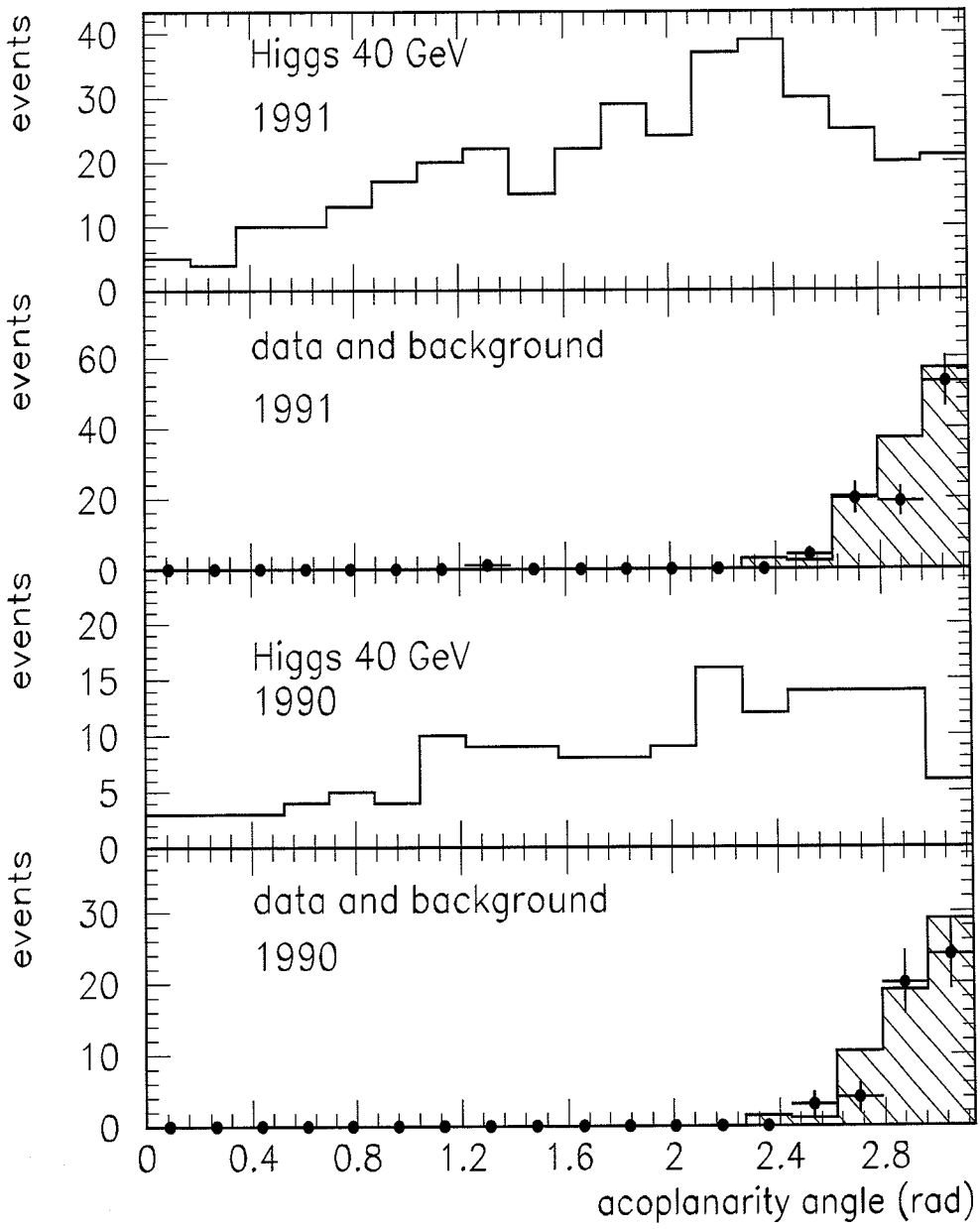

Figure G.8: Distribution of the acoplanarity angle in the $\tau\nu\tau\nu$ channel.

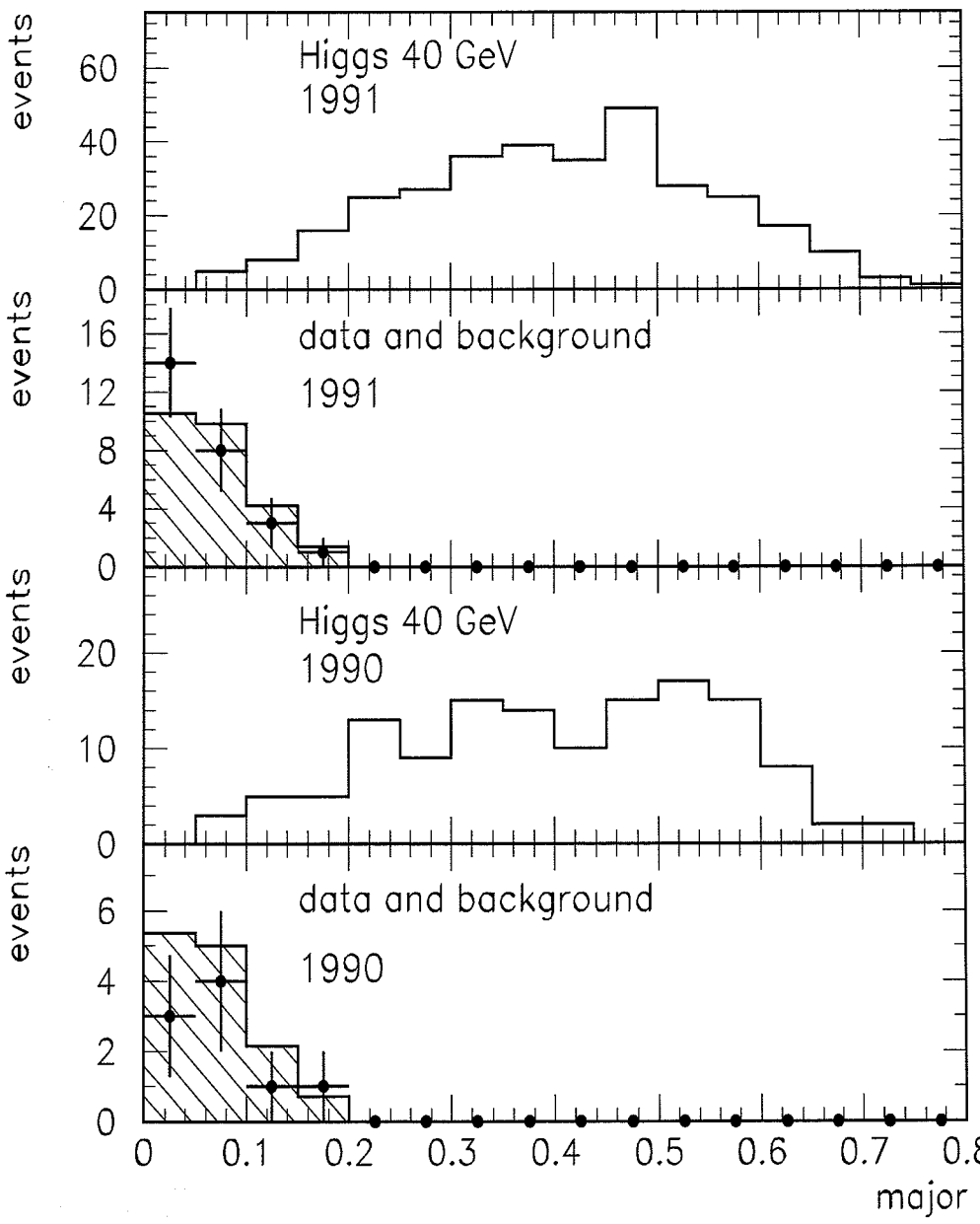

Figure G.9: Distribution of the major in the $\tau\nu\tau\nu$ channel.

References

[1] J. Rafelski, B. Müller, "Die Strukture des Vakuums" (Verlag Harri Deutsch, 1985).

[2] Y. Nambu, *Phys. Rev.* **117** (1960) 648;
Y. Nambu and G. Jona-Lasinio, *Phys. Rev.* **122** (1961) 345.

[3] V.L. Ginzburg and L.D. Landau, *Zh. Eksp. Teor. Fiz.* **20** (1950) 1064.

[4] J. Goldstone, *Nuo. Cim.* **19** (1961) 15.

[5] M. Gellman and Y.Ne'eman, "The Eightfold Way" (Benjamin Press, New York, 1964).

[6] P.W. Higgs, *Phys. Lett.* **12** (1964) 132;
P.W. Higgs, *Phys. Rev. Lett.* **13** (1964) 508;
P.W. Higgs, *Phys. Rev.* **145** (1966) 1156;
F. Englert and R. Brout, *Phys. Rev. Lett.* **13** (1964) 321;
G.S. Guralnik, C.S. Hagen and T.W.B. Kibble, *Phys. Rev. Lett.* **13** (1964) 585.

[7] S.L. Glashow, *Nucl. Phys.* **22** (1961) 579;
A. Salam, *Phys. Rev.* **127** (1962) 331;
A. Salam, in: "Elementary Particle Theory", ed. N. Svartholm (Stockholm, 1968), 361;
S. Weinberg, *Phys. Rev. Lett.* **19** (1967) 1264.

[8] G. 't Hooft, *Nucl. Phys.* **B 35** (1971) 167;
G. 't Hooft and M. Veltmann, *Nucl. Phys.* **B 33** (1971) 173.

[9] K. Hikasa *et al.*, "Review of Particle Properties", *Phys. Rev.* **D 45** (1992) 1.

[10] CDF Collaboration, F. Abe *et al.*, *Phys. Lett.* **64** (1989) 143;
CDF Collaboration, F. Abe *et al.*, Preprint Fermilab, Pub-91/280-E (1991).

[11] P. Langacker, Preprint Univiversity of Pennsylvania, UPR-0468T (1991).

[12] UA2 Collaboration, Preprint CERN, PPE/91-163 (1991);
ALEPH, DELPHI, L3, OPAL Collaborations, Preprint CERN, PPE/91-232 (1991);
G.V. Chibisov, *Usp. Fiz. Nauk* **119** (1976) 551.

[13] J. Zinn-Justin, "Quantum Field Theory and Critical Phenomena" (Oxford Science Publications, 1989).

[14] M. Sher, *Phys. Rep.* **179** (1989) 273.

[15] I.V. Krive and A.D. Linde, *Nucl. Phys.* **B 117** (1976) 265.

[16] S. Coleman, E. Weinberg, *Phys. Rev.* **D 7** (1973) 1888.

[17] D.A. Kirzhits, *JETP Lett.* **15** (1972) 745;
D.A. Kirzhits and A. Linde, *JETP Lett.* **19** (1974) 320.

[18] G. Fuller, private communications.

[19] J. Kuti, L. Lin and Y. Shen in "Lattice Higgs Workshop", Florida State University May 16-18, 1989, eds. B. Berg, G. Bhanot, M. Burbank, M. Creutz, J.Owens (World Scientific) p.140 and references therein.

[20] A. Sopczak, Plenary Talk given on "Higgs Searches at LEP-I" at the XV International Meeting on Elementary Particle Physics, Kazimierz, Poland, 25–29 May 1992, to be published by World Scientific, L3 note #1230, August 1992 and Preprint CERN, PPE/92-137 (1992).

[21] J. D. Bjorken, in Proceedings of the 1976 SLAC Summer Institute on Particle Physics, Stanford, edited by M. C. Zipf (Stanford Linear Accel. Center, Stanford, CA, 1977).

[22] F. A. Berends and R. Kleiss, *Nucl. Phys.* **B 260** (1985) 32.

[23] M. Consoli and W. Hollik, in "Z Physics at LEP 1", eds. G. Altarelli, R. Kleiss and C. Verzegnassi, CERN Report CERN-89-08, Vol. 1 (1989) p. 39 and references therein.

[24] S. Dawson and S. Willebrock, *Phys. Lett.* **B 211** (1988) 200;
Z. Hioki, *Phys. Lett.* **B 224** (1989) 417.

[25] M. Voloshin and V. Zakharov, *Phys. Rev. Lett.* **45** (1980) 688;
M. Voloshin, *Sov. J. Nucl. Phys.* **44 (3)** (1986) 478;
S. Raby and G.B. West, *Phys. Rev.* **D 38** (1988) 3488.

[26] J.P. Franzini and P. Taxil in "Z Physics at LEP 1", eds. G. Altarelli, R. Kleiss and C. Verzegnassi, CERN Report CERN-89-08, Vol. 2 (1989) p. 65 and references therein.

[27] Fermilab-Conf.-90/29-T (1990).

[28] M. Savage, *Phys. Lett.* **B 266** (1991) 135,
For a review, see K. Hikasa *et al.*, "Review of Particle Properties", *Phys. Rev.* **D 45** (1992) 1.

[29] S.L. Glashow and S. Weinberg, *Phys. Rev.* **D 15** (1977) 1958.

[30] H.E. Haber, private communications.

[31] H.I. Behrend *et al.*, *Phys. Lett.* **B 193** (1987) 376 and references therein.

[32] F.J. Gilman and Y. Nir, *Ann. Rev. Nucl. Phys.* **40** (1990) 213.

[33] L3 Collaboration, B. Adeva *et al.*, Preprint CERN, PPE/92-84 (1992).

[34] G.G. Athanasiu, P.J. Franzizi and F.J. Gilman, *Phys. Rev.* **D 32** (1985) 3010.

[35] L. Taylor, Talk given at the "XXVII Rencontres de Moriond", Les Arcs, France (15 March - 22 March, 1992).

[36] J. Freund, G. Kreyerhoff and R. Rodenberg, Aachen Preprint 91-0232, (1991). Published in the Proceedings of the "Joint International Lepton-Photon Symposium & Europhysics Conference on High Energy Physics", Geneva (25 July - 1 August 1991).

[37] A.T. Davies, Preprint, LAL, 91-48 (1991). Published in the Proceedings of the "Joint International Lepton- Photon Symposium & Europhysics Conference on High Energy Physics", Geneva (25 July - 1 August 1991).

[38] M.E. Shaposhnikov, *Nucl. Phys.* **B 287** (1987) 535;
P. Arnold, *Phys. Rev.* **D 36** (1987) 581;
L.M. Krauss, Preprint Yale, YCTP-P36-91 (1991).

[39] J. Maalampi, J. Sirkka and I. Vilja, Preprint HU-TFT, 91-16 (1991).

[40] Y.A. Golfand and E.P. Likhtman, *JETP Lett.* **13** (1971) 323;
D.V. Volkhov and V.P. Akulov, *Phys. Lett.* **B 46** (1973) 109;
J. Wess and B. Zumino, *Nucl. Phys.* **B 70** (1974) 39;
P. Fayet and S. Ferrara, *Phys. Rep.* **32** (1977) 249;
A. Salam and J. Strathdee, *Fortschr. Phys.* **26** (1978) 57;
H.P. Nilles, *Phys. Rep.* **110** (1984) 1.

[41] G. 't Hooft *et al.*, "Recent Developments in Gauge Theory", NATO Advanced Study Institute, Cargese, (Plenum Press, 1979).

[42] N. Sakai, *Z. Phys.* **C 11** (1981) 153 and references therein.

[43] L3 Collaboration, B. Adeva *et al.*, *Phys. Lett.* **B 233** (1989) 530;
H. Newman, L3 Note 801, (1990).

[44] U. Amaldi *et al.*, Preprint CERN, PPE/91-233 (1991).

[45] S. Dawson, J.F. Gunion, H.E. Haber and G.L. Kane, "The Physics of the Higgs Bosons: Higgs Hunter's Guide" (Addison Wesley, Menlo Park, 1989).

[46] L3 Collaboration, B. Adeva *et al.*, *Phys. Lett.* **B 251** (1990) 331.

[47] J. Ellis, G. Ridolfi and F. Zwirner, *Phys. Lett.* **B 257** (1991) 83;
H.E. Haber and R. Hempfling, *Phys. Rev. Lett.* **66** (1991) 1815;
Y. Okada, M. Yamaguchi and T. Yanagida, *Prog. Theor. Phys. Lett.* **85** (1991) 1.

[48] S.P. Li and M. Sher, *Phys. Lett.* **B 140** (1984) 339;
J.F. Gunion and A. Turski, *Phys. Rev.* **D 39** (1989) 2701;
J.F. Gunion and A. Turski, *Phys. Rev.* **D 40** (1989) 2325;
J.F. Gunion and A. Turski, *Phys. Rev.* **D 40** (1989) 2333;
M.S. Berger, *Phys. Rev.* **D 41** (1990) 225.

[49] R. Barbieri, M. Frigeni and F. Caravaglios, *Phys. Lett.* **B 258** (1991) 167;
R. Barbieri and M. Frigeni, *Phys. Lett.* **B 258** (1991) 395;
J. Ellis, G. Ridolfi and F. Zwirner, *Phys. Lett.* **B 257** (1991) 83;
A. Yamada, *Phys. Lett.* **B 263** (1991) 233;
Z. Kunszt and F. Zwirner, Preprint CERN-TH, 6150 (1991);
J.L. Lopez and D.V. Nanopoulos, *Phys. Lett.* **B 266** (1991) 397.

[50] R. Barbieri and M. Frigeni, *Phys. Lett.* **B 258** (1991) 395;
A. Brignole, J. Ellis, G. Ridolfi and F. Zwirner, *Phys. Lett.* **B 271** (1991) 123;
J.Ellis, G. Ridolfi and F. Zwirner, *Phys. Lett.* **B 262** (1991) 477.

[51] R. Barbieri and M. Frigeni, *Phys. Lett.* **B 258** (1991) 395.

[52] J.Ellis, G. Ridolfi and F. Zwirner, *Phys. Lett.* **B 262** (1991) 477.

[53] CDF Collaboration, F. Abe *et al.*, *Phys. Rev. Lett.* **62** (1989) 1825,
UA2 Collaboration, *Phys. Lett.* **B 235** (1990) 363.

[54] L. Rolandi, Plenary talk given at the XXVI International Dallas Conference on Particle Physics, Dallas, 6–12 August 1992.

[55] J. Ellis *et al.*, *Phys. Rev.* **D 39** (1989) 844.

[56] A. Hasenfratz *et al.*, Preprint UCSD, PTH 91-06 (1991).

[57] L3 Collaboration, B. Adeva *et al.*, *Phys. Lett.* **B 247** (1990) 177;
L3 Collaboration, B. Adeva *et al.*, *Phys. Lett.* **B 250** (1990) 205;
L3 Collaboration, B. Adeva *et al.*, *Phys. Lett.* **B 252** (1990) 713.

[58] G. Altarelli, R. Barbieri and S. Jadach, Preprint CERN, TH.6124/91 (1991).

[59] ALEPH Collaboration, Letter of intent, (1982);
DELPHI Collaboration, Letter of intent, (1982);
L3 Collaboration, Letter of intent, (1982);
OPAL Collaboration, Letter of intent, (1982).

[60] The LEP Injector Study Group, "LEP Design Report" Vol. I and II, CERN-LEP/84-01 (1984);
I. Wilson and H. Henke, "The LEP Main Ring Accelerator Structure", CERN 89-09 (1989).

[61] R. Bailey *et al.*, "LEP Energy Calibration", CERN, SL/90-95 (1990);
L. Arnaudon *et al.*, Preprint CERN, PPE/92-125 (1992).

[62] J.J. Aubert *et al.*, *Phys. Rev. Lett.* **33** (1974) 1404;
J.E. Augustin *et al.*, *Phys. Rev. Lett.* **33** (1974) 1406.

[63] UA1 Collaboration, G. Arnison *et al.*, *Phys. Lett.* **B 126** (1983) 398;
UA2 Collaboration, P. Bagnaia *et al.*, *Phys. Lett.* **B 129** (1983) 130.

[64] L3 Collaboration, B. Adeva *et al.*, *Nucl. Instrum. Methods* **A 189** (1990) 35.

[65] D.N. Ren, "The L3 Vertex Chamber Development and Infrastructure", Thesis, Swiss Federal Institute of Tech., Zürich, 1990.

[66] I.A. Bakken *et al.*, *Nucl. Instrum. Methods* **A 254** (1987) 1990;
M. Schneegans, *Nucl. Instrum. Methods* **257 A** (1987) 528.

[67] GEANT Version 3.13, September, 1989.
See R. Brun et al., "GEANT 3", CERN DD/EE/84-1 (Revised), Sept. 1987.

[68] H.M. Bischops, "Bau und Test der Triggerzähler des L3-Experimentes", Diplomarbeit, III Physikalisches Institut der RWTH Aachen, 1988;
U. Uwer, "Aufbau und Eichung der Scintillationszählers des L3-Experiments", Diplomarbeit, III Physikalisches Institut der RWTH Aachen, 1990 .

[69] Yu. Galaktionov *et al.*, *Nucl. Instrum. Methods* **A 251** (1986) 258;
B. Bleichert *et al.*, *Nucl. Instrum. Methods* **A 254** (1987) 529;
H. Martyn and J.F. Zhou, *Nucl. Instrum. Methods* **A 256** (1987) 143;
A. Arefiev *et al.*, *Nucl. Instrum. Methods* **A 285** (1989) 403;
A. Arefiev *et al.*, *Nucl. Instrum. Methods* **A 288** (1990) 364;
O. Adriani *et al.*, *Nucl. Instrum. Methods* **A 302** (1991) 53.

[70] Y. Peng, "The Muon Spectrometer of the L3 Detector at LEP", Thesis, University of Amsterdam, 1988;
B. Adeva *et al.*, *Nucl. Instrum. Methods* **A 277** (1989) 187;
J. Onvlee, "The Behaviour of the L3 Muon Chambers in a Magnetic Field", Thesis, University of Amsterdam, 1989.

[71] L3 Collaboration, B. Adeva *et al.*, *Z. Phys.* **C 51** (1991) 179.

[72] M. Böhm, A. Denner and W. Hollik, *Nucl. Phys.* **B 304** (1988) 687;
F.A. Berends, R. Kleiss and W. Hollik, *Nucl. Phys.* **B 304** (1988) 712.

[73] M. Bourquin *et al.*, *Nucl. Instrum. Methods* **306 A** (1991) 151.

[74] L3 Collaboration, B. Adeva *et al.*, *Phys. Lett.* **B 252** (1990) 713.

[75] T. Sjöstrand and M. Bengtsson, *Comput. Phys. Commun.* **43** (1987) 367;
T. Sjöstrand, in "Z Physics at LEP 1", eds. G. Altarelli, R. Kleiss and C. Verzegnassi, CERN Report CERN-89-08, Vol. 3 (1989) p. 143.

[76] L3 Collaboration, B. Adeva *et al.*, Preprint CERN, PPE/92-50 (1992).

[77] T. Sjöstrand in "Z Physics at LEP 1", eds. G. Altarelli, R. Kleiss and C. Verzegnassi, CERN Report CERN-89-08 (1989), Vol. 3, p. 143 and references therein.

[78] B. Andersson, G. Gustafson, G. Ingelman and T. Sjöstrand, *Phys. Rep.* **97** (1983) 31.

[79] L3 Collaboration, B. Adeva *et al.*, Preprint CERN, PPE/92-50 (1992).

[80] C. Peterson, D. Schlatter, I. Schmitt and P. Zerwas, *Phys. Rev.* **D 27** (1983) 105.

[81] L3 Collaboration, B. Adeva *et al.*, *Phys. Lett.* **B 261** (1991) 177.

[82] R. Clare, Talk given at the XXVI International Dallas Conference on Particle Physics, Dallas, 6–12 August 1992.

[83] S. Jadach *et al.*, "Z Physics at LEP 1", eds. G. Altarelli, R. Kleiss and C. Verzegnassi, CERN Report CERN-89-08 (1989), Vol. 3, p. 69.

[84] H.-U. Bengtsson and T. Sjöstrand, Comput. Phys. Commun. **46** (1987) 43.

[85] P.J. Franzini *et al.* in "Z Physics at LEP 1", eds. G. Altarelli, R. Kleiss and C. Verzegnassi, CERN Report CERN-89-08, Vol. 2 (1989) p. 59.

[86] Z. Kunszt, *Phys. Lett.* **B 99** (1981) 429;
J.A.M. Vermaseren, K.J.F. Gaemers and S.J. Oldham, *Nucl. Phys.* **B187** (1981) 301.

[87] L3 Collaboration, B. Adeva *et al.*, *Phys. Lett.* **B 248** (1990) 203.

[88] L3 Collaboration, B. Adeva *et al.*, "Search for Non-Minimal Higgs Bosons from Z^0 Decays", Preprint CERN, PPE/92-163 (1992) (submitted to *Z. Phys. C*).

[89] L3 Collaboration, B. Adeva *et al.*, *Phys. Lett.* **B 283** (1992) 454.

[90] F. A. Berends, P. H. Daverveldt and R. Kleiss, *Nucl. Phys.* **B 253** (1985) 441.

[91] L3 Collaboration, B. Adeva *et al.*, Preprint CERN, PPE/92-84 (1992).

[92] See L3 Collaboration, B. Adeva *et al.*, *Phys. Lett.* **B 252** (1990) 511.

[93] ALEPH, DELPHI, L3, OPAL Collaborations, Preprint CERN, PPE/91-232 (1991).

[94] F. Linde, Talk given at the "XXVII Rencontres de Moriond", Les Arcs, France (15 March - 22 March, 1992).

[95] D. Bardin *et al.*, *Nucl. Phys.* **B 351** (1991) 1;
D. Bardin *et al.*, *Z. Phys.* **C 44** (1989) 493;
D. Bardin *et al.*, *Phys. Lett.* **B 255** (1991) 290;
M. Bilenky and A. Sazonov, JNIR Dubna Preprint E2-89-792 (1989).

[96] J. Ellis, Preprint CERN, TH.6193/91 (1991).

[97] M. Davier, *Proc.* LP-HEP 91 Conference, Geneva, 1991.

[98] P. Langacker, Preprint Univiversity of Pennsylvania, UPR-0468T (1991).

[99] L3 Collaboration, B. Adeva *et al.*, *Z. Phys.* **C 51** (1991) 179;
J. Rose, "Bestimmung von Parametern der Elektroschwachen Theorie mit dem L3-Detektor bei LEP", Thesis, University of Aachen I, 1992.

[100] ALEPH Collaboration, D. Decamp *et al.*, *Phys. Lett.* **B 237** (1990) 291;
ALEPH Collaboration, D. Decamp *et al.*, *Phys. Lett.* **B 265** (1991) 475;
ALEPH Collaboration, D. Decamp *et al.*, *Phys. Lett.* **B 241** (1990) 623;
ALEPH Collaboration, D. Decamp *et al.*, *Phys. Lett.* **B 245** (1990) 289;
ALEPH Collaboration, D. Decamp *et al.*, Preprint CERN, PPE/92-59 (1992

[101] DELPHI Collaboration, P. Abreu *et al.*, *Nucl. Phys.* **B 245** (1990) 276;
DELPHI Collaboration, P. Abreu *et al.*, *Nucl. Phys.* **B 373** (1992) 3;
DELPHI Collaboration, P. Abreu *et al.*, *Nucl. Phys.* **B 241** (1990) 449;

DELPHI Collaboration, P. Abreu *et al.*, *Phys. Lett.* **B 343** (1990) 1;
DELPHI Collaboration, P. Abreu *et al.*, *Z. Phys.* **C 51** (1991) 25.

[102] L3 Collaboration, B. Adeva *et al.*, *Phys. Lett.* **B 251** (1990) 331;
L3 Collaboration, B. Adeva *et al.*, *Phys. Lett.* **B 252** (1990) 511;
L3 Collaboration, B. Adeva *et al.*, *Phys. Lett.* **B 252** (1990) 518.

[103] OPAL Collaboration, M.Z. Akrawi *et al.*, *Z. Phys.* **C 49** (1991) 1;
OPAL Collaboration, M.Z. Akrawi *et al.*, *Phys. Lett.* **B 242** (1990) 299;
OPAL Collaboration, P.D. Acton *et al.*, *Phys. Lett.* **B 251** (1990) 211;
OPAL Collaboration, P.D. Acton *et al.*, *Phys. Lett.* **B 268** (1991) 122.

[104] ALEPH Collaboration, D. Decamp *et al.*, Preprint CERN, PPE/91-149 (1991), ALEPH Collaboration: "Improved mass limits for the neutral Higgs bosons of the MSSM", internal note 92-24, Feb. 1992.

[105] DELPHI Collaboration, Contributed papers to the XXVI International Dallas Conference on Particle Physics, Dallas, 6–12 August. 1992.

[106] A. Sopczak *et al.*, L3 note #1213, July 1992 "Search for Non-Minimal Higgs Bosons from Z^0 Decays", L3 contributed paper to the XXVI International Dallas Conference on Particle Physics, Dallas, 6–12 August 1992.

[107] OPAL Collaboration: "Search for Higgs Bosons in the Minimal Supersymmetric Model Including One-Loop Radiative Corrections", internal notes PN041, Aug. 1991, and PN053, Feb. 1992.

[108] L3 Collaboration, B. Adeva *et al.*, *Phys. Lett.* **B 251** (1990) 331;
L3 Collaboration, B. Adeva *et al.*, *Phys. Lett.* **B 252** (1990) 518;
L3 Collaboration, B. Adeva *et al.*, *Phys. Lett.* **B 252** (1990) 511;
A. Sopczak, L3 note #1164 "Search for Z^0 Decays into Neutral and Charged Higgs Pairs", Dec. 1990;
A. Sopczak, L3 Note #1169, "Limits on Physics Beyond the Minimal Standard Model from LEP Line-Shape Data", May 1992;
M. Felcini and A. Sopczak, L3 note #1214 "Search for Higgs Bosons in the $\tau\tau\tau\tau$ and $\tau\tau$ jet jet Channels from Z^0 Decays", July 1992;
A. Gurtu and A. Sopczak, "Search for Z^0 Decays into Higgs Boson Pairs in Multi-Jet Channels" L3 note #1250, September, 1992;

L3 Collaboration, B. Adeva *et al.*, "Search for Non-Minimal Higgs Bosons from Z^0 Decays", Preprint CERN, PPE/92-140 (1992) (submitted to *Phys. Lett. B*);
L3 Collaboration, B. Adeva *et al.*, "Search for Non-Minimal Higgs Bosons from Z^0 Decays", Preprint CERN, PPE/92-163 (1992) (submitted to *Z. Phys. C*).